ADVANCES IN *IN-SITU* SPECTROELECTROCHEMICAL FOURIER TRANSFORM INFRARED SPECTROSCOPY

A Thesis Submitted to the College of

Graduate Studies and Research

In Partial Fulfillment of the Requirements

For the Degree of Doctor of Philosophy

In the Department of Chemistry

University of Saskatchewan

Saskatoon

By

SCOTT MICHAEL ROSENDAHL

PERMISSION TO USE

In presenting this thesis in partial fulfilment of the requirements for a Postgraduate degree from the University of Saskatchewan, I agree that the Libraries of this University may make it freely available for inspection. I further agree that permission for copying of this thesis in any manner, in whole or in part, for scholarly purposes may be granted by the professor or professors who supervised my thesis work or, in their absence, by the Head of the Department or the Dean of the College in which my thesis work was done. It is understood that any copying or publication or use of this thesis or parts thereof for financial gain shall not be allowed without my written permission. It is also understood that due recognition shall be given to me and to the University of Saskatchewan in any scholarly use which may be made of any material in my thesis.

Requests for permission to copy or to make other use of material in this thesis in whole or part should be addressed to:

Head of the Department of Chemistry

University of Saskatchewan

Saskatoon, Saskatchewan

S7N 5C9

Canada

ABSTRACT

The level of information provided by electrochemical measurements can be substantial as evident by the use of electrochemistry in varied disciplines spanning from materials research to cellular biochemistry. However, electrochemistry on its own does not provide direct information concerning redox induced changes in molecular structure. This information can only be elucidated by coupling spectroscopic and/or separation techniques with traditional electrochemical methodologies. In principle, infrared (IR) spectroelectrochemistry (SEC) is ideal for such studies but in practice coupling IR spectroscopy and electrochemistry are often experimentally incompatible. Since the inception of *in-situ* IR SEC techniques in the 1980's, two competing methodologies (using either external- or internal- IR reflection geometries), were developed to deal with the two major challenges associated with IR SEC (strong infrared absorption of the electrolytes and weak analytical signals). The primary focus of this thesis is the successful advancement of IR SEC techniques through the implementation of synchrotron infrared radiation with ultramicroelectrodes (UMEs; electrode diameters < 25 μm) to study spectroelectrochemical processes on the microsecond time scale.

Several examples using Surface Enhanced Infrared Absorption Spectroscopy (SEIRAS) are presented including the adsorption of dimethylaminopyridine (DMAP) on gold substrates and the proton-coupled electron-transfer (PCET) kinetics of electrochemically-active 1,4-benzoquinone terminated self-assembled monolayers (SAMs). These studies highlight the benefits of coupling electrochemistry and infrared spectroscopy. For instance, *in-situ* spectroscopic evidence shows that small amounts of DMAP's conjugate acid ($DMAPH^+$) adsorb on gold electrodes in acidic electrolytes and at negative potentials. This result was not

forthcoming from previous electrochemical measurements and was only realized through *in-situ* SEIRAS.

Finally, the largest contribution in advancing *in-situ* IR SEC methodologies was through the development of utilizing synchrotron infrared radiation on UMEs to study fast electrochemical processes. This work was technically very challenging and emphasized the interfacing of an electrochemical cell containing an UME with fast infrared data acquisition techniques (*i.e.* rapid scan and step-scan interferometry). The use of a prototypical electrochemical system, *i.e.* the mass-transport controlled reduction of ferricyanide, indicate that at short times the spectroscopic signal closely matches the electrochemical signal but at long time scales it deviates due to edge effects associated with the diffusion environment of the UME.

ACKNOWLEDGEMENTS

First, I would like to thank Prof. Ian Burgess for being my supervisor and more so, my mentor through the course of my graduate studies. It is through his support and constant encouragement that made this thesis possible.

To my parents, there are no words to describe how grateful I am to have the love and support you have provided me throughout my academic career. Your advice and encouragement has helped me understand that through hard work and perseverance I can accomplish anything I set my mind on. To my brother Wayne, thank you for reminding me not to take everything so seriously. My wife Ashley, I do not know how I would have done any of this without you and I look forward to spending the rest of my life with you. Finally, to my friends, please do not take this lightly but I truly appreciate all that you do for me and I thank you for being a part of my life.

A Special thanks to my committee, Prof. Andrzej Baranski and Prof. Richard Bowles for their support, guidance and helpful suggestions. In addition, without the support of the Beamline Scientists at the Canadian Light Source, Dr. Ferenc Borondics and Mr. Tim May, none of synchrotron experiments in this thesis would have been possible. Also, Mr. Blair Chomyshen and Mr. Ted Toporowski in the Physics Machine Shop at the University of Saskatchewan for turning my design sketches into actual objects to perform every one of the experiments presented in this thesis.

I would like to thank the organizations that have played a major role in the work done in this thesis. To start, the financial support of National Science and Engineering Research Council (NSERC) through the Post Graduate Scholarship program and the University of Saskatchewan for support through the Herzberg Memorial Scholarship program. Finally, the research described in this paper was performed at the Canadian Light Source, which is funded by the Canada Foundation for Innovation, the Natural Sciences and Engineering Research Council of Canada, the National Research Council Canada, the Canadian Institutes of Health Research, the Government of Saskatchewan, Western Economic Diversification Canada, and the University of Saskatchewan.

To my mother and father, thank you for your guidance, love and support through all these years.
To my beloved wife Ashley, who helped me each step of the way.

TABLE OF CONTENTS

LIST OF TABLES

LIST OF FIGURES

LIST OF SCHEMES

LIST OF ABBREVATIONS

AES	Auger Electron Spectroscopy
AIRES	Anomalous Infrared Enhanced Spectroscopy
ATR	Attenuated Total-Internal Reflection
BQ	1,4-Benzoquinone
CAD	Computer Aided Drafting
DC	Differential Capacity
DFT	Discrete Fourier Transform
DMAP	Dimethylaminopyridine
DMPC	1,2-dimyristoyl-sn-glycero-3-phosphocholine
EELS	Electron Energy Loss Spectroscopy
EMIRS	Electrochemically Modulated Infrared Spectroscopy
EPR	Electron Paramagnetic Resonance
ERS	External Reflection Spectroscopy
FTIR	Fourier Transform Infrared
IR	Infrared
IRE	Internal Reflection Element
IRS	Internal Reflection Spectroscopy
LEED	Low-Energy Electron Diffraction
LOD	Limit Of Detection
NDT	1,9-nonanedithiol
NIR	Near Infrared

NMR	Nuclear Magnetic Resonance
OPD	Optical Path Difference
OT	Octanethiol
PCET	Proton Coupled Electron Transfer
PEM	Photoelastic Modulator
PM-IRRAS	Polarization Modulation Infrared Reflection Absorption Spectroscopy
PTFE	Polytetrafluoroethylene
PVC	Polyvinyl Chloride
RAIRS	Reflection Absorption Infrared Spectroscopy
SAM	Self-Assembled Monolayer
SEC	Spectroelectrochemical
SEIRAS	Surface Enhanced Infrared Absorption Spectroscopy
SERS	Surface Enhanced Raman Scattering
SNIFTIRS	Subtractively Normalized Interfacial Fourier Transform Infrared Spectroscopy
UME	Ultramicroelectrode
UV	Ultra Violet
VI	Virtual Instrument
VIS	Visible
XAS	X-Ray Absorption Spectroscopy
XPS	X-ray Photoelectric Spectroscopy
ZPD	Zero Path Difference

CHAPTER 1

INTRODUCTION

It is recognized by electrochemists that measurements of electrical voltages, currents, charges and capacitances at electrical interfaces do not always provide definite identification of electroactive species or intermediates that are produced at, or near, the electrode surface. Although a current signal might be correlated to a known species based on the formal potential for a redox process in a given media, the molecular identity can only be inferred. In more complex environmental and biological systems for example, overlap of formal potentials is quite common leading to the superposition of electrical responses from multiple reactions. The ability to probe additional physical characteristics of these electroactive species to monitor electrode processes, under dynamic or equilibrium conditions, would be immensely valuable. Historically, this concept has motivated electrochemists to attempt to couple various spectroscopic techniques to traditional electrochemical methods to provide better understanding of electron transfer reactions pathways, and adsorption of molecules or ions at electrified interfaces.

The variety and versatility of spectroscopic techniques available to researchers is steadily increasing as is the number of research groups working towards the development and successful use of *in-situ* spectroelectrochemical (SEC) techniques.[1] A few examples include Electron Paramagnetic Resonance (EPR),[2,3] Ultra-Violet/Visible/Near Infrared (UV/VIS/NIR)[2] absorption spectroscopy, X-Ray Absorption Spectroscopy (XAS)[4] and Nuclear Magnetic Resonance (NMR)[3,5] which make use of various molecular, electronic or nuclear properties of the species of interest. A non-exhaustive list includes physical properties such as molar absorptivities, vibrational absorption frequencies, and electronic or magnetic resonance frequencies. Coupling these measurements with traditional electrical parameters is being used routinely to provide new

insight into fundamental electrochemical processes. A particular technique that has garnered a great deal of interest from researchers is the combination of electrochemistry and infrared vibrational spectroscopy. The availability of modern Fourier Transform Infrared (FTIR) spectrometers as well as the wealth of knowledge that can be obtained from infrared spectroscopy provides an accessible means for researchers to study both surface and solution electrochemical species.

In-situ infrared spectroelectrochemistry is a powerful means to acquire collaborating data between molecular spectroscopy and electrochemistry. In particular this technique has found valuable uses in two broad electrochemical research areas: molecular adsorption on electrodes and electrode reactions (electron and charge transfer processes). *In-situ* infrared spectra can provide information about the identity and molecular structure, orientation of adsorbed species and insight into the bonding of these species to the electrode surface. An example of this can be seen in the oxidation of methanol (for use in fuel cells for the production of electricity) as various intermediates (*i.e.* formic acid and formaldehyde) and reaction pathways have been identified through the use of *in-situ* infrared SEC.[6]

In-situ infrared SEC has relatively early beginnings with reports appearing in the primary literature starting with Bewick[7,8] in the early 1980s. Chapter 2 of this thesis will focus on the historical development of *in-situ* infrared SEC techniques and will provide a description of the progression towards modern infrared SEC techniques and methodologies. This Chapter will go on to describe how the development of *in-situ* infrared SEC has been driven by two major experimental problems and has resulted in two distinct methodologies, internal and external infrared reflection techniques to minimize their effects. Both these methods attempt to reduce the most formidable problem in the field, the large absorption of infrared radiation by the bulk

solvent that constitutes the electrolyte. Each approach, while adding valuable knowledge to the fields of electrochemistry and surface science, introduces a host of experimentally challenging problems to overcome. For instance, mass transport becomes problematic when working with a thin-cavity SEC cell configurations and requires careful considered in the interpretation of the results.[9–11] The other aforementioned experimentally challenging problem is the sensitivity of the electrochemical system of interest. Typically the number of molecules under study is quite small and spectroscopic measurements have insufficient signal-to-noise making it increasingly difficult to evaluate the system under examination. Both *in-situ* internal and external infrared reflectance techniques will be employed to study a variety of problems in this thesis highlighting the advantages and disadvantages of each.

The work presented in this thesis focuses primarily on the challenging instrumental developments required to utilize *in-situ* infrared spectroelectrochemistry using both internal and external reflection geometries. These improvements required the adaptation of previously developed methods (*i.e.* surface enhanced infrared absorption spectroscopy; SEIRAS), leading to completely new areas of research where synchrotron infrared radiation is used in conjunction with ultramicroelectrodes to make *in-situ* measurements on the microsecond time scale. As a result, significant understanding of electrochemical related phenomena was realized on topics related to surface adsorption, proton-coupled electron transfer processes and diffusion in thin-cavity environments.

In Chapter 3, the theoretical details of infrared vibrational spectroscopy will be explored including the various means to measure and acquire data (Rapid-Scan and Step-Scan) using Fourier Transform Infrared Spectrometers. The main emphasis of this chapter is to provide the reader with the background required to fully understand the remaining chapters on the

improvements made to various *in-situ* spectroelectrochemical techniques. Chapter 3 will also provide an overview of the theoretical framework of Fourier Transform Infrared spectroscopy with particular emphasis on minimizing data collection times while maintaining data quality. Further instrumentation and methodological discussions will also include the interfacing of the various hardware components required to perform both static and time-resolved *in-situ* SEC experiments and the implementation of synchrotron infrared radiation as a highly brilliant infrared source. Chapter 3 also provides a description of another extensively used *in-situ* SEC technique, Attenuated Total-Internal Reflection Surface Enhanced Infrared Reflection Absorbance Spectroscopy (ATR-SEIRAS) which was extensively used in this thesis. ATR-SEIRAS is an internal reflectance technique that provides high surface sensitivity allowing for the electrochemical study of the structure of the double-layer, adsorption/desorption of molecules or molecular ions, characterization of self-assembled monolayers, and monitoring of electrochemical reactions.

Chapter 4 describes the experimental results of successfully implementing SEIRAS *in-situ* SEC techniques. In this Chapter, SEIRAS was employed to further the understanding of the adsorption of dimethylaminopyridine (DMAP) on gold substrates.[12] Previous work using only electrochemical data and thermodynamic models demonstrated various adsorption geometries of DMAP depending on surface charge densities and pH. With *in-situ* SEC studies of this electrochemical system, the molecular vibrational data of molecules confined to the surface was obtained and demonstrated that the thermodynamic model of adsorption was consistent with SEIRAS. Beyond this result, it was recognized for the first time that in acidic electrolytes and negative electrode potentials, there is a small amount of adsorption of the conjugate acid ($DMAPH^+$), likely due to an electrostatic attraction. This result was not forthcoming in the

previous electrochemical studies and only through the use of an *in-situ* SEC technique was it possible to reveal this new information concerning the interfacial adsorption of DMAP/$DMAPH^+$ at the interface. Chapter 4 highlights the value of adding molecular spectroscopic techniques to traditional electrochemical methods and emphasizes the importance of experimental considerations to acquiring high-quality data.

Chapter 5 examines the use of SEIRAS based *in-situ* SEC techniques by further advancing the measurement technique from electrochemical systems under equilibrium conditions to the study of the kinetics of an electrochemical reaction. This increases the complexity of the collection and processing of infrared data but provides a foundation to start studying more complicated electrochemical systems. In this Chapter, time-resolved information on proton-coupled electron transfer (PCET) redox reactions on modified self-assembled monolayers are analyzed using Rapid-Scan FTIR spectroscopy.[13] A chemically modifiable self-assembled monolayer (SAM) was used to graft 1,4-benzoquinone to the electrode surface thus providing a nearly ideally Nernstian redox layer. The resulting surface bound quinone terminated SAM was then used to study the thermodynamics and kinetics of PCET reactions. As will be described in detail in Chapter 5, the gathered infrared data on formal potential and the calculated heterogeneous rate constants agrees well with those measured using strictly electrochemical techniques.

Moving to faster electrochemical kinetic problems, from those described in Chapter 5, requires the use of small electrodes. This creates a problem when trying to perform *in-situ* SEC experiments as a large fluxes of photons are normally required (typically from a large surface) to acquire high signal to noise data. To overcome these problems, Chapter 6 describes the

methodologies that were developed to exploit the highly focused incident infrared radiation produced by synchrotrons.[14,15]

Following the initial successes of coupling synchrotron radiation to near ultramicroelectrode sized electrodes (~ 250 μm radius); Chapter 7 of this thesis describes a major accomplishment, *i.e.* the development of the methodology required to perform fast, coupled electrochemical and infrared spectroscopic data collection. To that end, true ultramicroelectrodes (~ 25 μm radius) were used in conjunction with an infrared microscope utilizing synchrotron radiation.[16] With this arrangement, a faster FTIR measurement technique, Step-Scan Interferometry, is introduced vastly improving the time-resolution of the measurements. A further discussion on the diffusion-controlled electrochemistry with a thin-cavity cell will be discussed in some depth. Chapter 7 concludes by highlighting the present limitations of this technique and also reiterating the significant advances that have been made.

In the thesis conclusion, Chapter 8 provides a summary and discussion on the advances made through this research and offers suggestions to continue advancing the field of *in-situ* infrared spectroelectrochemisty. This Chapter comprises a final description of the progression made from internal reflection *in-situ* infrared spectroscopy to the study of fast electrochemical reactions using ultramicroelectrodes, spectromicroscopy, and synchrotron radiation.

1.1. References

1. Dunsch, L. Recent Advances in in Situ Multi-spectroelectrochemistry. *Journal of Solid State Electrochemistry* **2011**, *15*, 1631–1646.

2. Haubner, K.; Luspai, K.; Rapta, P.; Dunsch, L. The Charging of the Carbon Nanotube/oligothiophene Interphase as Studied by in Situ Electron Spin resonance/UV-Vis-NIR Spectroelectrochemistry. *Physical chemistry chemical physics : PCCP* **2011**, *13*, 13403–9.

3. Klod, S.; Dunsch, L. A Combination of in Situ ESR and in Situ NMR Spectroelectrochemistry for Mechanistic Studies of Electrode Reactions: The Case of P-benzoquinone. *Magnetic Resonance in Chemistry* **2011**, *49*, 725–729.

4. Gründer, Y.; Mosselmans, J. F. W.; Schroeder, S. L. M.; Dryfe, R. A. W. In Situ Spectroelectrochemistry at Free-Standing Liquid–Liquid Interfaces: UV–vis Spectroscopy, Microfocus X-ray Absorption Spectroscopy, and Fluorescence Imaging. *The Journal of Physical Chemistry C* **2013**, *117*, 5765–5773.

5. Klod, S.; Ziegs, F.; Dunsch, L. In Situ NMR Spectroelectrochemistry of Higher Sensitivity by Large Scale Electrodes. *Analytical chemistry* **2009**, *81*, 10262–7.

6. Chen, Y. X.; Miki, A.; Ye, S.; Sakai, H.; Osawa, M. Formate, an Active Intermediate for Direct Oxidation of Methanol on Pt Electrode. *Journal of the American Chemical Society* **2003**, *125*, 3680–3681.

7. Bewick, A.; Kunimatsu, K.; Stanley Pons, B. Infra Red Spectroscopy of the Electrode-electrolyte Interphase. *Electrochimica Acta* **1980**, *25*, 465–468.

8. Bewick, A.; Kunimatsu, K.; Pons, B. S.; Russell, J. W. Electrochemically Modulated Infrared Spectroscopy (EMIRS): Experimental Details. *Journal of Electroanalytical Chemistry and Interfacial Electrochemistry* **1984**, *160*, 47–61.

9. Hubbard, A. T.; Anson, F. C. Linear Potential Sweep Voltammetry in Thin Layers of Solution. *Analytical Chemistry* **1966**, *38*, 58–61.

10. Aoki, K.; Tokuda, K.; Matsuda, H. Theory of Linear Sweep Voltammetry with Finite Diffusion Space. *Journal of Electroanalytical Chemistry and Interfacial Electrochemistry* **1983**, *146*, 417–424.

11. Keller, H. E.; Reinmuth, W. H. Potential Scan Voltammetry with Finite Diffusion. Unified Theory. *Analytical Chemistry* **1972**, *44*, 434–442.

12. Rosendahl, S. M.; Danger, B. R.; Vivek, J. P.; Burgess, I. J. Surface Enhanced Infrared Absorption Spectroscopy Studies of DMAP Adsorption on Gold Surfaces. *Langmuir* **2009**, *25*, 2241–7.

13. Rosendahl, S. M.; Burgess, I. J. Charge Transfer and SEIRAS Studies of 1,4-benzoquinone Functionalized Mixed Monothiol/dithiol Self-assembled Monolayers. *Electrochimica Acta* **2011**, *56*, 4361–4368.

14. Rosendahl, S. M.; Borondics, F.; May, T. E.; Pedersen, T. M.; Burgess, I. J. Synchrotron Infrared Radiation for Electrochemical External Reflection Spectroscopy: a Case Study Using Ferrocyanide. *Analytical Chemistry* **2011**, *83*, 3632–9.

15. Rosendahl, S. M.; Borondics, F.; May, T. E.; Pedersen, T. M.; Burgess, I. J. Interface for Time-resolved Electrochemical Infrared Microspectroscopy Using Synchrotron Infrared Radiation. *The Review of Scientific Instruments* **2011**, *82*, 083105.

16. Rosendahl, S. M.; Borondics, F.; May, T. E.; Burgess, I. J. Step-Scan IR Spectroelectrochemistry with Ultramicroelectrodes : Non-Surface Enhanced Detection of Near Femtomole Quantities Using Synchrotron Radiation. *Analytical Chemistry* **2013**, *85*, 8722–8727.

CHAPTER 2

LITERATURE REVIEW

2.1. Introduction

The determination of the structure of the electrode/electrolyte interface is an important part of electrochemistry and electrocatalysis to solve applied problems in biological, environmental and industrial systems. Electrochemists have recognized that measurements of electrical voltages, currents, charges and capacitances at electrical interfaces do not always provide a definitive identification of electroactive materials. It becomes even more difficult when investigating complex systems, for example those occurring in environmental or biological matrices, where electrochemical-structure related problems might not be clearly resolved.

Early studies to gain insight into the structure of the electrode/electrolyte interface, specifically the nature of potentially adsorbed species, relied solely on electrochemical measurements. These measurements involved applying specific potentials and measuring the resulting currents. By knowing either the number of molecules involved or surface active sites for adsorption and by numerically integrating the current, the number of electrons involved in the process could be calculated. With this data, the researcher would typically be able to infer the nature of the electrified interface, electrogenerated intermediates and resulting products. It was often difficult, if not impossible, to completely understand reaction mechanisms and the structure of the interface which resulted in numerous controversies in the literature.

This motivated many researchers to develop *in-situ* spectroscopic techniques to aid in the determination of molecular structure information at the interface. For example, *in-situ* measurements should be able to provide information concerning: the properties of the electrode

surface, the nature and the structure of adsorbed species (including the double-layer), and the quantities and interactions between the absorbed species and the substrate. The earliest of techniques to combine spectroscopic information with electrochemistry included low-energy electron diffraction (LEED), Auger electron spectroscopy (AES), X-ray photoelectric spectroscopy (XPS) and electron energy loss spectroscopy (EELS).[1] These techniques allow a high degree of information to be obtained; however, it is important to point out that these techniques required high- or ultrahigh-vacuum conditions and were not directly applicable for *in-situ* investigations. It was not until the 1980s that infrared reflection/adsorption spectroscopy was recognized as a powerful technique for *in-situ* spectroelectrochemical (SEC) studies.[2,3] Other optical spectroscopic techniques have also been applied to *in-situ* electrochemical investigations, including: spectroscopic ellipsometry,[4] Raman,[5–7] and sum-frequency generation.[8,9]

At first, the development of infrared reflection techniques for *in-situ* SEC was met with uncertainty, as it was believed that the presence of an aqueous electrolyte, which has strong infrared adsorption bands, would prevent the measurement of small analyte signals. Although still considered one of the major challenges to using infrared spectroscopy for *in-situ* studies, the ability of various modulation techniques (*i.e.* photon polarization and electrode potential) and instrument improvements made it possible to recover small analyte signals in large-amplitude backgrounds. The first successful demonstration of *in-situ* infrared SEC was by Bewick *et al.* in 1980.[2] They utilized a potential modulation technique and *in-situ* infrared spectroscopy to study the electrosorption of indole on a platinum electrode as well as the electrochemical generation of long-lived intermediates. Electrochemically modulated infrared spectroscopy (EMIRS) was the first experimental technique to successfully demonstrate *in-situ* infrared SEC. The pioneering

work by Bewick, Kunimatsu and Pons[2] used a square wave potential modulation applied to an electrode in a thin-electrolyte layer external reflection spectroelectrochemical cell. Using a dispersive spectrometer and by modulating the potential at a given infrared wavelength, the measured signal at the detector is proportional to the difference of absorbance between the different potential states. Using this technique, Bewick *et al.* were able to adequately measure infrared absorbance changes on the order of 10^{-4} for a variety of electrochemical systems.[3] With the advent of Fourier Transform Infrared (FTIR) Spectrometers, better detectors and infrared sources, *in-situ* infrared SEC has become a readily accessible and recognized tool for studying electrochemical interfaces.

There are two major experimental problems when measuring *in-situ* infrared spectroelectrochemistry of species at or near the electrode/electrolyte interface. The first problem is the large bulk solvent absorption of infrared radiation. Aqueous solvents are especially problematic as water absorbs strongly throughout the mid-infrared region. The second problem is sensitivity. The number of molecules under study is typically very small. Since conventional infrared sources are weak and detectors very noisy it can be difficult to measure the absorbance of the species of interest. These two problems have driven the efforts of utilizing infrared for *in-situ* spectroelectrochemistry into two predominant methodologies. The two methods use different optical geometries, internal and external reflection (Figure 2.1), to overcome the solvent absorption problem. The resolution of this problem, however, ultimately means that ideal electrochemical behaviour has to be sacrificed as will be discussed in the coming sections. A short introduction to these two geometries is given below. A more rigorous discussion of the two geometries can be found in Chapter 3.

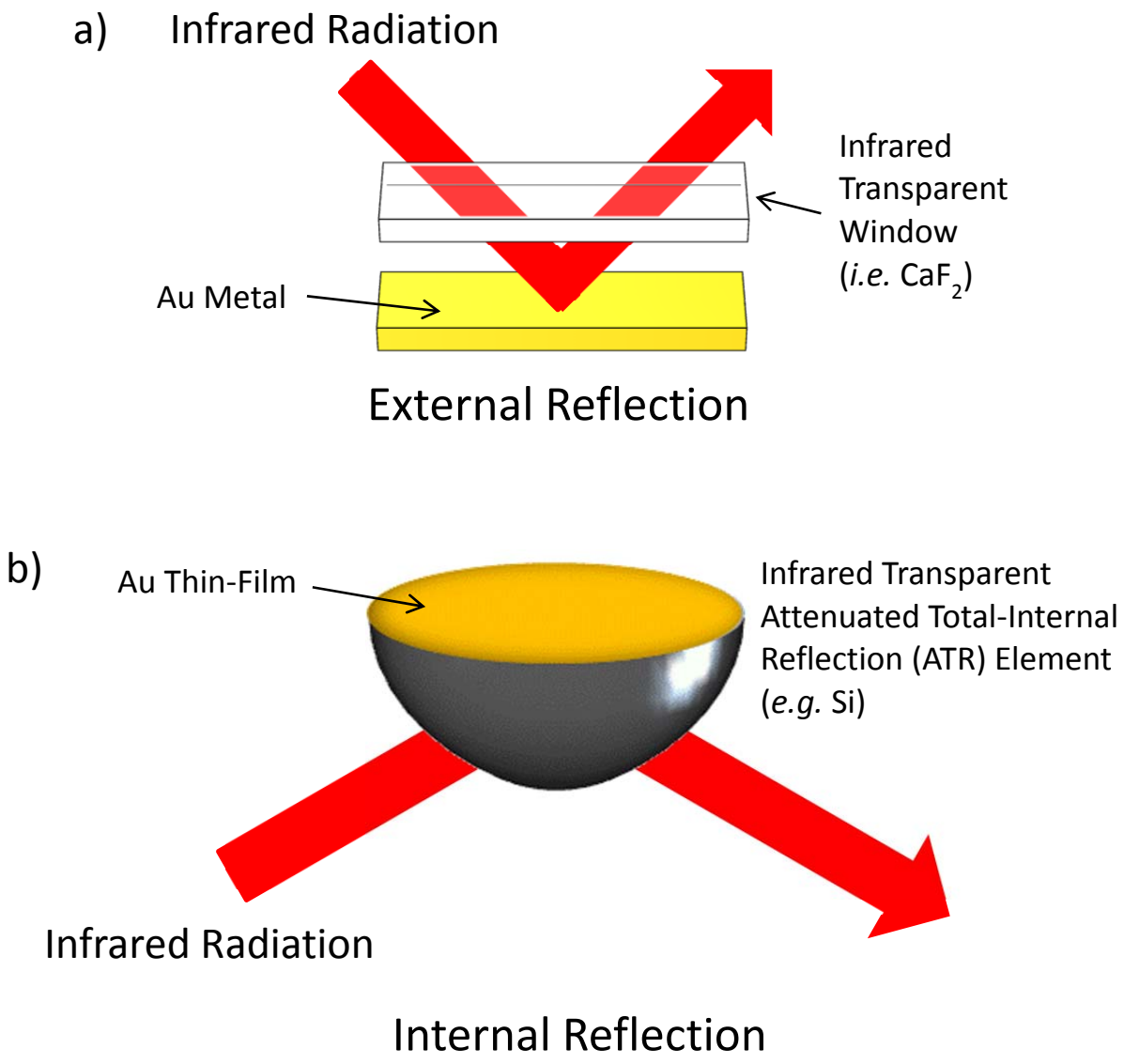

Figure 2.1. a) Optical geometry for external reflection spectroscopy (ERS) and b) internal reflection spectroscopy (IRS) spectroscopy demonstrating the use of Attenuated Total-Internal Reflection (ATR).

For external reflection geometries (such as infrared reflection absorption spectroscopy; IRRAS), a thin-layer cell is typically used to limit the thickness of solvent that the infrared radiation must pass through to be on the order 10 μm. In practice, electrochemical measurements in such a cell become kinetically hindered due to the high resistance of the thin-volume of electrolyte and non-uniform accessibility of the electrode (*i.e.* restricted mass-transport). Internal reflection geometries (also termed attenuated total-internal reflection, ATR), in contrast do not need thin-cavities and do not suffer the same limitations. With ATR, the infrared radiation is directed into and out of an optical element and is totally internally reflected. Materials that are suitable for ATR optical elements must be infrared transparent and have high-refractive indices. The former criterion excludes most conductive materials that are commonly used as electrodes. However, ATR substrates can be modified by the deposition of a thin layer of metal such as gold or platinum. Once the infrared reflection element (IRE) has been suitably modified it is relatively simple to mate it to a suitable electrochemical cell. Such a setup is known as the Kretschmann configuration (see Figure 2.1b).[10] ATR techniques are relatively exempt to bulk electrolyte absorption as the infrared radiation does not pass directly through the electrolyte. Furthermore, if the metal film is suitably structured, surface enhancements of incident infrared electric fields are possible giving rise to very low detection limits.

As previously mentioned, IRRAS techniques use a thin-layer SEC cell where a very-small volume of electrolyte separates an infrared transparent window from a reflective electrode (Figure 2.1a). In this configuration, an incident beam is transmitted through the window and electrolyte layer and is then reflected off the electrode passing back through the electrolyte and window before being collected at the detector. A distinct advantage to this technique over the ATR configuration is that single-crystal electrodes can be employed and the effect of

crystallography on the structure of adsorbed layers can be studied. However, the strong absorption from the electrolyte still results in a large background signal that can be difficult to remove to isolate the typically small analyte signals. Several techniques have been developed to address this problem where the background is corrected by means of modulation of the potential or polarization of the incident infrared radiation. Examples include, subtractively normalized interfacial Fourier transform infrared spectroscopy (SNIFTIRS)[11,12] and polarization modulation infrared reflection absorption spectroscopy (PM-IRRAS).[13–16]

2.2. Subtractively Normalized Interfacial Fourier Transform Infrared Spectroscopy (SNIFTIRS)

In SNIFTIRS, the electrode is modulated between a reference potential, E_{REF}, and a sample or variable potential, E_{VAR}. Spectra of the reflected infrared radiation is recorded at each of these potentials and the resulting spectrum ($\Delta S/S$), plotted as a function of wavenumber, is calculated by,

$$\frac{\Delta S}{S} = \frac{(S_{VAR} - S_{REF})}{S_{REF}} \tag{2.1}$$

where S_{REF} and S_{VAR} are the spectra recorded at the reference and sample potentials respectively. As a result of the subtraction used to calculate ($\Delta S/S$), SNIFTIRS spectra are without the common background of the electrolyte solvent and depict the small changes associate with potential dependent electrochemical processes. For this reason, the reference potential is often chosen to coincide with values where the molecule of interest is completely desorbed from the surface (for adsorption studies), or the electroactive species is present in only one redox or structural state. In SNIFTIRS spectra, a positive going band is indicative of a decrease of that particular infrared absorption and *vice versa* for a negative going band.

The SNIFTIRS method has allowed the development of quantitative analysis to investigate the oriented adsorption of organic molecules on gold surfaces. The first such studies include the adsorption of pyridine on Au(110),[17] citrate on Au(111)[18] and 2-mercaptobenzimidazole on Au(111)[19] substrates. Pyridine has long been used as a model system for investigating coordination to different crystallographic and metal substrates. A large body of thermodynamic information has been acquired for this system from chronocoulometric techniques.[20–23] Given that its behaviour on low-index gold surfaces was so-well studied, the adsorption of pyridine on Au made an ideal electroactive system to test the performance of the SNIFTIRS instrument. An important catalytic analogue of pyridine (dimethylaminopyridine; DMAP) was studied in Chapter 4.

2.3. Polarization Modulation-Infrared Reflection Absorption Spectroscopy (PM-IRRAS)

The development of PM-IRRAS began in 1981 by Golden *et al.*[13] after Hipps and Crosby[16] introduced the photoelastic modulator in 1979. Although these early experiments were carried out in ultrahigh vacuum conditions and used dispersive spectrometers, Golden and co-workers were eventually able to measure *in-situ* SEC systems using Fourier transform instruments a few years later.[14] In PM-IRRAS, the electric field of the incident infrared radiation is modulated between two orthogonal directions, one perpendicular to the plane of incidence (s-polarized) and one parallel to the plane of incidence (p-polarized) using a photoelastic modulator (PEM). The PEM consists of a piezoelectric transducer attached to a ZnSe crystal. As an oscillating voltage is applied to the transducer, a periodic mechanical wave is introduced in the ZnSe crystal causing an expansion or compression along one direction of the crystal. This motion introduces an optical retardation along this axis and a shift in the phase of the incident

radiation causing the polarization of the beam to oscillate accordingly between the two different polarizations. In terms of spectroscopy at the metal surface, the electric field of the s-polarized light becomes negligible whereas that of p-polarized light is enhanced.[24] The implication of this is when molecules are on or near the metal surface only those vibrational dipole moments perpendicular to the surface are enhanced. The s-polarized incident infrared light is insensitive to the molecules on the surface and as a result can be used to produce a background spectrum and isolate the surface molecules of interest. Once measured, the reflection absorption spectrum is obtained by,

$$\frac{\Delta R}{\langle R \rangle} = \frac{|R_S - R_P|}{(R_S + R_P)/2} \tag{2.2}$$

where R_S and R_P represent the single beam spectra obtained for s- and p-polarized light respectively. A consequence of using polarization modulation is the common-mode rejection of absorption signals when the s- and p-polarized light are identical. This is especially true for atmospheric CO_2 and H_2O as random orientations of these molecules result in nearly equal absorptions for both polarizations. This result was studied extensively by Faguy *et al.*[25,26] and has prompted interest in the studying insoluble surfactant monolayers at the air/water interface of a Langmuir trough.[27–30] As more research groups began to utilize PM-IRRAS methods, major advancements continued and a key innovation was introduced in 1991 by Corn and co-workers through their use of a synchronous sampling demodulator.[31,32] This device allowed for an almost two-fold improvement in measuring modulated signals compared to conventional lock-in amplifiers and has become the device of choice for researchers using PM-IRRAS.

Some of the first quantitative PM-IRRAS studies with electrochemistry applications involved the investigation of the tilt angle of the acyl chains in a phospholipid bilayer, DMPC (1,2-dimyristoyl-sn-glycero-3-phosphocholine), on Au(111) electrode surfaces. In this work,[33]

Horswell *et al.* used the ratio of the various integrated asymmetric and symmetric CH_2 and CH_3 infrared vibrational bands to determine the relative tilt angle of the adsorbed film. Recently, PM-IRRAS has been applied in biomimetic research studies concerning the potential-induced changes in orientation and conformational structure of molecules used in model biological membranes when supported on electrodes.[34,35] These efforts allow the study of important voltage regulated biological phenomena such as the opening/closing of ion channels and bio-electrochemical sensors.[36]

Utilization of SNIFTIRS and PM-IRRAS is becoming increasingly common for studying *in-situ* spectroelectrochemical processes. The availability of sensitive FTIR spectrometers and detectors has allowed electrochemists and surface scientists to study a host of systems using these techniques. The next section deals with the developments of internal reflection geometries, particularly attenuated total-internal reflection surface enhanced infrared absorption spectroscopy (ATR-SEIRAS).

2.4. Surface Enhanced Infrared Absorption Spectroscopy (SEIRAS)

Surface Enhanced Infrared Absorption Spectroscopy is an internal reflection technique pioneered by Osawa and co-workers.[37,38] Many of the problems associated with external reflection techniques can be largely mitigated through the use of an ATR configuration. This technique uses a thin-metal film deposited onto an infrared transparent element with a high index of refraction (*i.e.* silicon, germanium) which is then used as the working electrode. Infrared radiation from the light source is focused at the back of the thin-metal film electrode through the prism where it is totally internally reflected and collected at a detector. An electrochemical cell can be built on the opposite side of the prism to allow for the electrochemical study of

electrochemical processes. A unique feature of this technique is that an approximate 10^3 enhancement of infrared absorption by molecules adsorbed on the surface can be realized if the thin-metal film contains micrometer-scale roughness compared to surfaces without the metal film. In comparison to external reflective techniques, SEIRAS measurements allow for the almost complete removal of the solvent background. A significant experimental challenge with ATR-SEIRAS is grafting the working electrode metal to the ATR element which is not always a straightforward process. A more complete description of the means to achieve this is described in Chapter 3.

A unique feature of ATR-SEIRAS measurements is that they are extremely surface sensitive. As such, the majority of *in-situ* SEC problems have been related to analysis of the double-layer structure, adsorption/desorption, characterization of self-assembled monolayers (SAMs) and monitoring of electrochemical surface reactions. Redox reactions involving metal proteins (*i.e.* cytochrome C), are known to be promoted when electrode surfaces are covered by a SAM of nitrogen containing heterocycles.[39] SAMs prepared under different conditions are known to exhibit different levels of protein binding activity and to understand this phenomenon, real-time monitoring using ATR-SEIRAS measurements were performed on the kinetics of the self-assembly of 4-pyridinethiol (4-PySH).[40] SEIRAS spectra were collected every 5 seconds and tracked the changes in the band intensity of the pyridine's ring breathing mode. Under different electrolyte pH and potentiostatic conditions it was shown that the rate of formation of the SAM dramatically played a role in the resulting activity of the SAM. In particular, the faster the SAM was formed the higher its measured activity in promoting the redox of cytochrome C. A study of this nature is virtually impossible without some form of signal enhancement from the monolayer and ATR-SEIRAS was shown to be very effective for this purpose.

One of the most fundamental and studied electrochemical reactions is the electrocatalytic hydrogen evolution reaction (HER) on Pt electrodes.[41–44] The HER occurs through two successive elementary steps where a proton from solution is reduced and adsorbed onto the Pt surface ($H^+ + e^- \rightarrow H_{ads}$). Following this step, the reaction between two adsorbed hydrogen atoms ($2\ H_{ads} \rightarrow H_2$) or through the reaction of the adsorbed hydrogen with a proton and electron ($H^+ + e^- + H_{ads} \rightarrow H_2$) occurs, affording H_2 as the final product. Aspects of this process, in particular intermediates, needed spectroscopic evidence to fully understand the HER. One problem studied was in relation to electrochemical data suggesting that the underpotential deposition of hydrogen is not a HER reaction intermediate. First attempts to study this problem where made by IRRAS techniques and had significant problems at large overpotentials stemming from the use of thin-cavity cells. At large overpotentials, H_2 gas is evolved and can become trapped in the thin-layer disturbing both electrochemical and spectroscopic measurements. This limitation resulted in a small window of overpotentials that could be studied using IRRAS techniques. This is an example where using ATR-SEIRAS can prove to be more convenient in that evolved H_2 has less impact on the *in-situ* SEC measurements and a greater degree of surface sensitivity can be achieved. Further to this, the increased surface sensitivity of ATR-SEIRAS aided in these studies as the infrared measurements were made specifically on the surface bound hydrogen to platinum species (~2100 cm^{-1}) infrared band.[45]

Methanol has been extensively cited as a potentially useful fuel for electricity production in fuel cells. In particular, the electro-oxidation of methanol to CO_2 on Pt electrodes has been studied extensively over the past few decades.[41–44] Numerous IRRAS studies on the reaction intermediates have demonstrated a variety of intermediate products (including formaldehyde and formic acid) that decrease the efficiency of methanol oxidation.[46,47] The results of these studies

were not very reproducible amongst groups and lead to a great deal of uncertainty in the reaction pathways. In 2003, Osawa and co-workers were finally able to successfully demonstrate evidence of the identity of the reaction intermediates produced during methanol oxidation.[48] From this work, the authors were able to show that at positive enough potentials, the infrared bands associated with CO bound to the platinum surface disappear and only one new band associated with formate appears. This interesting result (suggested by the authors), is that formate is acting as a reaction intermediate in the oxidation of methanol and no other intermediates were measured contrary to the inferred non-reproducible results from previous IRRAS studies.[48] This is just one example of how the surface sensitivity of *in-situ* ATR-SEIRAS can be used in understanding the nature of adsorbates and reaction intermediates that cannot be measured in thin-cavity electrolyte volumes.

A problem with SEIRAS is that often large electrode areas are required to measure infrared spectra with sufficient signal-to-noise. As a result of larger electrode sizes, the cell time-constant (RC) is effectively large enough to limit the time-resolution of dynamic electrochemical processes to milliseconds. This cell time-constant is the product of the electrode capacitance (C) and the solution resistance (R), and is proportional to area of the electrode of the electrode. By decreasing the radius of the electrode, the time required to adjust the charge on the electrode surface by a potential step perturbation (5 times RC) also decreases. By moving to smaller electrodes, on the scale of micrometers, the time-resolution of electrochemical processes can now be measured on the millisecond to microsecond time scale allowing for the measurement of fast electrochemical kinetics. This is important as many processes at an electrified interface (*i.e.* electron transfer and mass transport/diffusion), can occur very rapidly including the creation and consumption of short lived reaction intermediates. Understanding

these processes is important in increasing the efficiency of fuel cells used to generate electricity as various reaction intermediates given rise to different deleterious by-products.[48]

In an attempt to overcome these problems, smaller electrodes (approaching micrometer dimensions) are often employed but start to decrease the effective surface area that can be used to measure the weak infrared signals. In other words, with smaller electrodes the number of molecules and the number of photons that can be used to probe the surface is decreased reducing the sensitivity of the infrared measurements. As such, several research groups have moved towards external reflection SEC cells suitable for use under infrared microscopes and have employed highly bright synchrotron infrared sources.

2.5. Infrared Spectromicroscopy and Synchrotron Sources

The work by Sun and co-workers utilized infrared microscopy to focus infrared radiation from a conventional Globar onto very large ultramicroelectrodes (radius 200 μm; technically this exceeds the accepted definition of a UME but the term is kept in order to be consistent with the primary literature).[49–54] Their work used conventional infrared thermal sources and was very successful in reporting processes displaying surface enhancement *via* anomalous infrared enhanced spectroscopy (AIRES)[55] occurring on the electrode surface on the time scale of tens to hundreds of microseconds. Their studies used both continuous (rapid-scan)[51] and step-scan[49,50] interferometry to increase the temporal resolution of the measurements. It is very likely that further attempts to improve the temporal resolution were prohibited by insufficient signal-to-noise levels when equivalent experiments using smaller platinum UMEs were attempted or on other electrochemical systems not displaying AIRES. The signal-to-noise of conventional thermal sources is increasingly limited by the ability of the instrument to focus large photon

intensity onto very small areas providing a motivation to move to non-conventional sources of infrared radiation such as synchrotron infrared radiation for studying dynamic electrochemical processes.

The use of synchrotron infrared radiation for electrochemical studies was first demonstrated through the work of Melendres and co-workers.[56–64] These authors have primarily used far-IR (1000-10 cm^{-1}) synchrotron radiation to study processes related to copper oxidation, and ion adsorption on metal electrodes. The first preliminary report published by Melendres *et al*.[59] in 1995 presented initial results on utilizing synchrotron far-infrared radiation for *in-situ* studies and provided sufficiently promising proof-of-concept results to warrant continued investigations. Since that time, the group has been actively coupling synchrotron radiation to electrochemical cells through various methods utilizing a far-infrared microscope and grazing incident objectives. The primary motivation is to alleviate the large absorption of aqueous electrolytes that overpower conventional thermal sources typically found in bench-top spectrometers for the far-infrared region and to gain valuable knowledge in adsorption processes on electrode surfaces. As a result, Melendres and co-workers have been able to report on the adsorption of ions on gold[62,63], silver[64] and platinum[59,61] in the far-infrared region. For example, the adsorption of chloride and bromide ions on gold electrodes has been studied extensively in electrochemistry. With the advent of far-infrared measurements utilizing synchrotron radiation, experimental *in-situ* data demonstrated an Au–Cl surface vibrational bond at 263 cm^{-1} and an Au–Br stretching mode at 182 cm^{-1} in aqueous electrolytes.[62] Further experiments studied the adsorption of various oxyanions[63], the vibrational properties of cyanate ions, OCN-, on silver[64] and hydroxide adsorption on platinum electrodes.[59]

Aside from the research effort involving the adsorption of anions on metal electrodes, a considerable area of focus for Melendres and co-workers was to study processes related to copper oxidation using *in-situ* far-infrared synchrotron radiation. Their early studies looked at the composition of electrogenerated surface films formed during the general and localized corrosion of copper in alkaline and bicarbonate solutions.[60] An important point about this early work is that the window used for electrochemical measurements still had to be removed from the cell to measure the infrared spectra. A true *in-situ* experiment was not fully realized until 2008[56] when a thin-cavity cell employing a 500 μm size Cu working electrode pressed against a far-infrared window made from Mylar. The results from this work demonstrate that it was possible to obtain *in situ* spectra with excellent signal-to-noise ratios for electrochemically formed surface oxide films. In addition, these results were in good agreement with their previous studies and were consistent with thermodynamic calculations adding further credit to the technique. Melendres and co-workers were finally able to demonstrate the collection of entirely *in-situ* far-infrared spectra of surface films formed upon anodic oxidation of copper for the first time in aqueous solution environments using a synchrotron source.[56–58] However, in all the above cases utilizing synchrotron infrared radiation, dynamic electrochemical processes were not studied and only measurements taken on equilibrated interfaces were achieved.

Considering the successes of Melendres and co-workers, further improvements can be made to Sun *et al.*'s work with ultramicroelectrodes by utilizing synchrotron infrared sources for increased signal-to-noise levels. By building on the work of these two groups, the use of true ultramicroelectrodes ($\leq$ 25 μm) and synchrotron infrared radiation should provide adequate signal-to-noise levels to study fast electrochemical events both electrochemically and spectroscopically.

The combination of electrochemistry and infrared spectroscopy for *in-situ* spectroelectrochemical measurements has been continually advancing since the first reports by Bewick in the early 1980s. The need to supplement purely electrochemical measurements with molecular information was a driving force in the first developments with a need to understand the electrode/electrolyte interface under *in-situ* potentiostatic control. Infrared spectroscopy, although first overlooked due to large solvent absorptions, eventually became the most utilized *in-situ* spectroscopic technique and has proven to be successful in understanding various electrochemical processes. This thesis focuses on the continued development of *in-situ* infrared spectroelectrochemical techniques, using both internal and external reflection geometries, to further the understanding of molecular adsorption, diffusion currents and kinetics of proton-coupled electron transfer reactions. A significant achievement is in the first demonstration of coupling true ultramicroelectrodes, synchrotron infrared radiation and step-scan interferometry to measure very fast electrochemical processes.

2.6. References

1. *Spectroelectrochemistry: Theory and Practice*; Gale, R. J., Ed.; Plenum Press: New York, 1988.

2. Bewick, A.; Kunimatsu, K.; Stanley Pons, B. Infra Red Spectroscopy of the Electrode-electrolyte Interphase. *Electrochimica Acta* **1980**, *25*, 465–468.

3. Bewick, A.; Kunimatsu, K.; Pons, B. S.; Russell, J. W. Electrochemically Modulated Infrared Spectroscopy (EMIRS): Experimental Details. *Journal of Electroanalytical Chemistry and Interfacial Electrochemistry* **1984**, *160*, 47–61.

4. Christensen, P.; Hamnett, A. In-situ Techniques in Electrochemistry — Ellipsometry and FTIR. *Electrochimica Acta* **2000**, *45*, 2443–2459.

5. Ramesha, G. K.; Sampath, S. Electrochemical Reduction of Oriented Graphene Oxide Films: An in Situ Raman Spectroelectrochemical Study. *Journal of Physical Chemistry C* **2009**, *113*, 7985–7989.

6. Xu, M.; Zou, W.; Yao, J.; Fan, X.; Gu, R. In Situ Surface-enhanced Raman Spectroscopic Studies of Phenylacetylene Adsorbed on Gold Electrode. *Huaxue Xuebao* **2009**, *67*, 134–138.

7. Zhang, P.; Chen, Y.-X.; Cai, J.; Liang, S.-Z.; Li, J.-F.; Wang, A.; Ren, B.; Tian, Z.-Q. An Electrochemical in Situ Surface-Enhanced Raman Spectroscopic Study of Carbon Monoxide Chemisorption at a Gold Core-Platinum Shell Nanoparticle Electrode with a Flow Cell. *Journal of Physical Chemistry C* **2009**, *113*, 17518–17526.

8. Zhou, W.; Inoue, S.; Iwahashi, T.; Kanai, K.; Seki, K.; Miyamae, T.; Kim, D.; Katayama, Y.; Ouchi, Y. Electrochemical Double-layer Structure of Pt Electrode/ionic Liquids Interface Studied by in Situ IR-visible Sum Frequency Generation Spectroscopy. *ECS Transactions* **2009**, *16*, 545–557.

9. Bozzini, B.; Gian Pietro, G. De; Busson, B.; Humbert, C.; Six, C.; Gayral, A.; Tadjeddine, A. In Situ Spectroelectrochemical Measurements During the Electro-oxidation of Ethanol on WC-supported Pt-black, Based on Sum-frequency Generation Spectroscopy. *Journal of Power Sources* **2010**, *195*, 4119–4123.

10. Osawa, M.; Kuramitsu, M.; Hatta, A.; Suëtaka, W.; Seki, H. Electromagnetic Effect in Enhanced Infrared Absorption of Adsorbed Molecules on Thin Metal Films. *Surface Science* **1986**, *175*, L787–L793.

11. Davidson, T.; Pons, B. S.; Bewick, A.; Schmidt, P. P. Vibrational Spectroscopy of the Electrode/electrolyte Interface. Use of Fourier Transform Infrared Spectroscopy. *Journal of Electroanalytical Chemistry and Interfacial Electrochemistry* **1981**, *125*, 237–241.

12. Pons, S.; Davidson, T.; Bewick, A. Vibrational Spectroscopy of the Electrode-solution Interface. 2. Use of Fourier Transform Spectroscopy for Recording Infrared Spectra of Radical Ion Intermediates. *Journal of the American Chemical Society* **1983**, *105*, 1802–1805.

13. Golden, W. G.; Dunn, D. S.; Overend, J. A Method for Measuring Infrared reflection—Absorption Spectra of Molecules Adsorbed on Low-area Surfaces at Monolayer and Submonolayer Concentrations. *Journal of Catalysis* **1981**, *71*, 395–404.

14. Golden, W. G.; Kunimatsu, K.; Seki, H. Application of Polarization-modulated Fourier Transform Infrared Reflection-absorption Spectroscopy to the Study of Carbon Monoxide Adsorption and Oxidation of a Smooth Platinum Electrode. *The Journal of Physical Chemistry* **1984**, *88*, 1275–1277.

15. Golden, W. G.; Saperstein, D. D.; Severson, M. W.; Overend, J. Infrared Reflection-absorption Spectroscopy of Surface Species: a Comparison of Fourier Transform and Dispersion Methods. *The Journal of Physical Chemistry* **1984**, *88*, 574–580.

16. Hipps, K. W.; Crosby, G. A. Applications of the Photoelastic Modulator to Polarization Spectroscopy. *The Journal of Physical Chemistry* **1979**, *83*, 555–562.

17. Li, N.; Zamlynny, V.; Lipkowski, J.; Henglein, F.; Pettinger, B. In Situ IR Reflectance Absorption Spectroscopy Studies of Pyridine Adsorption at the Au(110) Electrode Surface. *Journal of Electroanalytical Chemistry* **2002**, *524–525*, 43–53.

18. Nichols, R. J.; Burgess, I.; Young, K. L.; Zamlynny, V.; Lipkowski, J. A Quantitative Evaluation of the Adsorption of Citrate on Au(111) Using SNIFTIRS. *Journal of Electroanalytical Chemistry* **2004**, *563*, 33–39.

19. Doneux, T.; Buess-Herman, C.; Lipkowski, J. Electrochemical and FTIR Characterization of the Self-assembled Monolayer of 2-mercaptobenzimidazole on Au(111). *Journal of Electroanalytical Chemistry* **2004**, *564*, 65–75.

20. Stolberg, L.; Richer, J.; Lipkowski, J.; Irish, D. E. Adsorption of Pyridine at the Polycrystalline Gold Solution Interface. *Journal of electroanalytical chemistry and interfacial electrochemistry* **1986**, *207*, 213–234.

21. Stolberg, L.; Lipkowski, J.; Irish, D. E. Adsorption of Pyridine at the Au(110)-solution Interface. *Journal of Electroanalytical Chemistry and Interfacial Electrochemistry* **1990**, *296*, 171–189.

22. Stolberg, L.; Lipkowski, J.; Irish, D. E. Adsorption of Pyridine at the Au (100)-solution Interface. *Journal of Electroanalytical Chemistry and Interfacial Electrochemistry* **1987**, *238*, 333–353.

23. Stolberg, L.; Morin, S.; Lipkowski, J.; Irish, D. E. Adsorption of Pyridine at the Au (111)-solution Interface. *Journal of electroanalytical chemistry and interfacial electrochemistry* **1991**, *307*, 241–262.

24. Zamlynny, V.; Lipkowski, J. Quantitative SNIFTIRS and PM IRRAS of Organic Molecules at Electrode Surfaces. *Diffraction and Spectroscopic Methods in Electrochemistry* **2006**, *9*, 315–376.

25. Faguy, P. W.; Richmond, W. N.; Jackson, R. S.; Weibel, S. C.; Ball, G.; Payer, J. H. Real-Time Polarization Modulation in Situ Infrared Spectroscopy Applied to the Study of Atmospheric Corrosion. *Applied Spectroscopy* **1998**, *52*, 557–564.

26. Faguy, P. W.; Richmond, W. N. Real-time Polarization Modulation Infrared Spectroscopy Applied to the Study of Water and Hydroxide Ions at Electrode Surfaces. *Journal of Electroanalytical Chemistry* **1996**, *410*, 109–113.

27. Pelletier, I.; Bourque, H.; Buffeteau, T.; Blaudez, D.; Desbat, B.; Pézolet, M. Study by Infrared Spectroscopy of Ultrathin Films of Behenic Acid Methyl Ester on Solid Substrates and at the Air/Water Interface. *The Journal of Physical Chemistry B* **2002**, *106*, 1968–1976.

28. Bourque, H.; Laurin, I.; Pézolet, M.; Klass, J. M.; Lennox, R. B.; Brown, G. R. Investigation of the Poly(l -lactide)/Poly(d -lactide) Stereocomplex at the Air−Water Interface by Polarization Modulation Infrared Reflection Absorption Spectroscopy †. *Langmuir* **2001**, *17*, 5842–5849.

29. Blaudez, D.; Buffeteau, T.; Desbat, B.; Fournier, P.; Ritcey, A.-M.; Pézolet, M. Infrared Reflection−Absorption Spectroscopy of Thin Organic Films on Nonmetallic Substrates: Optimal Angle of Incidence. *The Journal of Physical Chemistry B* **1998**, *102*, 99–105.

30. Blaudez, D.; Buffeteau, T.; Cornut, J. C.; Desbat, B.; Escafre, N.; Pezolet, M.; Turlet, J. M. Polarization-Modulated FT-IR Spectroscopy of a Spread Monolayer at the Air/Water Interface. *Applied Spectroscopy* **1993**, *47*, 869–874.

31. Barner, B. J.; Green, M. J.; Saez, E. I.; Corn, R. M. Polarization Modulation Fourier Transform Infrared Reflectance Measurements of Thin Films and Monolayers at Metal Surfaces Utilizing Real-time Sampling Electronics. *Analytical Chemistry* **1991**, *63*, 55–60.

32. Green, M. J.; Barner, B. J.; Corn, R. M. Real-time Sampling Electronics for Double Modulation Experiments with Fourier Transform Infrared Spectrometers. *Review of Scientific Instruments* **1991**, *62*, 1426.

33. Horswell, S. L.; Zamlynny, V.; Li, H.-Q.; Merrill, A. R.; Lipkowski, J. Electrochemical and PM-IRRAS Studies of Potential Controlled Transformations of Phospholipid Layers on Au(111) Electrodes. *Faraday Discussions* **2002**, *121*, 405–422.

34. Bin, X.; Zawisza, I.; Goddard, J. D.; Lipkowski, J. Electrochemical and PM-IRRAS Studies of the Effect of the Static Electric Field on the Structure of the DMPC Bilayer Supported at a Au(111) Electrode Surface. *Langmuir* **2005**, *21*, 330–47.

35. Zawisza, I.; Bin, X.; Lipkowski, J. Spectroelectrochemical Studies of Bilayers of Phospholipids in Gel and Liquid State on Au(111) Electrode Surface. *Bioelectrochemistry* **2004**, *63*, 137–147.

36. Kycia, A.H.; Su, Z.; Brosseau, C. L. . L. J. In Situ PM–IRRAS Studies of Biomimetic Membranes Supported at Gold Electrode Surfaces. In *Vibrational Spectroscopy at Electrified Interfaces*; Wieckowski, A.; Korzeniewski, C.; Braunschweig, B., Ed.; Wiley, 2013; p. 345.

37. Osawa, M. In-situ Surface-enhanced Infrared Spectroscopy of Electrode/Solution Interface. In *Handbook of Vibrational Spectroscopy*; Chalmers, J.M., Griffiths, P. R., Ed.; Wiley: Chichester, 2002; p. 785.

38. Osawa, M. In-Situ Surface-enhanced Infrared Spectroscopy of the Electrode/Solution Interface. In *In Diffraction and Spectroscopic Methods in Electrochemistry*; Alkire, R. C., Kolb, D., Lipkowski, J., Ross, P. N., Ed.; 2006; pp. 269–314.

39. Taniguchi, I.; Yoshimoto, S.; Sunatsuki, Y.; Nishiyama, K. No Title. *Electrochemistry* **1999**, 1197.

40. Taniguchi, I.; Yoshimoto, S.; Yoshida, M.; Kobayashi, S.; Miyawaki, T.; Aono, Y.; Sunatsuki, Y.; Taira, H. Simple Methods for Preparation of a Well-defined 4-pyridinethiol Modified Surface on Au(111) Electrodes for Cytochrome c Electrochemistry. *Electrochimica Acta* **2000**, *45*, 2843–2853.

41. Parsons, R.; VanderNoot, T. The Oxidation of Small Organic Molecules. *Journal of Electroanalytical Chemistry and Interfacial Electrochemistry* **1988**, *257*, 9–45.

42. Jarvi, T.D.; Stuve, E. M. No Title. In *Electrocatalysis*; Lipkowski, J.; Ross, P. N., Ed.; Wiley-VCH: New York, 1998; p. 75.

43. Sun, S.-G. No Title. In *Electrocatalysis*; Lipkowski, J.; Ross, P. ., Ed.; Wiley-VCH: New York, 1998; p. 243.

44. Marković, N. M.; Ross Jr., P. N. Surface Science Studies of Model Fuel Cell Electrocatalysts. *Surface Science Reports* **2002**, *45*, 117–229.

45. Kunimatsu, K.; Senzaki, T.; Tsushima, M.; Osawa, M. A Combined Surface-enhanced Infrared and Electrochemical Kinetics Study of Hydrogen Adsorption and Evolution on a Pt Electrode. *Chemical Physics Letters* **2005**, *401*, 451–454.

46. Samjeské, G.; Miki, A.; Ye, S.; Yamakata, A.; Mukouyama, Y.; Okamoto, H.; Osawa, M. Potential Oscillations in Galvanostatic Electrooxidation of Formic Acid on Platinum: a Time-resolved Surface-enhanced Infrared Study. *The journal of physical chemistry. B* **2005**, *109*, 23509–16.

47. Samjeské, G.; Osawa, M. Current Oscillations During Formic Acid Oxidation on a Pt Electrode: Insight into the Mechanism by Time-resolved IR Spectroscopy. *Angewandte Chemie (International ed. in English)* **2005**, *44*, 5694–8.

48. Chen, Y. X.; Miki, A.; Ye, S.; Sakai, H.; Osawa, M. Formate, an Active Intermediate for Direct Oxidation of Methanol on Pt Electrode. *Journal of the American Chemical Society* **2003**, *125*, 3680–3681.

49. Zhou, Z.-Y.; Sun, S.-G. In Situ Step-scan Time-resolved Microscope FTIR Spectroscopy Applied in Irreversible Electrochemical Reactions. *Electrochimica Acta* **2005**, *50*, 5163–5171.

50. Zhou, Z.-Y.; Lin, S.-C.; Chen, S.-P.; Sun, S.-G. In Situ Step-scan Time-resolved Microscope FTIR Spectroscopy Working with a Thin-layer Cell. *Electrochemistry Communications* **2005**, *7*, 490–495.

51. Zhou, Z.-Y.; Tian, N.; Chen, Y.-J.; Chen, S.-P.; Sun, S.-G. In Situ Rapid-scan Time-resolved Microscope FTIR Spectroelectrochemistry: Study of the Dynamic Processes of Methanol Oxidation on a Nanostructured Pt Electrode. *Journal of Electroanalytical Chemistry* **2004**, *573*, 111–119.

52. Gong, H.; Sun, S.-G.; Chen, Y.-J.; Chen, S.-P. In Situ Microscope FTIRS Studies of CO Adsorption on an Individually Addressable Array of Nanostructured Pt Microelectrodes - An Approach of Combinatorial Analysis of Anomalous IR Properties. *Journal of Physical Chemistry B* **2004**, *108*, 11575–11584.

53. Gong, H.; Sun, S.-G.; Li, J.-T.; Chen, Y.-J.; Chen, S.-P. Surface Combinatorial Studies of IR Properties of Nanostructured Ru Film Electrodes Using CO as Probe Molecule. *Electrochimica Acta* **2003**, *48*, 2933–2942.

54. Chen, Y.-J.; Sun, S.-G.; Chen, S.-P.; Li, J.-T.; Gong, H. Anomalous IR Properties of Nanostructured Films Created by Square Wave Potential on an Array of Pt Microelectrodes: An in Situ Microscope FTIRS Study of CO Adsorption. *Langmuir* **2004**, *20*, 9920–9925.

55. Lu, G. Q.; Sun, S. G.; Cai, L. R.; Chen, S. P.; Tian, Z. W.; Shiu, K. K. In Situ FTIR Spectroscopic Studies of Adsorption of CO, SCN-, and Poly(o-phenylenediamine) on Electrodes of Nanometer Thin Films of Pt, Pd, and Rh:Abnormal Infrared Effects (AIREs). *Langmuir* **1999**, *16*, 778–786.

56. Hahn, F.; Mathis, Y.-L.; Bonnefont, A.; Maillard, F.; Melendres, C. A. In Situ Synchrotron Far Infrared Micro-spectroelectrochemistry with a Grazing Angle Objective. *Infrared Physics and Technology* **2008**, *51*, 446–449.

57. Hahn, F.; Mathis, Y.-L.; Bonnefont, A.; Maillard, F.; Melendres, C. A. In Situ Synchrotron Far-infrared Spectromicroscopy of a Copper Electrode at Grazing Incidence Angle. *Journal of Synchrotron Radiation* **2007**, *14*, 446–448.

58. Hahn, F.; Melendres, C. A. Synchrotron Infrared Reflectance Micro-spectroscopy Study of Film Formation and Breakdown on Copper. *Journal of Synchrotron Radiation* **2010**, *17*, 81–85.

59. Melendres, C. A.; Beden, B.; Bowmaker, G. A. Far Infrared Spectroscopy of a Platinum Electrode “In-situ” Using a Synchrotron Source. *Journal of Electroanalytical Chemistry* **1995**, *383*, 191–193.

60. Melendres, C. A.; Bowmaker, G. A.; Leger, J. M.; Beden, B. In-situ Synchrotron Far Infrared Spectroscopy of Surface Films on a Copper Electrode in Aqueous Solutions. *Journal of Electroanalytical Chemistry* **1998**, *449*, 215–218.

61. Melendres, C. A.; Bowmaker, G. A.; Leger, J. M.; Beden, B. No Title. *Proc. - Electrochem. Soc.* **1996**, *96*, 280–291.

62. Melendres, C. A.; Hahn, F. `In-situ’ Observation of Halide Ion Adsorption on a Gold Electrode Using Synchrotron Far Infrared Spectroscopy. *Journal of Electroanalytical Chemistry* **1999**, *463*, 258–261.

63. Melendres, C. A.; Hahn, F.; Bowmaker, G. A. Oxyanion Adsorption and Competition at a Gold Electrode. *Electrochimica Acta* **2000**, *46*, 9–13.

64. Bowmaker, G. A.; Leger, J.-M.; Rille, A. L.; Melendres, C. A.; Tadjeddine, A. Investigation of the Vibrational Properties of OCN- on a Silver Electrode by in Situ Synchrotron Far Infrared Spectroscopy and Visible-infrared Sum Frequency Generation Spectroscopy. *Journal of the Chemical Society - Faraday Transactions* **1998**, *94*, 1309–1313.

CHAPTER 3

THEORY AND METHODOLOGY

3.1. Introduction

The primary focus of this Chapter is to provide specific details on the various theories and methodologies used throughout this thesis. From Chapter 2 an understanding of where the field has moved from its early beginnings to current technologies and the wide variety of experimental techniques available to the *in-situ* spectroelectrochemist was discussed. This Chapter starts by providing a theoretical background in infrared vibrational spectroscopy followed by an in depth analysis of the finer points of Fourier Transform Infrared (FTIR) spectrometers. Two different FTIR techniques, continuous rapid-scan and step-scan, will be discussed and compared for time-resolved measurements.

Further instrumentation discussions include the interfacing of the hardware components required to perform both static and time-resolved *in-situ* spectroelectrochemistry (SEC) experiments and the implementation of synchrotron infrared radiation as a highly brilliant infrared source. Another extensively used *in-situ* SEC technique is Attenuated Total-Internal Reflection – Surface Enhanced Infrared Reflection Absorbance Spectroscopy (ATR-SEIRAS). ATR-SEIRAS is a highly surface sensitivity technique based on the pioneering work by Osawa and co-workers.[1,2] This technique is very well-suited for the study of electrochemical processes relating to the structure of the double-layer, adsorption/desorption of molecules or ions and the characterization of self-assembled monolayers on metal surfaces.

The main emphasis of this Chapter is to provide the reader with the background required to fully understand advancements in *in-situ* spectroelectrochemistry presented in this thesis.

3.2. Infrared Vibrational Spectroscopy

Infrared (IR) spectroscopy deals with the interaction of infrared radiation with matter. The infrared spectrum of a compound can provide useful information about the molecular structure. The infrared region of the electromagnetic spectrum is generally considered to span from 0.770 μm to 1000 μm wavelength corresponding to 12 900 cm^{-1} to 10 cm^{-1} in common infrared spectroscopy units. This energy range is on the order of the energies sufficient to excite vibrational transitions within a molecule. The IR region is further subdivided into the near-infrared (12 900 to 4000 cm^{-1}), mid-infrared (4000 to 700 cm^{-1}) and the far-infrared (700 to 10 cm^{-1}).[3]

Nearly all molecules absorb infrared radiation with the exception of homonuclear diatomic molecules *(e.g.* H_2, O_2 and N_2). The infrared spectrum of polyatomic molecules can be complex as a result of the many possible vibrational transitions and the existence of overtones, sum and difference bands. However, infrared absorption bands are usually quite sharp and contain characteristic frequencies for certain groups in the molecule allowing for qualitative structural analysis. Further, the infrared spectrum for a given molecule is unique and can be used for the identification of unknown compounds with the aid of spectral libraries. Detailed analysis of infrared absorption bands can be extremely useful in describing and determining the structure of molecules. Similar to ultra-violet/visible (UV-VIS) spectroscopy, infrared spectroscopy has the potential to provide quantitative information using Beer's law. As a result, infrared spectroscopy is well suited to studying various electrochemical processes *in-situ* such as molecular structure, orientation and identification of intermediates.

3.3. Molecular Vibrations

Infrared spectra result from transitions between quantized vibrational energy states. A molecular vibration can range from the simple coupled motion of two atoms in a diatomic molecule to much more complex motion where every atom in a large polyatomic molecule vibrates. Molecules with *N* atoms have 3*N* degrees of freedom, three of which represent translational motion in mutually perpendicular directions (*x*-, *y*- and *z*-axes) and three rotational motions around these axes.[3–5] The remaining 3*N*-6 degrees of freedom give the number of ways the atoms in a molecule can vibrate (the number of vibrational modes), and is further discussed in Section 3.3.2. Each vibrational mode involves the approximate harmonic displacement of the associated atoms from their equilibrium positions. These modes, *i*, for the atoms involved will vibrate at a certain characteristic frequency, ν_i.

The potential energy of this motion, $V(r)$, is often described by a harmonic oscillation and is shown as a function of the distance between the atoms, *r*, as the dotted line in Figure 3.1. For any mode in which the atoms vibrate with simple harmonic motion (*i.e.* obey Hooke's law), the vibrational energy states, V_{iv}, can be described by Equation 3.1.

$$V_{iv} = h\nu_i \left(n_i + \frac{1}{2}\right) \tag{3.1}$$

where *h* is Planck's constant, ν_i is the fundamental frequency of the particular mode and n_i is the vibrational quantum number of the *i*th mode (n_i = 0, 1, 2,…). The energy for transitions between the ground state ($n = 0$) and the first excited state ($n = 1$) of most vibrational modes corresponds to the energy of electromagnetic radiation in the mid-infrared spectrum.

A more accurate description of the variation of the potential energy as a function of the displacement of the atoms from their equilibrium positions is shown by the solid green line in Figure 3.1. From this curve it can be seen that Equation 3.1 is only valid for low values of the

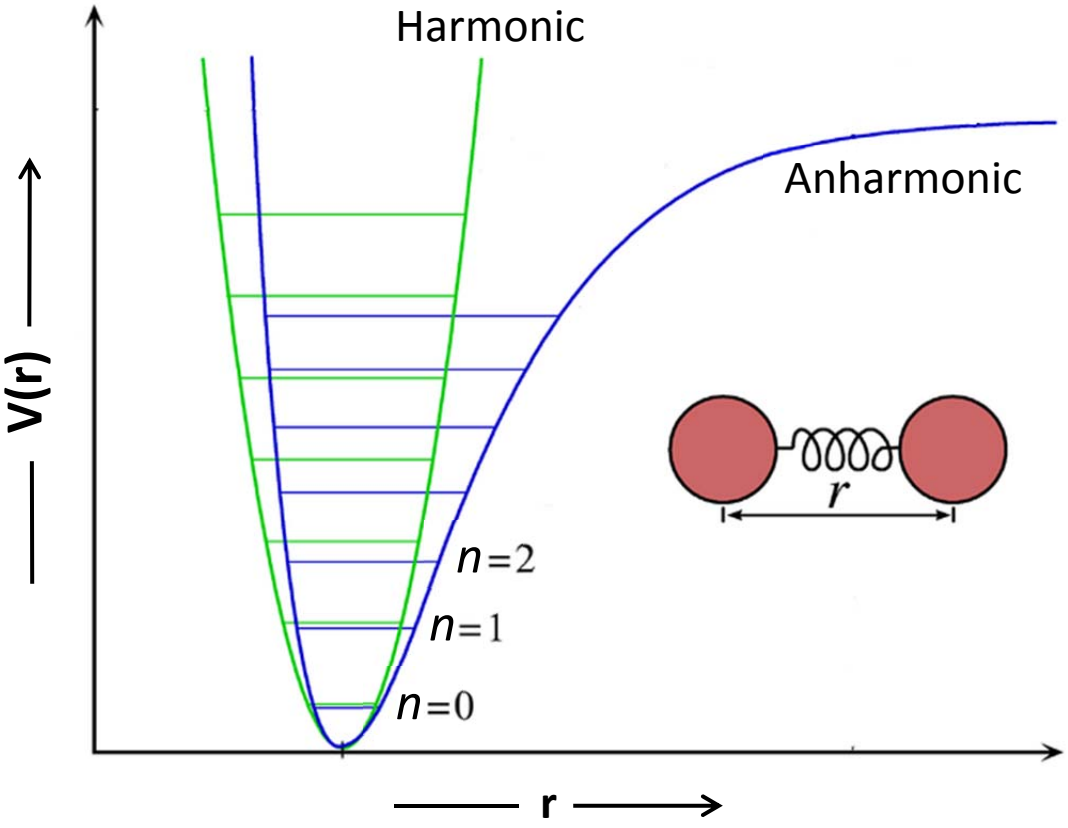

Figure 3.1. Potential energy curve for a diatomic molecule demonstrating the vibration differences between harmonic and anharmonic oscillators.

vibrational quantum number, and is not valid when n_i is large. In practice, V_{iv} must be described instead using an anharmonic potential function as shown by the solid blue line in Figure 3.1. To a first approximation, this is mathematically described by,

$$V_{iv} = h\nu_i \left(n_i + \frac{1}{2}\right) + h\nu_i x_i \left(n_i + \frac{1}{2}\right)^2 \tag{3.2}$$

where x_i is the anharmonicity constant and has values that typically range from -0.001 and -0.02 depending on the mode.

If all vibrational modes were strictly harmonic, no transitions involving changes in v_i by more than ±1 would be allowed. The effect of anharmonicity is to relax this selection rule to allow bands caused be $\Delta v_i > 1$.

3.3.1. Basis of Infrared Absorption

The selection rules for infrared absorption can be determined by evaluating the transition moment (Equation 3.3),[3,5,6]

$$R = \int \psi_i^* \mu \psi_j d\tau \tag{3.3}$$

where *R* is the transition moment for a transition between states *i* and *j*. The integration is calculated over all space, dτ, for the electric dipole moment of a vibrational transition moment, μ, expressed by,

$$\mu = \mu_0 + (r - r_e)\left(\frac{\partial \mu}{\partial r}\right)_0 + \frac{1}{2}(r - r_e)^2 \left(\frac{\partial^2 \mu}{\partial r^2}\right)_0 + \cdots \tag{3.4}$$

with μ_0 being the permanent dipole moment, *r* the internuclear distance, and r_e being the equilibrium bond length. By neglecting all but the first two terms in Equation 3.4 (dipole approximation),

$$R = \int \psi_i^* \left[\mu_0 + (r - r_e)\left(\frac{\partial \mu}{\partial r}\right)_0\right]\psi_j d\tau \tag{3.5}$$

which can be further reduced as follows, since μ_0 is constant and $\int \psi_i^* \psi_j d\tau = 0$ due to orthogonality, to

$$R = \int \psi_i^* \left[(r - r_e)\left(\frac{\partial \mu}{\partial r}\right)_0\right]\psi_j d\tau \tag{3.6}$$

From this equation, it is clear that there must be a change in dipole moment during the vibration in order for the molecule to absorb infrared radiation.

The intensity of a particular vibrational band in the infrared region is dependent on the square of the transition moment and thus to the square of the dipole moment derivative from the above equation (Equation 3.6). This implies that a molecule may have a small permanent dipole moment and a large dipole moment derivative and vice versa. For example, carbon dioxide, CO_2, has a very small dipole moment, 0.11 D, but has a large absorption cross-section in the infrared due to a very large dipole moment derivative. This explains why homonuclear diatomic molecules, having $\mu = 0$ for all inter-nuclear distances, have no infrared absorption. These particular modes, vibrations that do not involve a change in the dipole moment, are said to be *infrared-inactive*.

The strength of an infrared absorption can be described in terms of the molar absorptivity, ε, of the measured infrared band. The molar absorptivities of the strongest absorbing groups in the infrared region are still one to three orders of magnitude lower than the molar absorptivities of the most intense electronic transitions in the UV-VIS region. For instance, the highly polar bonds in C-F and C-Cl have large dipole moment derivatives and may have infrared ε values of only 100 to 1000 L mol^{-1} cm^{-1}, whereas these highly absorbing transitions in the UV-VIS have ε values on the order of 10 000 to 100 000 L mol^{-1} cm^{-1}.[3]

3.3.2. Number of Vibrational Modes

In general, molecules with N atoms will have $3N - 6$ normal modes of vibration; however, this is not the case for linear molecules which are expected to have $3N - 5$ such modes as the rotation about the molecular axis cannot be observed. Commonly used examples to illustrate normal modes of vibration are water, H_2O, and carbon dioxide, CO_2.[3–6] In the case of the nonlinear water molecule, there are three fundamental modes of vibration. Looking closely at H_2O, a permanent dipole moment arises in the molecule due to the separation of charge between the oxygen and hydrogen atoms and a change in dipole moment accompanies the absorption of infrared radiation at all three of the fundamental modes (Figure 3.2a). As such, these modes are called *infrared-active* vibrational modes. When analyzing the linear CO_2 molecule in a similar manner (Figure 3.2b), four fundamental modes of vibration are expected. Conversely, the symmetric stretch in CO_2 does not give rise to a change in dipole moment and is infrared-inactive. In the infrared spectrum for CO_2, however, only two fundamental vibration absorption frequencies are observed. The two bending modes are degenerate and absorb at the same frequency and demonstrate the complexity that can develop when analyzing an infrared spectrum. In addition to the vibrational modes presented in Figure 3.2, with extra atoms in a molecule more complicated vibrational modes can develop (see Figure 3.3).[3–6]

Although the number of expected vibrations can be calculated from the number of degrees of freedom for a given molecule, often polyatomic molecules experimentally show fewer absorption bands, and in a few cases more, than expected. For example, fewer absorption bands may be measured when there are: inactive infrared vibrational modes, degenerate vibrations,

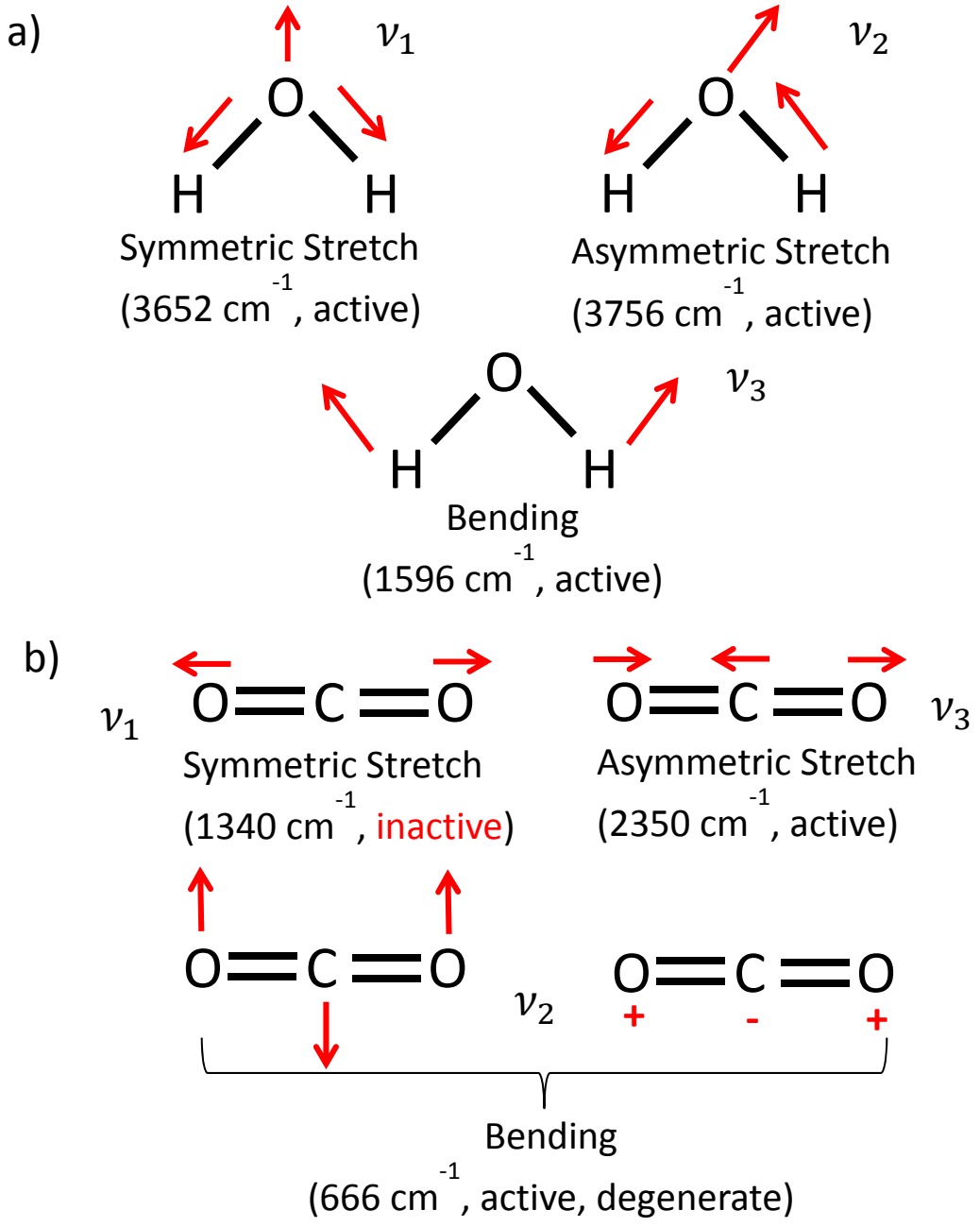

Figure 3.2. Vibrational modes in H_2O (a) and CO_2 (b).

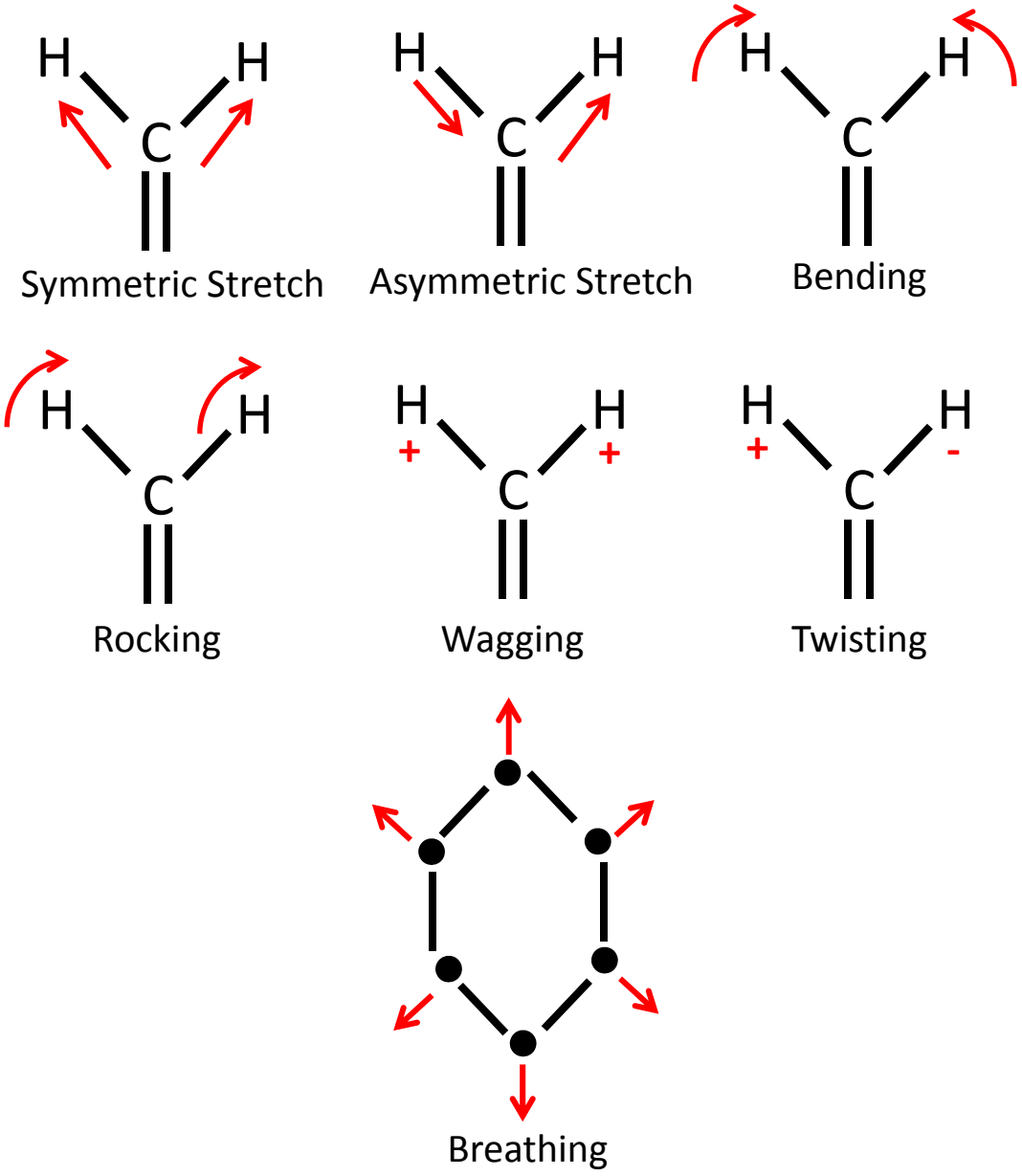

Figure 3.3. Vibrational modes for a methylene group and the breathing vibration for a ring compound.

weak absorption cross-sections and instrumental aspects including, but not limited to, poor resolution and spectral range. When more infrared absorption bands are observed, overtones, combination and difference bands may be the cause. For the latter two examples, a combination band may arise if two vibrational modes are excited simultaneously. Finally, it is important to note that these non-fundamental transitions are much weaker in intensity than the fundamental transitions.

3.3.3. Group Frequencies

An interesting phenomenon is often exploited when studying infrared spectra and that is that with certain functional or structural groups, their vibrational frequencies are nearly independent of the rest of the molecule. An example of this is the stretching vibrations of the carbonyl group in various aldehydes and ketones are almost always observed between 1650 cm^{-1} and 1740 cm^{-1}. Such frequencies are characteristic of the functional or structural group and are called group frequencies and are only slightly affected by the composition of the rest of the molecule. The presence of these group frequencies in an infrared spectrum are a great asset for the determination of a molecule and its structure.

These group frequencies are typically found in the mid-infrared spectral region (4000 – 1000 cm^{-1}) and in practice this region is called the group frequency region of the infrared spectrum.[3–6] The fingerprint region of the infrared spectrum (1200 –700 cm^{-1}) is so-called because the vibrational frequencies are influenced by the entire molecule and can be used for identification purposed by comparison to spectral libraries.

3.3.4. Vibrational Coupling

The frequency of a specific vibrational mode may be influenced by the presence of other vibrations in the molecule through vibrational coupling. Strong coupling can occur between two stretching vibrations if, for example, the two vibrations share a common atom. Interactions can also occur between two bending modes that share a common bond between the groups. Vibrational coupling is strongest when the energies of the isolated vibrational frequencies are approximately equal in magnitude, share the same symmetry and an appreciable interaction between the groups exists. For instance, if the two groups are separated from each other by two or more bonds vibrational coupling is unlikely to occur. A simple example of this is in the infrared spectra between methanol and ethanol where an additional C-C bond interaction in ethanol results in a 20 cm^{-1} shift in the carbonyl C-O stretching frequency compared to the same stretch in methanol. It is therefore not possible for the absolute position of an absorption band to be specifically known for a given group frequency with every molecule.[3] These slight shifts allow for valuable qualitative analysis and a unique infrared spectrum for different molecules.

In the situation when an overtone or combination frequency interacts with a fundamental vibration, the resulting interaction is called a Fermi resonance. The result of these interactions effectively raises one frequency and lowers the other. The separation and resulting intensities of the bands depends strongly on how close in frequency the two unperturbed vibrations are. An example of this is in the case of the CH stretch in aldehydes at 2800 cm^{-1} interacting with the first overtone of the 1400 cm^{-1} in-plane CH stretch. The resulting spectrum has a doublet peak in the infrared region between 2700 and 2900 cm^{-1} as a result of the Fermi resonance.

3.4. Fourier Transform Infrared Spectroscopy

3.4.1. Michelson Interferometer

Infrared spectroscopic measurements are routinely acquired using the two-beam interferometer designed by Michelson in 1891.[7] Other designs have followed, but the theory behind the operation remains the same. Essential for all scanning two-beam interferometers is a device that divides a beam of radiation into two paths, using a beam splitter, and two mirrors to reflect the beams back before recombining them after introducing a path difference (optical path difference OPD; often called the retardation, δ). When this occurs, a condition can develop in which interference between the two beams is produced. The variation in the intensity of the beam emerging from the interferometer is measured by a suitable detector as a function of the path length difference created by moving one of the mirrors with respect to the other. Figure 3.4 depicts this simple concept with two mirrors mutually perpendicular to each other but with only one of the two mirrors capable of moving along the axis of incident radiation.

An important component of the Michelson interferometer is the beamsplitter which intersects the fixed and movable mirror to create a condition where the incident beam is partially reflected along each path and recombined upon exiting the interferometer. An interesting aspect often overlooked in the Michelson interferometer is that the beam that exits the interferometer has an equivalent beam that radiates back towards the source. As such, the intensity of the beam that exits the interferometer is further decreased as a result of the partial reflected radiation back towards the source.

The movable mirror can be moved either at a constant velocity (a continuous scan interferometer) or in discrete positions along the movable mirror axis (step-scan interferometer).

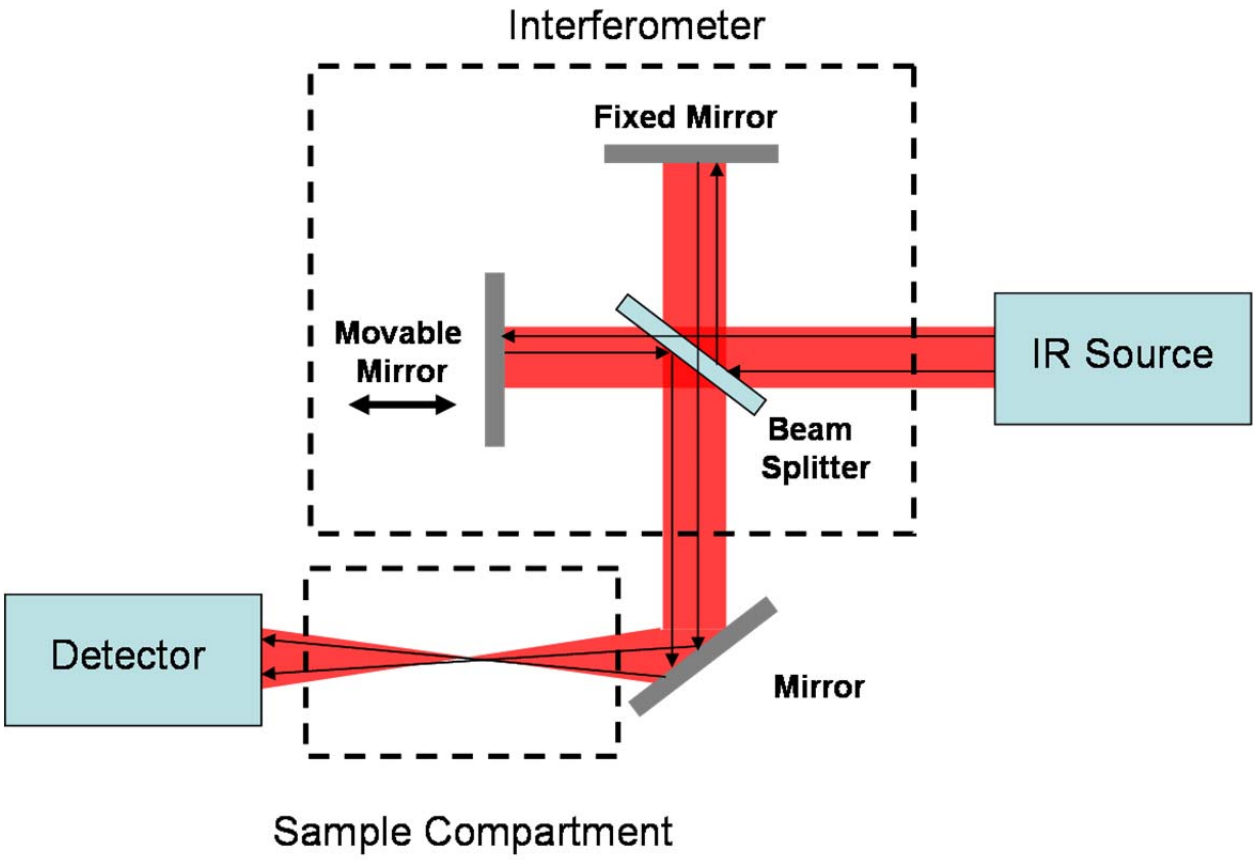

Figure 3.4. Simple two-beam Michelson Interferometer.

When the mirror drive in a continuous scan interferometer operates at relatively high rates, the interferometer is often called a rapid-scan interferometer. Both rapid-scan and step-scan interferometers are utilized in *in-situ* spectroelectrochemical (SEC) kinetic measurements in this thesis.

To better understand the processes that occur in a Michelson interferometer it is often convenient to consider an idealized situation using a monochromatic radiation source and an ideal beamsplitter (*i.e.* one that does not absorb any of the radiation and both the reflection and transmission is exactly 50% of the intensity). When the fixed and movable mirrors are equidistant from the beamsplitter (zero retardation or zero path difference, ZPD) a unique situation develops in that the two beams are perfectly in-phase with each other upon recombination and the beam experiences constructive interference. All the light reaches the detector and none is reflected back towards the source. This is the result of the 90^0 phase change a beam undergoes at each reflection and in this case, destructive interference of the radiation at the beamsplitter cancels out all light directed along the path back to the source. At the ZPD all the incident beam power is transmitted to the detector and no light returns to the source.

For a monochromatic source, there is no way to determine whether a maximum signal data point along the retardation axis is the ZPD or a retardation equal to an integer number of wavelengths from the incident wavelength. If the mirror is driven at constant velocity, the resulting signal measured at the detector, $S(\delta)$, would appear to be sinusoidal with a maximum intensity at integral multiples, $\delta = n\lambda_0$, of the incident wavelength, λ_0. The measured signal at the detector is referred to as an interferogram and in the simple case of monochromatic radiation can be expressed as,

$$S(\delta) = B(\tilde{\nu}_0)cos2\pi\tilde{\nu}_0\delta \tag{3.7}$$

where $\tilde{\nu}_0$ is the corresponding incident radiation wavenumber and $B(\tilde{\nu})$ is the intensity of the source at the corresponding wavelength.

When the source is no longer monochromatic but produces continuous radiation, $\tilde{\nu}$, the measured interferogram is the superposition result of the interferograms corresponding to each individual wavelength. The resulting interferogram can be expressed as follows,[4,8]

$$S(\delta) = \int_{-\infty}^{+\infty} B(\tilde{\nu}) cos 2\pi\tilde{\nu}\delta d\tilde{\nu} \tag{3.8}$$

Mathematically, $S(\delta)$ is the cosine Fourier Transform of $B(\tilde{\nu})$ and as a result a spectrum can be calculated from an interferogram of this form by computing the Fourier Transform and is called Fourier Transform Spectrometry. When the incident radiation used is in the infrared region of the electromagnetic spectrum, the technique is referred to as Fourier Transform Infrared (FTIR) Spectroscopy.

In practice it is not possible to sample the interferogram at the infinitely high resolution expressed in Equation 3.8. The interferogram can only be sampled at finite sampling intervals and places resolution limits on the measured interferogram and computed spectrum. For practical purposes, the Discrete Fourier Transform (DFT) is used in the transformation from interferogram to spectrum.[4,8]

$$S(n\Delta x) = \sum_{n=0}^{N-1} B(k\Delta\nu)\, exp(i2\pi nk/N) \tag{3.9}$$

where the continuous variables δ and $\tilde{\nu}$ have been replaced by $n\Delta x$ and $k\Delta\nu$ respectively.

Consider two peaks that are separated by $\Delta\tilde{\nu} = (\tilde{\nu}_1 - \tilde{\nu}_2)$ and will become out of phase at $0.5(\Delta\nu)^{-1}$ and will be back in phase after a retardation of $(\Delta\tilde{\nu})^{-1}$.[4] To measure one complete period of this beat frequency, and resolve the two peaks, a retardation of $(\Delta\tilde{\nu})^{-1}$ would need to be measured. The smaller the difference between the two peaks (small values of $\Delta\tilde{\nu}$), the greater

the retardation needs to be before the two cosine waves become in phase and can be resolved. That said, the apparent spectral resolution depends in the maximum retardation of the interferometer. Instrumentally this means for high resolution measurements of FTIR spectroscopy, a long mirror drive is required. For example, to acquire a spectrum with a spectral resolution near 0.001 cm^{-1}, a several meter long mirror drive would be required. Typically, mid-infrared spectral resolutions on the order of 4 cm^{-1} are adequate for routine measurements and have much smaller maximum retardations on the order of centimeters.

Several important considerations need to be accounted for when sampling the interferogram at finite positions over a discrete optical retardation range. Typically, modern FTIR spectrometers make use of the interference pattern of a monochromatic source, HeNe laser, to control the change in the optical path difference. By discretely sampling the interferogram of the continuous light source at the zero-point crossings of the HeNe laser, an internal wavelength reference with accuracy determined solely by the precision of the laser beam itself allows for highly accurate infrared spectra to be produced. However, various artifacts can be mathematically introduced into the resulting Fourier transformed spectra. Some of the more prevalent spectral artifacts are resolution bias error (also known as the picket-fence effect), aliasing and leakage.[8] Aliasing will be discussed in further detail later in this Chapter as a technique to undersample interferograms in effort to decrease interferogram data collection times for step-scan interferometry which are strategically utilized in Chapter 7.

In the picket-fence effect, the calculated Fourier transformed spectrum is a discrete spectrum and consists of estimates of what the spectral level is at specific frequencies. These frequencies are determined by the analysis and data acquisition parameters and have nothing to do with the signal being analyzed. This has the potential that there probably are peaks in the true

spectrum of the signal that are between the lines of the discrete Fourier Transform analysis. Experimentally, the peaks in a Fourier Transformed spectrum will be measured too low in level, and the valleys will be measured too high. Moreover, the true frequencies where the peaks and valleys exist may not be those indicated by the calculated Fourier Transform spectrum. This phenomenon is called resolution bias error, but is colloquially known as the *picket fence effect*. In other words, when looking at a Fourier Transformed spectrum, it is like looking at mountain range through a picket fence.

Resolution biasing errors can be overcome by adding zeros to the end of the interferogram, called zero-filling, before the discrete Fourier Transform is performed. By doing this the number of points per wavenumber in the spectrum is increased and the noise is reduced. It is recommended that one should choose a zero-filling factor of two, essentially doubling the number of data points present in the interferogram. However, if the expected line-shape widths are similar to the spectral sample spacing, larger values for the zero-filling factor, up to 8, may be more appropriate. This solution does not introduce any further errors in the spectrum as it does not change the instrumental line shape.

Unlike the picket-fence effect, spectral leakage is not due to the digitization of a continuous interferogram, but instead is caused by the data truncation of the interferogram at a finite optical path difference. Instrumentally speaking, there is a finite distance a mirror can be driven in an interferometer. When the data collection abruptly stops, exact integer multiples of the wavelengths of radiation may not have been recorded. When an interferogram is Fourier Transformed the spectral response displays not only a spectral peak, but numerous 'side lobes' or 'feet' to the peaks. The spectral component of interest no longer contains the complete intensity but rather contains the energy of adjacent components and noise. The leakage from a larger

signal component may significantly overshadow smaller signals making them difficult to identify or detect. The solution to this problem is to truncate the interferogram less abruptly. In other words, find a suitable mathematical function, an apodization function (Greek for 'removal of feet'), to apply to the interferogram to mitigate the effects of spectral leakage and the restriction of having a limited observation interval. Numerous functions of this nature exist, with the most commonly used functions being the Happ-Genzel and the 3-Term Blackman-Harris function.[4]

3.4.2. Spectral Aliasing

Another source of error in the Discrete Fourier Transform (DFT) is aliasing.[4,8] To understand what is meant by aliasing consider the basic DFT equation (Equation 3.9) which describes how a spectrum measured at wavenumbers $(k \cdot \Delta v)$ can be transformed from an interferogram sampled at optical path differences, $(n \cdot \Delta x)$. Both *n* and *k* will run from 0 to *N*-1 generating *N* complex output data points from *N* generally real measured data inputs producing the expected output in Figure 3.5a. However, this is not what occurs in practice. When the DFT calculation is performed on the interferogram, it yields not just a single spectrum but rather the spectrum plus its mirror image such that the first *N*/2 points represents the expected spectrum and the second starting at $k = N/2$ equaling its mirror image (Figure 3.5b). Practically this means that a DFT of an *N*-point interferogram yields *N*/2 meaningful output data points. As this second set of *N*/2 points is a mirror image of the first it is redundant and is discarded. To understand this, if index *k* is substituted by *N*-*k*, using the identity $exp(i2\pi k) = 1$, the obtained result describes a mirror symmetry $S([N-k]) = S(-k)$ about a so-called "folding" or "Nyquist" wavenumber v_f.[8]

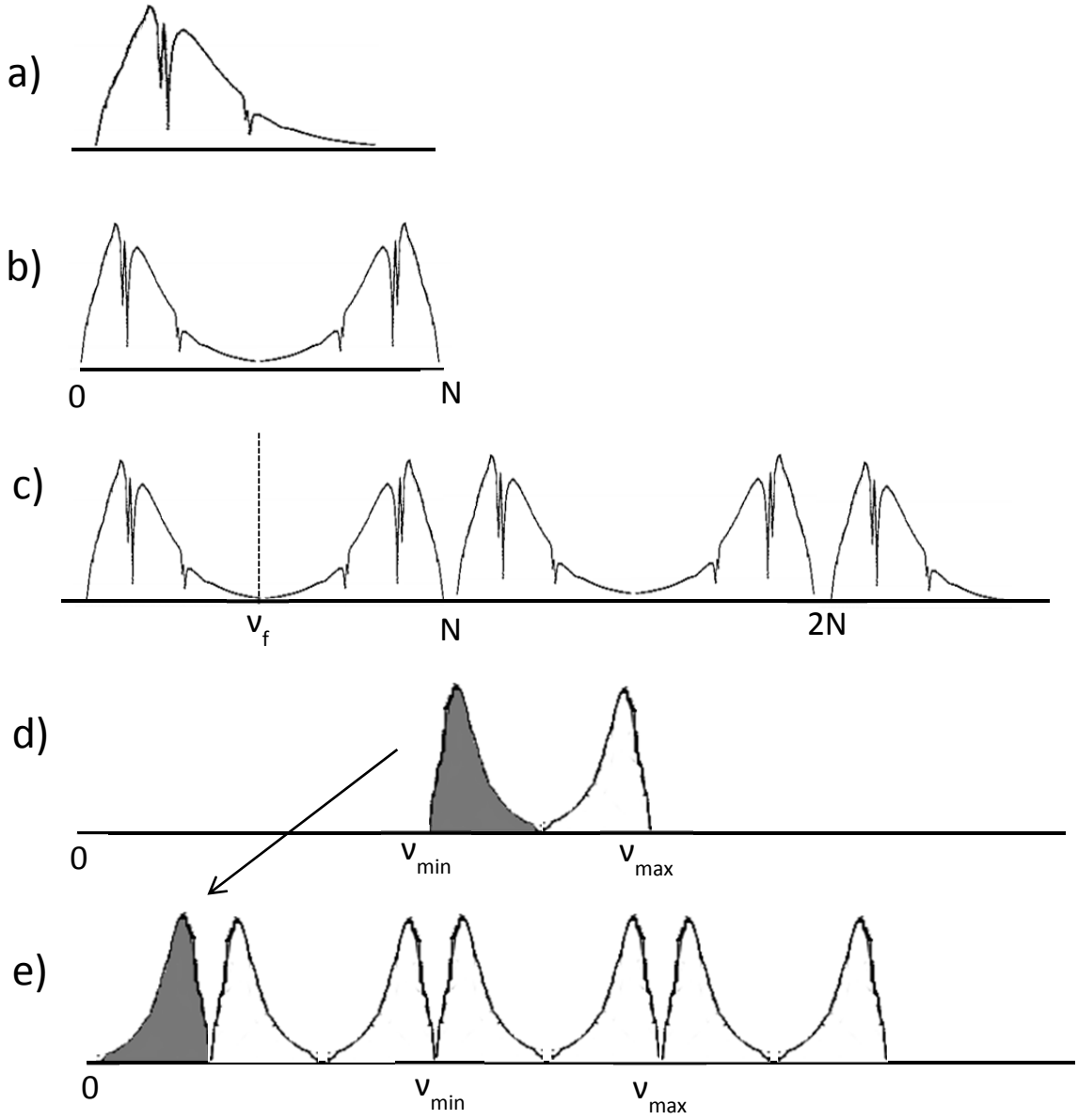

Figure 3.5. a) Expected Fourier transform spectrum, b) DFT of an N-point interferogram, demonstrating the mirror imaging that occurs as a result, c) The effect of aliasing on the spectrum pictured in b), d) A spectrum demonstrating the requirements for undersampling (note the spectrum is zero everywhere but between the folding limits) and e) Aliases resulting from undersampling the interferogram.

Further to the point, inspection of Equation 3.9 reveals that not only is the index *k* valid from 0 to *N*-1, but for all integer values including negative numbers. Considering this, if *k* is replaced by $k + mN$ in Equation 3.9, where *m* is an integer, the final result is $S([k + mN]) = S(k)$. In other words, the mirror symmetry described in an N-point sequence is repeated periodically as indicated by Figure 3.5c. This replication of the original spectrum and its mirror image on the wavenumber axis across *k*-space is termed aliasing.

3.4.2.1. Alias Overlap

It is clear from Figures 3.5b and 3.5c that a unique spectrum can only be realized if the spectrum does not overlap with its mirror-symmetrical replicate. This condition is valid only if the spectrum is zero above a maximum wavenumber v_{max} and is smaller than the folding wavenumber, v_f. However, if there is a non-zero contribution above the folding wavenumber, v_f, this contribution will be "folded back" below v_f and will result in the appearance of a spectral artifact, *i.e.* a spectral feature at the wrong position on the frequency scale. This possible type of error is known as an aliasing artifact.

In most conventional FTIR spectrometers, the interferogram sampling positions are defined by the zero-crossings of a HeNe laser having a wavelength of 15 800 cm^{-1}. In terms of the maximum bandwidth that can be sampled without spectral overlap (aliasing), the folding-wavenumber is also 15 800 cm^{-1}.

3.4.2.2. Undersampling

Given the above discussion, it is possible to reduce the interferogram size through a technique known as undersampling which can save considerable amounts of time in data

collection.[4,8] This can only be achieved if the spectral intensity is zero below a lower band limit, ν_{min} (ν_{min} is not equal to zero), and the spectrum band limits, $\nu_{min}$and ν_{max}, are between a lower, $\nu_{f,LOW}$, and the upper folding limit, $\nu_{f,HIGH}$ (as shown in Figure 3.5d). As a further note, the upper folding number, $\nu_{f,HIGH}$, must be an integer multiple ($n = 1,2,3, ...$) or a natural fraction ($1/4\,, 1/3\,, 1/2\,, ...$) of the HeNe laser wavenumber in order to correctly fold the spectrum into the right wavenumber space.

If the sample spacing is increased by a factor of *n*, the spectrum (Figure 3.5d) will overlap appreciably resulting in the spectrum filling the previous empty range from 0 to $\nu_{f,LOW}$ with *n*-1 copies of the original spectrum (Figure 3.5e). Since these copies are identical, with the exception of their absolute wavenumber, the desired spectrum does not have to be calculated with a true *N*-point interferogram. Instead, a calculation involving the alias of the lowest wavenumber by an *N*/n-point interferogram followed by correcting the wavenumber scaling results in the desired spectrum measured with fewer interferogram points while maintaining spectral quality.

Modern FTIR spectrometers and software determine the appropriate sampling and undersampling conditions based on the input of the desired spectral range by the user. This can be dangerous to the user's data if they do not understand the experimental conditions required to facilitate this type of measurement. In particular, the user is still required to ensure that there are no spectroscopic contributions outside the entered spectral range (between $\nu_{min}$and ν_{max}). One way this is often achieved is through the use of optical or electronic filers. If suitable care is not taken into account, unwanted aliasing may occur and produce artifacts in the final calculated spectrum.

3.4.3. Phase Correction

The last mathematical step in the conversion of an interferogram into a spectrum is a phase correction.[4] A phase correction is required because at the ZPD it is possible that not all the optical frequencies are in phase partly due to the optical response of the beamsplitter, electronic filters and amplifiers. In other words, the interferogram may not be symmetric about the ZPD and after processing the interferogram an inaccurate representation of the true spectrum would result. There are many techniques to accomplish this process with one of the most commonly used techniques formulated by Mertz.[9] A complete description of the Mertz technique is beyond the scope of this thesis.

3.5. Introduction to Continuous-Scan and Step-Scan Interferometry

3.5.1. Continuous Scan Interferometers

Continuous scan interferometers account for the majority of currently used FTIR spectroscopic measurements. As previously mentioned, the mirror in the interferometer is in constant state of motion during the collection of the interferogram, with digitization occurring at the zero-point crossings of the reference HeNe laser. Typically, the signal-to-noise is improved by repeating the data collection and co-adding numerous interferograms to produce a single spectrum. For accurate phase correction, it is important that the data collection for an interferogram starts at a point before the ZPD and that the data is acquired over the maximum retardation required for the desired resolution. When the mirror has reached the desired retardation, it is decelerated and depending on the interferogram data acquisition type will traverse backwards collecting another interferogram (forward-backward scanning) or immediately return to the start position and proceed with another interferogram from the starting

point (forward only scanning). Another option exists where interferograms can be collected as either double- or single-sided. In double-sided forward-backward collection, essentially four single-sided interferograms are acquired as the mirror drive starts at the maximum retardation on one side of the ZPD and traverses forward and backward for the desired retardation paths. It is important to note that the forward and backward collected interferograms must be processed separately into infrared spectra before they can be co-added. Even though the interferograms are essentially optically identical, different responses from electronic filters and amplifiers for the detector are measured and produce direction dependent phase responses. This particular aspect becomes important for signal averaging rapid-scan time-resolved FTIR spectra presented Chapters 5 and 6 of this thesis.

3.5.2. Step-Scan Interferometer

In contrast, step-scan interferometry involves translating the moving mirror to discrete measurement positions, essentially halting at specific retardations determined by the zero-point crossings of the reference HeNe laser and the desired spectral resolution. The interferogram is then sampled one point at a time building an interferogram as data is collected at the various stepped mirror positions. This form of data collection allows for much higher temporal resolutions compared to those that than can be obtained from measurements made using continuous scanning mode which are limited to the mirror drive velocity.[10–13] To achieve the high temporal resolution required to match the fast electrochemistry using ultramicroelectrodes, step-scan interferometry was an essential component of the experimental methodology designed and utilized in Chapter 7 of this thesis.

3.5.3. Final Word on Fourier Transform Infrared Spectroscopy

Fourier transform infrared spectroscopy is the most widely used technique to measure molecular vibrations. As discussed, there are several important aspects of using FTIR spectroscopy to consider when perform typical (and not so typical) infrared measurements. Aside from these, it is important to mention the numerous advantages to using FTIR spectroscopy over dispersive instruments. The first such advantage is a multiplexing advantage (sometimes called the Fellgett advantage).[4] In dispersive spectrometers, the absorption of vibrational energy in a molecule is observed sequentially as a grating optic is scanned across the wavenumber space. In contrast, continuous scan FTIR spectrometers allow for the observation of all wavelengths of light at the same time allowing for faster measurements of equal quality. Comparing a dispersive instrument and a FTIR spectrometer under identical conditions (spectra collected in the same measurement time, at the same resolution, and with the same source, detector, optical throughput, and optical efficiency) a 2 cm^{-1} resolution 800 - 8000 cm^{-1} spectrum measured using a dispersive spectrometer could take 30 minutes. A spectrum with similar signal-to-noise for a FTIR spectrometer could take on the order of seconds. If additional scans are required to boost the signal-to-noise, adding a couple of seconds to a measurement *versus* minutes to hours with dispersive instruments decreases the overall time for an experiment.

The second advantage often discussed when using a FTIR spectrometer is the throughput advantage (sometimes referred to as the Jacquinot advantage).[4] This is achieved because FTIR instruments do not require optical slits (in the traditional sense) to achieve resolution which necessarily decrease the amount of incident radiation on the sample in dispersive instruments. Therefore, a much higher throughput is capable with FTIR instruments as all the light exiting the interferometer can be used to measure a given sample with the maximum number of available

photons. Another consequence of using a FTIR spectrometer over a dispersive instrument is the higher achievable level of spectral resolution. The spectral resolution of a spectrometer is a measure of how well it can distinguish between closely spaced spectral features. To adjust the spectral resolution in a dispersive spectrometer, it is often necessary to decrease the slit width, thereby decreasing the amount of available light for the measurement (adding noise and increasing the time required to take a high resolution measurement). In the case of a FTIR spectrometer, the value of the spectral resolution is a function of the maximum achievable value of optical path difference (OPD). This implies that in order to achieve a given resolution over a specified wavenumber region all that is needed is to increase the retardation length of the scanning mirror; without decreasing the amount of incident radiation probing the sample. These advantages highlight the successes of using Fourier transform infrared spectrometers to make infrared vibration measurements. In the next section, the topic of Surface Enhanced Infrared Reflection Absorption Spectroscopy (SEIRAS) will be described before a further discussion on infrared sources and time-resolved techniques is presented.

3.6. Surface Enhanced Infrared Reflection Absorption Spectroscopy

Surface enhanced infrared reflection absorption spectroscopy (SEIRAS) is a powerful internal reflection technique for *in-situ* spectroelectrochemistry given the strong sensitivity and selectivity towards electroactive molecules on or near the surface. Many of the challenges that limit the use of external reflection spectroscopy (*i.e.* strong background absorption from solvents and low sensitivity to adsorbed molecules), can be overcome using SEIRAS techniques. The nature of SEIRAS is very similar to surface enhanced Raman spectroscopy (SERS) in that both techniques utilize textured metal surfaces to achieve electric field enhancement effects.[14] The

various aspects of the theory of SEIRAS and certain experimental considerations will be discussed in this section starting with a discussion on the mechanisms responsible for the measurable enhancements.

3.6.1. The Mechanism of SEIRAS

The largest contributing factor to the SEIRAS phenomena is due to the electromagnetic (EM) interactions between the incident light and the molecules on or near a roughened metal surface. To model this effect, Osawa assumed the metal film consists of metal islands (evidenced by atomic force microscopy[15]) and that each island can be represented as a metal ellipsoid particle (as shown in Figure 3.6). If the metal particle is smaller than the wavelength of light incident upon it, the particle will become polarized as a result and generate a larger EM field around it then the incident light alone.[16] It is estimated that this new EM field is approximately 10 times larger than the incidence field.[17] Added to this effect, an additional enhancement occurs when a molecular vibration induces a dipole moment in the metal further perturbing the EM polarization of the metal particles. This perturbation, induced by the adsorbed molecules, is only significant at the frequencies of vibrations present in the molecule and is negligible everywhere else. This has the effect of amplifying the molecular vibrations as they are mirrored through a change in absorption or reflectance of the metal film. This is a consequence of the absorption coefficient of the metal film being much larger than the molecules in the infrared region. Simply put, the metal particles act as an amplifier of the infrared absorption of adsorbed molecules giving rise to the enhancement observed in SEIRAS. The larger the illuminated surface area, the more amplified this effect becomes.

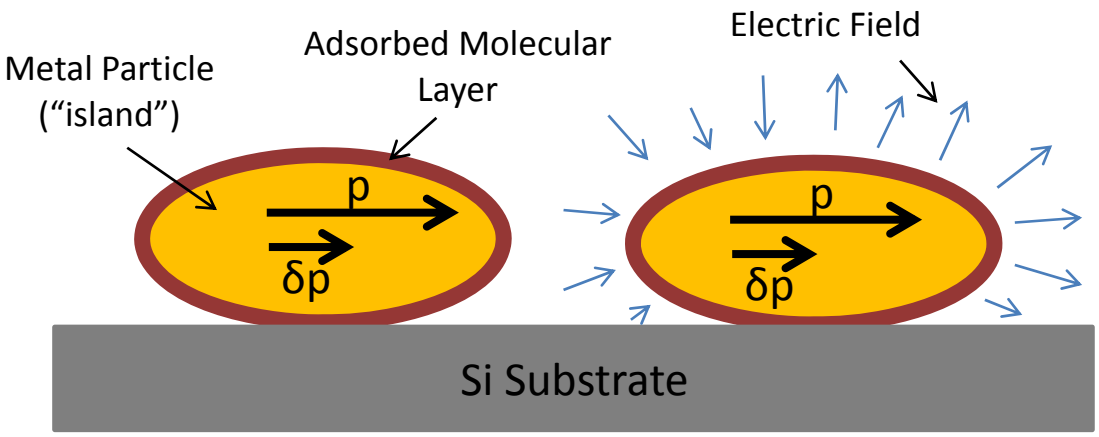

Figure 3.6. Schematic representation of the electromagnetic mechanism of Surface Enhanced Infrared Absorption Spectroscopy (SEIRAS) as described by the model developed by Osawa. The dipole, p, generating an electromagnetic field around the particle upon excitation of an incident photon and the molecular vibration inducing an addition dipole, δp, in the metal island that effect the optical properties of the metal particles at the particular molecular vibration frequency.

A feature of the enhanced surface EM field around the metal particles is that it is essentially polarized along its surface normal as shown in Figure 3.6. As a consequence, only molecular vibrations with a transition dipole moment that is perpendicular to the surface are enhanced. This surface selection rule is important to consider when analyzing ATR-SEIRAS measurements and is similar to infrared absorption reflection spectroscopy (IRRAS) in that regard.[18] To further elaborate on this concept, consider the transition dipole of the adsorbed molecule perpendicular to the surface. This dipole moment will constructively interfere with the dipole formed in the metal island upon excitation from the incident radiation and thus provides a surface selection rule enhancement for adsorbed molecules. The distance dependence of this SEIRAS enhancement effect is proportional to $1/r^6$ where r is the distance from the dipole moment induced in the metal particle. This is a further reason that the SEIRAS effect is confined to molecules adsorbed at the surface and is why SEIRAS is a considered a surface sensitive technique. Utilizing this technique for *in-situ* spectroelectrochemical measurements has some specific and challenging experimental aspects. The remainder of this section will highlight some of these important aspects that were critical for the experimental results presented in Chapters 4 and 5.

3.6.2. Attenuated Total-Internal Reflection (ATR)

An important element in successfully acquiring SEIRAS measurements in internal reflection is the attenuated total-internal reflection (ATR) phenomenon. In ATR, the incident infrared beam is directed onto an infrared transparent crystal (internal reflection element; IRE) with a relatively high refractive index (*i.e.* Si: 3.4, Ge: 4.0, ZnSe: 2.4).[19,20] The infrared beam reflects from an internal surface of the crystal and an evanescent wave is produced that projects

orthogonally through the reflecting surface. This evanescent wave can interact with the metal island film placed on top of the reflecting plane and the returning reflected beam measured at the detector. It is important that the angle of incidence is equal to or greater than the critical angle of the interface. If the critical angle is not met, the resulting spectrum could result only from the external reflectance. Both the angle of incidence, and infrared polarization, also plays a crucial role in the optimization of SEIRAS measurements and further details will be discussed in a subsequent section.

For completeness, the penetration depth, d_p, of the evanescent wave (defined as the distance required for the electric field amplitude to fall to e^{-1}) is often discussed when considering ATR techniques. The wavelength dependence on the depth into the sample is given by,[19,20]

$$d_p = \frac{\lambda}{2\pi(n_1^2 sin^2\theta - n_2^2)^{1/2}} \tag{3.10}$$

where λ is the wavelength of the incident light, θ the angle of incidence, and n_1 and n_2 are the refractive indices of the crystal and sample respectively. Typical penetration values for mid-infrared radiation are on the order of a few microns and demonstrate some level of surface sensitivity as a result. By exploiting this ATR optical geometry, an *in-situ* spectroelectrochemical apparatus can be realized taking advantage of SEIRAS. A significant obstacle, however, in the development of any ATR-SEIRAS setup, is in the grafting of a thin-metal film to the IRE for suitable surface enhancement.

3.6.3. Preparation of the Thin-Metal Film Electrodes

A unique feature of using ATR-SEIRAS for *in-situ* SEC is that the thin-metal film required achieving surface enhancement, serves a double role as it also functions as the working

electrode in an electrochemical cell. In the work presented in Chapter 4 and 5, Au metal films were prepared by electrolessly depositing the metal to the surface of the reflecting plane of the Si hemisphere IRE. Aside from the aforementioned technique, vacuum evaporation is another means to deposit the metal to the IRE.[21] In the case of the vacuum evaporation, a roughly 20 nm thick film needs to be slowly deposited onto the IRE to obtain SEIRAS active films.[22]

Recently, methods of electrolessly depositing the thin-metal film on Si and Ge have been developed producing stable SEIRAS active films.[15] This process is quite a bit more experimentally challenging compared to the vacuum evaporation technique, but the resulting films produced SEIRAS films were found in this thesis to provide more electrochemically stable metal films with more consistently higher infrared enhancement activity. The process of preparing these films consist of exposing the total reflecting plane of the prism (IRE) to a plating solution consisting of the desired metal salt and a reducing agent in a buffer.[15,23] Higher quality films can be obtained by performing the plating at elevated temperatures (~65^{o}C) and by initially cleaning the substrate. For the Si hemisphere IRE used throughout this thesis (25 mm diameter), the surface is contacted with a 40% NH_4F aqueous solution for a few minutes to remove the oxide layer and to terminate it with Si-H. Ensuring these steps are followed, the thin-films produced by electrolessly deposition will have good adhesion and be SEIRAS active approximately 80% of the time.

The final step in preparing the gold coated Si hemisphere IRE is to electrochemically clean the thin metal film. This is accomplished by running cyclic voltammetry (CV) in 0.5 M H_2SO_4 into the oxidation region of the gold film until a stable CV is produced. From start to finish, the process of preparing the Si IRE with a gold metal film for *in-situ* ATR-SEIRAS SEC measurements is approximately two hours.

3.6.4. *In-situ* ATR-SEIRAS SEC Experiment Considerations

An *in-situ* ATR-SEIRAS SEC experiment first begins by mechanically polishing the reflecting plane of the Si hemisphere before electrolessly plating a thin layer of gold on this surface. Once complete, the process of electrochemically cleaning the thin-film is performed in the *in-situ* SEC cell which has been preset in the sample compartment of the FTIR spectrometer. This allows for infrared measurements to be taken of the thin film before and after and to assess if the film is SEIRAS active or not before continuing on with the desired experiment. This was typically accomplished by analyzing the infrared absorption of water before and after the electrochemical cleaning process.

It is important to mention that once the *in-situ* SEC cell has been assembled (Figure 3.7), with the thin-metal film, due to the design of the cell the thin-film does not survive the disassembling process. In addition, the mechanical stability of the thin-film can be further extended by keeping the film under solution and through the careful exchange of any solutions thereafter. With a fully assembled *in-situ* SEC cell, experiments on the adsorption properties of DMAP (Chapter 4) and on the time-resolved kinetics of proton-coupled electron-transfer reactions (Chapter 5) can be performed. Specific details on the experimental parameters used in each of these studies are provided in their corresponding Chapters.

3.7. Infrared Light Sources

3.7.1. Conventional Globar Sources

Conventional infrared sources found in most modern FTIR spectrometers rely on the emission from a blackbody radiator. Typically, this device is made from a sintered silicon-

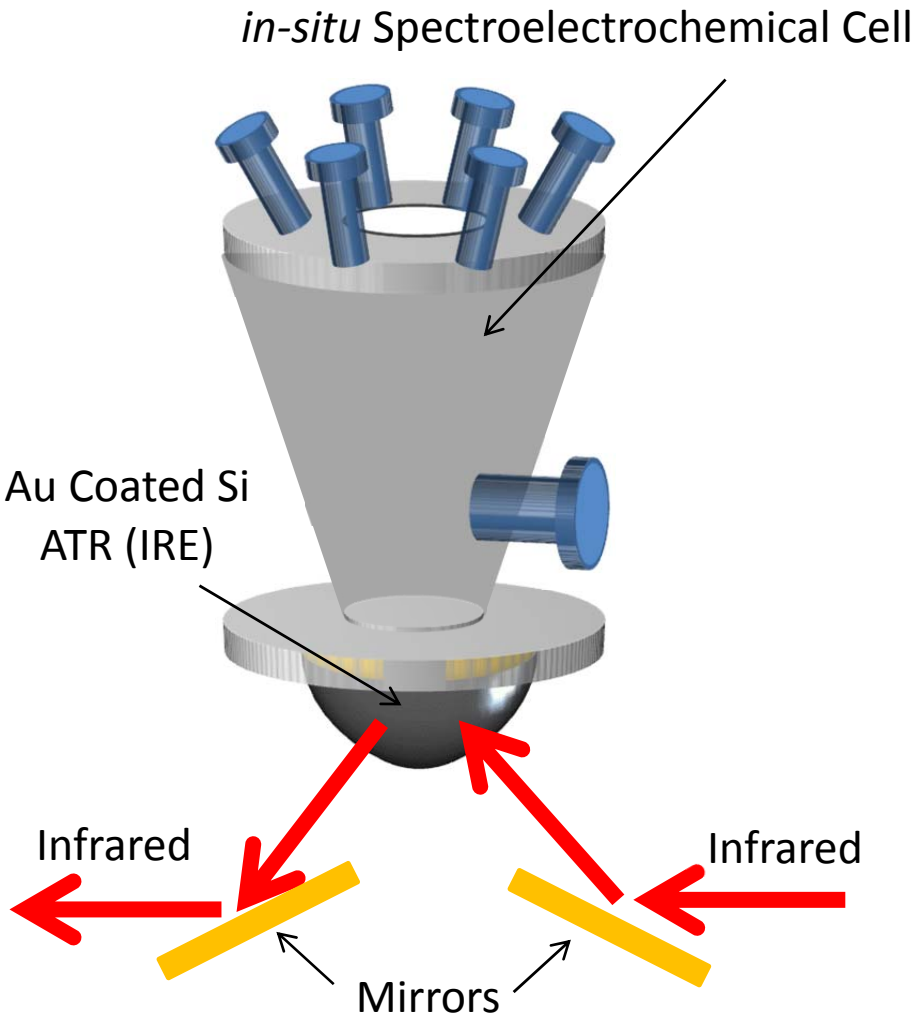

Figure 3.7. Pictorial representation of the assembled in-situ spectroelectrochemical cell used for ATR-SEIRAS measurements.

carbide element (trade name Globar®) and heated to a temperature of about 2000 K by passing an electrical current through it. The infrared radiation produced is emitted in all directions and must be collected through the use of focusing mirrors before it can be passed through an interferometer.

3.7.2. Synchrotron Infrared Radiation Sources

The brightness of incident light is an important parameter in the determination of which source to use for a given experiment. Brightness, also known as brilliance, is a measure of the intensity (*i.e.* flux emitted into a unit solid angle) for a unit area of the source. It is independent of the distance (but not direction) to the observer and is an intrinsic property of the source. With small samples, higher brilliance incident radiation is desired and some cases necessary in order to achieve reasonable signal-to-noise ratios.

Synchrotron light is produced by the interaction of electrons (or any charged particles, *e.g.* positrons) with a magnetic field as they travel. During the interaction of the charged particle with the magnetic field, energy is lost. Some of this energy is given off in the form of synchrotron light which covers the electromagnetic spectrum from the far infrared to higher energy X-rays. This radiation is given off tangential to the electron's path in the magnetic field and has a high brilliance factor compared to a conventional infrared Globar source. For this reason, synchrotron infrared radiation is highly desirable for applications requiring high brightness and demanding spatial resolution.[24]

It should be noted that a conventional Globar source usually has a higher photon flux than a synchrotron source. The highly focused light of a synchrotron results in a brightness

values that are 2 – 3 orders of magnitude higher than that of a conventional infrared source. This can be seen if we consider the expression for the flux of a blackbody radiator,[25]

$$B_{bb}(\omega) = \frac{\hbar\omega^3}{(2\pi)^2 c^2} \frac{d\omega}{e^{\hbar\omega/KT} - 1} \tag{3.11}$$

When written in terms of wavenumbers and assuming the emission is into 2π sr (T = 2000 K), Equation 3.11 can be simplified to,

$$B_{bb}(\tilde{\nu}) = 6 \times 10^{-15} \nu^{-3} \frac{d\tilde{\nu}}{e^{\tilde{\nu}/1400} - 1} \tag{3.12}$$

This equation can be compared to the description of synchrotron radiation source, typically governed by diffraction limitations in the mid-infrared region as,[25]

$$B_{sr}(v) \approx 10^{-8} I v^2 \ (W\ mm^{-2} sr^{-1} cm) \tag{3.13}$$

By plotting Equation 3.12 and Equation 3.13 in Figure 3.8 it becomes quite clear that there is a significant advantage in using synchrotron radiation over the traditional Globar source in terms of brightness. For this reason, synchrotron infrared radiation is utilized for *in-situ* SEC studies on ultramicroelectrodes in Chapters 6 and 7. The advancements of *in-situ* infrared SEC techniques for studying fast electrochemical processes require the use of small electrodes to minimize the cell-time constant (discussion to follow). With these smaller electrodes, highly focused, very bright infrared sources are required in order to acquire infrared spectra with sufficient signal-to-noise to measure small analyte signals. The advantages of synchrotron infrared radiation sources over conventional Globar sources make these measurements possible.

3.8. Rapid-Scan and Step-Scan Time Resolved FTIR Spectroscopy

Rapid-scanning spectrometers are limited in the temporal resolution that can be achieved by the speed at which the interferometer mirror can be translated. For instance, the temporal

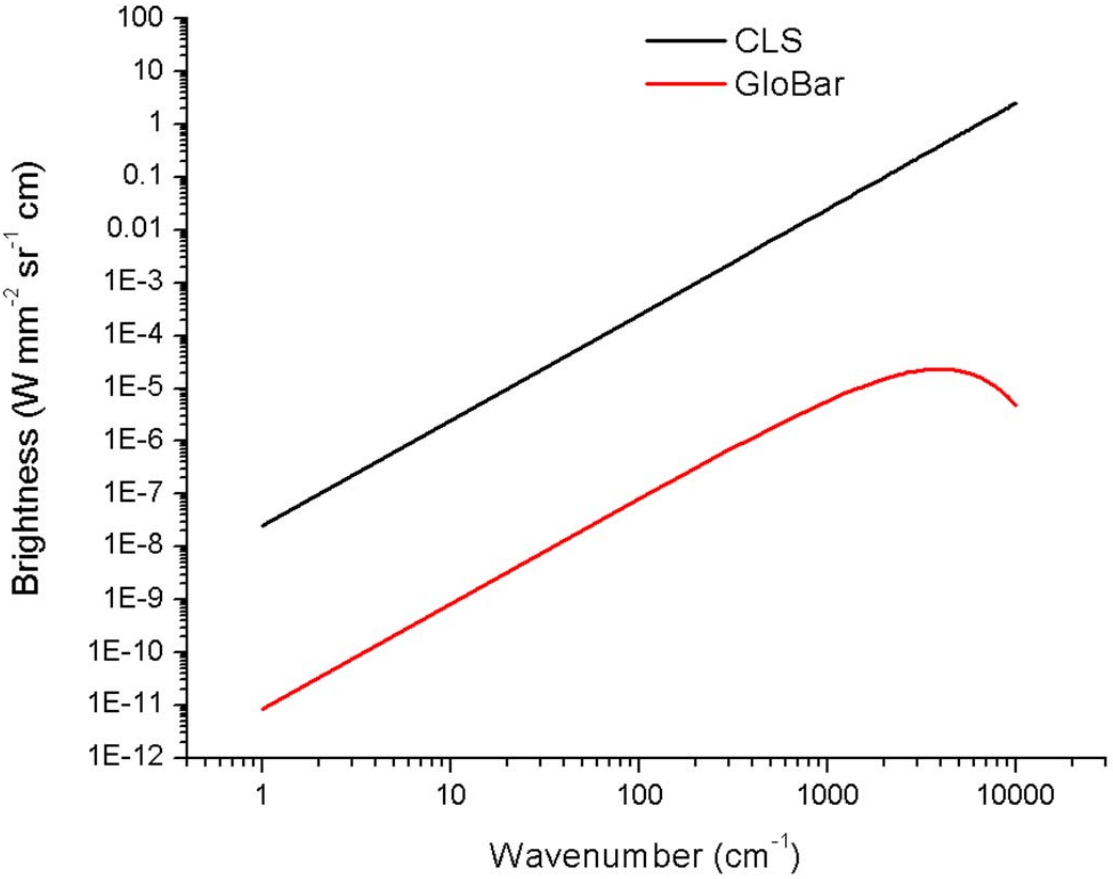

Figure 3.8. Calculated brightness for a synchrotron infrared radiation source (Canadian Lightsource, CLS) and a conventional Globar infrared source.

resolution is obtained by looking at the time difference between two successive acquired interferograms. Currently, the fastest conventional interferometers can only achieve approximately 100 spectra per second but only at low (10 cm^{-1}) spectral resolution resulting in the measurement of time dependent phenomenon on the order of approximately 10 milliseconds. Moreover, if better spectral resolution is required, the time resolution must decreases as the distance the mirror needs to translate must also increase. This implies that a fundamental limit in the temporal resolution for a Rapid-Scan FTIR spectrometer is essentially the rate of mirror drive and the distance needed to travel by the moving mirror and the sampling rate limited by the speed of the detector.

In contrast, step-scan FTIR spectrometers can obtain a much higher temporal resolution as the data collection occurs in a different manner. In a step-scan measurement, the moving mirror is translated (stepped) to a fixed position and held there so that the OPD remains temporarily constant. A reproducible experiment is then initiated and the infrared light intensity at that mirror position is recorded at specific time intervals for a given length of time. The mirror is then stepped to the next position, and the repeatable experiment is once again triggered and the infrared intensity recorded. This process of stepping and holding the mirror, then triggering the time-resolved event is repeated until the time-varying intensities are recorded for a complete set of mirror positions.

At the conclusion of the infrared experiment, a two-dimensional matrix of intensity data points are analyzed by first rotating the matrix into a series of retardation-spaced intensities (interferograms) for different times. Each of these interferograms corresponds to one of the fixed times after the trigger. The interferograms are then Fourier Transformed into a series of time-slice spectra each corresponding to one of the digitization times after the experimental

trigger. The major advantage of the technique is that so long as the process of interest is reproducible the achievable temporal resolution is limited only by the detector and digitizer electronic bandwidths and not the translational velocity of the mirror.

Although the first interferometers, such as those constructed by Michelson were step systems, it is more technically challenging to realize a step-scan interferometer than to build a rapid-scan system. The reason for this is ultimately in the precise and accurate control the interferometer needs in the movement of the mirror to make a step-scan measurement.

3.8.1. Mirror Stability in Step-Scan Time-Resolved Measurements

Another major consideration for time-resolved FTIR step-scan measurements is the positional stability of the movable mirror in the interferometer.[4,26] For example, if at a given mirror position the OPD is not truly fixed, the intensity value at that nominal mirror position will introduce significant errors in intensity. This is especially true near the ZPD where the intensity changes occur very rapidly versus the optical path difference. Such an artifact distorts the entire spectrum, as one distorted point affects the entire interferogram. To minimize these types of systematic errors, an active feedback system is often employed into the interferometer and mirror translation electronics. Typically, this feedback system is tied to the HeNe reference laser.[4]

3.8.2. Step-Scan Electronic Considerations

The electronic considerations in step-scan time-resolved measurements are an important aspect one must consider when designing these experiments. Ideally, one wants to have sufficient time-resolution to measure the process of interest while still ensuring that the available hardware can make the desired measurement. In general, the temporal resolution of the

measurement should not be increased beyond this point because as the time resolution of measurement is improved, the bandwidth of the detector must be increased. Degradation of signal-to-noise ratios results from unnecessary high measurement speeds because thermal noise is proportional to the square root of the bandwidth. For example, if a 10 kHz process is measured with a 10 MHz detection system, the electronic noise level will be 32 times larger compared to a 10 kHz measurement.[26]

It is also important to ensure that each of the three essential detection components, transducer, preamplifier and digitizer, all have the sufficient bandwidth required to make the measurement. If one component is slower than the rest, it effectively becomes the rate limiting component in temporal resolution. Consideration of the digitization used in the analog-to-digital converter to transform the analog signal from the detector to a digital signal for processing is also important to note. In particular, the amplitude of the infrared signal and the bit resolution of the device play an important role in the quality of the resulting spectrum. It is extremely important to fill the dynamic range of the ADC without overfilling it. In the situation where the analog signal overfills this range (often called clipping), the measured interferogram and subsequent spectrum will be highly distorted as a result. Converse to this, if the signal is too small, that is the digitizer is underfilled, the signal may suffer relative to the bit noise, particularly when the optical path difference is far removed from the ZPD, resulting in a noisy spectrum. The experimental conditions under which step-scan FTIR is utilized in this thesis suffered mostly from these types of noise problems.

In order to overcome this, an ADC with a large bit resolution is required which ultimately slows down the measurement. For example comparing an 8 bit ADC and a 16 bit ADC, the level of digitization noise with a dynamic range of ±10 V is 78 mV for the 8 bit digitizer and 305 μV

for the 16 bit digitizer. The key point here is that the 16 bit digitizer is 256 times more sensitive than the 8 bit digitizer. For small signals, this becomes very important as it provides a greater distinction between the various intensity levels measured at the detector. However, as previously mentioned, with improved bit resolution one typically sees a decrease in the temporal resolution and it can be as dramatic as nanosecond time resolution for a low bit digitizer to microsecond time resolution for a high bit digitizer (10^2 - 10^3 times slower).

Typically, when measuring an interferogram, measuring the rapid changes in the intensity of the infrared signal measured by the detector is important to producing high quality interferograms. This is achieved by amplifying only those rapidly changing interferogram points (electrically speaking the alternating current (AC) component), and by removing the direct current (DC) offset of the measured detector signal to maximize the dynamic range of the digitizer. This process is carried out in the pre-amplifier (trans-impedance amplifier), component of the detection system. For continuous scanning FTIR modes, this setup is ideal as the intensity on the detector is essentially modulated by the scanning rate of the interferometer which is on the order of kHz. This scheme also works in step-scan measurements if the process of interest occurs rapidly and is completed very quickly (*i.e.* there is large signal perturbation over a very short interval). In the situation where the process of interest initially occurs rapidly but does not go to completion for a long time (*i.e.* 0.5 seconds), this scheme fails as the pre-amplifier is only sensitive to large differential changes in the signal and becomes increasingly insensitive to long, slowly evolving intensity signals. This is effectively the situation experienced in the potential step measurements made in Chapter 7. It is therefore necessary to adjust the pre-amplifier to maintain the DC signal level measured by the detector through DC-coupling the amplifier. Through this method, the long, slowly changing signal intensity measured at the detector can be

digitized and used to follow the kinetic event. However, DC-coupling the detection system, means that slow changes in the environment (such as ambient temperature variations) maybe convolved with the analytical signal.[26,27]

3.9. Electrochemical Considerations

The majority of the electrochemical experimental details have been purposely excluded from the discussion in this Chapter as the primary focus of this thesis is on the development of the Fourier Transform Infrared spectroscopic measurements to study electrochemical problems. Electrochemical concepts required to understand the experimental results are described in each individual experimental Chapter.

3.10. Conclusions

This Chapter has highlighted the background information required to better understand the improvements made to various *in-situ* spectroelectrochemical techniques presented throughout this thesis. An overview of the theoretical framework of Fourier Transform Infrared spectroscopy along with descriptions on methods to minimize data collection times while still maintaining data quality were investigated. Two different methods are described to measure FTIR time-resolved spectroscopy, rapid-scan and step-scan interferometry and the implementation of synchrotron infrared radiation as a highly brilliant infrared source. In addition, a detailed description of Attenuated Total-Internal Reflection Surface Enhanced Infrared Reflection Absorbance Spectroscopy (ATR-SEIRAS) for use in *in-situ* spectroelectrochemistry was discussed. ATR-SEIRAS is an internal reflectance technique allowing for the electrochemical study of the structure of the double-layer, adsorption/desorption

of molecules or ions, characterization of self-assembled monolayers, and monitoring of electrochemical reactions owing to the high surface sensitivity this technique provides.

The remaining Chapters of this thesis go into experimental results utilizing the information presented in this Chapter starting with the adsorption properties of DMAP on gold electrodes and use *in-situ* ATR-SEIRAS SEC techniques to provide new insight into this chemical system.

3.11. References

1. Osawa, M. In-situ Surface-enhanced Infrared Spectroscopy of Electrode/Solution Interface. In *Handbook of Vibrational Spectroscopy*; Chalmers, J.M., Griffiths, P. R., Ed.; Wiley: Chichester, 2002; p. 785.

2. Osawa, M.; Kuramitsu, M.; Hatta, A.; Suëtaka, W.; Seki, H. Electromagnetic Effect in Enhanced Infrared Absorption of Adsorbed Molecules on Thin Metal Films. *Surface Science* **1986**, *175*, L787–L793.

3. Ingle, J.D.; Crouch, S. R. Infrared Spectrometry. In *Spectrochemical Analysis*; Prentice Hall: Upper Saddle River, NJ, 1988; pp. 404–437.

4. Griffiths, P.R.; de Haseth, J. A. Introduction to Vibrational Spectroscopy. In *Fourier Transform Infrared Spectroscopy*; John Wiley and Sons, Inc.: Hoboken, NJ, 2007; pp. 1–18.

5. Atkins, P.; de Paula, J. Spectroscopy 1: Rotational and Vibrational Spectra. In *Physical Chemistry*; W.H. Freeman and Compan: New York, 2002; pp. 481–537.

6. Harris, D.C.; Bertolucci, M. D. Vibrational Spectroscopy. In *Symmetry and Spectroscopy*; Oxford University Press: Mineola, NY, 1978; pp. 93–224.

7. Michelson, A. A. XXXVIII. On the Application of Interference-methods to Spectroscopic measurements.—I. *Philosophical Magazine Series 5* **1891**, *31*, 338–346.

8. Gronholz, J.; Herres, W. Understanding FT-IR Data Processing. *Instrum. Comput* **1985**, *3*, 10–19.

9. Mertz, L. *Transfomations in Optics*; John Wiley and Sons, Inc.: New York, 1965.

10. Biggs, P.; Hancock, G.; Heard, D.; Wayne, R. P. A Step-scan Interferometer Used for Time-resolved FTIR Emission Spectroscopy. *Meas. Sci. and Techn.* **1990**, *1*, 630–636.

11. Hancock, G.; Heard, D. E. Time-resolved Pulsed FTIR Emission Studies of Atom-radical Reactions: Product Chemiluminescence from the O(3P) + CF2(X1A1) Reaction. *Chem. Phys. Lett.* **1989**, *158*, 167–171.

12. Palmer, R.A.; Manning, C.J.; Rzepiela, J.A.; Widder, J.M.; Chou, J. L. Time-resolved Spectroscopy Using Step-scan Fourier Transform Interferometry. *Appl. Spectr.* **1989**, *43*, 193–195.

13. Uhmann, W.; Becker, A.; Taran, C.; Siebert, F. Time-resolved FT-Ir Absorption Spectroscopy Using a Step-scan Interferometer. *Appl. Spectr.* **1991**, *45*, 390–397.

14. Chang, R.K.; Furtak, T. E. *Surface Enhanced Raman Scattering*; Plenum Press: New York, 1982.

15. Miyake, H.; Ye, S.; Osawa, M. Electroless Deposition of Gold Thin Films on Silicon for Surface-enhanced Infrared Spectroelectrochemistry. *Electrochemistry Communications* **2002**, *4*, 973–977.

16. Kittle, C. *Introduction to Solid State Physics*; 7th ed.; Wiley: New York, 1996.

17. Osawa, M.; Ikeda, M. Surface-enhanced Infrared Absorption of P-nitrobenzoic Acid Deposited on Silver Island Films: Contributions of Electromagnetic and Chemical Mechanisms. *The Journal of Physical Chemistry* **1991**, *95*, 9914–9919.

18. Hoffmann, F. Infrared Reflection-absorption Spectroscopy of Adsorbed Molecules. *Surface Science Reports* **1983**, *3*, 107.

19. Chazalviel, J.-N.; Ozanam, F. IR Spectroscopy of the Semiconductor/Solution Interface. In *Diffraction and Spectroscopic Methods in Electrochemistry*; Alkire, R.; Kolb, D.; Lipkowski, J.; Ross, P., Ed.; Wiley-VCH Verlag GmbH & Co. KGaA: Weinheim, Germany, 2006; pp. 199–230.

20. Mirabella Jr, F. M. Principles, Theory, and Practice of Internal Reflection Spectroscopy. In *Internal Reflection Spectroscopy*; Marcel Dekker: New York, 1993; pp. 17–52.

21. Osawa, M. Surface Enhanced Infrared Absorption Spectroscopy. In *Handbook of Vibrational Spectroscopy*; Chalmers, J.M.; Griffiths, P. R., Ed.; Wiley: Chichester, 2002; p. 785.

22. Nishikawa, Y.; Nagasawa, T.; Fujiwara, K.; Osawa, M. Silver Island Films for Surface-enhanced Infrared Absorption Spectroscopy: Effect of Island Morphology on the Absorption Enhancement. *Vibrational Spectroscopy* **1993**, *6*, 43–53.

23. Delgado, J. M.; Orts, J. M.; Pérez, J. M.; Rodes, A. Sputtered Thin-film Gold Electrodes for in Situ ATR-SEIRAS and SERS Studies. *Journal of Electroanalytical Chemistry* **2008**, *617*, 130–140.

24. Jackson, J. *Classical Electrodynamics Third Edition*; Wiley, 1998.

25. Williams, G. P. Synchrotron and Free Electron Laser Sources of Infrared Radiation. In *Handbook of Vibrational Spectroscopy*; Chalmers, J.M.; Griffiths, P. R., Ed.; John Wiley & Sons, Ltd: West Sussex, UK, 2002; pp. 341–348.

26. Braiman, M.S.; Xiao, Y. Step-Scan Time-Resolved FT-IR Spectroscopy of Biopolymers. In *Vibrational Spectroscopy of Biological and Polymeric Materials*; CRC Press, 2006; pp. 353–415.

27. Taniguchi, I.; Yoshimoto, S.; Yoshida, M.; Kobayashi, S.; Miyawaki, T.; Aono, Y.; Sunatsuki, Y.; Taira, H. Simple Methods for Preparation of a Well-defined 4-pyridinethiol Modified Surface on Au(111) Electrodes for Cytochrome c Electrochemistry. *Electrochimica Acta* **2000**, *45*, 2843–2853.

CHAPTER 4

SURFACE ENHANCED INFRARED ABSORPTION SPECTROSCOPIC STUDIES OF DIMETHYLAMINOPYRIDINE (DMAP) ADSORPTION ON GOLD SURFACES

4.1. Introduction

The molecular adsorption of dimethylaminopyridine (DMAP) on gold surfaces has been a subject of electrochemical studies in recent years.[1–3] In this Chapter, a description of the initial development and utilization of an *in-situ* spectroelectrochemical system is described. The results are used to provide further evidence and validation of electrochemically derived models of DMAP adsorption on gold.

Corroborating evidence from extra-thermodynamic techniques such as scanning probe microscopy or spectroscopic methods can often offer new insight concerning molecular adsorption. For example, *in-situ* vibrational spectroscopy has emerged as a tremendously powerful analytical tool for characterizing thin molecular films at electrode surfaces.[4] Surface enhanced Raman scattering (SERS) is one such technique that can provide great sensitivity to adsorbed molecules. However, SERS is usually restricted to roughened surfaces of coinage metals precluding extraction of information concerning molecular orientation. In contrast, external reflection absorption infrared spectroscopy (RAIRS)[5] and sum-frequency generation[6] experiments can be performed on single-crystal smooth electrodes but offer lower sensitivity relative to SERS. In the past decade another technique has emerged, surface enhanced infrared absorption spectroscopy (SEIRAS). Pioneered by Osawa and co-workers,[7] SEIRAS has been shown to have surface sensitivity over 10 times greater than that of infrared-reflectance absorption spectroscopy techniques. Both SEIRAS and SERS require some degree of surface

anisotropy to achieve large electric field enhancements. Metal electrodes can be prepared through repetitive oxidative-reduction potential cycling but result in very rough and ill-defined surfaces.[8] Alternatively much better defined metal films, consisting of ~100 nm elliptical sized islands, can be prepared by vapour sputtering or electrolessly depositing the films onto appropriate substrates. These surfaces have been shown to provide excellent enhancement for both SEIRAS and SERS measurements.[9,10] Therefore, even though the gold surfaces used in SEIRAS experiments are not as polished as single-crystal substrates, such as those commonly employed in RAIRS measurements, qualitative and quantitative information on molecular orientation can still be extracted.

The attention by researchers to the adsorption of DMAP stems largely from the reports of water-dispersible, DMAP stabilized Au nanoparticles (DMAP-AuNP) first described by Gittins and Caruso.[11] Unlike thiol stabilized AuNP analogues, the absence of a chemical bond between molecule and metal allows for facile ligand exchange on DMAP-AuNP surfaces.[12,13] In addition to this characteristic, DMAP-AuNP have been shown to be positively charged,[3,11,12,14,15] and can be further exploited by providing strong electrostatic interactions with oppositely charged molecules or substrates. Utilization of these unique properties have allowed for numerous examples in the literature ranging from polyelectrolyte adsorption (layer-by-layer assembly),[16–20] electrochemical sensing,[21,22] and DNA templating.[23] The demonstration that the basicity of the pyridine derivative is an important property in the phase-transfer and stabilization of metal nanoparticles was described by Lennox and Gandubert.[3] These authors reasoned that DMAP ($pK_b = 4.3$) and not pyridine ($pK_b = 8.7$) stabilized MNPs can be prepared because of the increased basicity of DMAP due to the presence of its para-substituent. This suggests possible differences between the adsorption behaviour of pyridine and DMAP on metal surfaces.

On gold electrodes, it is well known that pyridine undergoes a potential-dependent phase transition. This phenomenon has been explained by the interaction between π electrons and negatively charged metal surfaces, causing pyridine to adsorb in a flat-laying, low density monolayer. If the surface is charged positively, the molecules tend to orient to form a more compact, vertical layer involving a strong physisorption bond between the nitrogen atom and the gold.[24] Previous chronocoulometric studies at low pH (*ca.* 4-5), provided electrochemical evidence showing that DMAP follows a similar horizontal-to-vertical transition at potentials close to the potential of zero charge (E_{pzc}).[1] This transition also encompasses a near doubling of the corresponding surface coverage. This purely electrochemical study indicated that the horizontally adsorbed species was most likely the protonated dimethylaminopyridinium ($DMAPH^+$) species rather than the neutral form of the molecule. Also, during the transition from the horizontal to the vertical phase, deprotonation of $DMAPH^+$ was required and was speculated to occur even when the bulk solution pH is nearly 5 orders of magnitude below the pK_a of $DMAPH^+$. Another important difference between DMAP and pyridine adsorption on gold is the tendency of DMAP to adsorb in a vertically oriented higher density monolayer at pH values near the pK_a. A final contrast worth noting between DMAP and pyridine physisorption on gold[25,26] occurs at pH values ≥ 9.7. At this pH, both horizontal and vertical phases are observed for the pyridine system whereas in the DMAP system no electrochemical evidence of the horizontal adsorption state on polycrystalline gold was found.

The adsorption model summarized above for DMAP, and its conjugated acid, is the result of purely electrochemical studies and is based on the electrostatic models and the thermodynamics of adsorption on ideally polarized electrodes. In this Chapter, the results of *in-situ* spectroelectrochemistry on the adsorption behaviour of DMAP and its conjugate acid are

discussed. In a particularly relevant study to this work, Cai *et al.* employed *in-situ* spectroelectrochemical experimental techniques to study the adsorption of pyridine on an Au(111) textured electrodes.[27] From their results, they confirm that there is a horizontal to vertical transition that had not been forthcoming from previous infrared[28] and SERS[29] related studies. Herein, SEIRAS studies of DMAP adsorbed on gold films are measured under variable pH and electrochemical conditions. Briefly, the infrared results in basic solution are complementary to previous electrochemical studies on the adsorption of DMAP whereas measurements at low pH provide new details on the adsorption behaviour of the conjugate acid.

4.2. Experimental

4.2.1. Reagents, Solutions, and Electrode Materials

4-(Dimethylamino)pyridine (DMAP) (99%), sodium fluoride (99.998%), potassium perchlorate monohydrate (+99%), potassium hydroxide (Semiconductor grade, +98%), perchloric acid (70%, double distilled), ammonium fluoride (+98%), ammonium chloride (+98%), sodium sulfite (+98%), sodium thiosulfate (99%), and hydrogen tetrachloroaurate III (99.9%) were purchased from Aldrich and were used as received. All aqueous solutions were prepared from Milli-Q (> 18.2 MΩ cm^{-1}) water or deuterium oxide (D, 99.9%) (Cambridge Isotope Laboratories, Inc., Andover, MA), as indicated in the text. Ethanol (95%), used for cleaning the silicon hemisphere, was purchased from Commercial Alcohols Inc. (Brampton, ON, Canada).

4-Dimethylamino-pyridinium perchlorate, (DMAP)$HClO_4$,was prepared as per Barlow *et al.*[1] *Caution:* Although the reactivity of (DMAP)$HClO_4$ is not reported, organic perchlorate salts similar in nature have the potential to be explosive and should be handled with great care.

4.2.2 Electroless Deposition of Gold onto Silicon Hemispherical Prism

For deposition of gold onto the silicon hemispherical prism, the original procedure reported by Osawa *et al.*[30] was followed with the modification described by Delgado *et al.*[9] Briefly, the reflecting plane of a 25 mm diameter, non-doped, silicon hemispherical prism (Harrick Scientific Products, Pleasantville NY, US) was successively polished with finer grade diamond suspensions (Leco Corporation, St. Joseph, MI, US) down to 0.5 μm. The prism was then degreased by sonication in ethanol and finally rinsed in Milli-Q water before metal deposition. To remove the oxide layer and to terminate the silicon surface with hydrogen, the reflecting surface was left in contact with 40% (w/w) solution of NH_4F. After 4 minutes, the ammonium fluoride solution was removed from the crystal, and the crystal was placed in a hot 55 °C water bath. Immediately, the plating solution containing the Au (5 mg $HAuCl_4$, 0.3 M Na_2SO_4, 0.1 M $Na_2S_2O_3$, 0.1 M NH_4Cl and 2% HF (2:1 in volume)) was added to just cover the crystal surface (~1 mL). After about 10 seconds an Au film appeared and at this point most of the plating solution was removed from the crystal and replaced with another aliquot of the plating solution. This process was repeated until all the Au plating solution had been used, or the crystal had obtained a metallic gold colour.

Once completed, the gold deposition was quenched by carefully rinsing the prism and thin film with copious amounts of Milli-Q water. The gold film was then electrochemically cycled into the gold oxidation region in 0.5 M H_2SO_4 electrolyte until stable voltammograms were obtained. Finally, the modified gold substrate was rinsed with Milli-Q water.

4.2.3. In-situ spectroelectrochemical SEIRAS Cell

The *in-situ* spectroelectrochemical (SEC) cell was machined from PTFE using a custom design to accommodate the necessary experimental and instrument requirements (Figure 4.1). Specifically, the cell needed to provide a water-tight seal (with a slight argon gas over pressure) to the basal plane of the 25 mm diameter Si attenuated total-internal reflection (ATR) hemisphere. This was accomplished through an O-ring sandwiched between the Si hemisphere and a circular groove machined out of the underside of the cell face adjoining the hemisphere. PTFE was chosen as the cell material to allow for adequate cleaning and to withstand caustic and acidic solutions. This posed a challenge in that the softness of this material allowed it to be easily deformed and as such required additional elements of the overall cell design to include aluminum flanges.

Another important design consideration was the electrical connection to the thin-metal film working electrode. In this scheme, it was decided that a loop of wire would be pressed against the thin-film electrode from above, through an access port in the cell lid. This arrangement proved to work sufficiently for these experiments, but was considered to be the weakest point in the strategy of this *in-situ* SEC cell. In fact, this was the main driving force to change the design of the cell after these experiments were completed and these modifications will be discussed in the Chapter 5 in detail.

With the additional access ports in the cell lid, the counter electrode and various inlet and outlet gas connections allowed for *in-situ* SEC experiments to be performed in an argon environment while utilizing a three-electrode configuration through a proper reference electrode connected *via* a salt-bridge in the side of the SEC cell.

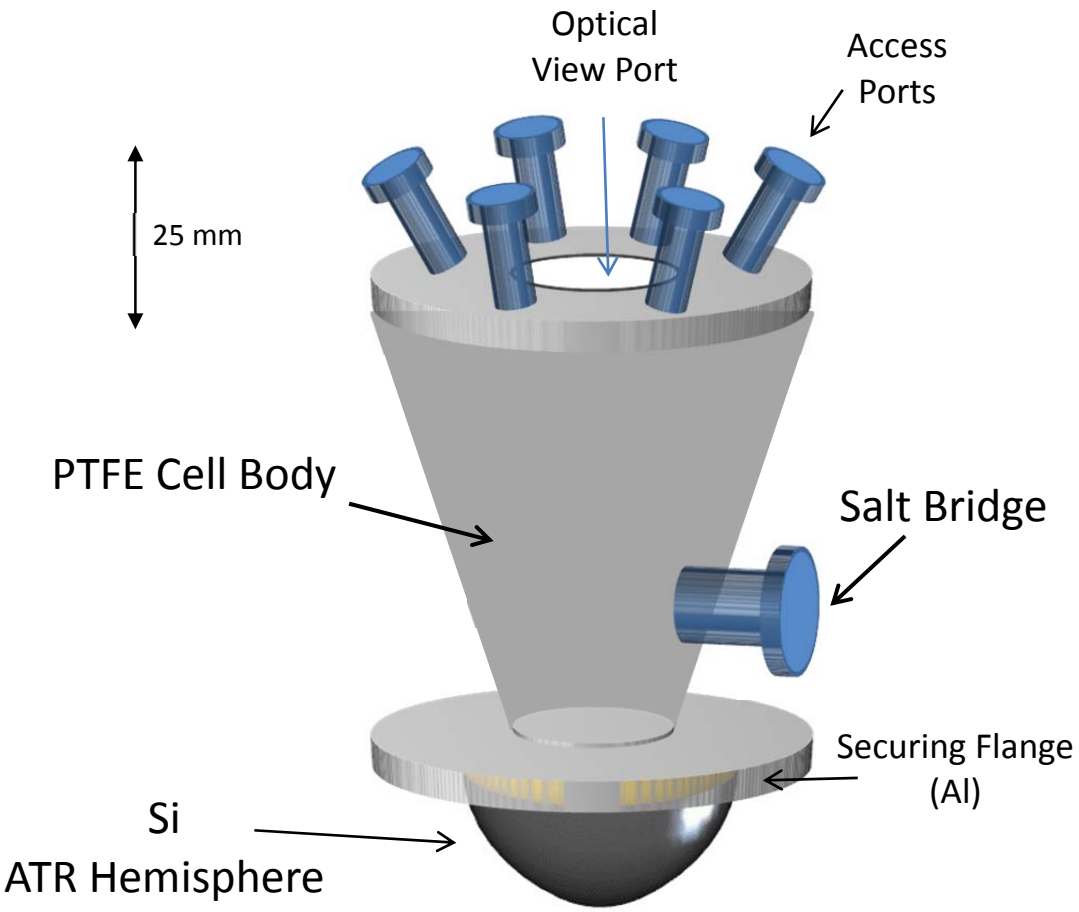

Figure 4.1. a) Drawing of designed *in-situ* spectroelectrochemical cell used throughout the experiments in this Chapter.

4.2.4. Infrared Optical Layout

A major obstacle to overcome in the experimental apparatus was providing the necessary optics to direct the source infrared radiation into and out of the ATR element at relatively large angles (> 60^{o}). Given the high angle of incidence required to achieve maximum SEIRAS enhancements[4] and the space within the sample compartment of the Nicolet 6700 Fourier Transform Spectrometer, an additional accessory (VeeMax II, Variable Angle Specular Reflectance Accessory, Pike Technologies, Inc.; Madison WI, USA) was used and modified to provide a platform to support the *in-situ* SEC cell in a Kretschmann configuration. This multi-bounce reflective optical accessory allows for the adjustment of the angle of incidence and reflection of the infrared radiation between 30^{o} – 70^{o} with the *in-situ* SEC cell in place. In addition, the optical path of the infrared radiation also needed to be enclosed to create a carbon dioxide (CO_2) and water vapour free environment to prevent large interferences in the spectroscopic signals measured. This meant that the entire reflection accessory and *in-situ* SEC cell needed to be compact enough to fit in the predefined sample compartment space of the spectrometer.

4.2.5. ATR-SEIRAS Measurements

All the ATR-SEIRAS measurements were performed using an experimental setup adapted from previous reports[31,32] and described above. Electrochemical potential control was maintained using a PAR 173 potentiostat and a custom virtual instrument (VI) written in the LabVIEW (National Instruments) programming environment. The electrolyte was deaerated by purging with argon gas for 30 minutes, with a continual blanket of argon gas maintained over the electrolyte throughout the experiment. The pH of the electrolyte was adjusted by using either

potassium hydroxide or perchloric acid. All SEIRAS spectra were measured using p-polarized incident radiation at 70° with a resolution of 4 cm^{-1} on a Nicolet 6700 Fourier Transform Infrared (FTIR) Spectrometer equipped with a mercury cadmium telluride (MCT) liquid nitrogen cooled detector. The spectrometer was controlled autonomously through custom written macros written for the spectrometer control software (OMNIC) and communicated to a LabVIEW VI to control the potential of the working electrode in the cell. All transmission infrared spectra were measured similarly to the SEIRAS spectra except at a higher spectral resolution of 2 cm^{-1}. The sample chamber of the spectrometer was purged throughout the experiment using CO_2 and H_2O free air supplied by a Parker Balston FT-IR purge gas generator 75-62 (Parker Hannifin Corporation, Haverhill, MA).

4.2.6. Differential Capacity Measurements

Differential capacity (DC) measurements were performed in an all-glass cell using the working electrode positioned on the electrolyte surface in a hanging meniscus configuration or with the electrode immersed in the electrolyte. The working electrodes used were; a gold coated silicon wafer prepared identically to the ATR element, a polished polycrystalline gold, and finally an Au (111) single crystal. In all cases a coiled gold wire served as the counter electrode, and a KCl saturated Ag/AgCl electrode was used as the reference electrode. The pH of the electrolyte (50 mM $KClO_4$) was adjusted to pH 9.7 using KOH and electrolyte solutions were deaerated by purging with argon for a minimum of 30 minutes prior to an experiment. During the experiments, an argon blanket was maintained over the solution to prevent air from interfering with the electrochemical measurements. The DC was calculated by measuring the in-phase and out-of-phase currents arising from the superposition of a 5 mV s^{-1} direct-current

potential sweep and an alternating-current perturbation (5 mV rms at 25 Hz) assuming a resistor-capacitor equivalent series circuit. Measurements were carried out at room temperature, 20 °C, using a SRS730 Lock-in Amplifier (Standford Research Systems, Sunnyvale, CA) and a HEKA Potentiostat PG590 (HEKA, Mahone Bay, NS, Canada). A more rigorous explanation of differential capacity measurements is provided elsewhere.[33]

4.3. Results and Discussion

4.3.1. Electrochemistry

In this section, a description of the SEIRAS data for DMAP adsorption on gold films electrolessly deposited on a Si ATR element will be discussed. In order to compare previous electrochemical data concerning DMAP adsorption and the results of this study, it was first necessary to determine the crystallography of the chemically deposited gold films. Previous reports in the literature have claimed that Au films thermally evaporated on Si provide (111) textured surfaces,[9,27,31] and it would be beneficial to know the orientation that results from electrolessly depositing Au on the Si ATR substrates. This was accomplished by electrochemical methods, in particular differential capacity measurements, of various gold substrates in pH 9.7 electrolyte solutions containing a formal DMAP concentration of 0.1 mM. From Figure 4.2 one can see the positive going differential capacity curves for a polished polycrystalline gold electrode (solid line), an Au(111) single crystal (dotted line), and finally a Si wafer coated by a thin Au layer by chemical deposition as described in the experimental section of this Chapter (dashed line). The Au(111) single crystal electrode shows several differences in the adsorption behaviour of DMAP compared to the smooth polycrystalline electrode. One can

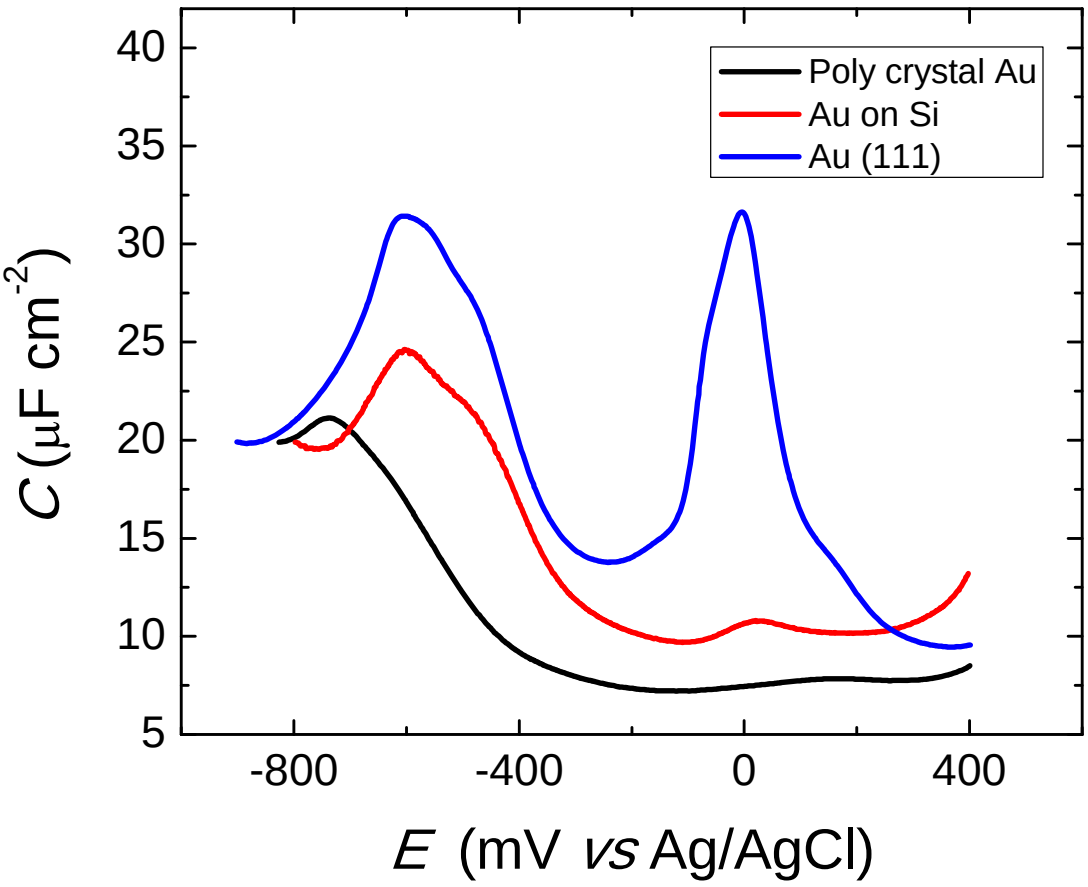

Figure 4.2. Differential Capacity (DC) measurements for various gold substrates with 0.1 mM formal DMAP concentration in 50 mM $KClO_4$ (pH 9.7, adjusted using KOH): a polished polycrystalline gold electrode (black), a single crystal Au(111) electrode (blue), and a gold coated (electrolessly as described in the Experimental section) Si wafer (red).

see that there is a pseudocapacitive peak which is interpreted as the onset of molecular adsorption and occurs at E ~ -600 mV for DMAP. The polycrystalline gold electrode also has this peak, however, it is superimposed on a much broader pseudocapacitive feature which is centered at E = -600 mV. The DC curve for this electrode shows a potential-independent capacitance after the initial adsorption and agrees with previous studies that model the adsorption of DMAP as a single state for polycrystalline gold at high electrolyte pH.[1] In contrast, the corresponding curve for the Au(111) electrode shows a distinct phase transition peak at E = 0 mV. The presence of this peak is somewhat remarkable implying that even at high pH, multiple states of adsorption for DMAP can occur on Au(111) but not on Au polycrystalline surfaces.

The adsorption behaviour of pyridine has been extensively studied using a variety of gold single crystal electrodes and has shown a dependence on which low-index surface is exposed to the electrolyte solution.[24] The differential capacity results presented in Figure 4.2 imply that the adsorption behaviour of DMAP also depends on the surface crystallography of the gold substrate. With these distinct adsorption behaviours of DMAP on polycrystalline and Au(111) electrodes, one should be able to explain some of the DMAP adsorption characteristics on the chemically deposited Au coated Si substrates. The adsorption pseudocapacitive peak of DMAP on gold coated silicon occurs at E = -600 mV which registers nearly identically to the position described as the adsorption peak for DMAP on Au(111). This result implies that the surface is slightly preferentially (111) oriented. On the other hand, the phase transition peak at E = 0 mV, which is very pronounced for the single crystal, is only weakly apparent on the deposited Au film. The low intensity of this peak on Au coated silicon in contrast to Au(111) can be rationalized by the fact that discontinuous Au(111) domains on the Au coated silicon result from

the chemical deposition and make the phase transition less distinct compared to a perfect Au(111) crystal.

4.3.2. Infrared Absorption Spectroscopy of DMAP

An important aspect to any *in-situ* spectroelectrochemical measurements is an understanding of the spectral response of the electrochemical species of interest. This information can usually be inferred by theoretical means and with this information a meaningful analysis of the acquired spectral data can be described. Figure 4.3 shows the infrared absorption spectra of DMAP and (DMAP)$HClO_4$ measured using a simple KBr pellet (commonly used transmission method) and also in aqueous solutions in conjunction with an uncoated Si ATR element (internal reflection method). A summary of the assignments (both in solid state and in solution) of the various measured infrared bands for DMAP and $DMAPH^+$ are presented in Table 4.1. Based on experimental and theoretical work performed by Kozhevina *et al.,*[34,35] the point group of DMAP is C_s as there is a slight divergence from a planar molecule due to the methyl groups. The important modes of vibration can be generally assigned to vibrations in the dimethylamino group and in-plane distortions of the pyridine ring. The normal modes of vibration for DMAP can be divided into both *A'* and *A''* symmetry classes displaying overall transition dipole moments oriented collinear with the mirror plane (*A'*) and orthogonal to the mirror plane (*A"*), respectively. Computational work done by Kozhevina and Rybachenko show that upon protonation a positive charge delocalizes in the heterocycle which leads to a positive shift in the vibrational frequencies involving the stretching vibrations of the C-C and C-N bonds found within the pyridinium ring.[34,35] It is not surprising that this is also

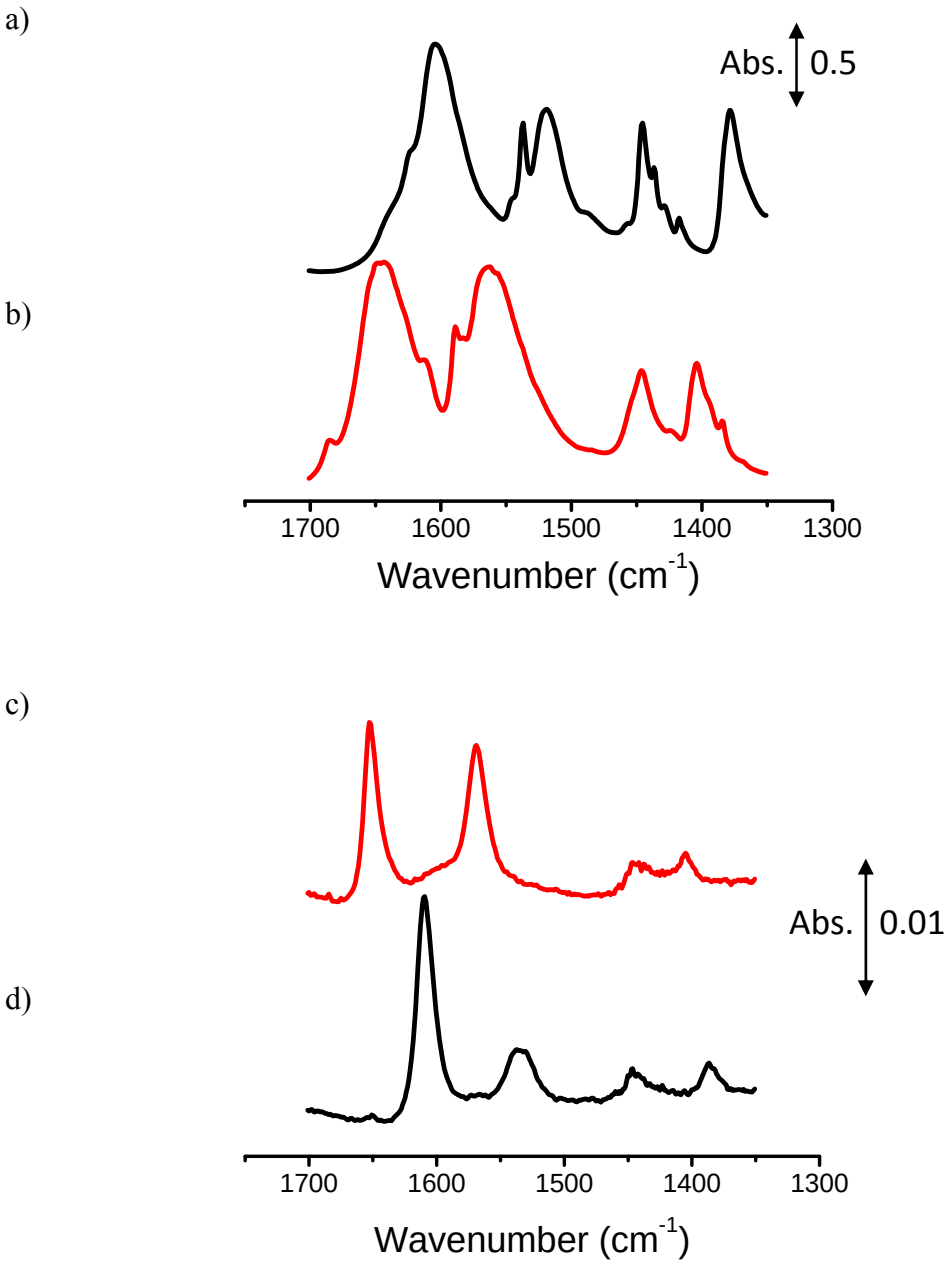

Figure 4.3. Top panel: Absorbance infrared spectra of a) DMAP and b) $DMAPH^+$ measured in KBr pellets. Bottom panel: Absorbance spectrum of concentrated aqueous $DMAP(H^+)$ solutions in ATR mode at c) pH 11 and d) pH 3.5. In all cases the FTIR spectra were measured with 2 cm^{-1} resolution.

Table 4.1. Assignments of Infrared Vibrational Bands for DMAP and $DMAPH^+$ Measured in a KBr Pellet and in Aqueous Solution

DMAP (dimethylaminopyridine) Infrared Vibrations

mode description	**symmetry**	**DMAP (KBr Pellet)**	**DMAP (solution, pH 11)**
ring distortion + C-N stretch	*A'*	1605 cm^{-1} (vs)	1609 cm^{-1} (vs)
ring distortion	*A"*	1540 cm^{-1} (shp)	n/a
ring distortion	*A'*	1520 cm^{-1} (b)	1534 cm^{-1} (m,b)
methyl-group bending	*A'*	1447 cm^{-1} (s)	1447 cm^{-1} (w)
C-N single bond stretch	*A'*	1385 cm^{-1} (s)	1385 cm^{-1} (w)

$DMAPH^+$ (dimethylaminopyridinium) Infrared Vibrations

mode description	**symmetry**	**$DMAPH^+ \bullet ClO_4$ (KBr Pellet)**	**DMAP (solution, pH 3.5)**
ring distortion + C-N stretch	*A'*	1647 cm^{-1} (vs)	1652 cm^{-1} (vs)
ring distortion	*A"*	1590 cm^{-1} (sh)	n/a
ring distortion	*A'*	1564 cm^{-1} (b)	1569 cm^{-1} (2)
methyl-group bending	*A'*	1446 cm^{-1} (m)	1445 cm^{-1} (w)
C-N single bond stretch	*A'*	1404 cm^{-1} (m)	1405 cm^{-1} (w)

*vs, very strong; s, strong; m, medium; b, broad; shp, sharp; sh, shoulder; n/a, band not observed.

known to occur in DMAP.[36,37] Given that the *in-situ* SEIRAS SEC measurements will be measured in aqueous electrolytes, understanding any differences seen between solution and solid-state measurements is valuable to the overall understanding of the spectral response of DMAP.

The measurements in solution, taken at pH 11, (Figure 4.3) reveal four principal peaks corresponding to the *A'* bands seen in the solid state. However, there is a noticeable difference between the two measurements with the apparent loss of the weaker *A"* mode in the corresponding solution phase spectrum and that the position and relative intensities of the bands are slightly different. The slight shifts in the measured position of the bands in the two sets of spectra are attributed to solvation effects and the fact that the frequency of ATR absorption bands are dependent of the refractive index of the sample as well as the penetration depth, d_p.[38] The relative intensities also differ and can be explained by not having corrected ATR spectral data for the differences in path length and depth of penetration, d_p, of the evanescent wave.

Another prominent feature seen in Figure 4.3 is the shift in spectral band position between the low and high pH forms of DMAP. At low pH, 3.5, almost all the bands shift to higher frequencies expect for the peak at 1447 cm^{-1}. The attributed reason is that this band is associated with the bending modes of the methyl group and is not influenced by protonation of the endocyclic nitrogen. The effect of pH was further explored by analyzing the dependence of the peak positions and intensity as performed *via* a titration of the solution phase DMAP. In Figure 4.4 the magnitude of the integrated intensities of the bands appearing at 1652 and 1609 cm^{-1} are plotted as a function of pH. These bands demonstrate a change in intensity but there was no shift in their positions. The sigmoidal shape of the curves in Figure 4.4 clearly exhibit

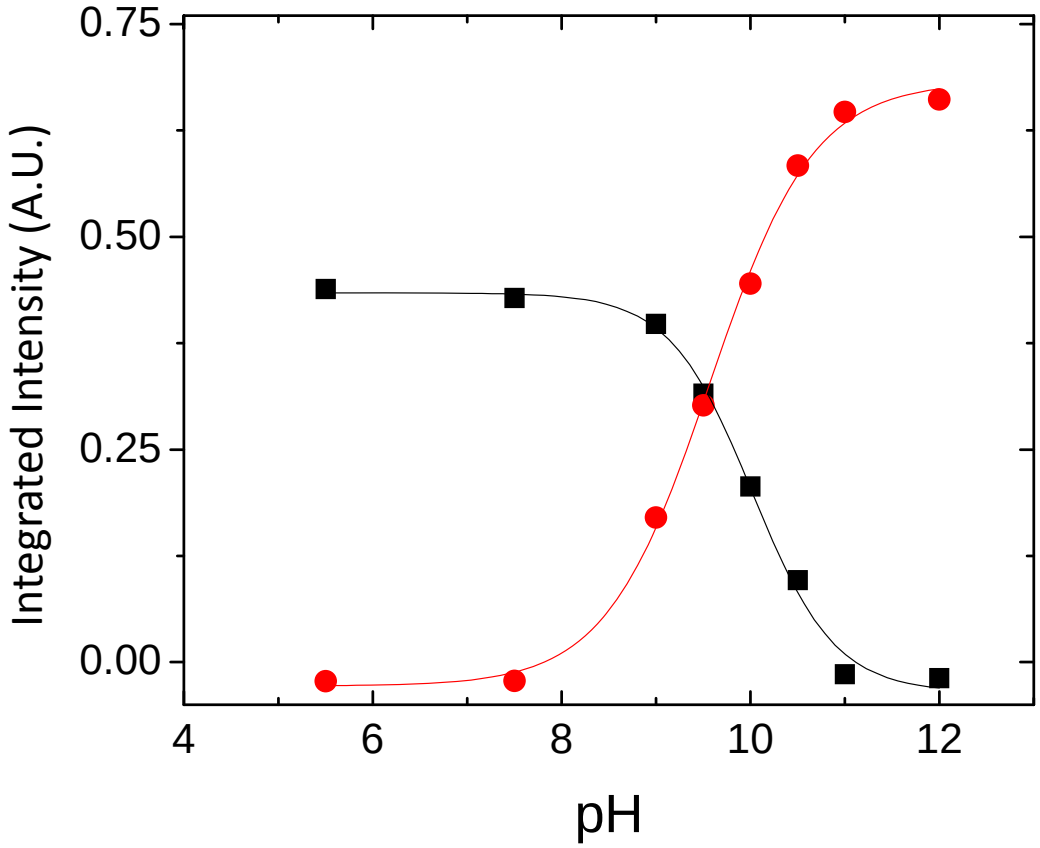

Figure 4.4. Scaled integrated intensities of the 1652 and 1609 cm^{-1} infrared vibration bands in the ATR infrared spectra of aqueous DMAP solutions as a function of pH.

the expected shape for a simple acid/base titration curve and provide a pK_a value of 10. This is in good agreement with the reported value of 9.7 for $DMAPH^+$.[20,39]

4.3.3. *In-situ* Spectroelectrochemistry SEIRAS

The *in-situ* ATR-SEIRAS SEC experiments on the adsorption behaviour of DMAP were performed at two pH values, 10 and 4.5, to analyze both acid and base forms of the molecule. In these experiments, the acquisition of 128 single beam infrared scans at a reference potential was followed by immediately stepping to a variable potential of interest. Before the collection of 128 scans at the new potential, a two minute wait time was used to allow the system to reach adsorption equilibrium. After stepping back and forth between the reference potential and several variable potentials (-800 mV < E < 500 mV) the resulting data set consisted of a family of reference and variable potential spectra. In order to increase the signal-to-noise in these experiments, four data sets were collected to provide a total of 512 single beam measurements. This limited the time at the reference potential for each measurement to extend the life of the thin metal layer deposited on the Si hemisphere. Once collected, an average was calculated based on the entire set of data before subtractively normalizing the averaged spectra as follows,

$$\frac{\Delta S}{S} = \frac{(\bar{S}_{VAR} - \bar{S}_{REF})}{\bar{S}_{REF}} \tag{4.1}$$

where $\bar{S}_{VAR}$ and $\bar{S}_{REF}$ are the average of 512 individual single beam signals at the variable and reference potentials respectively. The net result of these calculations is that a negative-going peak in the processed data set indicates an increase in that particular vibrational mode. This can be the result of either a greater density of vibrations (*i.e.* more molecules) or an increased alignment of that particular mode's transition dipole moment with respect to the surface normal

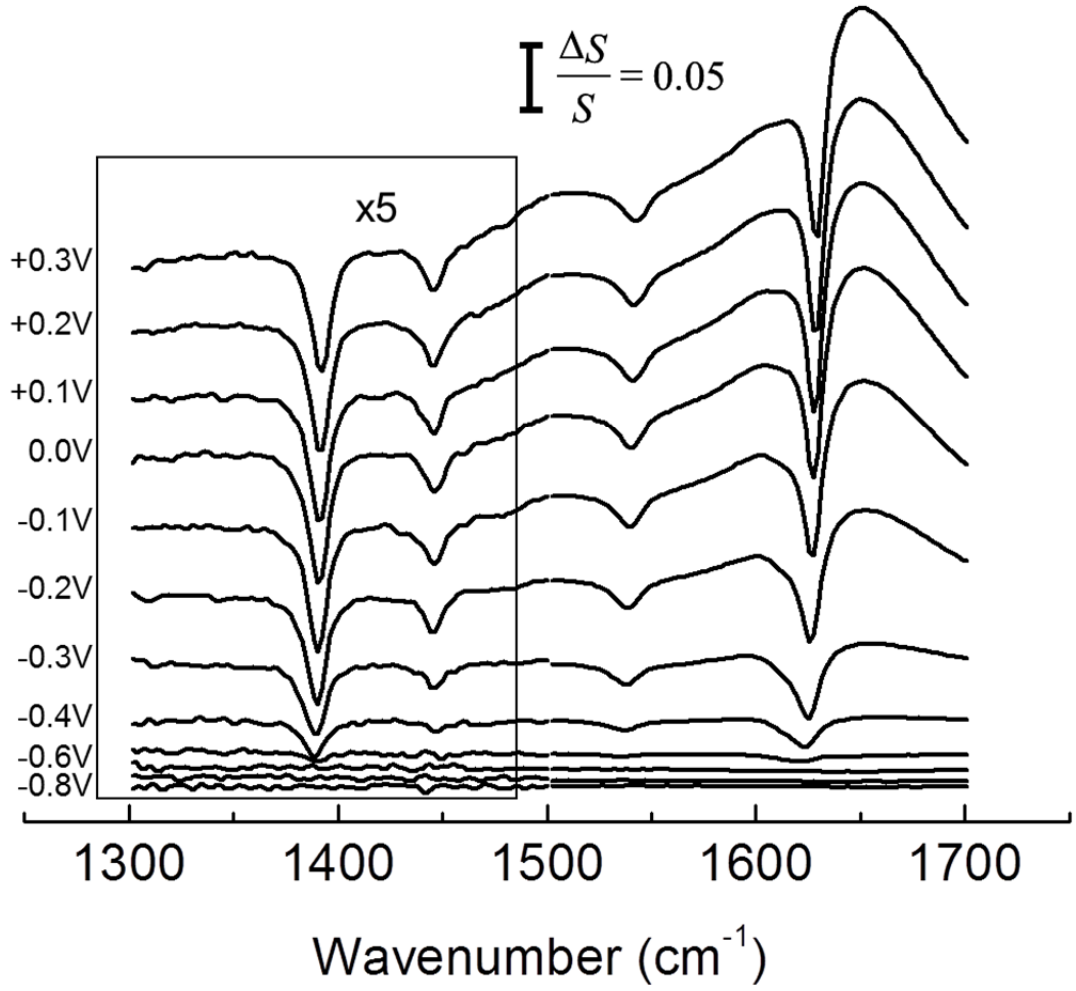

Figure 4.5. Subtractively normalized SEIRAS data for 0.1 mM formal DMAP concentration in 50 mM NaF (pH 10, adjusted using KOH) as a function of potential. The reference potential, E_{REF}, for this set of data was -800 mV (*vs* Ag/AgCl). There were a total of 512 co-added scans for each potential step, E_{VAR}.

of the electrode. Conversely, a positive-going infrared peak indicates a diminishment of that vibrational mode.

In Figure 4.5, one can see the results of these calculations for 0.1 mM DMAP species in pH 10, 50 mM supporting electrolyte. In this data set, the reference potential, E_{REF}, was -800 mV *versus* Ag/AgCl where DMAP species are completely desorbed from the electrode surface.[1] At variable potentials, E_{VAR}, more negative than -400 mV *versus* Ag/AgCl, the difference spectra are featureless and indicate that the surface remains surfactant free. However, with potentials -400 mV and greater, the data reveal four downward-going bands appearing at 1389, 1446, 1538 and 1623 cm^{-1} respectively. The most pronounced of these is at 1623 cm^{-1} which is slightly convoluted by the superimposition of a very broad, positive adsorption. This bimodal feature arises from the displacement of water molecules, which have a strong absorption at 1640 cm^{-1}, from the surface by the adsorption of DMAP. The position of the remaining bands at 1389, 1446 and 1538 cm^{-1} are in accordance with the *A'* modes described earlier (Figure 4.3) at pH 11 and provides a strong indication that the absorbed species is vertically aligned, deprotonated DMAP molecules. This result was previously inferred from electrochemical measurements[1] but the SEIRAS data provides supporting molecular structure information. Determination of whether the highest frequency absorption band is related to either DMAP or $DMAPH^+$ is initially problematic, as this band appears in-between the protonated and deprotonated forms observed from the measured transmission spectra (see Table 4.1). From the literature and recalling that this vibration is very strongly coupled with a symmetric ring deformation mode, it would be expected that this mode will be blue-shifted as the lone pair of electrons on the pyridine ring coordinate to the metal surface. This type of shift to higher frequencies has also been reported for pyridine upon N-bonded adsorption on Au(111).[27,28,40,41]

From this information, all four bands in the spectroelectrochemical data at pH 10 (Figure 4.5) are interpreted to be the corresponding *A'* modes of the deprotonated form of the DMAP molecule. The relative intensities of these signals are found to increase with increasingly positive potential. To demonstrate this, in Figure 4.6 a plot of the normalized integrated intensities for the 1538 and 1623 cm^{-1} infrared bands *versus* electrode potential was prepared. To provide a means to compare the electrochemical data, the differential capacity curve for 0.1 mM DMAP on Au coated Si has been overlaid. There was no special reason for the integration of just these two bands other than they provided the strongest signals. In fact, the integration of the 1389 and 1446 cm^{-1} peaks provides qualitatively identical results but with larger scatter (data not shown) due to the lower signal-to-noise ratio of these bands. Briefly, a higher DMAP surface coverage corresponds to a lower measured capacity, and as one can see in Figure 4.6 there is good correlation between the electrochemical and the integrated spectroscopic signals for $E > -200$ mV. The increase in the infrared signal intensity is congruent with the observation of a limiting capacity value of ~10-11 $\mu F\ cm^{-2}$. The maximum infrared signal occurs at a measured potential of $E = 200$ mV following which the signal begins to decrease. The DC curve reveals something analogous as the capacity begins to increase at potentials greater than 200 mV. This phenomenon is attributed to the onset of competitive hydroxide adsorption on the electrode surface in high pH solutions which will displace some of the DMAP molecules. The strong consistency between the electrochemically measured DC curve and the *in-situ* SEC measurements for $E > -200$ mV provides excellent corroborating evidence for vertically oriented DMAP adsorbing on gold surfaces at this pH. However, there are some minor discrepancies between the onset of a very broad pseudocapacitive peak in the differential capacity data and the initial appearance of infrared signal intensity. The lack of an infrared signal in the potential

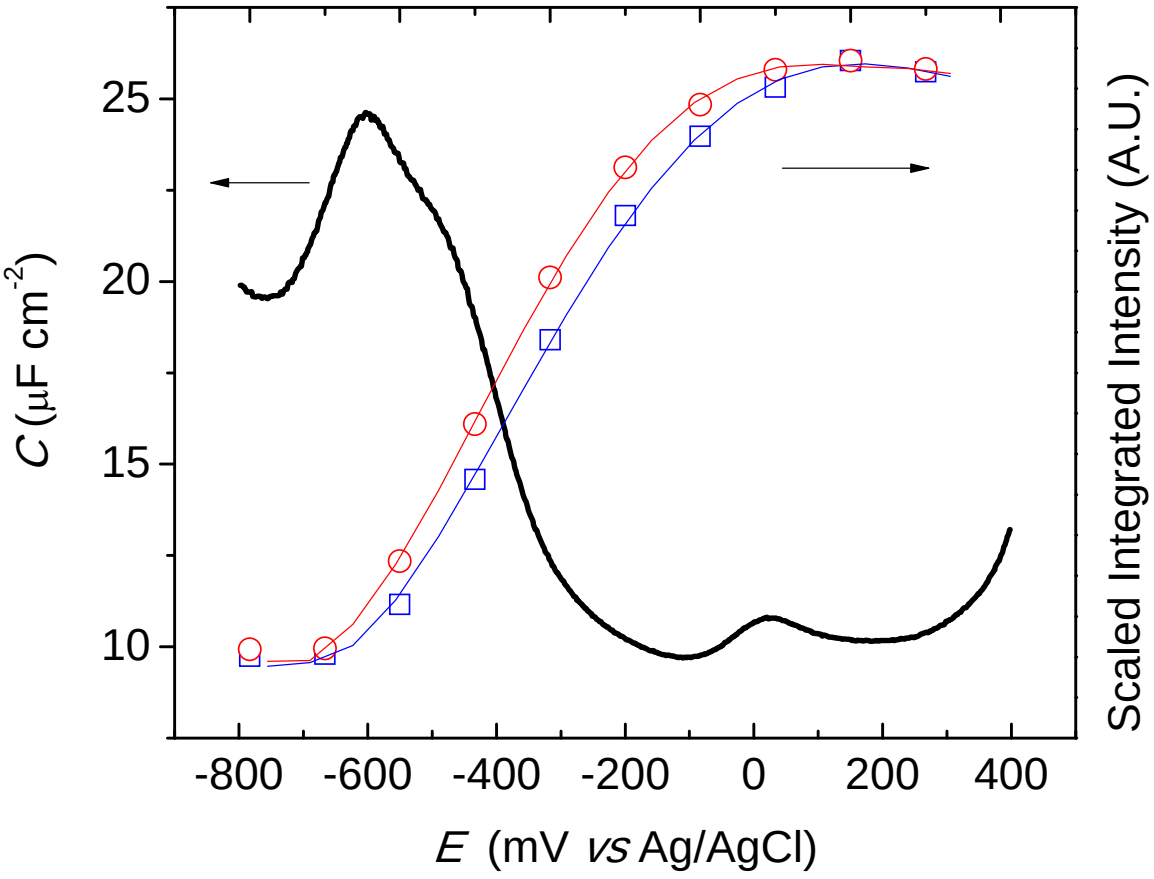

Figure 4.6. Scaled integrated intensities for the infrared vibration bands at 1538 (○) and 1623 (□) cm^{-1} as a function of the electrode potential. Superimposed on these plots is the measured differential capacity (DC) curve for 0.1 mM DMAP (formal concentration) on the Au coated Si wafer at pH 10.

range -700 mV < E < -500 mV may imply that even at pH 10, the DMAP species may initially adsorb horizontally on the surface. In an earlier electrochemistry study, it was observed that this pseduocapacitive peak (associated with the horizontal-to-vertical phase transition), shifts cathodically with increasing pH by approximately 60 mV pH^{-1}. At pH 10, this peak would correspond to the shoulder clearly visible on the positive side of the adsorption pseudocapacity peak (Figure 4.6). As horizontally adsorbed DMAP species are invisible due to the surface selection rules of ATR-SEIRAS, the narrow potential window between the initial adsorption and phase transition would explain why no infrared signal is measured until approximately $E \geq$ -400 mV.

Another metric to provide further evidence of an end on, vertical orientation of the DMAP molecule is the change of the peak position as a function of potential. Although, as previously mentioned, the band appearing at 1445 cm^{-1} is potential invariant, the remaining three bands shift to higher frequencies, with increasing potential. Similar potential induced shifts in infrared vibrations have been observed for many adsorbates, particularly CO adsorption on Pt surfaces.[42] There are two commonly cited mechanisms for this observation, the first is the Stark effect and the second is a charge-transfer model.[43] The Stark effect involves the coupling between a potential induced electric field and the polarizablity of electrons in the adsorbate molecule. In contrast, the charge-transfer model is based on changes in the bonding structure of the adsorbate related to changes in the charge density on the electrode. In Figure 4.7 plots of the peak position *versus* electrode potential for the nominally 1623, 1538 and 1390 cm^{-1} bands are shown to elicit further information about the adsorption orientation of DMAP. A simple linear equation was used to fit each data set. The slopes for the 1623 and 1538 cm^{-1} infrared bands were similar at 7-8 cm^{-1} mV^{-1}, whereas 1391 cm^{-1} has a smaller potential dependence with a

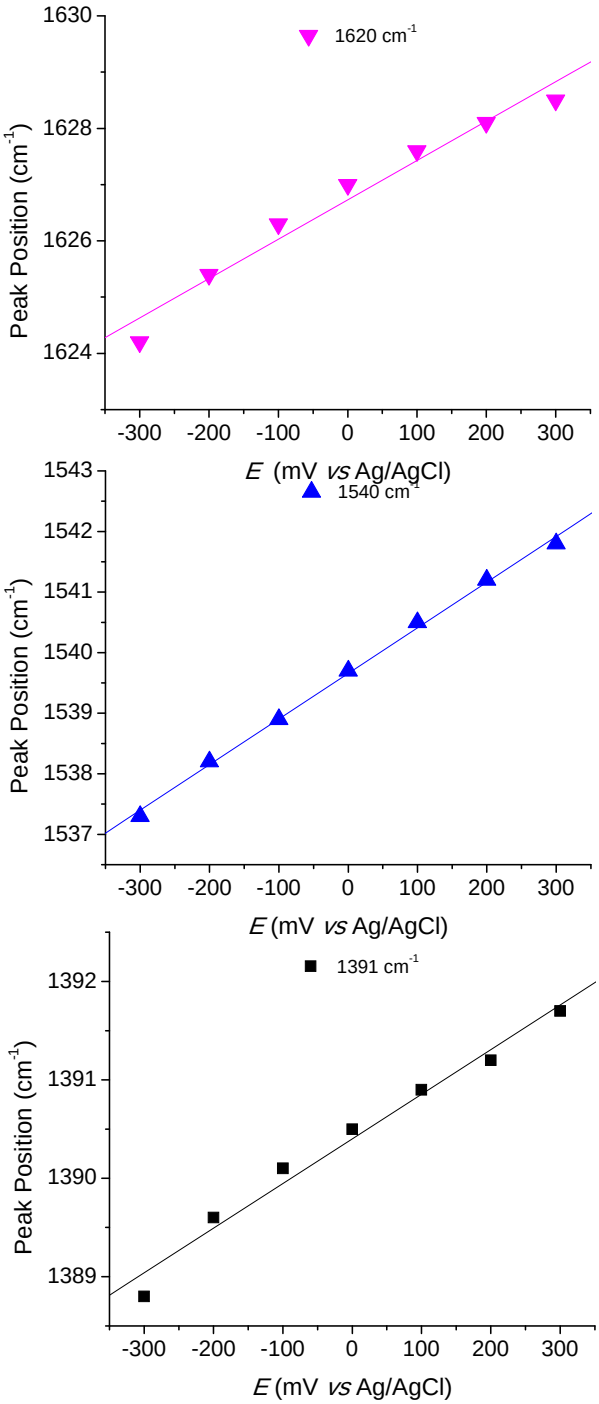

Figure 4.7. Peak position as a function of applied potential for the three strongest *A'* modes (infrared vibrational bands) of DMAP from Figure 4.5 at pH 10: a) 1623 cm^{-1}, b) 1538 cm^{-1} and c) 1391 cm^{-1}.

slope of 4.5 cm^{-1} mV^{-1}). For comparison, the A_1 ring vibration mode found in pyridine has demonstrated a 5-6 cm^{-1} mV^{-1} dependence[28] and has been cited as arising from either a weak Stark effect or a change-transfer effect resulting from the electron donation via the nonbonding orbital located on the nitrogen atom. Two vibrations (1623 and 1538 cm^{-1}) are strongly coupled to the nitrogen present in the pyridine ring, whereas the 1391 cm^{-1} vibrational band primarily involves the C-N stretch. If the Stark effect is involved in the potential induced shifts, the rapid drop of the electric field across the inner Helmholtz plane of the electrical double-layer should provide a greater Stark shift to the end of the molecule closest to the surface of the electrode. Qualitatively, there is a larger potential-induced shift in the ring-dependent modes (1623 and 1538 cm^{-1}) compared to those of the C-N vibration (1391 cm^{-1}) and provides further indications that DMAP adsorbs vertically on the Au surface through its endocyclic nitrogen at high pH and at potentials greater than -400 mV.

More insight into the adsorption behaviour of DMAP/$DMAPH^+$ in low pH electrolytes was desired and was further analyzed by *in-situ* ATR-SEIRAS SEC techniques. These measurements were performed in 50 mM $KClO_4$ + 0.1 mM (DMAP)$HClO_4$ with the pH adjusted to 4.5 using high purity $HClO_4$. As a previous electrochemical study suggested that there is a greater possibility that both DMAP and $DMAPH^+$ signals will be present on the surface at these conditions, H_2O was substituted with D_2O to remove any potential solvent absorptions. This avoids convolution of the H-O-H deformation signal, ~1640 cm^{-1}, with the 1653 cm^{-1} signal from $DMAPH^+$ and the 1623 cm^{-1} signal from DMAP respectively. In Figure 4.8, one can see the results of these measurements once again using a reference potential, E_{REF}, of -800 mV *versus* Ag/AgCl. This reference potential was chosen based on previous differential capacity measurements which indicated that the electrode is surfactant free at these potentials for low

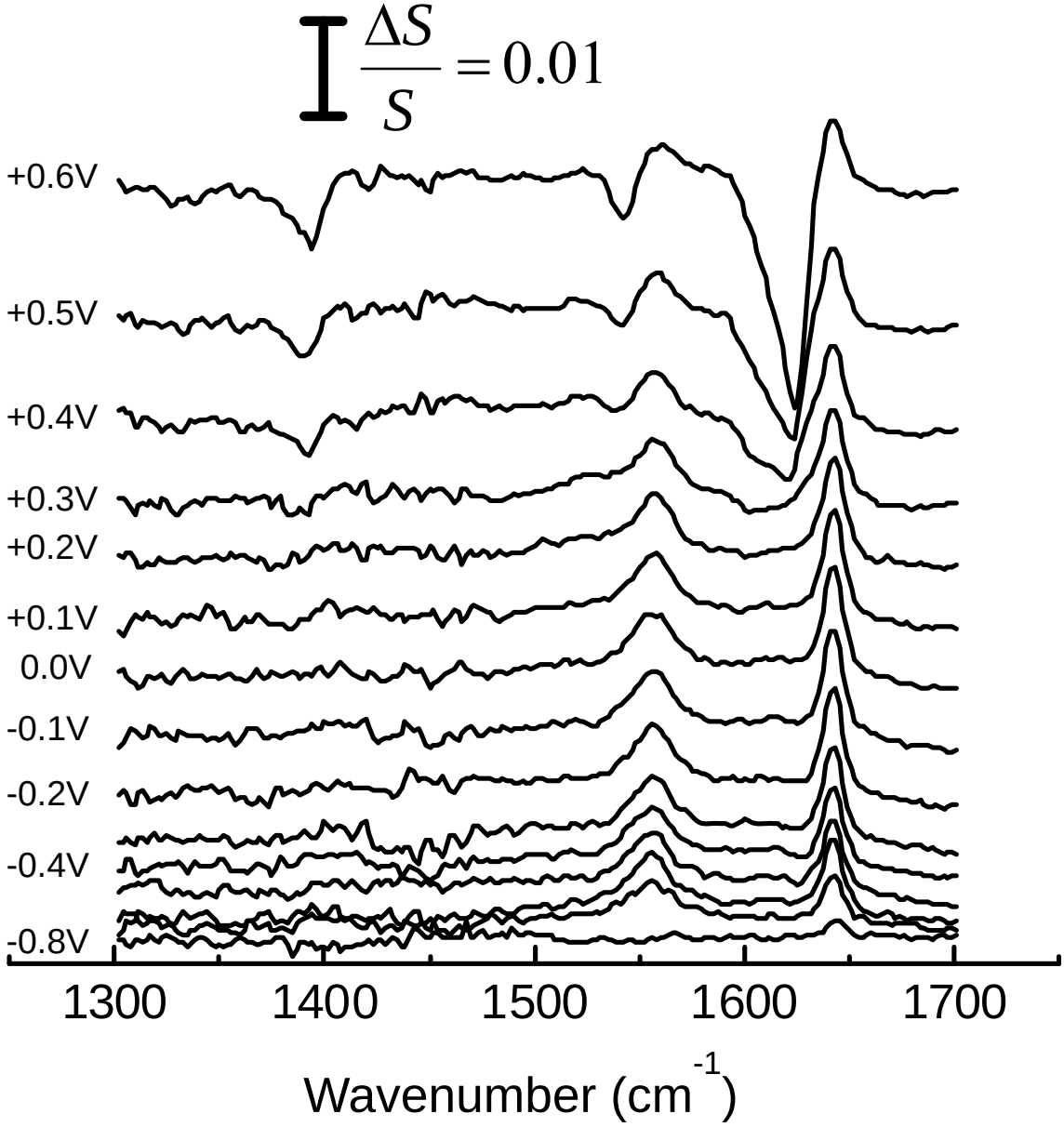

Figure 4.8. Subtractively normalized SEIRAS data for 0.1 mM formal (DMAP)$HClO_4$ concentration as a function of applied potential. The 50 mM $KClO_4$ electrolyte was adjusted to a pH of 4.5 using double-distilled $HClO_4$. There were 128 co-added scans for each infrared measurement using a reference potential, E_{REF}, of -800 mV (vs Ag/AgCl).

solution DMAP concentrations. However, using this reference potential was slightly problematic as there is a significant amount of hydrogen evolution at -800 mV in pH 4.5 electrolytes. This hydrogen evolution reaction (HER) led to the deterioration of the thin gold films deposited onto the Si ATR element. This effect has also been commented on by Osawa *et al.*[27] As a consequence of this, repeatedly stepping into the HER to acquire a reference spectrum, resulted in slight changes in the optical response of these films from one data set to the next. As such, although replicate measurements are qualitatively identical, co-addition and averaging of large numbers of multiple data sets had the deleterious effect of decreasing the signal-to-noise ratio. Consequentially, the spectra in Figure 4.8 correspond to only 128 scans rather than 512 scans.

From previous electrochemical studies, a proposed adsorption model had horizontally adsorbed $DMAPH^+$ at potentials negative of the potential of zero charge, E_{PZC}, which underwent a transition to vertically oriented DMAP with $E > E_{PZC}$. As the surface selection rules for SEIRAS render the horizontally adsorbed $DMAPH^+$ invisible it was speculated that the acquired spectra for the pH 4.5 experiments would be featureless for $E <$ -200 mV and would show negative going bands for $E >$ -200 mV (similar to the previous measurements performed at pH 10). However, the subtractively normalized data in Figure 4.8 indicates the appearance of two positive-going bands (1643 and 1559 cm^{-1}) starting at E = -700 mV. These bands increase in intensity with increasing positive potential to E = -300 mV *versus* Ag/AgCl. The frequency of these peak centers indicate that these signals are arising from the *protonated* $DMAPH^+$ ion. One will notice that these infrared signals are potential-dependent and demonstrate a shift in frequency compared to Figure 4.5. The positive direction of these bands qualitatively describes a

decrease in either the concentration of the molecule or a change in alignment (relative to the surface normal), of $DMAPH^+$.

Starting at $E \sim 300$ mV, new negative infrared bands appear in the subtractively normalized spectra at 1622, 1538 and 1390 cm^{-1}, producing pronounced bimodal features for the *A'* vibrational modes. The frequency of these negative-going bands strongly indicates that they correspond to the neutral DMAP molecule as they are nearly identical in position to the bands seen in the high pH experiment. Although only visible over a short range of potentials, the negative-going infrared band signals show a clear Stark effect as seen by a shift to higher frequencies with increasing positive potentials. In contrast, the peak positions of the positive modes in Figure 4.8 do not shift with potential. In order to rationalize the presence of the positive-going bands, one can surmise that the chosen reference potential (E_{REF} = -800 mV) did not correspond to a state of complete surface desorption as originally suspected. Considering the electrode surface is highly negative at E_{REF}, it is speculated that the $DMAPH^+$ ion is held electrostatically to the electrode surface with a vertical orientation to maximize charge compensation. Then, when the potential is stepped to more positive values, the magnitude of the negative surface charge density decreases and the $DMAPH^+$ ions adopt a lower coverage, horizontally oriented state of adsorption. In this model, one can accept that the charged molecules will switch from being infrared active at the reference potential to infrared inactive in the adsorbed state (-700 mV < E < -200 mV). This would then explain both the appearance of the positive-going bands and the absence of a Stark shift associated with these bands in Figure 4.8. Moving to more positive potentials, the sign of the surface charge density will then switch from negative to positive and will result in the deprotonation of $DMAPH^+$ ions which reorient vertically on the surface. Compared to the reference potential state of electrostatically bound,

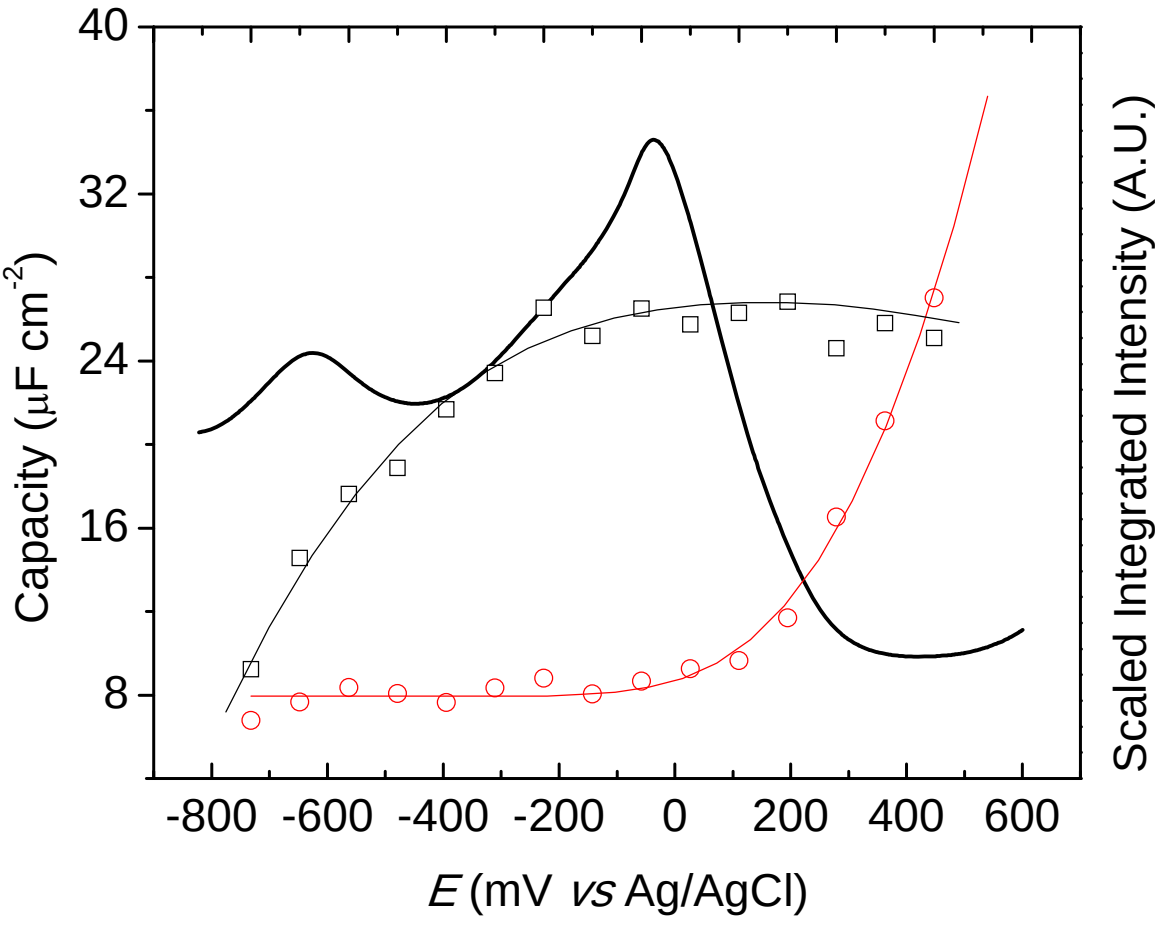

Figure 4.9. Scaled integrated intensities of the positive-going 1643 cm^{-1} band (□) and the negative-going 1623 cm^{-1} vibrational band (○) as a function of applied potential. Plots are superimposed on differential capacity (DC) measurements of 0.1 mM DMAP (formal concentration) on an Au coated Si wafer at pH 4.5 (black).

vertical ions, this would equate to a loss of $DMAPH^+$ signal and the appearance of negative-going bands corresponding to the now adsorbed DMAP molecule. This conversion of adsorbed $DMAPH^+$ to DMAP also explains the bimodal character of the infrared bands seen in Figure 4.8 for $E > 200$ mV.

In Figure 4.9, the absolute integrated infrared band intensities for the positive-going 1643 cm^{-1} band and the negative-going 1623 cm^{-1} band are plotted as a function of electrode potential. Superimposed on this plot is the corresponding differential capacity curve for this system. One can see from this figure that the 1643 cm^{-1} band plateaus in intensity at $E \sim -300$ mV correlated with the onset of the 1623 cm^{-1} signal and the region of potentials with the lowest capacity in the DC curve. This latter point is convincing evidence that in acidic electrolytes, deprotonated DMAP molecules are still adsorbed onto Au surfaces at positive potentials. The intensity of the 1643 cm^{-1} band begins to increase at potentials corresponding to the first pseudocapacity peak in the DC curve ($E \sim -650$ mV) and plateaus at the onset of the second pseudocapacity peak ($E \sim -250$ mV). The implication of this is that the first pseudocapacity peak represents the vertical ion to horizontal ion transition of the $DMAPH^+$ ion rather than the onset of molecular adsorption as was originally inferred from previous electrochemical studies. The fact that the area under the 1643 cm^{-1} band does not plateau until -300 mV indicates that between $-700 \text{ mV} < E < -300$ mV the electrode is covered by a mix of both phases of $DMAPH^+$ ion orientations. However, at more positive potentials, the positively charged molecular ion is completely absent from the surface.

4.4. Summary and Conclusions

In summary, this Chapter illustrates the successful demonstration of *in-situ* SEC ATR-SEIRAS to obtain infrared spectra of DMAP and its conjugate acid, $DMAPH^+$, adsorbed on gold surfaces. The application of this *in-situ* SEC technique has allowed for the collection of high quality data as evidenced by the excellent signal-to-noise ratios obtained and through the large magnitude peaks observed in the subtractively normalized data. As a result, further evidence and new insight concerning the adsorption behaviour of DMAP and $DMAPH^+$ has been obtained. The electrolessly prepared Au film used for the SEIRAS measurements was analyzed electrochemically and indicated that the gold surface is preferentially (111) oriented but the size of these domains is still probably quite small. The net result of these films is a surface that shows intermediate behaviour between a well-ordered (111) single crystal and a polished polycrystalline electrode.

The infrared data at high pH (pH 10) show large potential-dependent absorption signals that correspond to the various *A'* ring deformation modes of the DMAP molecule but no evidence of modes corresponding to its conjugate acid. These results confirm the existence of a monolayer of vertically oriented DMAP molecules over a very wide range of double-layer potentials. Experiments performed at pH 4.5 show infrared signals that arise mainly from the base form of DMAP despite the fact that in the bulk of solution this species exists exclusively in the form of the conjugate acid. However, there are no infrared features observed until $E > 200$ mV even though the differential capacity data clearly indicate that DMAP species are adsorbing on the surface between $-600 \text{ mV} < E < -100 \text{ mV}$. This is consistent with the model previously inferred from purely electrochemical measurements of a horizontal-to-vertical reorientation of DMAP species. Due to the surface selection rules, direct infrared measurements of horizontally

absorbed DMAP (or $DMAPH^+$) are prohibited and therefore conclusive evidence to verify this phase transition cannot be made from infrared measurements alone. Nonetheless, the infrared data offers no contradicting evidence to this model and tacitly supports a potential dependent horizontal-to-vertical transition with a pH 4.5 electrolyte aqueous solution. The *in-situ* infrared measurements also confirm that at relatively positive potentials (and corresponding positive surface charge densities) a deprotonation of $DMAPH^+$ occurs upon the adsorption onto the Au surface. This result implies that the metal (Au) – electrolyte interface pKa of $DMAPH^+$ is considerably different compared to the bulk of solution. Although this perturbation of the acidity of a molecule at a surface is well-known,[44–46] the DMAP system is an excellent example of how the electrical state of the interface may also perturb the acid/base behaviour of surface bound molecules.

An unexpected result was also obtained from working in low pH electrolyte solutions with *in-situ* infrared measurements. The presence of positive going bands from the *A'* vibrational modes of dimethylaminopyridinium reveal that the $DMAPH^+$ ions are still adsorbed on the electrode surface at very negative potentials presumably due to an electrostatic attraction. This last result was not entirely forthcoming from previous electrochemical studies (differential capacity and chronocoulometry), and highlights the power of combining electrochemical measurements *in-situ* with molecular spectroscopic techniques in revealing new information concerning interfacial adsorption at electrified interfaces. Chapter 5 of this thesis builds upon the successes of this work by moving towards more experimentally challenging methods than those presented here. While continuing to use the internal reflection ATR-SEIRAS apparatus described here, the molecular structure and electrochemical properties of proton-coupled electron-transfer (PCET) kinetic processes will be examined.

4.5. References

1. Barlow, B. C.; Burgess, I. J. Electrochemical Evaluation of 4-(dimethylamino)pyridine Adsorption on Polycrystalline Gold. *Langmuir* **2007**, *23*, 1555–63.

2. Larson, I.; Chan, D. Y. C.; Drummond, C. J.; Grieser, F. Use of Atomic Force Microscopy Force Measurements To Monitor Citrate Displacement by Amines on Gold in Aqueous Solution. *Langmuir* **1997**, *13*, 2429–2431.

3. Gandubert, V. J.; Lennox, R. B. Assessment of 4-(Dimethylamino)pyridine as a Capping Agent for Gold Nanoparticles. **2005**.

4. Osawa, M. In-Situ Surface-enhanced Infrared Spectroscopy of the Electrode/Solution Interface. In *In Diffraction and Spectroscopic Methods in Electrochemistry*; Alkire, R. C., Kolb, D., Lipkowski, J., Ross, P. N., Ed.; 2006; pp. 269–314.

5. Zamlynny, V.; Lipkowski, J. Quantitative SNIFTIRS and PM IRRAS of Organic Molecules at Electrode Surfaces. *Diffraction and Spectroscopic Methods in Electrochemistry* **2006**, *9*, 315–376.

6. Tadjeddine, A.; Rille, A. Le Sum and Difference Frequency Generation at Electrode Surfaces. *Interfacial Electrochemistry* **1999**, 317–343.

7. Osawa, M. Surface-enhanced infrared absorption. In *Near-Field Optics and Surface Plasmon Polaritons*; Springer, 2001; pp. 163–187.

8. Wu, D.-Y.; Li, J.-F.; Ren, B.; Tian, Z.-Q. Electrochemical Surface-enhanced Raman Spectroscopy of Nanostructures. *Chemical Society reviews* **2008**, *37*, 1025–41.

9. Delgado, J. M.; Orts, J. M.; Pérez, J. M.; Rodes, A. Sputtered Thin-film Gold Electrodes for in Situ ATR-SEIRAS and SERS Studies. *Journal of Electroanalytical Chemistry* **2008**, *617*, 130–140.

10. Posey, K. L.; Viegas, M. G.; Boucher, A. J.; Wang, C.; Stambaugh, K. R.; Smith, M. M.; Carpenter, B. G.; Bridges, B. L.; Baker, S. E.; Perry, D. A. Surface-Enhanced Vibrational and TPD Study of Nitroaniline Isomers. *Journal of Physical Chemistry C* **2007**, *111*, 12352–12360.

11. Gittins, D. I.; Caruso, F. Spontaneous Phase Transfer of Nanoparticulate Metals from Organic to Aqueous Media. *Angewandte Chemie (International ed. in English)* **2001**, *40*, 3001–3004.

12. Rucareanu, S.; Gandubert, V. J.; Lennox, R. B. 4-(N , N -Dimethylamino)pyridine-Protected Au Nanoparticles: Versatile Precursors for Water- and Organic-Soluble Gold Nanoparticles. *Chemistry of Materials* **2006**, *18*, 4674–4680.

13. Raguse, B.; Chow, E.; Barton, C. S.; Wieczorek, L. Gold Nanoparticle Chemiresistor Sensors: Direct Sensing of Organics in Aqueous Electrolyte Solution. *Analytical Chemistry* **2007**, *79*, 7333–9.

14. Vivek, J. P.; Burgess, I. J. Insight into Chloride Induced Aggregation of DMAP-Monolayer Protected Gold Nanoparticles Using the Thermodynamics of Ideally Polarized Electrodes. *Journal of Physical Chemistry C* **2008**, *112*, 2872–2880.

15. Gittins, D. I.; Susha, A. S.; Schoeler, B.; Caruso, F. Dense Nanoparticulate Thin Films via Gold Nanoparticle Self-Assembly. *Advanced Materials* **2002**, *14*, 508–512.

16. Cho, J.; Caruso, F. Investigation of the Interactions Between Ligand-Stabilized Gold Nanoparticles and Polyelectrolyte Multilayer Films. *Chemistry of Materials* **2005**, *17*, 4547–4553.

17. Dong, W.-F.; Sukhorukov, G. B.; Mhwald, H. Enhanced Raman Imaging and Optical Spectra of Gold Nanoparticle Doped Microcapsules. *Physical Chemistry Chemical Physics* **2003**, *5*, 3003.

18. Dorris, A.; Rucareanu, S.; Reven, L.; Barrett, C. J.; Lennox, R. B. Preparation and Characterization of Polyelectrolyte-coated Gold Nanoparticles. *Langmuir* **2008**, *24*, 2532–8.

19. Skirtach, A. G.; Déjugnat, C.; Braun, D.; Susha, A. S.; Rogach, A. L.; Sukhorukov, G. B. Nanoparticles Distribution Control by Polymers: Aggregates Versus Nonaggregates. *The Journal of Physical Chemistry C* **2007**, *111*, 555–564.

20. Gandubert, V. J.; Lennox, R. B. Surface Plasmon Resonance Spectroscopy Study of Electrostatically Adsorbed Layers. **2006**.

21. Zhang, L.; Yuan, R.; Chai, Y.; Li, X. Investigation of the Electrochemical and Electrocatalytic Behavior of Positively Charged Gold Nanoparticle and L-cysteine Film on an Au Electrode. *Analytica Chimica Acta* **2007**, *596*, 99–105.

22. Yu, A.; Liang, Z.; Cho, J.; Caruso, F. Nanostructured Electrochemical Sensor Based on Dense Gold Nanoparticle Films. *Nano Letters* **2003**, *3*, 1203–1207.

23. Stanca, S. E.; Eritja, R.; Fitzmaurice, D. DNA-templated Assembly of Nanoscale Architectures for Next-generation Electronic Devices. *Faraday Discussions* **2006**, *131*, 155.

24. Lipkowski, J.; Stolberg, L. Molecular Adsorption at Gold and Silver Electrodes. *Adsorption of Molecules at Metal Electrodes* **1992**, 171–238.

25. Stolberg, L.; Richer, J.; Lipkowski, J.; Irish, D. E. Adsorption of Pyridine at the Polycrystalline Gold Solution Interface. *Journal of electroanalytical chemistry and interfacial electrochemistry* **1986**, *207*, 213–234.

26. Stolberg, L.; Morin, S.; Lipkowski, J.; Irish, D. E. Adsorption of Pyridine at the Au (111)-solution Interface. *Journal of electroanalytical chemistry and interfacial electrochemistry* **1991**, *307*, 241–262.

27. Cai, W.-B.; Wan, L.-J.; Noda, H.; Hibino, Y.; Ataka, K.; Osawa, M. Orientational Phase Transition in a Pyridine Adlayer on Gold(111) in Aqueous Solution Studied by in Situ Infrared Spectroscopy and Scanning Tunneling Microscopy. *Langmuir* **1998**, *14*, 6992–6998.

28. Ikezawa, Y.; Sawatari, T.; Kitazume, T.; Goto, H.; Toriba, K. In Situ FTIR Study of Pyridine Adsorbed on a Polycrystalline Gold Electrode. *Electrochimica Acta* **1998**, *43*, 3297–3301.

29. Stolberg, L.; Lipkowski, J.; Irish, D. E. An Examination of the Relationship Between Surface Enhanced Raman Scattering (SERS) Intensities and Surface Concentration for Pyridine Adsorbed at the Polycrystalline Gold/aqueous Solution Interface. *Journal of electroanalytical chemistry and interfacial electrochemistry* **1991**, *300*, 563–584.

30. Miyake, H.; Ye, S.; Osawa, M. Electroless Deposition of Gold Thin Films on Silicon for Surface-enhanced Infrared Spectroelectrochemistry. *Electrochemistry Communications* **2002**, *4*, 973–977.

31. Ataka, K.; Yotsuyanagi, T.; Osawa, M. Potential-Dependent Reorientation of Water Molecules at an Electrode/Electrolyte Interface Studied by Surface-Enhanced Infrared Absorption Spectroscopy. *The Journal of Physical Chemistry* **1996**, *100*, 10664–10672.

32. Wandlowski, T.; Ataka, K.; Pronkin, S.; Diesing, D. Surface Enhanced Infrared spectroscopy—Au(1 1 1)/sulphuric Acid—new Aspects and Challenges. *Electrochimica Acta* **2004**, *49*, 1233–1247.

33. *Fundamentals of Electrochemistry*; Bagotsky, V. S., Ed.; Wiley-VCH, 2005.

34. Kozhevina, L. I.; Chotii, K. Y.; Goncharova, L. D.; Rybachenko, V. I.; Titov, E. V No Title. *Ukr. Khim. Zh* **1989**, *55*, 83–88.

35. Kozhevina, L. I.; Rybachenko, V. I. Interpretation of IR Spectra of the N-acethyl-4-dimethylaminopyridinium Salts. *Journal of Applied Spectroscopy* **1999**, *66*, 165–170.

36. Cook, D. VIBRATIONAL SPECTRA OF PYRIDINIUM SALTS. *Canadian Journal of Chemistry* **1961**, *39*, 2009–2024.

37. Travert, A.; Vimont, A.; Lavalley, J.-C. An Example of Misinterpretation of IR Spectra of Adsorbed Species Due to Gas Phase H2O: Comment on "The Surface Acidity and Characterization of Fe-montmorillonite Probed by in Situ FT-IR Spectroscopy of Adsorbed Pyridine" [Appl. Catal. A 294 (2005) 156–16. *Applied Catalysis A: General* **2006**, *302*, 333–334.

38. Mirabella Jr, F. M. Principles, Theory, and Practice of Internal Reflection Spectroscopy. *Internal Reflection Spectroscopy: Theory and Applications* **1993**, *15*, 17.

39. *Lange's Handbook of Chemistry*; Dean, J. A., Ed.; 15th ed.; McGraw-Hill: New York, 1999.

40. Hoon-Khosla, M.; Fawcett, W. R.; Chen, A.; Lipkowski, J.; Pettinger, B. A SNIFTIRS Study of the Adsorption of Pyridine at the Au(111) Electrode–solution Interface. *Electrochimica Acta* **1999**, *45*, 611–621.

41. Nanbu, N.; Kitamura, F.; Ohsaka, T.; Tokuda, K. Adsorption of Pyridine on a Polycrystalline Gold Electrode Surface Studied by Infrared Reflection Absorption Spectroscopy. *Journal of Electroanalytical Chemistry* **1999**, *470*, 136–143.

42. Mehandru, S. P.; Anderson, A. B. Potential-induced Variations in Properties for Carbon Monoxide Adsorbed on a Platinum Electrode. *The Journal of Physical Chemistry* **1989**, *93*, 2044–2047.

43. Nichols, R. J. IR Spectroscopy of Molecules at the Solid--solution Interface. *Adsorption of molecules at metal electrodes, J. Lipkowski, PN Ross (Eds.)(VCH, New York 1992) Chapter 7* **1992**, *7*, 172–173.

44. Fawcett, W. R.; Fedurco, M.; Kovacova, Z. Double Layer Effects at Molecular Films Containing Acid/Base Groups. *Langmuir* **1994**, *10*, 2403–2408.

45. Bryant, M. A.; Crooks, R. M. Determination of Surface pKa Values of Surface-confined Molecules Derivatized with pH-sensitive Pendant Groups. *Langmuir* **1993**, *9*, 385–387.

46. Andreu, R.; Fawcett, W. R. Discreteness-of-Charge Effects at Molecular Films Containing Acid/Base Groups. *Journal of Physical Chemistry* **1994**, *98*, 12753–12758.

CHAPTER 5

CHARGE TRANSFER AND SERIAS STUDIES OF 1,4-BENZOQUINONE FUNCTIONALIZED MIXED MONO/DITHIOL SELF-ASSEMBLED MONOLAYERS

5.1. Introduction

This chapter builds on the work from the previous chapter by moving from measuring equilibrated electrochemical systems to measuring dynamic electrochemical processes. This increases the complexity of the collection and processing of infrared data but provides a foundation to start studying more complicated electrochemical systems, in particular electrochemical kinetic processes. The work presented here still utilizes internal reflection geometry optics and a slightly improved *in-situ* spectroelectrochemical cell compared to the one described in the previous chapter. The main instrumental challenge presented here was in the development of Rapid-Scan (continuous mirror drive) FTIR spectroscopic techniques including the interfacing needed to automate the collection of replicate measurements for improved signal-to-noise. In this chapter, time-resolved information concerning proton-coupled electron transfer (PCET) redox reactions on modified self-assembled monolayers (SAMs) is obtained using Rapid-Scan FTIR spectroscopy. A chemically modifiable SAM was reacted with an electroactive moiety, namely 1,4-benzoquinone. The resulting surface bound quinone terminated SAM was then used to study the thermodynamics and kinetics of PCET reactions. The gathered infrared data on formal potential and the time-resolved calculated heterogeneous rate constants agree well with those measured using strictly electrochemical techniques.

Redox active self-assembled monolayers (SAMs) provide an excellent platform for the study of electrochemical charge transfer processes and specifically for the development of time-

resolved ATR-SEIRAS methodologies. Distinct advantages of studying surface confined redox centers includes the removal of mass transfer limitations and the ability to manipulate heterogeneous electron transfer rates through control of the spacer thickness separating the redox center from the electrode surface. Simply modifying the length[1–6] and chemical nature of the thiol backbone spacer[7–12] has been found to be particularly useful for determining the mechanism of electronic coupling between substrate and redox center as well as verifying Marcus theory predications.[4,13,14] One such electrochemical system is the benzoquinone (BQ)/hydroxybenzoquinone (HBQ) terminated SAM. This system has been extensively studied[8–11,15–27] and is of particular fundamental interest owing to the importance of quinone moieties in biological[28] and industrial[29] processes. Unlike simple electron transfer redox couples, the reduction of BQ to HBQ in aqueous solutions involves the coupled transport of both two electrons and two protons ($2e^-2H^+$). The theoretical treatment of the observed apparent heterogeneous rate constants dependence on pH is based on either a step-wise mechanism (discrete proton and electron transfer steps)[30–35] or a concerted mechanism (simultaneous transfer of both forms of charge).[36–40] A modification to the step-wise mechanism was described by Finklea[41] to handle PCET processes confined to an electrode surface.

Based on previous work[42,43] a procedure to form a nearly ideal electroactive BQ monolayer by covalently attaching 1,4-benzoquinone (BQ) to a pre-formed amine terminated monolayer *via* Michael addition was developed in our laboratory.[44] This system provides minimal heterogeneity and Nernstian responses at very slow voltammetric sweep rates and was used to demonstrate that the resulting aminobenzoquinone terminated monolayer exhibits two-electron, three-proton step-wise PCET electrochemical reaction.[45] Although this aminobenzoquinone system is an excellent model system for electrochemical determination of

formal potentials and charge transfer rate constants, it was found that the monolayer suffered from a gradual loss of electrochemical activity, presumably due to C-N bond hydrolysis. A more robust chemical linkage is preferable in order to minimize these losses as they would greatly affect the signal-to-noise ratio of the time-resolved infrared measurements.

In this Chapter mixed monolayers of nonanedithiol (NDT) diluted in octanethiol (OT) are first prepared before the covalent tethering (bonding) of 1,4-benzoquinone through a Michael addition to the free thiol terminus. Highly facile and nearly quantitative yields have recently been reported for similar reactions involving freely dissolved thiols and benzoquinone in aqueous solution[46,47] and as demonstrated in this Chapter these reactions can also be extended to surface confined reactions. Furthermore, unlike the amino functionalized monolayers, the reaction with the thiol terminated SAM does not require elevated temperatures which simplifies their preparation. This method of preparing a quinone terminated SAM provides a more stable redox active monolayer than the aminobenzoquinone system, albeit with an increase in the heterogeneity of the redox center microenvironments.

The greater robustness of this preparative method has allowed the extension of kinetic and thermodynamic methodologies beyond voltammetry and chronocoulometry to coupling *in-situ* ATR-SEIRAS to characterize these redox active monolayers. Herein, the agreement between thermodynamic (apparent formal potentials) and kinetic (apparent heterogeneous rate constants) parameters obtained from purely electrochemical (cyclic voltammetry, chronocoulometry) and *in-situ* spectroelectrochemical SEIRAS techniques are reported.

5.2. Experimental

5.2.1. Chemicals, Reagents and Gold Substrate Preparation

Octanethiol (95%), 1,9-nonanedithiol (95%), $NaClO_4 \cdot H_2O$ (> 99%), Na_2HPO_4 (ACS Grade), NaH_2PO_4 (ACS Grade) and $HClO_4$ (Ultrahigh Purity Grade) were all purchased from Sigma–Aldrich and were used as received. Ethanol (95%) was purchased from Commercial Alcohols Inc. (Brampton ON, CA). 1,4-Benzoquinone (BQ) (Alfa Aesar, < 98%) was purified by sublimation at a slightly elevated temperature (37 ^{0}C) before use. All aqueous solutions were prepared from Milli-Q (> 18.2 MΩ cm^{-1}) water. The procedure for fabricating the polycrystalline bead electrodes from gold wire (Alfa Aesar, 99.99%) has been described elsewhere.[48] Prior to incubation, the polycrystalline gold bead working electrodes were cleaned by immersion in *piranha* solution (3:1 H_2SO_4:H_2O_2) for a minimum of 30 minutes and then rinsed copiously with Milli-Q water. The electrodes were flame annealed and quenched with Milli-Q water immediately before use. Details on the deposition of a thin-layer of gold onto the silicon ATR hemispherical prism was described in some depth in the previous chapter (Chapter 4, Experimental Section).

5.2.2. Self-Assembled Monolayer Preparation

The cleaned gold substrates were incubated in 3 mM octanethiol (OT) ethanolic solutions for 5 hours before being rinsed thoroughly with ethanol. Subsequently, the gold substrates were incubated in ethanolic solutions containing 3 mM 1,9-nonanedithiol (NDT) to afford partial place-exchanged monolayers. After 15 minutes of the place-exchange process, the substrates were rinsed with ethanol and finally rinsed with Milli-Q water before being exposed to an aqueous solution of ~10 mM 1,4-benzoquinone for 18 hours at room temperature. Finally, the

quinone-terminated modified gold substrates were rinsed with copious amounts of Milli-Q water before performing any given experiment.

5.2.3. Electrochemical Measurements

A three-electrode arrangement was used to analyze the electrochemical features of the modified gold substrate SAMs. These measurements were performed in an all-glass sealed cell connected to the external reference electrode (Ag/AgCl, saturated KCl) *via* a salt bridge. The counter electrode was a loop of gold wire flame annealed before every experiment. All the glassware used for an experiment were heated in a mixture of concentrated H_2SO_4 and HNO_3 (2:1 by volume) and then rinsed and soaked overnight in Milli-Q water prior to an experiment. The electrolytes used were de-oxygenated with argon before the introduction of the working electrode and a continual blanket of argon was maintained over the electrolyte for the duration of all electrochemical experiments. Cyclic voltammetric and chronocoulometric measurements were made using a computer controlled system with software written in the LabVIEW (National Instruments Corporation, Austin, TX, USA) environment, consisting of a HEKA Potentiostat PG590 (HEKA, Mahone Bay, NS, Canada) with data collected using a multifunction DAQ card (PCI 6251 M Series, National Instruments Corporation, Austin, TX, USA). The electrochemical techniques used in this Chapter are briefly described below. A more detailed description of these techniques can be found elsewhere.[49]

5.2.3.1. Cyclic Voltammetry

Cyclic voltammetry (CV) involves the measurement of a current (i) as a varying DC electrical potential (E) is applied to an electrode using a potentiostat. The applied electrode

potential ramps linearly, between two set points, as a function of time at a specific scan rate (mV s^{-1}). In a three-electrode electrochemical cell, the potential is applied between the reference electrode and the working electrode and the current is measured between the working and the counter electrode. The measured data is then typically plotted as current (*i*) *versus* potential (*E*).

5.2.3.2. Chronocoulometry

As its name implies, chronocoulometry (CC) is the measurement of charge (Q; coulombs) as a function of time. CC is a controlled-potential technique and uses a potential step waveform. An experiment typically starts at a specific potential, E_{REF}, and held there for a sufficient duration so that the interface reaches an equilibrated state. The potential is then changed "instantaneously" (stepped) to a value, E_{VAR}, that drives an electrochemical process such as the oxidation of a surface bound molecule. During this step to E_{VAR} the current is continuously recorded and then integrated to obtain the charged passed. In a single potential step experiment, the potential step sequence is repeated albeit with a new choice of E_{VAR}. In a double potential step experiment, a second current transient is recorded during a subsequent potential step prior to a return to the base potential, E_{REF}. The data is typically plotted as a function of measured charge (Q) *versus* the applied potential, E_{VAR}.

5.2.4. Improved *In-situ* spectroelectrochemical SEIRAS Cell

As briefly described in the previous chapter (Chapter 4, Experimental) a major challenge in the reliability of the *in-situ* spectroelectrochemical cell was the physical contact to the thin-film gold working electrode deposited on the Si ATR hemisphere. When attempting to make the electrical contact to the thin metallic-film, the loop of Au wire frequently scratched the Au

coated Si hemisphere and electrical contact was lost. In order to improve reliability, the *in-situ* spectroelectrochemical cell was redesigned in such a way to allow three conductive springs to be compressed against the thin-metal film outside the electrolyte solution. Figure 5.1 is a computer model of the improved cell design. The cell was still constructed out of PTFE and aluminum and was designed to be more modular to allow for a variety of different experiments. Once again an O-ring was used to seal the cell against the basal plane of the Si ATR hemisphere prism. The design still allowed for a reference electrode (Ag/AgCl, saturated KCl) to be connected through a glass salt bridge. With several ports built into the lid of the cell, purge gases and access for the coiled Au counter electrode could still be achieved.

5.2.5. *In-situ* Spectroelectrochemical Measurements

All *in-situ* measurements were performed in the spectroelectrochemical cell described above and arranged in the inverted Kretschmann attenuated total internal reflection (ATR) configuration (as described in the Experimental section of Chapter 4). Potential control was maintained using a HEKA PG590 potentiostat and custom software written in LabVIEW. The electrolyte was deaerated by purging with argon for 30 minutes prior to an experiment and a continual blanket of argon was maintained over the electrolyte throughout the duration of an experiment. All ATR-FTIR spectra were measured using p-polarized incident radiation at 60^{o} with respect to the normal of the ATR element. A Nicolet Nexus 870 Fourier Transform Infrared (FTIR) Spectrometer equipped with a mercury cadmium telluride (MCT) liquid nitrogen cooled detector was used to make the IR measurements at a resolution of 4 cm^{-1}. This particular spectrometer is capable of working in rapid-scan mode with an approximate minimum time per interferogram of 77 milliseconds at 4 cm^{-1} resolution. The sample chamber of the spectrometer was purged using

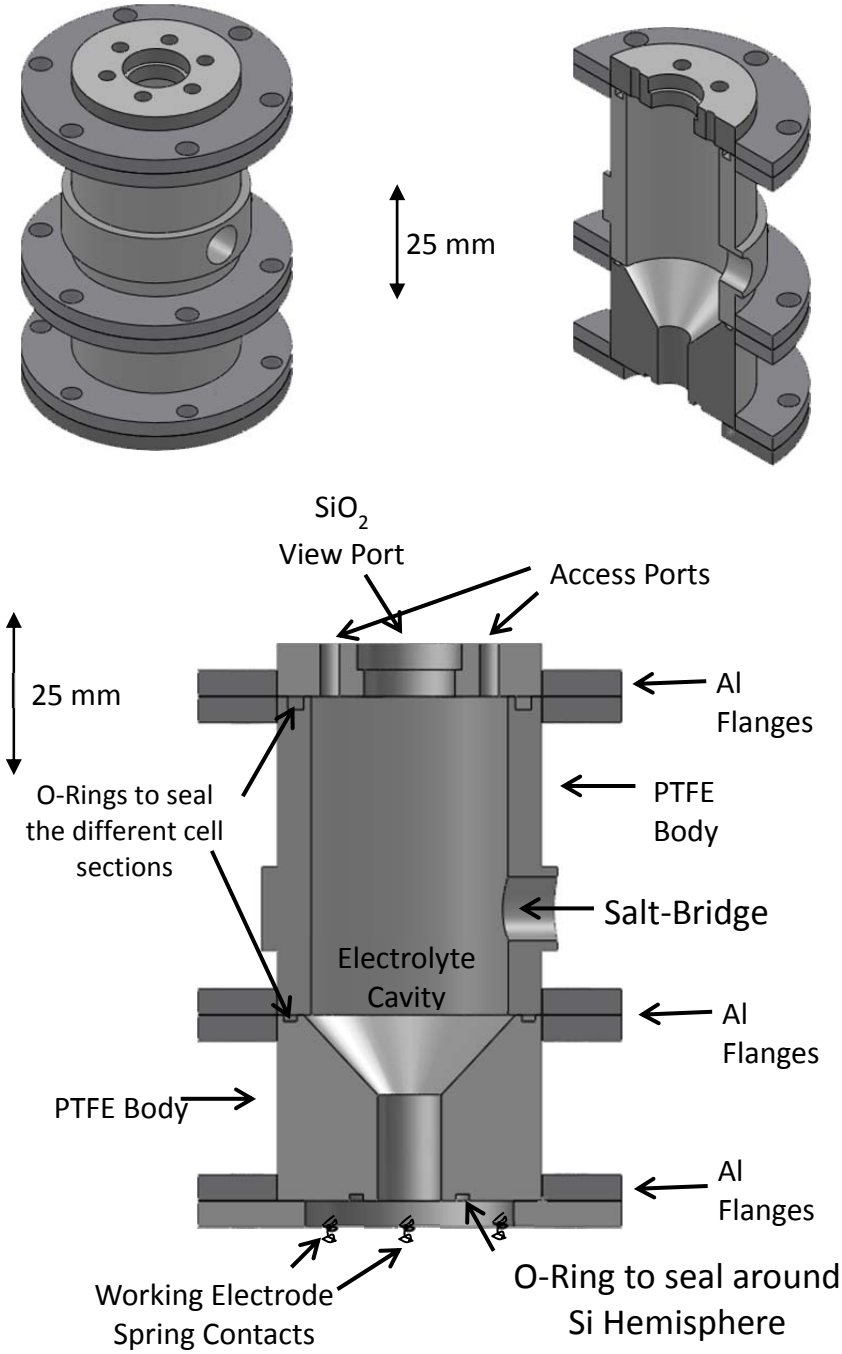

Figure 5.1 Computer Aided Drafting (CAD) drawing of the modified *in-situ* spectroelectrochemical cell used throughout the experiments in this chapter.

CO_2 and H_2O free air supplied by a Parker Balston FT-IR Purge Gas Generator 75-62 (Parker Hannifin Corporation, Haverhill, MA, US).

5.2.6. *In-situ* Spectroelectrochemical Kinetic Measurements

To perform the kinetic SEIRAS experiments, it was necessary to trigger the start of the infrared spectra measurements simultaneously with the change in the working electrode potential upon a step to the formal potential, E^0. To repetitively achieve this, the spectrometer was triggered using the commercially available Nicolet Start-Accessory and custom written LabVIEW software synchronizing the potential step and commencement of infrared data collection. In these kinetic experiments, 8 interferograms were measured at 4 cm^{-1} resolution and binned into 1.3 second intervals with total data acquisition times lasting 120 seconds. In order to build adequate signal-to-noise ratios for these infrared measurements, this process was repeated 128 times providing a total of 1024 co-added spectra for each 1.3 second time interval. It is important to note that as the rate of mirror drive in a Fourier Transform instrument is increased, the signal-to-noise is decreased. As a result, a relatively higher number of scans are required to achieve suitable signal-to-noise from the collected data.

5.3. Results and Discussion

5.3.1. Mixed Monolayers

To prepare a thiol terminated, mixed monolayer system on gold the literature provided several different reported techniques including passive incubations of neat 1,9-nonanedithiol (NDT) solutions in various solvents,[50–52] electrochemical methods (potential assisted deposition),[53–56] and passive place exchange incubations.[57] However, dithiol monolayers formed

through passive incubation and subsequently exposed to BQ were found to exhibit poor electrochemical responses. The weakly discernible and unstable voltammetric signal with very large peak was not desirable for further experimentation. Furthermore, there is a significant decrease in peak current intensity with each potential cycle. This is interpreted as evidence of physisorption of BQ mixed in the aliphatic hydrocarbon matrix of the SAM's alkane backbone rather than the desired chemical attachment of BQ to the ω-functionalized monolayer. The absence of a chemical linkage to the BQ is most likely caused by the propensity of both thiol headgroups of the same NDT molecule to attach to the gold substrate which has been reported elsewhere.[58] There was only minimal improvement observed when deoxygenated organic solvents were used[52] for the passive incubation of NDT monolayers. Another approach was to use a potential assisted deposition method reported by Rifai *et al.*[53,54] which was very successful but proved to be quite cumbersome to implement, especially when working with gold thin films used in the SEIRAS i*n-situ* SEC cell. The final approach, which provided the best results, was to build a mixed mono/dithiol monolayer formed by passive place-exchange method.

Firstly, the gold substrate was incubated in an alkane thiol (octanethiol, OT, 1 mM) for five hours affording a well ordered SAM. This was followed by a short incubation in 1,9-nonanedithiol (NDT, 10 mM). The choice to use OT was made on the basis of the relative lengths of OT and NDT. Assuming a fully extended hydrocarbon region, NDT will be physically longer than OT by the length of a methylene and thiol unit which ensures that the resulting mixed SAM has a readily exposed thiol group, accessible for the addition of the electroactive quinone moiety. This method provided monolayers with the best reactivity towards BQ and as a result was exclusively used for the electrochemical and infrared measurements throughout the remainder of the discussion in this Chapter.

To monitor and analyze the incubation process of the SAMs, SEIRAS measurements were taken before and after the incubation of the NDT to confirm that the place-exchange reaction had taken place. Figure 5.2 is the resulting plot of the normalized difference spectrum (as discussed in Chapter 4), $\Delta S/S = (S_{VAR} - S_{REF})/S_{REF}$ with S_{REF} and S_{VAR} representing the single beam signals for the monolayer before and after the place exchange reaction. Four major infrared absorption bands are present, two upward going bands (2874 and 2972 cm^{-1}) and two downward going bands (2853 and 2922 cm^{-1}). The two upward going bands are associated with the symmetric and asymmetric C-H stretching modes of the CH_3 moiety (of the octanethiol) and the two downward bands are for similar modes in the CH_2 group.[59–61] It is clear that during the place exchange process there is a loss of signal from CH_3 groups and a gain in signal from the CH_2 groups. This expected decrease in the number density of methyl groups at the surface qualitatively confirms the success of the place exchange reaction of OT with NDT as methyl groups are replaced with $–CH_2$-SH moieties. Conversely, the place exchange process leads to a gain in the number of CH_2 groups present at the surface indicating the addition of NDT to the monolayer. One should also expect to see a downward going back associated with the thiol (S-H) functional group but due to the weak absorption cross-section of S-H, such a band was not observed.

With the mixed mono/dithiol SAM grafted to the thin gold films, electroactive quinone functionalization of the free thiol endgroup was achieved through a Michael-like addition with 1,4-benzoquinone. The end product of this reaction should be the reduced form (i.e. dihydrobenzoquinone) of the redox center; however, Budavari *et al.* have shown that the negative shift in the reduction potential for the tethered species results in its oxidation by excess free benzoquinone in the incubating solution.[42,43] Cyclic voltammetric experiments clearly

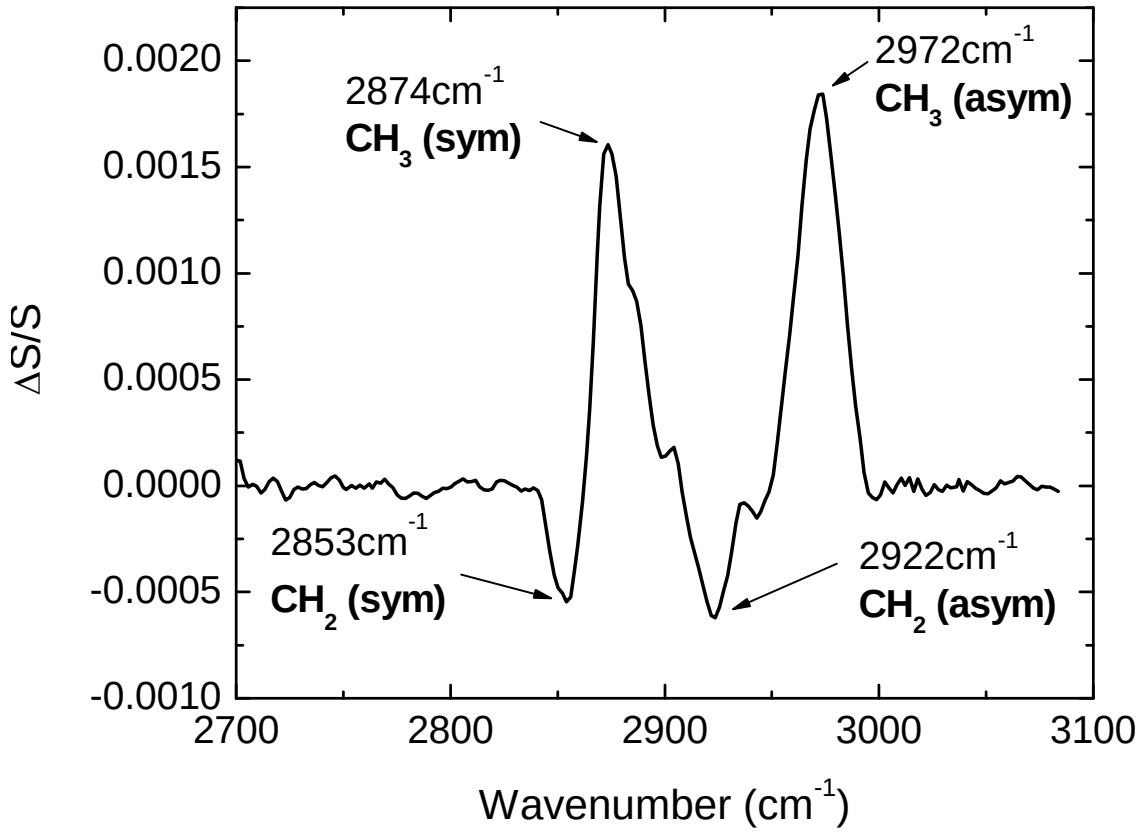

Figure 5.2. Infrared normalized difference spectrum of the CH stretching vibration region demonstrating the changes to the self-assembled monolayer after the place exchange reaction has taken place. The reference spectrum is the octanethiol-SAM before the place exchange reaction.

demonstrated that this system could be readily toggled between its two redox states and that it was amenable for various electrochemical and (*in-situ*) infrared experiments. It was of interest to estimate the initial loading of the quinone electroactive moiety on the mixed monolayer to determine how successful and active the quinone coupling was. A series of independent electrochemical experiments determined the ratios of the charge associated with the reductive desorption of the mixed thiol monolayer (in the absence of quinone) and the charge passed in the quinone redox reaction. These measurements indicated that the ratio was (0.95 ± 0.5):1. Assuming one electron transfer for thiol reduction and two electron transfer for quinone electrochemistry, it is estimated that the initial loading of benzoquinone to be approximately 50%.

5.3.2. Electrochemical Characterization

As previously mentioned, the stability of the amino-quinone SAM was a concern for the expected long duration of the time-resolved infrared experiments but could be greatly alleviated by using thio-quinone linkages. Comparisons of the stability of the two systems were measured through a series of cyclic voltammetric (CV) experiments for both the amino-quinone and thio-quinone SAM modified electrodes. The procedure used for the preparation of the amino-quinone modified electrode was described elsewhere.[44] From the CVs collected for each separately prepared electrode, a ratio of the peak height from a given scan to the first scan is plotted in Figure 5.3 to illustrate the stability of the BQ electrochemical activity. In both cases one can see that there is some loss in the electrochemical response of the quinone moiety during each CV scan cycle; however, this loss is more substantial for the amino-quinone system. After nearly one hour of continuous potential scanning, the loss of signal from the thio-quinone based system

was only 5% compared to the nearly 33% attenuation observed in the amino-quinone system. This loss of electrochemical activity is speculated to arise from the hydrolysis of the C-N bond linkage. As a further point of comparison, the amino-quinone system was found to be completely unstable at pH > 9. This finding suggests that the C-S bond in the thio-quinone SAM has a greater degree of resistance to the hydrolysis of the linkage bond compared to that of the C-N bond in the amino-quinone SAM.

After successfully devising a method to reproducibly build electroactive BQ modified SAMs on gold substrates, the system was characterized through a variety of electrochemical techniques to elicit information about the kinetics of the PCET process. To start, CVs of the system in 5 mM phosphate buffers of various pH were measured. To ensure common ionic strength of all the electrolyte solutions used, these phosphate buffered solutions were prepared using an excess of $NaClO_4$ (100 mM). Figure 5.4 depicts typical CVs of three separately prepared electrodes in the different pH ionic strength balanced electrolytes. The CVs in all cases were background corrected by removing capacitive currents measured due to the charging of the double layer. From the CVs in Figure 5.4, one will notice a shift in peak position as a function of pH which is well-known for electrochemical systems that involve proton-coupled electron transfer.

The kinetics of this BQ-SAM system were prepared to be extremely slow by adjusting the separation between the redox moiety and the electrode surface.[1–6] An effect of this is that it makes it very difficult to ensure equilibrium is reached on the time scale of the potential sweep in a CV measurement, even at slow scan rates. As an alternative to ultraslow potential scanning, chronocoulometric techniques were employed with the following potential step sequence. The working electrode was initially biased at a rest potential, E_{REF}, ~200 mV negative of the formal

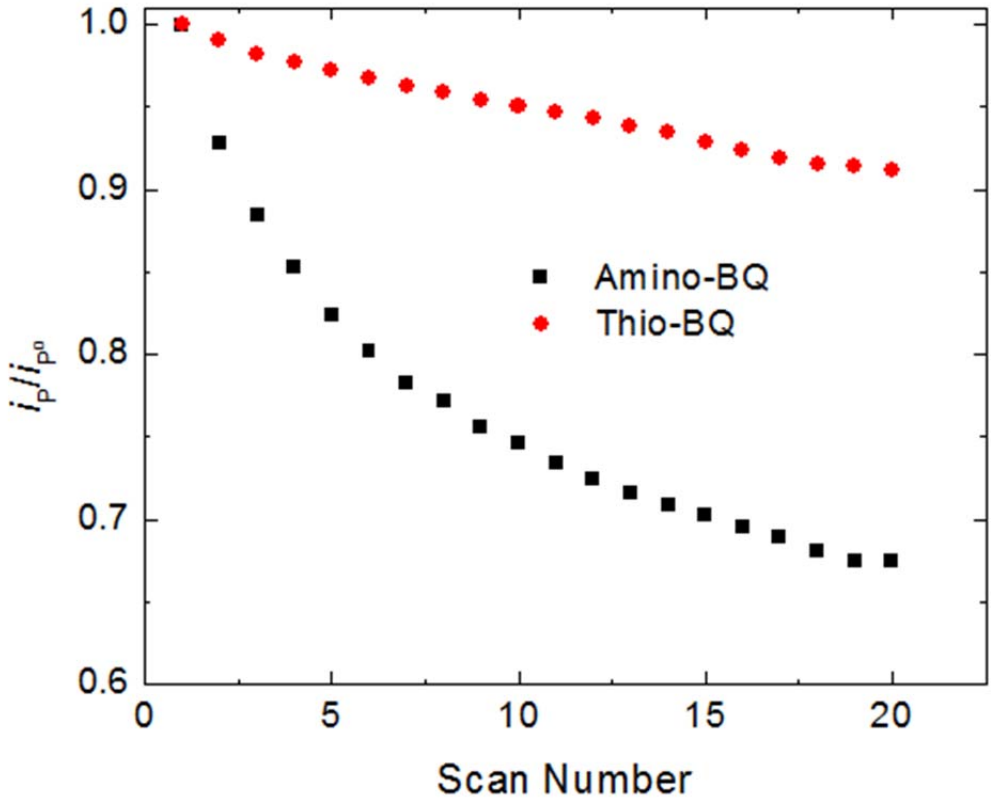

Figure 5.3. Relative stability of the electrochemical anodic peak measured in cyclic voltammetric experiments at 10 mV s^{-1} for an amino-quinone and thio-quinone self-assembled monolayer systems. The electrolyte was the same for both (5 mM NaPBS, pH 5, 100 mM $NaClO_4$) with the potential scanning between ± 500 mV from the formal potential, $E^{0'}$.

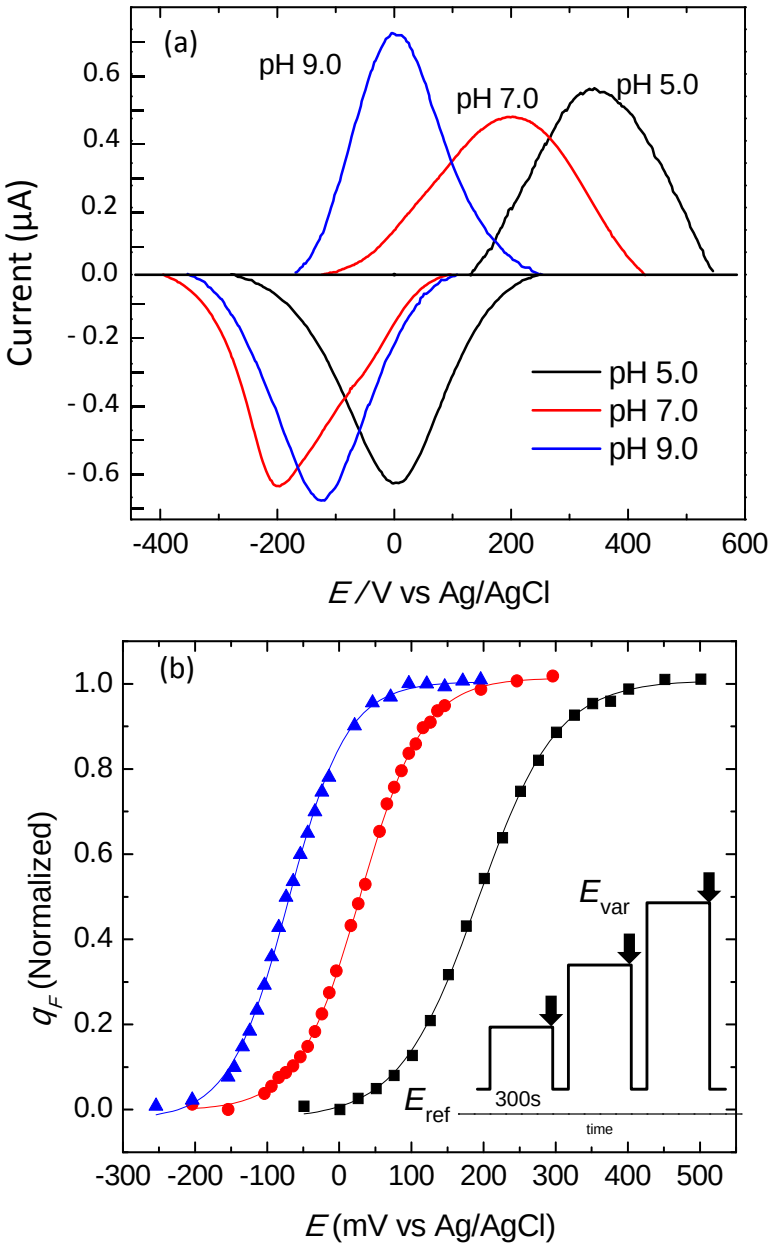

Figure 5.4. (a) Cyclic voltammograms (CV) of the benzoquinone self-assembled monolayer (BQ-SAM) system in 5 mM NaPBS, 100 mM $NaClO_4$ buffered electrolyte solutions at a scan rate of 10 mV s^{-1}. The CVs have been normalized by peak area. (b) Normalized Faradaic charges of BQ-SAM in the same electrolytes described in (a). The inset in (b) is the potential step-sequence. The downward arrows indicate the transient measured edges.

potential (roughly determined by CV), $E^{0'}$, for 5 seconds to ensure all BQ moieties were in their fully reduced redox state. The potential was then stepped to a variable potential, E_{VAR}, and held for 300 seconds, well beyond the time required for the system to reach equilibrium. After this set time, the potential was immediately stepped back to E_{REF} and the current transient was measured and numerically integrated to provide the difference in the total charge, ΔQ, between E_{REF} and E_{VAR}. This potential step sequence was repeated using increasingly positive values of E_{VAR} over a few hundred millivolt potential range. From these measurements of ΔQ, the background charge, associated with any capacitive processes, was subtracted leaving only the Faradaic charge, q_F, associated with the BQ moiety's redox activity. A detailed description of the background correction procedure is described elsewhere.[44] Similar to the CV results, one can see from Figure 5.4 that there is the expected analogous shift in the formal potential to more positive values with decreasing pH (-60 mV pH^{-1}). This dependence on pH with the formal potential was theoretically treated by both Laviron[31] and Finklea[41] for a two electron two proton electrochemical reaction and is in excellent agreement with these experimental results. The chronocoulometry measurements allow a more accurate means to determine the apparent formal potential by fitting a sigmoidal function to the data and numerically differentiating the resulting curve to provide the apparent formal potential.

Figure 5.5 plots the formal potential, $E^{0'}$, as a function of electrolyte pH for BQ modified SAMs in phosphate buffered electrolyte. The data presented in this plot is a compilation of two different electrochemical techniques and one *in-situ* spectroelectrochemical technique (to be discussed later) and are averages of 3-5 replicates per point. As demonstrated in this plot, a best fit line through the data points has a slope of -63 mV pH^{-1} in the pH range 1-10. The results are

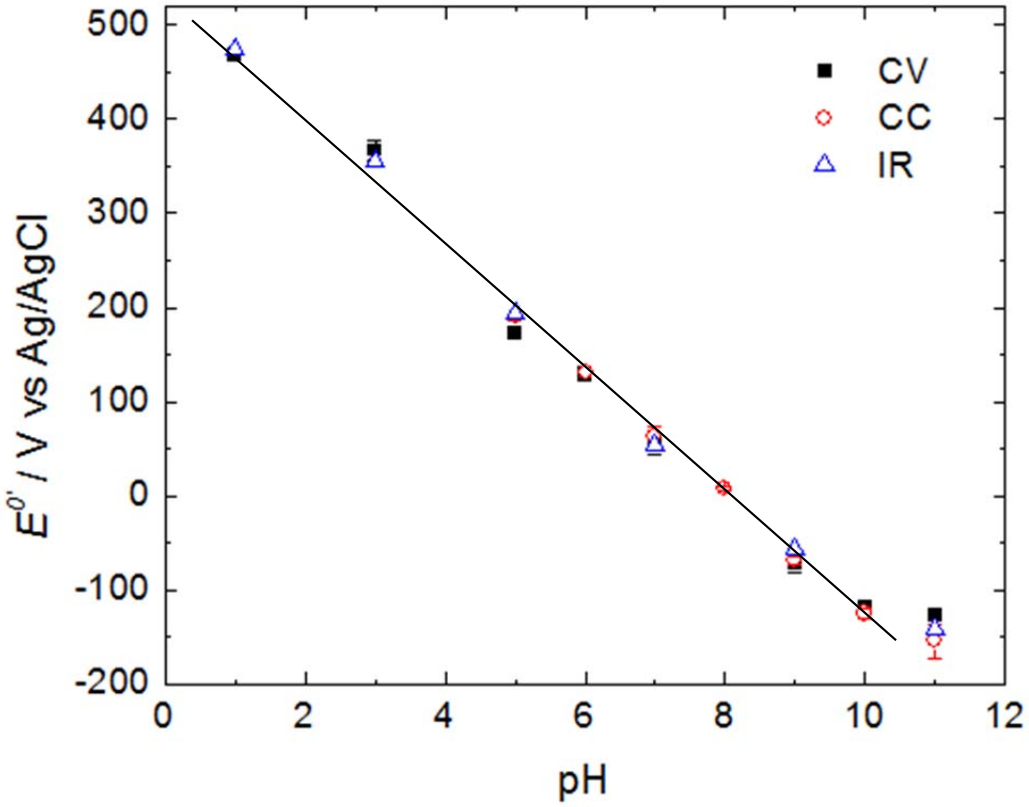

Figure 5.5. The formal potential, $E^{0'}$, of the benzoquinone self-assembled monolayer (BQ-SAM) system measured in 5 mM NaPBS, 100 mM $NaClO_4$ variable pH electrolytes using different techniques. Cyclic voltammetry values were determined from measurements made at a scan rate of 10 mV s^{-1}. Chronocoulometry (CC) values were determined from numerical differentiation of the baseline corrected charge data. Infrared (IR) values from integrated peak areas of the carbonyl vibrational band (1660 cm^{-1}).

comparable to within 5% error between the three different experimental techniques used to determine the formal potential (CV, CC and *in-situ* SEIRAS SEC). For completeness it is noted that there is the presence of an inflection point in the data at pH ≥ 10. This change in slope is predicted by Laviron[32] to be due to a difference in the number of protons transferred during the PCET step for quinone based electrochemical systems.

One will notice from Figure 5.5 that there are no data points for the chronocoulometry results below pH 5. As the pH of the electrolyte solution is decreased, the formal potential shifts to more positive potentials. Eventually, the potential shifts to a point where the interferences due to background currents become substantially more difficult to accurately remove. This was also true, but to a lesser extent, for the CVs measured at these pHs causing the results to be slightly less reliable. The measured shift in formal potential can be explained using Laviron's theory of coupled proton electron-transfer,[31] which was later modified by Finklea for monolayer systems.[41] The slope calculated from the data points in Figure 5.5 are consistent with the expected shift in the formal potential (-60 mV pH^{-1}). An important note is that the infrared measurements are not hindered by these limitations and provide an alternate approach to calculate the formal potential of this system.

5.3.3. *In-situ* Spectroelectrochemical Results

Two fundamentally different *in-situ* spectroelectrochemical experiments were used to examine the thermodynamic and kinetic aspects of the prepared BQ modified SAMs. As previously mentioned, *in-situ* SEC measurements were made to determine the formal potential of the BQ-SAM as a function of pH. This was accomplished by using a set of normalized difference spectra calculated for the BQ modified SAM with a constant reference potential and

varying a series of stepped potentials. The chosen value for the reference potential was several hundred millivolts negative of the estimated formal potential (approximated from the CV data) to ensure only the reduced form of the BQ moiety existed on the electrode surface. After the application of the potential step, a delay of appropriate duration (300 seconds, *i.e.* the same value used in the CC measurements) was implemented before collection of the infrared spectra to ensure the interface was equilibrated. Representative data showing the ΔS/S measured difference spectra for pH 3 are shown in Figure 5.6. It is known that when BQ undergoes a PCET reaction that the molecular structure of the electrochemically active moiety changes in accordance with Scheme 5.1. Upon the oxidation of 1,4-dihydroxybenzoquinone to 1,4-benzoquinone there is a loss of two hydroxyl (OH) groups which are transformed into two carbonyl (C=O) functional groups. The carbonyl vibrational stretch provides an intense (sharp and strong) signal in the infrared at ~1660 cm^{-1} and provides an excellent molecular marker for the redox state of the quinone moiety. One can see from Figure 5.6 that the carbonyl stretch progressively increases in intensity (*i.e.* becomes a more pronounced negative going peak) with increasing positive potential. An important note (as previously discussed in Chapter 4) is that this region of the infrared spectrum is usually complicated by the presence of a strong water absorption band due to an H-O-H deformation mode at 1640 cm^{-1}. To verify that the observed intense infrared signal in Figure 5.6 was in fact due to the carbonyl and not due to water, a similar experiment was repeated in a D_2O based electrolyte. From this experiment, the infrared band at 1660 cm^{-1} did not show a large shift in wavenumber that would be expected if the peak was associated with a change from H_2O to D_2O solvents. Parallel to the changes in the carbonyl signal, a decrease in the benzene ring breathing stretch and single bond C-O stretch are expected upon oxidation of the redox center. These spectral features should appear as upward going bands

at approximately 1450 cm^{-1} and 1200 cm^{-1}, respectively.[26] While the latter is below the cut-off frequency for the Si ATR element and as a result not measurable, inspection of Figure 5.6 shows that only at the most positive potentials is there a very weak upward signal at ~1460 cm^{-1}. It is possible that the lack of a pronounced signal be attributed to the loss of the HBQ arises from changes in the molecular orientation upon oxidation of the redox center. If the reduced HBQ is aligned in such a way that the principle C_2 molecular axis of the quinone moiety is roughly parallel to the reflecting plane, then surface selection rules render both the benzene ring stretch and the C-O stretching infrared modes inactive. Correspondingly, no apparent loss of these associated infrared signals will be measured upon oxidation. In contrast, the strong signals arising from the carbonyl stretches indicate that the BQ must have an orientation perpendicular to the gold surface. The weak change observed in Figure 5.6 for the CH stretching region (2850 cm^{-1} to 3000 cm^{-1}) provides additional evidence that there is a potential dependent distortion of the hydrocarbons which would be consistent with molecular rearrangement within the SAM upon oxidation.

The intensity of the carbonyl infrared band increases with potential until reaching a plateau. To quantify this result, the integrated infrared band associated with this stretch is plotted as a function of potential for a variety of pHs in Figure 5.6. From this Figure, the data points for a given pH were fit to a sigmoidal function and the formal potential, $E^{0'}$, was determined from the inflection point. As the potential is stepped through the formal potential, there is a rapid change in the C=O stretching region similar in shape to the calculated charge from the chronocoulometry experiment. Between pH 1-11 there is some variation in the width of the sigmoidal curves (Figure 5.6b) which is attributed to the different extents of heterogeneity from monolayer to monolayer.

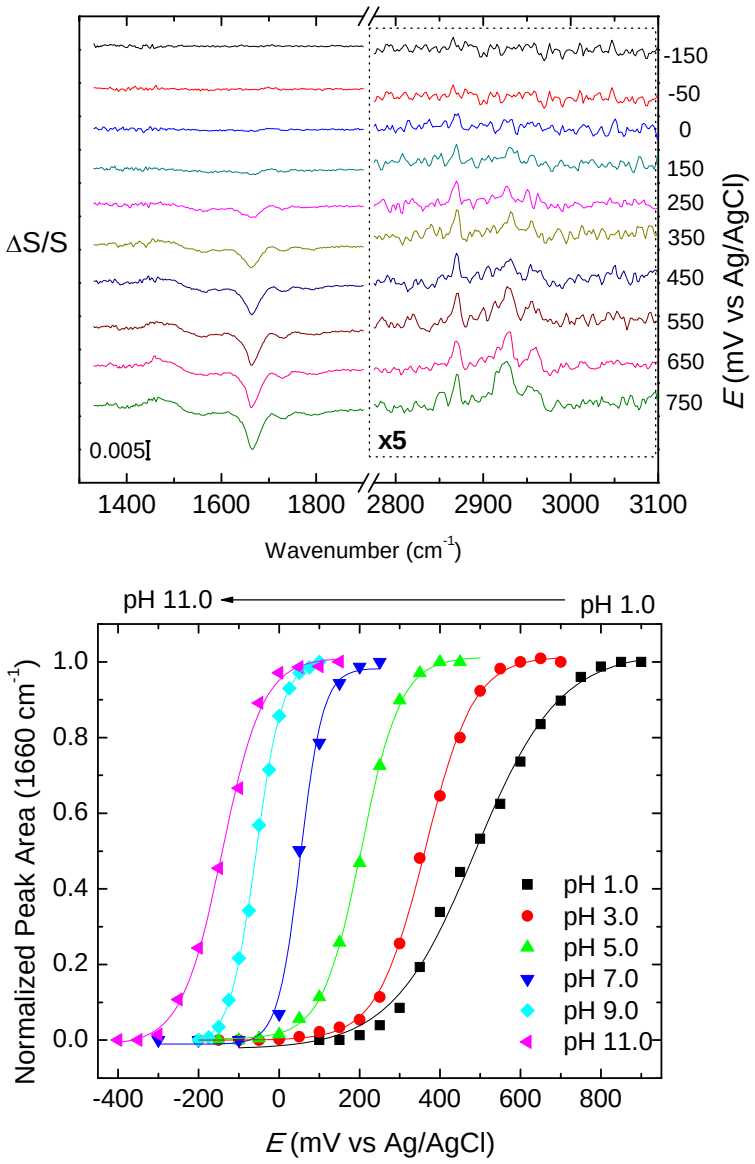

Figure 5.6. (a) Infrared normalized difference spectral data for the benzoquinone self-assembled monolayer (BQ-SAM) system in 5 mM NaPBS (pH 3), 100 mM $NaClO_4$ supporting electrolyte. The reference potential, E_{REF}, was -250 mV *vs* Ag/AgCl and each spectra is comprised of the co-addition of 1024 scans. (b) Normalized carbonyl (C=O) vibrational peak areas associated with the BQ-SAM at different pH values and potentials. Electrolytes were prepared at different pHs using 5 mM NaPBS and 100 mM $NaClO_4$.

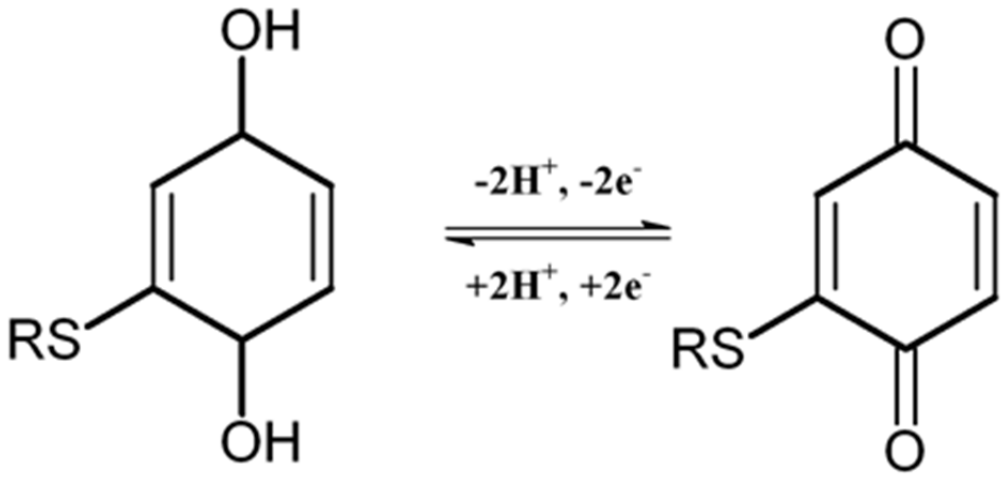

Scheme 5.1. Changes in molecular structure of 1,4-benzoquinone under proton coupled electron transfer (PCET) reactions.

However, one should notice that the data for pH 1 has an appreciably larger width indicating that at very low pH, longer wait times are required to ensure that the system is measured at equilibrium conditions as the system is much slower. As will be discussed in the next section, this is consistent with the decrease in the standard rate constant with decreasing pH.

5.3.4. Proton Couple Electron Transfer Kinetics

The debate on the charge transfer mechanism for proton-coupled electron transfer electrochemical reactions has been active over the last few decades and includes step-wise[13,30–35,62] and concerted mechanisms.[36–39] A means to measure and assess aspects of Nernstian like systems (that follow the Nernst equation) is to look at the full-width half maximum (FWHM) of a redox peak measured by CV. For instance, for a two electron Nernstian system, it is expected that the measured FWHM should be 45 mV.[63] However, in the case of these prepared BQ-SAMs, the FWHM of the redox peaks was typically measured to be ~100-150 mV. A plausible explanation for this is that there are a multitude of local environments (microenvironments) surrounding each quinone moiety, each having various Frumkin interactions. These microenvironments are a likely result of the place exchange process involving the dithiol molecules and their tendency to form island domains in alkane SAMs.[57] These dithiol domains allow for an increase in the interactions between neighbouring redox-centers and could possibly result in double-tethering of the quinone centers to the monolayer.[42,43] The net result is a breadth of kinetic behaviour as previously demonstrated by electrochemical measurements.

Given that these BQ terminated SAMs do not behave in an ideally Nernstian manner, obtaining details of the PCET mechanism becomes rather complicated. Details, however, on the pH dependence of the apparent rate constant, $k_{s,app}$, for this reaction will be determined through

several electrochemical methods and highlight collaborating evidence acquired with *in-situ* spectroelectrochemical techniques. The apparent rate constant can be determined, as shown by Laviron, by studying the redox peak separation at varying scan rates.[62] This technique has seen extensive use in the literature as a means to measure $k_{s,app}$. This method necessarily assumes that the transfer coefficient for the process is potential independent which Finklea has argued is not the case for PCET occurring in monolayer systems.[41]

To minimize and prevent errors three different experimental techniques were employed based on: cyclic voltammery (CV), chronocoulometry and finally by *in-situ* spectroelectrochemistry. All three methods will measure the apparent standard rate constant of this BQ-SAM system on measurements at or very near the formal potential, $E^{0'}$. The first method used to obtain the rate kinetics was developed by Finklea *et al.* based on data obtained from CV measurements.[13,64] Briefly, the Faradiac current, i_F, is isolated from the double-layer charging currents by subtracting the non-Faradiac currents from the measured CVs. The charge is then found by integrating these background corrected CVs. At the apparent formal potential, the apparent standard rate constant can now be calculated using the following equation,

$$k_{s,app} = \frac{i_F}{q_{F,total}(1 - 2\chi_{\eta=0})} \qquad (5.1)$$

where $\chi_{\eta=0}$ is the fraction of BQ moieties reduced or oxidized in the cathodic or anodic sweep to the formal potential. For each CV the above equation was then used to calculate, $k_{s,app}$ for both the forward and reverse potential scans with the average value reported herein.

To study the kinetics using chronocoulometric methods, the double-step experiment described previously was modified as follows. A potential, E_{REF}, ~200 mV more negative than the formal potential was first applied to the working electrode to afford a fully reduced monolayer of BQ moieties. The potential was then stepped to the formal potential, $E^{0'}$, and held

for a variable amount of time, t_{VAR}. At this point, the potential was then stepped back to E_{REF} and the current transient measured. Once this measurement was completed, another set of potential steps were applied to the system in order to provide a means to correct for the slow loss of quinone as the experiment proceeded. This was accomplished by stepping the potential 200 mV more positive than the formal potential to now fully oxidize the BQ moieties. Finally upon stepping the potential back to E_{REF} the current transient is once again measured. This process is repeated numerous times with changes to t_{VAR} to longer times up towards a final time of 300 seconds. The collected transient data is first corrected by subtracting the charge associated with background process and then normalized by using the charge obtained when stepping from the formal potential to the fully oxidized BQ moieties. These results are then plotted (Figure 5.7) as a function of time. This data can then be fit to an exponential function to extract the average apparent standard rate constant of the redox centers. Again, due to the multitude of microenvironments surrounding each electroactive center only the average heterogeneous rate constant can be calculated.

Finally, an alternative approach to using purely electrochemical techniques to measure the heterogeneous rate constant is to use an *in-situ* time-resolved infrared spectroscopic method. Here, the infrared data was collected during a potential step from a reference potential to the apparent formal potential, as described in more detail in the experimental section of this Chapter. From this data, the infrared peak intensity at 1660 cm^{-1} is numerically integrated, normalized and plotted with respect to time (Figure 5.7). Exponential fitting of this data can then be used to measure the rate of formation of BQ. A comparison of kinetic data obtained with chronocoulometric and IR measurements is shown in Figure 5.7. There is some discrepancy between the chronocoulometric and *in-situ* SEC data. This difference is attributed to the slow

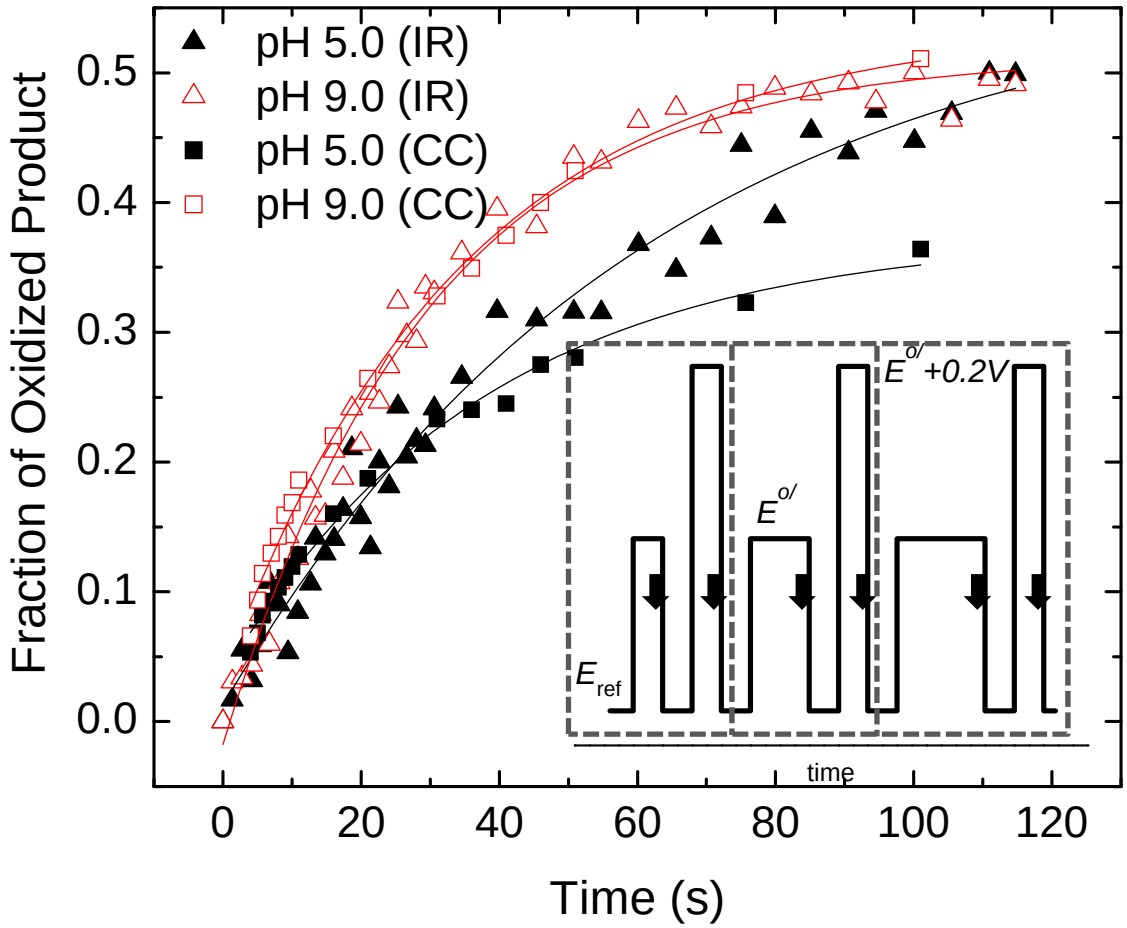

Figure 5.7. Comparison between a purely electrochemical technique, double-step chronocoulometry, and *in-situ* spectroelectrochemistry for the determination of the heterogeneous rate constant, $k_{s,app}$. Electrolytes of the two pH values were prepared from 5 mM NaPBS and 100 mM $NaClO_4$. Inset depicts the potential step-sequence used to make the chronocoulometric measurements. Downward arrows indicate the potential step edges where the transient data was measured.

loss of the quinone signal over the long experiment times required to make the time-resolved infrared measurement; whereas, the modified double-step chronocoulometric potential sequence provides a way to account for the slow loss of quinone from the monolayer. To qualitatively verify this, independent electrochemical experiments were measured using CVs before and after subjecting the electrode to the exact same conditions implemented with the infrared measurements. Through this, it was determined that roughly 15-20% of the quinone is lost over the time period required to make the infrared measurements which will perturb the signal transients such as those shown in Figure 5.7. In general, the evolution of the spectroscopic signal closely resembles that of the charge-based signal but is perturbed by a systematic error due to slow losses in the amount of surface quinone.

The heterogeneous rate constants obtained for each of the three methods, as a function of pH, have been superimposed for comparison in Figure 5.8. One will notice that above pH > 5 the agreement between the three techniques is very good but at low pH there is more scatter between the various techniques. It becomes increasingly more difficult to accurately subtract the background signal for both the CV and chronocoulometry methods at low pH as the redox potentials of the quinone moiety begin overlapping with non-analytical signals most likely due to the onset of the oxidation of the Au-thiol bond. This is particularly problematic in the CV method where the slow electron transfer kinetics mandate that relatively large overpotentials are applied to the electrode for long periods of time to observe the quinone electrochemistry at the scan rates required (≥ 1 mV s^{-1}). Accounting for the background currents is further compromised by the asymmetry of the apparent transfer coefficient. This result is demonstrated by significantly broadening and poorer defined anodic peaks compared to that of the cathodic peak; this increases the error in the rate constant as determined by the method described by

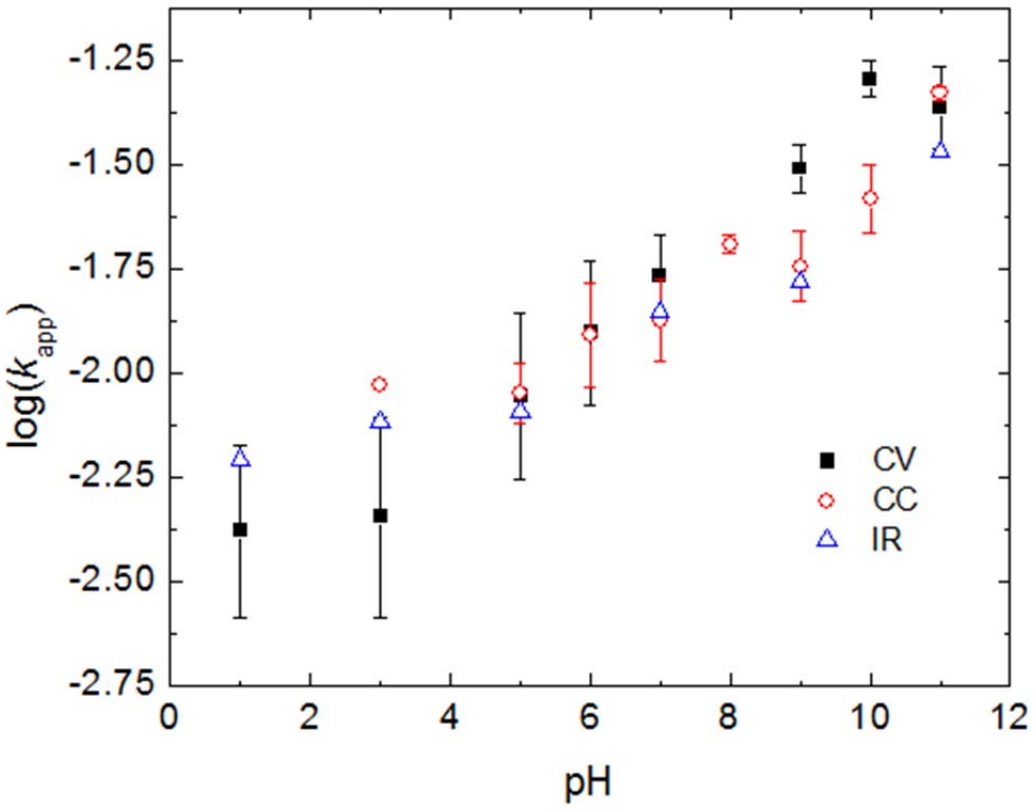

Figure 5.8. Plot of the heterogeneous rate constant, $k_{,s,app}$, determined by the three different measurement techniques (two purely electrochemical and one using *in-situ* spectroelectrochemistry). The values were determined for a series of different pH electrolytes made from 5 mM NaPBS and 100 mM $NaClO_4$ for the benzoquinone self-assembled monolayer (BQ-SAM) system.

Finklea *et al.* and becomes quite noticeable at low pHs. The infrared technique is not affected by this limitation and the apparent rate constant for the PCET process can be measured with equal degree of accuracy over the entire pH range. In general, the heterogeneous rate constants measured using solely electrochemical techniques closely resemble those calculated spectroscopically. This result indicates that this *in-situ* molecular spectroscopic technique is as accurate as the electrochemical measurements in determining $k_{s,app}$. Figure 5.8 also demonstrates that the rate constant appears to have an overall linear dependence on pH. This strongly deviates from the expected theory for a two-electron, two-proton step-wise PCET which predicts that the shape of Figure 5.8 should be more consistent with a "W shaped" plot.[13,44,64] The apparent linear trend reported may result from the large heterogeneity subsequent from the construction of the thiobenzoquinone monolayers which also accounts for the greater distributions (large error bars) in the measured values reported in Figure 5.8.

5.4. Summary and Conclusions

This Chapter outlined a place-exchange method to afford a mixed monolayer which includes dithiol molecules covalently attached to gold surfaces through only one thiol end group. It has been shown that these monolayers can be further modified chemically, and made electroactive, in aqueous solution at room temperature by the Michael addition of 1,4-benzoquinone. With this chemically modified electrode, the thermodynamics and kinetics of the quinone redox moiety using electrochemical and *in-situ* spectroelectrochemical techniques has been analyzed. Briefly, the formal potential and the heterogeneous rate constant have been measured using electrochemical and spectroscopic techniques over a wide range of pHs and are in good agreement. The formal potential is found to shift to more positive potentials with

increasing electrolyte acidity at a rate of ~60 mV pH^{-1} which is expected for a two-proton two electron system. However, what was not predicted by either step-wise or concerted PCET models was how the logarithm of the apparent standard rate constant decreased linearly with pH. It is speculated that more subtle changes in the rate constant dependence are most likely obscured by the kinetic heterogeneity of the system.

Finally, this Chapter highlights the successes of measuring the *in-situ* spectroelectrochemical pH dependences of benzoquinone terminated self-assembled monolayers that undergo proton-coupled electron-transfer electrochemical reactions. However, this electrochemical system was tailored in such a way as to provide kinetics sufficiently slow enough to be observed with rapid-scan SEIRAS. In order to measure faster electrochemical systems a smaller working electrode is required to decrease the cell time constant associated with a potential step. However, decreasing the size of the working electrode would also decrease the infrared photon throughput. With fewer infrared photons probing an electrode with a fewer number of electrochemically active molecules, the diminishing loss of sensitivity in the spectroscopic measurements limits the feasibility of moving towards faster electrochemical systems measured with faster infrared spectroscopic techniques. This paradox is the foundation for the remainder of this thesis and illustrates the primary motivation and largest contributions made in advancing *in-situ* infrared SEC techniques.

In attempt to study much faster electrochemical systems, the next Chapter deals with a change in methodology from using internal infrared reflection and SEIRAS techniques towards external infrared reflection spectromicroscopy techniques utilizing synchrotron infrared radiation. The value of internal infrared reflection and SEIRAS techniques should not be

understated as plenty of electrochemical systems and problems can be solved using *in-situ* SEC SEIRAS and rapid-scan techniques.

5.5. References

1. Finklea, H. O. Electroanalytical Chemistry. *Electroanalytical Chemistry* **1996**.

2. Chidsey, C. E. D.; Bertozzi, C. R.; Putvinski, T. M.; Mujsce, A. M. Coadsorption of Ferrocene-terminated and Unsubstituted Alkanethiols on Gold: Electroactive Self-assembled Monolayers. *Journal of the American Chemical Society* **1990**, *112*, 4301–4306.

3. Finklea, H. O.; Hanshew, D. D. Electron-transfer Kinetics in Organized Thiol Monolayers with Attached Pentaammine(pyridine)ruthenium Redox Centers. *Journal of the American Chemical Society* **1992**, *114*, 3173–3181.

4. Forster, R. J.; Faulkner, L. R. Electrochemistry of Spontaneously Adsorbed Monolayers. Equilibrium Properties and Fundamental Electron Transfer Characteristics. *Journal of the American Chemical Society* **1994**, *116*, 5444–5452.

5. Katz, E.; Itzhak, N.; Willner, I. Electron Transfer in Self-assembled Monolayers of N-methyl-N′-carboxyalkyl-4,4′-bipyridinium Linked to Gold Electrodes. *Langmuir* **1993**, *9*, 1392–1396.

6. Long, Y.-T.; Abu-Irhayem, E.; Kraatz, H.-B. Peptide Electron Transfer: More Questions Than Answers. *Chemistry - A European Journal* **2005**, *11*, 5186–5194.

7. Smalley, J. F.; Sachs, S. B.; Chidsey, C. E. D.; Dudek, S. P.; Sikes, H. D.; Creager, S. E.; Yu, C. J.; Feldberg, S. W.; Newton, M. D. Interfacial Electron-transfer Kinetics of Ferrocene through Oligophenyleneethynylene Bridges Attached to Gold Electrodes as Constituents of Self-assembled Monolayers: Observation of a Nonmonotonic Distance Dependence. *Journal of the American Chemical Society* **2004**, *126*, 14620–14630.

8. Trammell, S. A.; Lowy, D. A.; Seferos, D. S.; Moore, M.; Bazan, G. C.; Lebedev, N. Heterogeneous Electron Transfer of Quinone-hydroquinone in Alkaline Solutions at Gold Electrode Surfaces: Comparison of Saturated and Unsaturated Bridges. *Journal of Electroanalytical Chemistry* **2007**, *606*, 33–38.

9. Trammell, S. A.; Moore, M.; Lowy, D.; Lebedev, N. Surface Reactivity of the Quinone/hydroquinone Redox Center Tethered to Gold: Comparison of Delocalized and Saturated Bridges. *Journal of the American Chemical Society* **2008**, *130*, 5579–5585.

10. Trammell, S. A.; Moore, M.; Schull, T. L.; Lebedev, N. Synthesis and Electrochemistry of Self-assembled Monolayers Containing Quinone Derivatives with Varying Electronic Conjugation. *Journal of Electroanalytical Chemistry* **2009**, *628*, 125–133.

11. Trammell, S. A.; Seferos, D. S.; Moore, M.; Lowy, D. A.; Bazan, G. C.; Kushmerick, J. G.; Lebedev, N. Rapid Proton-coupled Electron-transfer of Hydroquinone through Phenylenevinylene Bridges. *Langmuir* **2007**, *23*, 942–948.

12. Sikes, H. D.; Smalley, J. F.; Dudek, S. P.; Cook, A. R.; Newton, M. D.; Chidsey, C. E. D.; Feldberg, S. W. Rapid Electron Tunneling through Oligophenylenevinylene Bridges. *Science* **2001**, *291*, 1519–1523.

13. Finklea, H. O.; Haddox, R. M. Coupled Electron/proton Transfer of Galvinol Attached to SAMS on Gold Electrodes. *Physical Chemistry Chemical Physics* **2001**, *3*, 3431–3436.

14. Chidsey, C. E. D. Free Energy and Temperature Dependence of Electron Transfer at the Metal-electrolyte Interface. *Science* **1991**, *251*, 919–922.

15. Abhayawardhana, A. D.; Sutherland, T. C. Heterogeneous Proton-coupled Electron Transfer of an Aminoanthraquinone Self-assembled Monolayer. *Journal of Physical Chemistry C* **2009**, *113*, 4915–4924.

16. Bulovas, A.; Dirvianskyte, N.; Talaikyte, Z.; Niaura, G.; Valentukonyte, S.; Butkus, E.; Razumas, V. Electrochemical and Structural Properties of Self-assembled Monolayers of 2-methyl-3-(ω-mercaptoalkyl)-1,4-naphthoquinones on Gold. *Journal of Electroanalytical Chemistry* **2006**, *591*, 175–188.

17. Hong, H.-G.; Park, W. Electrochemical Characteristics of Hydroquinone-terminated Self-assembled Monolayers on Gold. *Langmuir* **2001**, *17*, 2485–2492.

18. Hong, H.-G.; Park, W.; Yu, E. Voltammetric Determination of Electron Transfer Kinetic Parameters in Hydroquinone-terminated Self-assembled Monolayers on Gold. *Journal of Electroanalytical Chemistry* **1999**, *476*, 177–181.

19. Larsen, A. G.; Gothelf, K. V Electrochemical Properties of Mixed Self-assembled Monolayers on Gold Electrodes Containing Mercaptooctylhydroquinone and Alkylthiols. *Langmuir* **2005**, *21*, 1015–1021.

20. Lukkari, J.; Kleemola, K.; Meretoja, M.; Kankare, J. Polyaminoquinone Self-assembled Films on Electrodes: Synthesis of All-organic Molecular Wires by Solution Phase Epitaxy. *Chemical Communications* **1997**, 1099–1100.

21. March, G.; Reisberg, S.; Piro, B.; Pham, M.-C.; Delamar, M.; Noel, V.; Odenthal, K.; Hibbert, D. B.; Gooding, J. J. Electrochemical Kinetic Analysis of a 1,4-hydroxynaphthoquinone Self-assembled Monolayer. *Journal of Electroanalytical Chemistry* **2008**, *622*, 37–43.

22. Nagata, M.; Kondo, M.; Suemori, Y.; Ochiai, T.; Dewa, T.; Ohtsuka, T.; Nango, M. Electron Transfer of Quinone Self-assembled Monolayers on a Gold Electrode. *Colloids and Surfaces B: Biointerfaces* **2008**, *64*, 16–21.

23. Park, W.; Ahmed, J.; Kim, S. Heterogeneous Electron-transfer Kinetics for PQQ Covalently Attached to Aminoalkanethiol Monolayers on Gold. *Colloids and Surfaces B: Biointerfaces* **2009**, *68*, 120–124.

24. Sarkar, S.; Sampath, S. Stepwise Assembly of Acceptor-sigma Spacer-donor Monolayers: Preparation and Electrochemical Characterization. *Langmuir* **2006**, *22*, 3388–3395.

25. Sato, Y.; Fujita, M.; Mizutani, F.; Uosaki, K. Electrochemical Properties of the 2-mercaptohydroquinone Monolayer on a Gold Electrode. Effect of Solution pH, Adsorption Time and Concentration of the Modifying Solution. *Journal of Electroanalytical Chemistry* **1996**, *409*, 145–154.

26. Ye, S.; Yashiro, A.; Sato, Y.; Uosaki, K. Electrochemical in Situ FT-IRRAS Studies of a Self-assembled Monolayer of 2-(11-mercaptoundecyl)hydroquinone. *Journal of the Chemical Society - Faraday Transactions* **1996**, *92*, 3813–3821.

27. Zhang, L.; Lu, T.; Gokel, G. W.; Kaifer, A. E. Mixed Monolayers Formed by the Self-assembly on Gold of Thiol-functionalized Anthraquinones and 1-alkanethiols. *Langmuir* **1993**, *9*, 786–791.

28. Gunner, M. R.; Madeo, J.; Zhu, Z. Modification of Quinone Electrochemistry by the Proteins in the Biological Electron Transfer Chains: Examples from Photosynthetic Reaction Centers. *Journal of Bioenergetics and Biomembranes* **2008**, *40*, 509–519.

29. Goor, G.; Glenneberg, J.; Jacobi, S. Hydrogen Peroxide. In *Ullmann's Encyclopedia of Industrial Chemistry*; Wiley-VCH Verlag GmbH & Co. KGaA, 2000.

30. Laviron, E. Electrochemical Reactions with Protonations at Equilibrium. Part II. The 1e, 1 H+ Reaction (four-member Square Scheme) for a Heterogeneous Reaction. *Journal of Electroanalytical Chemistry* **1981**, *124*, 1–7.

31. Laviron, E. Electrochemical Reactions with Protonations at Equilibrium. Part VIII. The 2 E, 2 H+ Reaction (nine-member Square Scheme) for a Surface or for a Heterogeneous Reaction in the Absence of Disproportionation and Dimerization Reactions. *Journal of Electroanalytical Chemistry* **1983**, *146*, 15–36.

32. Laviron, E. Electrochemical Reactions with Protonations at Equilibrium. Part X. The Kinetics of the P-benzoquinone/hydroquinone Couple on a Platinum Electrode. *Journal of Electroanalytical Chemistry* **1984**, *164*, 213–227.

33. Laviron, E. Theoretical Study of a 1e, 1H+ Surface Electrochemical Reaction (four-member Square Scheme) When the Protonation Reactions Are at Equilibrium. *Journal of Electroanalytical Chemistry* **1980**, *109*, 57–67.

34. Laviron, E. Electrochemical Reactions with Protonations at Equilibrium. *Journal of Electroanalytical Chemistry* **1981**, *124*, 9–17.

35. Laviron, E. Electrochemical Reactions with Protonations at Equilibrium. Part VII. The 2e, 1 H+ Reaction (six-member Fence Scheme) for a Surface or for a Heterogeneous Reaction in the Absence of Disproportionation or Dimerization. *Journal of Electroanalytical Chemistry* **1983**, *146*, 1–13.

36. Costentin, C. Electrochemical Approach to the Mechanistic Study of Proton-coupled Electron Transfer. *Chemical Reviews* **2008**, *108*, 2145–2179.

37. Costentin, C.; Robert, M.; Savéant, J.-M. Electrochemical Concerted Proton and Electron Transfers. Potential-dependent Rate Constant, Reorganization Factors, Proton Tunneling and Isotope Effects. *Journal of Electroanalytical Chemistry* **2006**, *588*, 197–206.

38. Costentin, C.; Robert, M.; Savéant, J.-M. Concerted Proton-electron Transfer Reactions in Water. Are the Driving Force and Rate Constant Depending on pH When Water Acts as Proton Donor or Acceptor? *Journal of the American Chemical Society* **2007**, *129*, 5870–5879.

39. Costentin, C.; Robert, M.; Savéant, J.-M. Carboxylates as Proton-accepting Groups in Concerted Proton-electron Transfers. Electrochemistry of the 2,5-dicarboxylate 1,4-hydrobenzoquinone/2,5- Dicarboxy 1,4-benzoquinone Couple. *Journal of the American Chemical Society* **2006**, *128*, 8726–8727.

40. Hammes-Schiffer, S.; Soudackov, A. V Proton-coupled Electron Transfer in Solution, Proteins, and Electrochemistry. *Journal of Physical Chemistry B* **2008**, *112*, 14108–14123.

41. Finklea, H. O. Theory of Coupled Electron-proton Transfer with Potential-dependent Transfer Coefficients for Redox Couples Attached to Electrodes. *Journal of Physical Chemistry B* **2001**, *105*, 8685–8693.

42. Budavári, V.; Szucs, A.; Oszkó, A.; Novák, M. Formation and Electrochemical Behavior of Self-assembled Multilayers Involving Quinone. *Electrochimica Acta* **2003**, *48*, 3499–3508.

43. Budavári, V.; Szucs, Á.; Somlai, C.; Novák, M. Noncovalently Bonded Quinone on Self-assembled Molecular Layers. *Electrochimica Acta* **2002**, *47*, 4351–4356.

44. Zhang, W.; Rosendahl, S. M.; Burgess, I. J. Coupled Electron/Proton Transfer Studies of Benzoquinone-Modified Monolayers. *The Journal of Physical Chemistry C* **2010**, *114*, 2738–2745.

45. Zhang, W.; Burgess, I. J. Step-wise Proton-coupled Electron Transfer Extended to Aminobenzoquinone Modified Monolayers. *Physical Chemistry Chemical Physics* **2011**, *13*, 2151–2159.

46. Tandon, V. K.; Maurya, H. K. "On Water": Unprecedented Nucleophilic Substitution and Addition Reactions with 1,4-quinones in Aqueous Suspension. *Tetrahedron Letters* **2009**, *50*, 5896–5902.

47. Yadav, J. S.; Swamy, T.; Reddy, B. V. S.; Rao, D. K. Organic Synthesis in Water: Green Protocol for the Conjugate Addition of Thiols to P-quinones. *Journal of Molecular Catalysis A: Chemical* **2007**, *274*, 116–119.

48. Barlow, B. C.; Burgess, I. J. Electrochemical Evaluation of 4-(dimethylamino)pyridine Adsorption on Polycrystalline Gold. *Langmuir* **2007**, *23*, 1555–63.

49. Bard, A. J.; Faulkner, L. R. No Title. *Electrochemical Methods: Fundamentals and Applications* **1980**.

50. Kohli, P.; Taylor, K. K.; Harris, J. J.; Blanchard, G. J. Assembly of Covalently-coupled Disulfide Multilayers on Gold. *Journal of the American Chemical Society* **1998**, *120*, 11962–11968.

51. Carot, M. L.; Esplandiu, M. J.; Cometto, F. P.; Patrito, E. M.; MacAgno, V. A. Reactivity of 1,8-octanedithiol Monolayers on Au(1 1 1): Experimental and Theoretical Investigation. *Journal of Electroanalytical Chemistry* **2005**, *579*, 13–23.

52. Hamoudi, H.; Guo, Z.; Prato, M.; Dablemont, C.; Zheng, W. Q.; Bourguignon, B.; Canepa, M.; Esaulov, V. A. On the Self Assembly of Short Chain Alkanedithiols. *Physical Chemistry Chemical Physics* **2008**, *10*, 6836–6841.

53. Rifai, S.; Laferrière, M.; Qu, D.; Wayner, D. D. M.; Wilde, C. P.; Morin, M. Electrodeposition of Bilayers of Dithiols. *Journal of Electroanalytical Chemistry* **2002**, *531*, 111–118.

54. Rifai, S.; Lopinski, G. P.; Ward, T.; Wayner, D. D. M.; Morin, M. Electrochemically Driven Assembly of Mixed Dithiol Bilayers via Sulfur Dimers. *Langmuir* **2003**, *19*, 8916–8921.

55. Meunier-Prest, R.; Legay, G.; Raveau, S.; Chiffot, N.; Finot, E. Potential-assisted Deposition of Mixed Alkanethiol Self-assembled Monolayers. *Electrochimica Acta* **2010**, *55*, 2712–2720.

56. García-Raya, D.; Madueño, R.; Blázquez, M.; Pineda, T. Formation of 1,8-Octanedithiol Mono and Bilayers Under Electrochemical Control. *Journal of Physical Chemistry C* **2010**, *114*, 3568–3574.

57. Fuchs, D. J.; Weiss, P. S. Insertion of 1,10-decanedithiol in Decanethiolate Self-assembled Monolayers on Au(111). *Nanotechnology* **2007**, *18*.

58. Calvente, J. J.; López-Pérez, G.; Jurado, J. M.; Andreu, R.; Molero, M.; Roldán, E. Reorientation of Thiols During 2D Self-assembly: Interplay Between Steric and Energetic Factors. *Langmuir* **2010**, *26*, 2914–2923.

59. Bensebaa, F.; Voicu, R.; Huron, L.; Ellis, T. H.; Kruus, E. Kinetics of Formation of Long-chain N-alkanethiolate Monolayers on Polycrystalline Gold. *Langmuir* **1997**, *13*, 5335–5340.

60. Snyder, R. G.; Strauss, H. L.; Elliger, C. A. C-H Stretching Modes and the Structure of N-alkyl Chains. 1. Long, Disordered Chains. *Journal of Physical Chemistry* **1982**, *86*, 5145–5150.

61. MacPhail, R. A.; Strauss, H. L.; Snyder, R. G.; Eiliger, C. A. C-H Stretching Modes and the Structure of N-alkyl Chains. 2. Long, All-trans Chains. *Journal of Physical Chemistry* **1984**, *88*, 334–341.

62. Laviron, E. General Expression of the Linear Potential Sweep Voltammogram in the Case of Diffusionless Electrochemical Systems. *Journal of Electroanalytical Chemistry* **1979**, *101*, 19–28.

63. Bard, A J; Faulkner, L. R. Electrochemical Methods. In; Wiley: New York, 2001; pp. 589–595.

64. Haddox, R. M.; Finklea, H. O. Proton Coupled Electron Transfer of Galvinol in Self-assembled Monolayers. *Journal of Electroanalytical Chemistry* **2003**, *550-551*, 351–358.

CHAPTER 6

SYNCHROTRON RAPID-SCAN INFRARED RADIATION FOR ELECTROCHEMICAL EXTERNAL REFLECTION SPECTROSCOPY

6.1. Introduction

Infrared *in-situ* spectroelectrochemistry has been an active area of sustained interest among electrochemists for the better part of thirty years as described in the previous Chapters. Almost from the method's inception there have been two competing approaches in the technique's development: external reflection spectroscopy (ERS) and internal reflection spectroscopy (IRS). In the previous two chapters (Chapters 4 and 5), significant technical work was done to ultimately achieve time-resolved kinetic information using the IRS technique of SEIRAS to provide molecular details of electrochemical processes.[1] A substantial limitation with the previously described studies (Chapter 4 and 5) is the slow response of the electrochemistry as a result of using large area electrodes to accommodate the low brightness of commercial infrared sources. This was not a problem in the previous studies as in one case (Chapter 4) surface adsorption at equilibrium conditions did not include any kinetic work, and in the second case (Chapter 5) the kinetics of the system were tailored to accommodate the accessible time scale of the technique. In this Chapter, methodologies are developed utilizing ERS techniques with very bright focused synchrotron infrared radiation to achieve better time-resolved *in-situ* spectroelectrochemical information.

It is generally agreed among contemporary users that an advantage of ERS is that it allows the use of well-defined single-crystals but suffers from the disadvantage of restricted mass transport owing to the thin-electrolyte layers required to prevent complete infrared

attenuation by the solvent. An additional potential advantage to using ERS is through photon polarization to differentiate between solution and surface adsorbed species.[2]

Optimal conditions for performing vibrational spectroscopy in the presence of an electrolyte are completely opposed to optimal conditions for performing electrochemical measurements. This is particularly manifested in ERS where a thin-layer of broadband absorbing electrolyte (usually water based) is contained between an infrared transparent window and an infrared reflective metal such as gold or platinum. This thin-layer of electrolyte allows sufficient levels of radiation to pass through the cell cavity but leads to extremely large cell resistances and decreased mass-transport to the electrode.[3] As such, to increase the signal-to-noise ratio in vibrational spectra, a large working electrode area is employed to increase the photon flux sampling the interface of interest. Electrochemists are aware that the product of the electrolyte resistance and the working electrode's capacitance designates the electrochemical cell time constant. As the later term is directly proportional to the electrode area, a typical ERS electrochemical cell is characterized by a very large (on the order of 10 milliseconds or greater) cell constant (RC). In other words, when the potential is stepped to a new value there is an inherent lag (5xRC) in the response of the electrified interface to reach this new value related to this cell constant. This means that in a typical experiment, one can measure the optical response as fast as the system will allow, but the minimum time scale in time-resolved studies is limited to the cell constant when studying dynamic processes triggered by an electrochemical perturbation. As a consequence, the majority of electrochemical *in-situ* ERS measurements are non-dynamic in nature and are performed by acquiring spectra only after a state of equilibrium has been reached at the electrified interface. Examples include subtractively normalized interfacial Fourier Transform Infrared spectroscopy (SNIFTIRS) and polarization modulation infrared

reflection absorption spectroscopy (PM-IRRAS) which have emerged as the dominant external reflection methods in the infrared spectroelectrochemistry community.[4] Non-static methods, such as electrochemically modulated infrared spectroscopy (EMIRS),[5] use AC (alternating current) modulation of the applied potential to greatly reduce $1/f$ noise and provide dynamic information. However, with notable exceptions using step-scan interferometers,[6–10] the success of EMIRS in modern FTIR spectrometers is limited by both slow diffusion rates and large charging times. These temporal limitations can be somewhat alleviated by using IRS methods which eliminate the need for thin, highly resistive electrolyte layers. Still, when coupled with a conventional infrared source, a relatively large electrode area (> 1 cm^2) is required to increase signal intensity and the study of sub-millisecond kinetic processes with IRS has yet to be truly realized.

Nevertheless, decreasing the dimension of the working electrode in an external reflectance thin-cavity cell to micrometer size could, in principle, decrease the minimum time scale of electrochemical infrared experiments by at least an order of magnitude. Sun and co-workers have already made advances in this regard by coupling FTIR microspectroscopy with relatively large ultramicroelectrodes (radius of 200 μm).[11–16] They reported infrared spectroelectrochemical studies occurring on electrode surfaces on the time scale of tens to hundreds of microseconds.[11,12] Importantly, as the size of the electrode decreases so will the signal-to-noise ratio as the instrument's ability to focus large photon intensity onto very small illumination areas becomes increasingly difficult with conventional sources. The use of non-conventional sources of infrared radiation is required to make these measurements feasible. To the best of the author's knowledge, the only previous reports of coupling synchrotron (far) infrared radiation with electrochemistry are the non-dynamic studies of Russell *et al.*[17–19] and

Melendres *et al.*[20-28] These researcher groups have primarily used far-infrared synchrotron radiation to study processes related to copper oxidation[20–24] and ion adsorption on gold,[25,26] silver[17,27] and platinum electrodes.[24,28]

In this Chapter, a simple redox probe (ferro/ferricyanide) has been chosen to dynamically study the diffusion processes occurring at a relatively small electrode (500 μm diameter) in a thin-cavity ERS *in-situ* cell. The well-established redox couple, ferri/ferrocyanide, is particularly well suited for infrared spectroelectrochemistry[7,9,10,29,30] owing to a very clear spectral shift in the cyanide vibrational stretches of the reduced and oxidized forms which are both frequency resolved from water absorption bands. The goals of this present Chapter are to evaluate the feasibility of coupling synchrotron generated radiation through an infrared microscope onto a thin-cavity external reflectance cell and to contrast the time-resolved electrochemical and spectroscopic responses.

6.2. Experimental

6.2.1. Reagents and Solutions

Potassium hexacyanoferrate(II) trihydrate ($K_4Fe(CN)_6 \bullet 3H_2O$, 99.99% trace metals basis), Potassium hexacyanoferrate(III) ($K_3Fe(CN)_6$, 99.99% trace metals basis), sodium fluoride (99.998%) and sodium perchlorate monohydrate ($NaClO_4 \bullet 3H_2O$, 99.0% trace metals basis) were purchased from Sigma Aldrich and were used as received. Deuterium oxide (D, 99.9%) for the determination of the cavity thickness was supplied from Cambridge Isotope Laboratories, Inc. (Andover, MA). All aqueous solutions were prepared from Milli-Q (>18.2 MΩ cm^{-1}) water.

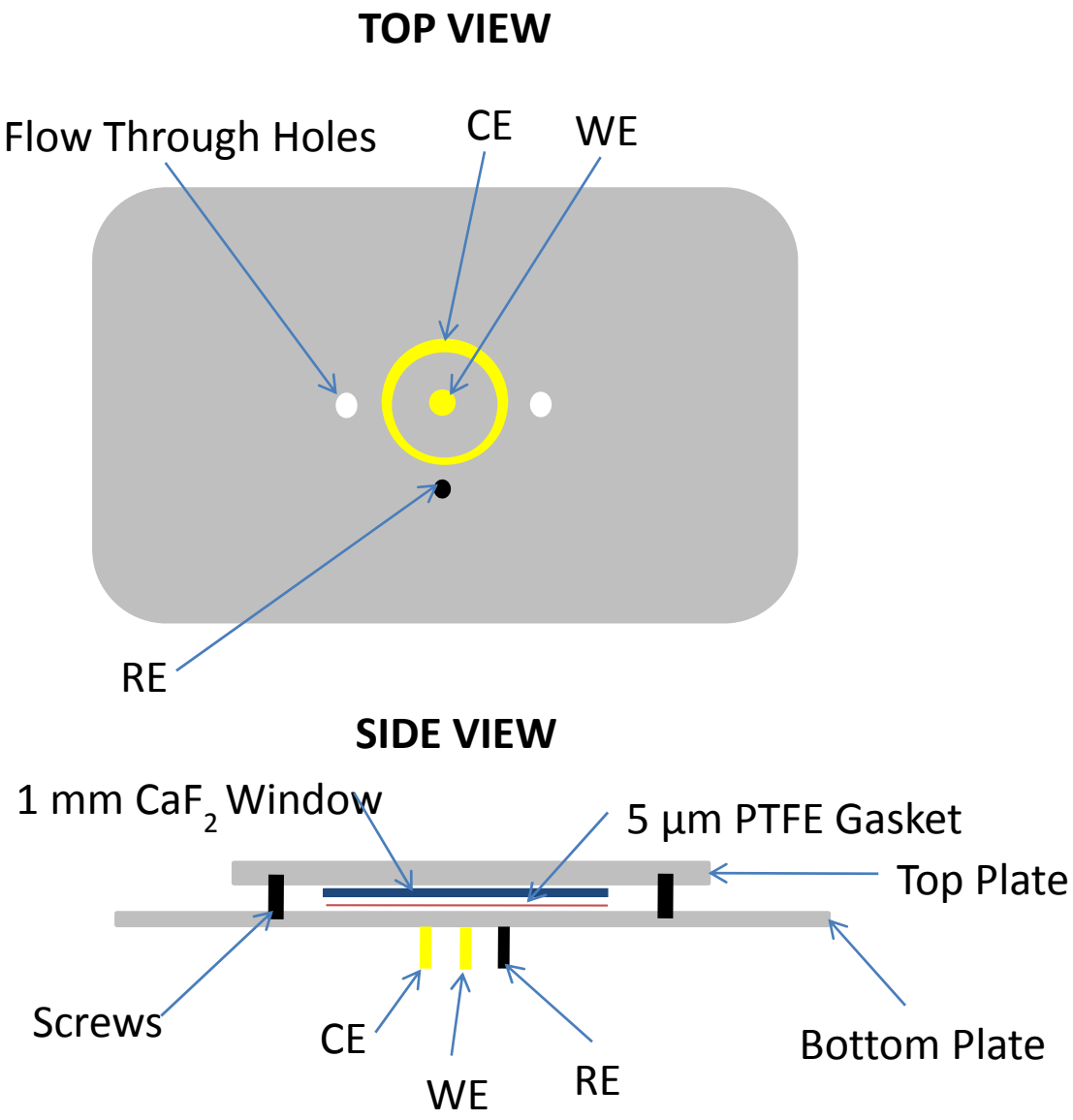

Figure 6.1. Diagram of the *in-situ* spectroelectrochemical (SEC) cell. The thin-cavity electrochemical cell was prepared by compressing a nominally 5 µm thick PTFE gasket between the main cell body (PVC plastic) and an infrared transparent window (CaF_2, 1 mm thick, 25 mm diameter). The working electrode (WE) and counter electrode (CE) were made from 0.5 mm diameter gold wire and the quasi-reference electrode (RE) from 0.5 mm silver wire. Flow-through holes were added to allow electrolyte solutions to be added after assembled dry.

6.2.2. Experimental *In-situ* Spectroelectrochemical Cell

The main body of the *in-situ* spectroelectrochemical (SEC) cell (Figure 6.1) was constructed to fit on the stage of the IR microscope. PVC plastic was chosen as the SEC cell material for its rigidity and electrical insulating properties. Similar designs for *in-situ* ERS SEC cells have been previously reported.[31,32] The thin-cavity was prepared by compressing a nominally 5 μm thick PTFE gasket between an infrared transparent window (CaF_2, 1 mm thick and 25 mm diameter) and the main body of the cell. A conventional three electrode arrangement was achieved with the working electrode (WE) and the counter electrode (CE) made from 0.5 mm diameter gold wire (Alfa Aesar, 99.95%) and a quasi-reference electrode (RE) from 0.5 mm diameter silver wire (Alfra Aesar, 99%). The electrodes were sealed in the main body using an epoxy, and the top (reflecting) surface was polished flat and to a mirror finish using successively finer grade diamond suspensions (Leco Corporation, St. Joseph MI, US) down to 0.5μm. The cell was designed as a flow-through cell to allow the electrolyte into and out of the thin cavity through two holes placed on extreme edges of the cavity after dry assembly.

6.2.2.1. Determination of *In-situ* SEC Cell Time Constant

To determine the time-constant of the cell (effectively the obtainable time resolution of the electrochemical measurements), electrochemical impedance spectroscopy (EIS) was used. A detailed description of EIS is beyond the scope of this Chapter but for more information is available in most standard electrochemistry books.[33,34] From these EIS measurements, the solution resistance and working electrode capacity in 0.5 M $NaClO_4$ were determined to be 3.4 kΩ and 76 nF, respectively. The time constant of the cell is ~0.25 milliseconds, and the time to

establish the desired potential at the interface is ~1.25 milliseconds (5RC). This is much faster than the measurable infrared spectral time resolution when using rapid-scan interferometry.

6.2.2.2. Determination of Cavity Thickness of Thin-Cavity *In-situ* SEC Cell

The determination of the cavity thickness between the PTFE gasket and the infrared window can be made from an analysis of the interference fringes obtained spectroscopically in the dry *in-situ* SEC cell and with the following equation,[35]

$$b = \frac{n}{2\Delta\nu} \tag{6.1}$$

where b is the pathlength, n is the number of fringes, and $\Delta\upsilon$ is the wavenumber spacing of the fringes. Interference patterns, such as the one shown in Figure 6.2a, arise due to multiple reflections from the internal walls of the cell. The validity of this method has also been confirmed using the absorption of small amounts of water in a deutrated water background. From Figure 6.2b, known molar absorptivities for the water stretching bands and Beer's law of absorption,[36] the cavity thicknesses measured by both techniques are within experimental error.

Through the utilization of the pre-described interference fringe method, the path length of the thin layer used in the experiments below was determined to be 13.7 μm. It is important to note that as the incident radiation converges on the focal point about a mean angle of 30^{o}, as calculated from the numerical aperture (NA) of the objective lens, from the surface normal, the actual cavity thickness is estimated to be 12 μm. The total volume of the cell is therefore ~6 μL.

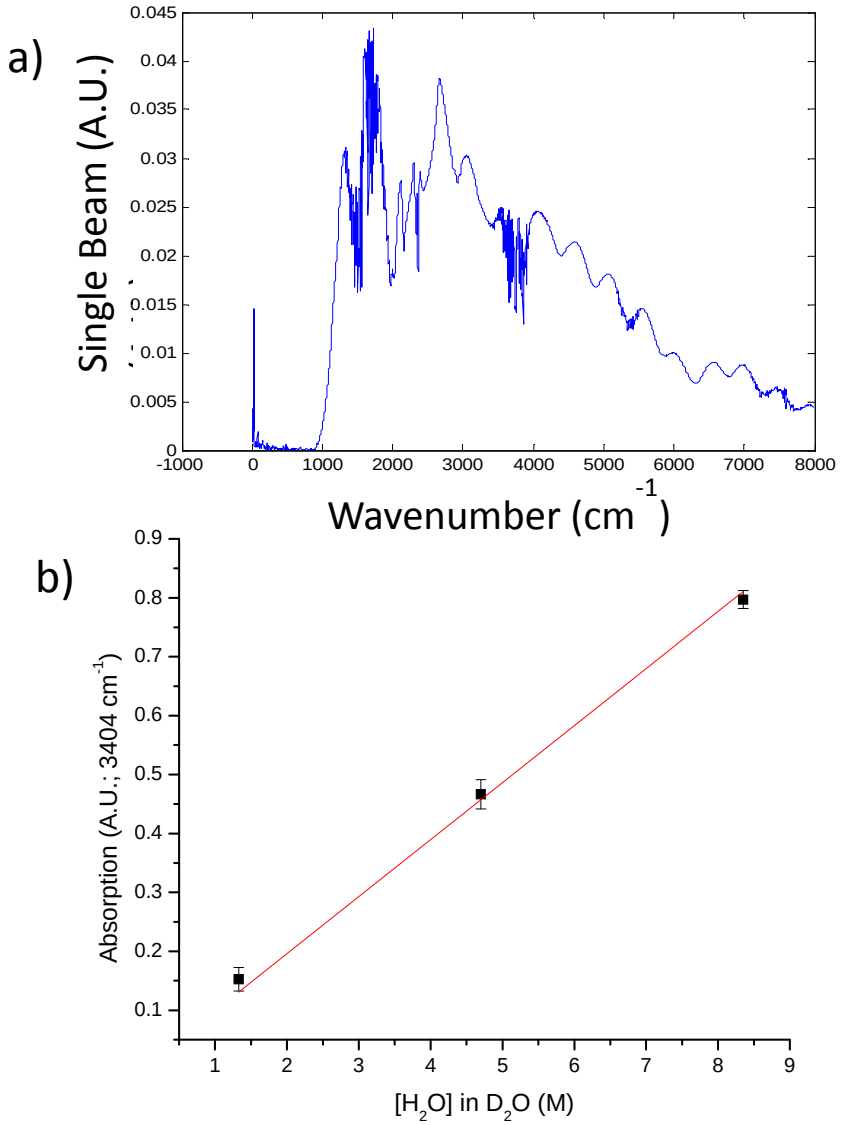

Figure 6.2. a) A representative single beam spectrum demonstrating the fringes that develops in the dry thin-cavity *in-situ* spectroelectrochemical (SEC) cell. From this information the cavity thickness can be determined for the assembled cell and for this particular cell setup the cavity thickness is 10.2 µm. b) Using the same *in-situ* SEC cell assembled in a), the cavity was filled with D_2O to determine a background before small amounts of H_2O were added. Depicted are the adsorption spectra for 3 different concentrations of H_2O. Using this information and Beer's Law, the cavity thickness was determined to be 9.8 µm thick.

6.2.3. Fourier Transform Infrared Measurements

Fourier Transform Infrared (FTIR) spectroscopy measurements were collected using the Mid-IR beamline facilities located at the Canadian Light Source (Beamline 01B1-01, Canadian Light Source, Inc., Saskatoon, SK, Canada). The beamline end station consisted of a Bruker Optics IFS66 v/S Spectrometer (with Rapid Scan) coupled to a Hyperion 2000 Infrared reflectance mode, onto the working electrode using a 36x Schwarzschild objective (NA 0.52) and measured using a narrowband 100 μm mercury cadmium telluride (MCT) (liquid nitrogen cooled) detector.

6.2.3.1. Rapid-Scan FTIR Measurements

The moving mirror in the time-resolved rapid scan experiments was driven at 100 kHz (measured in relation to the reference HeNe laser wavelength of 632.8 nm) with a spectral resolution of 8 cm^{-1}. Under these conditions, the spectrometer was able to collect one double-sided forward/backward interferogram every 120 milliseconds. Before each time-resolved experiment, a reference spectrum was collected (consisting of 100 scans) at the reference potential (200 mV *vs* Ag). This spectrum was used in the subtractively normalized calculation for each interferogram in a given time resolved experiment. In this manner any possible spectrometer drift throughout the course of the experiment would be minimized. Each complete rapid-scan experiment lasted ~6 seconds in which 52 reference corrected single beam spectra were obtained. However, with the high velocity of the moving mirror, there is an instrumental trade-off resulting in low signal-to-noise ratios for a given spectrum. This necessarily requires that a given set of time-resolved experiments must be measured and signal averaged numerous

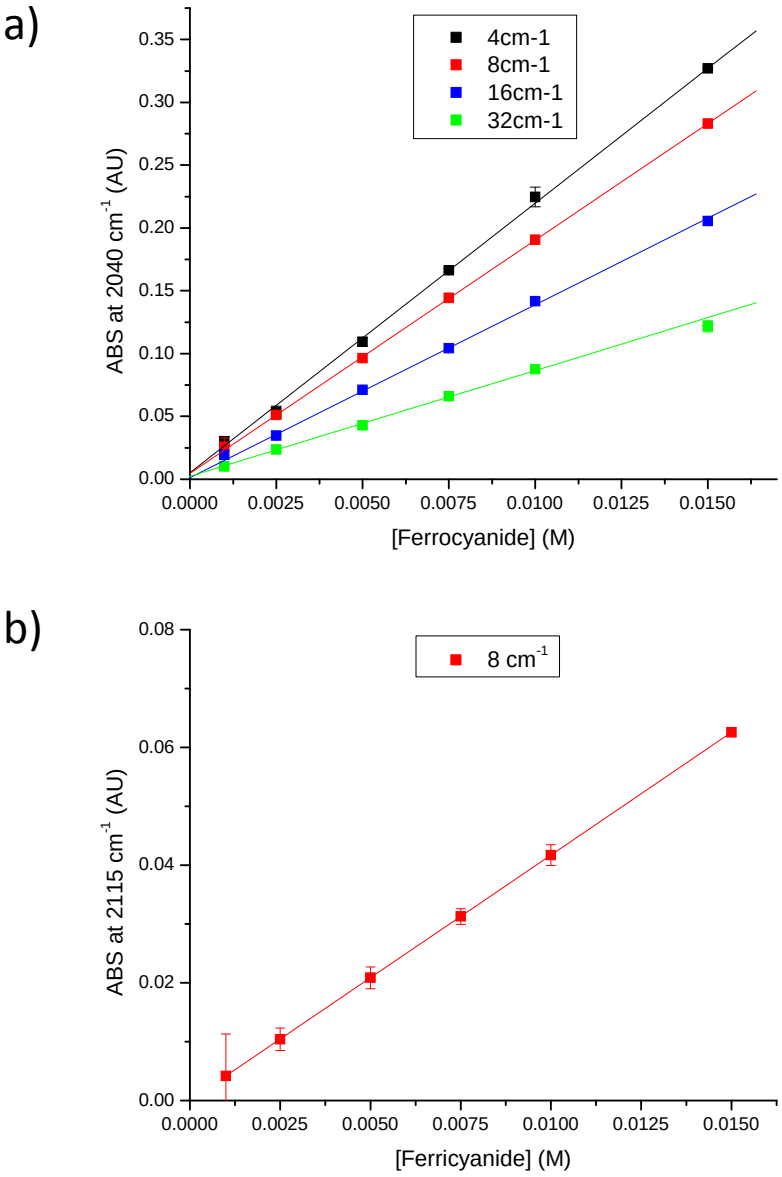

Figure 6.3. Absorbance values of the peak height at the 2040 and 2115 cm^{-1} infrared bands for varying concentrations of (a) ferrocyanide and (b) ferricyanide, respectively, (1.0 mM, 2.5 mM, 5.0 mM, 7.5 mM, 10.0 mM and 15.0 mM) in 0.5 M NaF aqueous solutions. The absorbance spectra were obtained by the co-additon of 256 scans at various resolutions, as indicated, (4 cm^{-1}, 8 cm^{-1}, 16 cm^{-1} and 32 cm^{-1}) using a blank aqueous solution containing 0.5 M NaF.

times (in this case, 256 replicates for the 20 x 20 μm aperture size and 1024 for the 8 x 8 μm aperture) for high signal-to-noise results.

6.2.4. Molar Absorptivity for Ferro/Ferricyanide in Aqueous Solutions

FTIR absorbance spectra were measured in 0.5 M NaF aqueous solutions containing various ferricyanide or ferrocyanide concentrations to determine the molar absorptivity of the 2115cm^{-1} and 2040 cm^{-1} infrared bands respectively (Figure 6.3). The measurements were made using the thin cavity *in-situ* SEC cell described above assembled with a 1 mm thick CaF_2 window and having a cavity thickness of 23.7 μm (determined using the interference fringe method). From this data, the peak height was plotted as a function of concentration with the slope then fit to Beer's Law to determine the molar absorptivity coefficient (Table 6.1). Each spectrum was the co-addition of 256 scans in reflection mode. The spectra were referenced to a blank aqueous solution containing only 0.5 M NaF.

6.2.5. Electrochemical Measurements

All electrochemical measurements were performed in the *in-situ* SEC cell using a HEKA PG 590 Potentiostat (HEKA, Mahone Bay, NS, Canada). Cyclic voltammetry (CV) and double-step chronocoulometry (CC) experiments were performed using software written in the LabVIEW (National Instruments Corporation, Austin, TX, USA) programming environment as described in Chapter 5 (Experimental section). Data acquisition, signal generation, and triggering for the *in-situ* SEC experiments were done with a National Instruments multifunctional Data Acquisition Card (DAQ) PCI 6251 M Series. For these measurements, an

Table 6.1. Ferrocyanide (2040 cm^{-1}) and Ferricyanide (2115 cm^{-1}) Molar Absorptivity Coefficients in 0.5 M NaF aqueous solutions.

Ferrocyanide

Spectral Resolution	**Molar Absorptivity 2040 cm^{-1}, ε (M^{-1} cm^{-1})**
4 cm^{-1}	4.561 x 10^3
8 cm^{-1}	3.898 x 10^3
16 cm^{-1}	2.852 x 10^3
32 cm^{-1}	1.701 x 10^3

Ferricyanide

Spectral Resolution	**Molar Absorptivity 2115 cm^{-1}, ε (M^{-1} cm^{-1})**
8 cm^{-1}	8.81 x 10^2

additional National Instruments DAQ card was used (PCI 6251 X Series) to measure the current transients during the *in-situ* SEC experiments. This second card was necessary to acquire the full 6 seconds of rapid-scan data as the first DAQ card had enough memory to hold 2 seconds worth of data at the very high sampling rates utilized to catch the experimental trigger signal.

6.2.6. Interfacing Hardware and Software

The major technical challenge in performing these experiments was interfacing the FTIR spectrometer and the potentiostat for consistent, synchronized measurements. The primary objective was to start the acquisition of the infrared spectra in synch with the application of a particular potential waveform while ensuring that this process was repeatable over many replicate measurements. This required a series of hardware and software triggering signals to ensure proper timing, communication, and data flow between the various instruments (Figure 6.4). Briefly, a sequence of transistor-transistor logic (TTL) hardware trigger signals were generated and received between the FTIR spectrometer and a computer controlling the potentiostat (through the LabVIEW software environment). These two TTL signals worked in parallel to gate the start and stop of the acquisition of the rapid-scan FTIR spectra (and electrochemical data) reproducibly with the application of the potential waveform to the working electrode. This two-way communication ensured that the proper sequence of events could be repeatedly achieved.

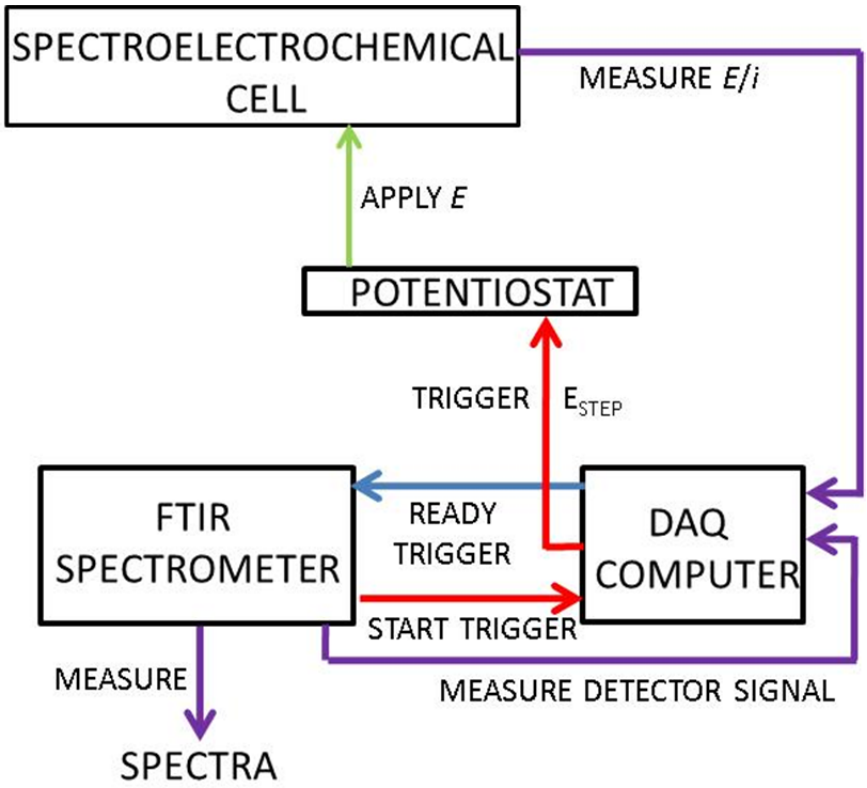

Figure 6.4. Detailed connection diagram for the various components interfaced together to allow for repetitive automated rapid-scan measurements for time-resolved infrared studies.

6.3. Results and Discussion

6.3.1. Diffusion Consideration

It is important to adequately discuss the electrochemical response of the *in-situ* spectroelectrochemical cell used in these experiments before a meaningful discussion of the synchrotron infrared spectroscopic results is made. The theory of diffusion currents in restricted geometries, including the thin-layer cell used here, under voltammetric conditions has been treated by several authors.[37–39] Although there are equations describing the flux of material in thin-cavity cells under constant current conditions, there does not seem to be an exact analytical solution for the corresponding diffusion controlled chronoamperometric experiment. In particular, for a disc electrode of radius, r_e, in a thin-layer cavity configuration of thickness h along the z direction, a rigorous treatment of this problem includes both axial and radial diffusion terms (best described by cylindrical diffusion),

$$\frac{\partial C(r,z,t)}{\partial t} = D\left[\frac{\partial^2 C(r,z,t)}{\partial r^2} + \frac{1}{r}\frac{\partial C(r,z,t)}{\partial r} + \frac{\partial^2 C(r,z,t)}{\partial z^2}\right] \tag{6.2}$$

with the following initial and boundary conditions

$$C(r,z,0) = C^*$$

$$\lim_{r\to\infty} C(r,z,t) = C^*$$

$$C(r,0,t) = 0 \;\; (r \le r_e, t > 0)$$

$$\lim_{z\to h} \frac{\partial C(r,z,t)}{\partial z} = 0$$

where D and C^* are the diffusion coefficient and the initial concentration of the redox species being consumed respectively. The spectroelectrochemical relevance of this problem has inspired the development of several models which invoke simplifying assumptions in an attempt to reduce the dimensionality of the problem.[40–42] For example, Micka *et al.* made the assumption

that for sufficiently large cavity thicknesses, radial diffusion can be entirely neglected and only linear diffusion along the normal axis of the electrode's surface (denoted as axial diffusion for the remainder of this Chapter) is of consequence. As such, the corresponding mass-transfer limited, chronoamperometric response can be represented as:[40]

$$i(t) = \frac{2nFADC^*}{h} \sum_{m=0}^{\infty} \exp\left[-\left(m+\frac{1}{2}\right)^2 \left(\frac{\pi}{h}\right)^2 Dt\right] \tag{6.3}$$

where $A = \pi r_e^2$ is the area of a perfectly smooth disc electrode, F is the Faraday constant, and n is the number of electrons transferred. A different expression was provided by Oglesby *et al.*[43] that uses the same boundary conditions and assumptions but leads to essentially identical results. For completeness, it should be noted that the expression derived by Oglesby *et al.* is more robust for calculating concentration profiles at short times.

A complementary scenario develops if the mass transfer in the axial direction, for $r \leq r_e$, is assumed sufficiently rapid enough such that there is nearly immediate exhaustion of electroactive material initially in the electrolyte volume above the electrode. This becomes especially true for very small values of h ($h < r_e$) and relatively large values of the diffusion coefficient, D. Under these conditions, the problem reduces to semi-infinite radial diffusion towards a cylinder of area $2h\pi r_e$, and can be approximated by Szabo *et al.*[44] as,

$$i(t) = 2h\pi nFDC^* \left[\frac{2\exp\left[-0.05(\pi\tau)^{1/2}\right]}{(\pi\tau)^{1/2}} + \frac{1}{\ln(5.2945 + 0.7493\tau^{1/2})}\right] \tag{6.4}$$

where $\tau = 4Dt/r_e^2$. For small values of τ, *i.e.* short times, only the first term in Equation 6.4 is significant and the resulting exponential approaches unity producing a modified Cottrell-like relationship as follows,

$$i(t) = \frac{2hr_e\pi^{1/2}nFD^{1/2}C^*}{t^{1/2}} \tag{6.5}$$

Alternatively, at sufficiently long enough times (large values of τ), the first term in Equation 6.4 approaches zero and a quasi-steady state current is expected,

$$i_{qss} = \frac{4h\pi nFDC^*}{\ln(\tau)} \tag{6.6}$$

Overall, it is predicted that currents arising from axial diffusion will dominate at short times provided that the radius of the disc electrode, r_e, and the depletion layer thickness above the electrode, h, are such that the area over which radial diffusion occurs is much smaller than the actual area of the electrode. However, regardless of the electrode disc radius, once the depletion layer normal to the electrode surface extends across the full thickness of the cavity, a quasi-steady state current condition will exist and be solely dominated by radial diffusion at sufficiently long times. Thus, even in the absence of an exact solution to the pre-described diffusion problem, a reasonable estimation is to assume that the current measured is largely dictated by Equation 6.5 for short times and controlled by Equation 6.6 at long times. This can be qualitatively evidenced in Figure 6.5 as both limiting conditions (Equations 6.5 and 6.6) are simulated (with the parameters used in the *in-situ* spectroelectrochemical experiments) to predict the current and charge densities for; C^* = 1 mM, h = 20 μm, r_e = 0.025 cm, and D = 6.4 x 10^{-4} cm^2 s^{-1}. Under these conditions, one can see from Figure 6.5 that both simulated currents are initially linearly dependent on $1/t^{1/2}$ (but have different corresponding slopes) and cross after 0.8 seconds as the axial current quenches. The axial diffusion charge *versus* $t^{1/2}$ curve is linear (Cottrell-like) at early times but eventually plateaus after less than a second as the electroactive species initially in the thin-cavity layer above the electrode is consumed. In contrast, the charge curve simulating the radially diffusing species continues to increase with increasing time. A consequence of these assumptions is that Equation 6.3 determines the current (and consequently the amount of electrogenerated species) at short times.

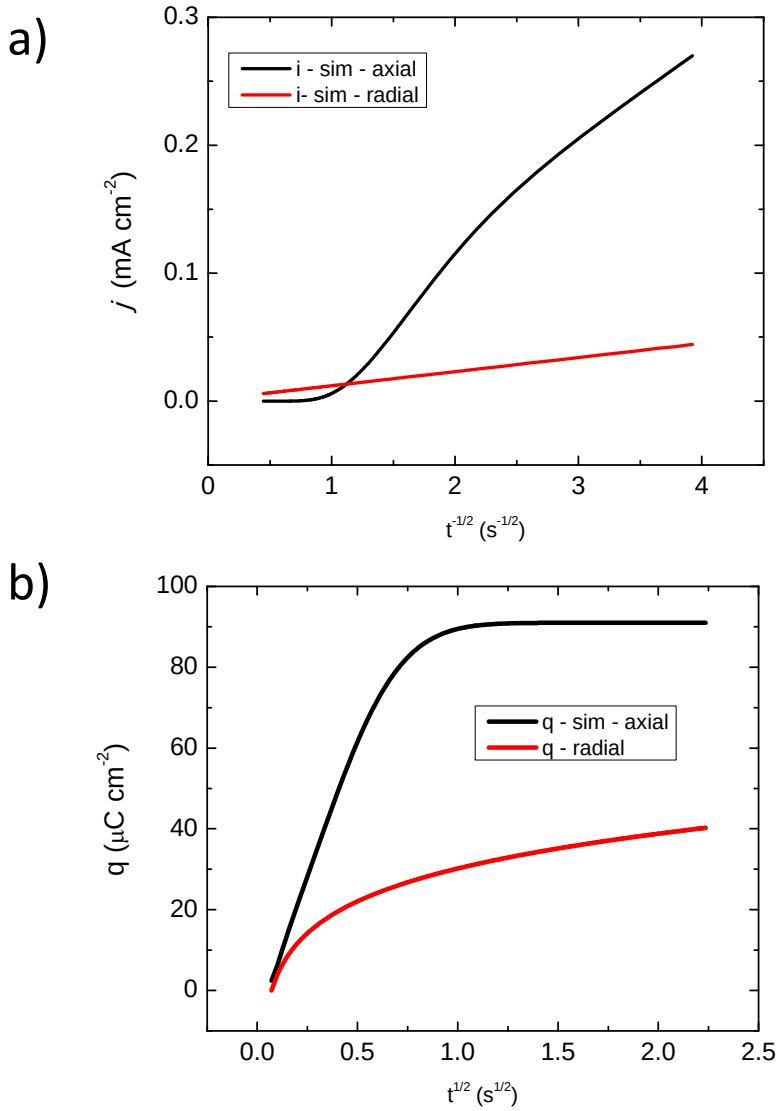

Figure 6.5. Simulated diffusion-controlled responses for electrochemical measurements taken in the thin-cavity, *in-situ* spectroelectrochemical cell. Current densities (a) have been plotted for finite-volume linear diffusion (black) and semi-finite radial diffusion (red) with the corresponding charge densities are shown in (b). The time domain has been transformed for all sets of transient data to allow easy comparison with Cottrell-like behaviour. The simulation was made with the following parameters: $C^* = 1$ mM, $h = 20$ µm, $r_e = 0.025$ cm, $D = 6.4 \times 10^{-4}$ cm^2 s^{-1}.

By keeping the cavity thickness above the electrode fixed, inspection of Equation 6.3 and 6.5 reveals that the diffusion current from Equation 6.3 is proportional to the square of the electrode radius while Equation 6.5 is linearly dependent on r_e. From this examination, it should be obvious that axial diffusion is dominant for large electrodes ($r_e \ll h$) and the results described by Micka *et al.*[40] adequately predict the current behaviour over the majority of the experimental time scale. Conversely, as the electrode size decreases, the radial contribution will become more significant at increasingly shorter times. An important note to consider is that the vast majority of species electrogenerated at the perimeter of the electrode, as a result of radial mass transport, will immediately diffuse away from the electrode and into the semi-infinite space parallel to the surface of the disc electrode. This has an important consequence in that the thin cavity cell for *in-situ* spectroelectrochemical electrolysis only spectroscopically reports on the concentration of species electrochemically formed directly above the electrode. For relatively large electrodes, this will correlate with the measured electrochemical signal at short times, but as one decreases the electrode radius, deviation between the infrared measured signal and the cumulative charge passed will increase. If the size of the electrode is reduced to the dimension of an ultramicroelectrode (r_e < ~25 μm), the mass transport problem is identical to diffusion to a scanning electrochemical microscope (SECM) tip above an insulating substrate.[45] This problem will be discussed in greater detail in the following chapter (Chapter 7).

6.3.2. Electrochemical Results

Figure 6.6 shows a typical cyclic voltammogram measured in the external reflection *in-situ* SEC cell at a scan rate of 50 mV s^{-1} with 1.13 mM ferrocyanide, $Fe(CN)_6^{-4}$, in 0.5 M $NaClO_4$

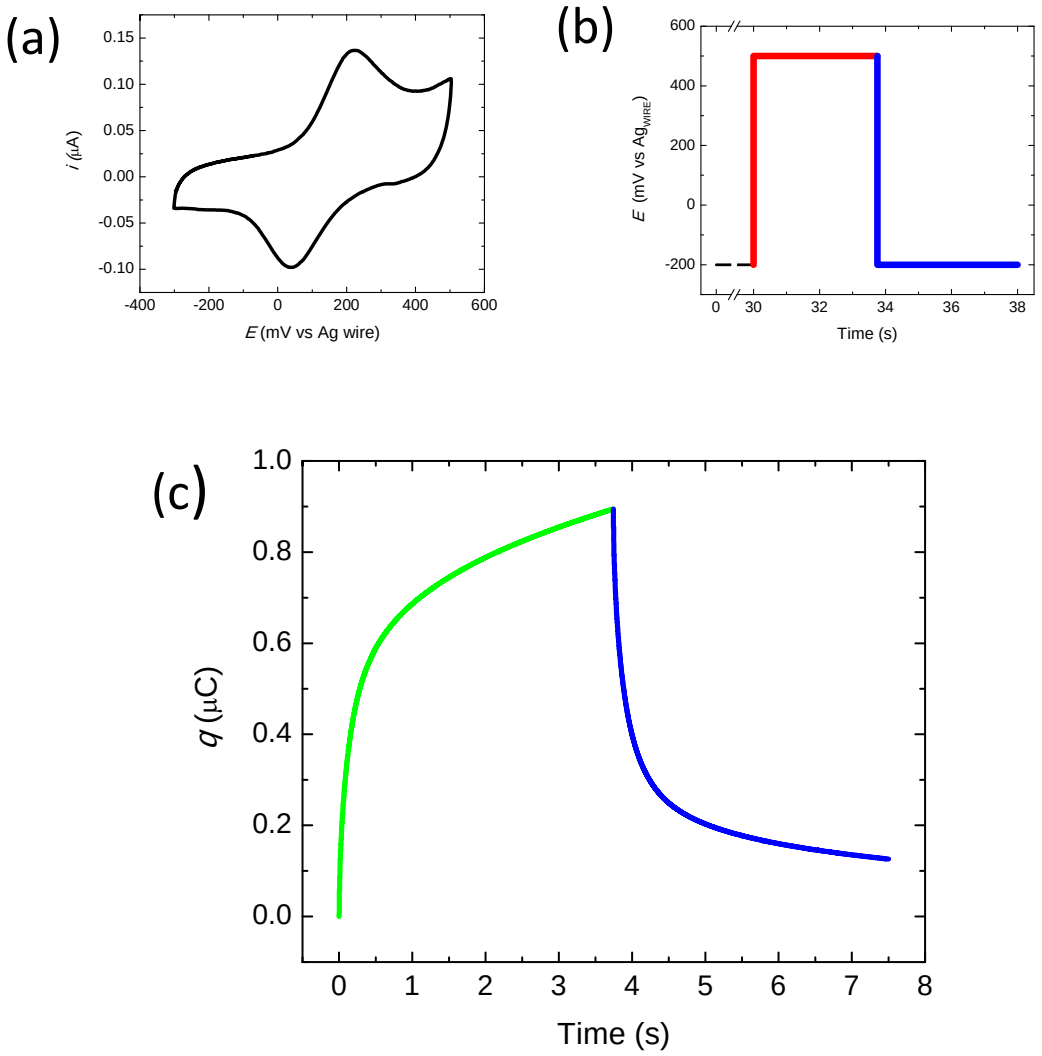

Figure 6.6. Measured electrochemistry of 1.13 mM $Fe(CN)_6^{-4}$ in 0.5 M $NaClO_4$ aqueous electrolyte solution using the *in-situ* spectroelectrochemical (SEC) thin-cavity cell with 0.5 mm diameter gold working electrode. a) A representative cyclic voltammogram (CV) for the above mentioned system and b) a pictorial representation of the double-potential step-sequence (forward step - solid red line and return step – solid blue line) used to make these measurements. c) The charge transient data obtained from numeric integration of the measured currents during the double-step forward(solid green line) and return step (solid blue line).

supporting electrolyte. The apparent formal potential of this system was ~150 mV and both the reduction and oxidation peaks display non-steady state, diffusional tailing. Prior to any synchrotron infrared radiation measurements, the *in-situ* cell was filled with a fresh volume of the above described electrolyte solution. The potential was initially held at -200 mV for 30 seconds and the current transients were recorded during the double potential step depicted in Figure 6.6. One can see from the numerically integrated current transients that there is a rapid initial change in the charge followed by a much slower changing tail which is consistent with the argument above that axial diffusion dominates at short times and radial diffusion at long times. It is interesting to note that there is a net positive charge passed in the total transient. That is, the charge tail at long times is appreciably "*flatter*" in the backward step compared to the forward step. To rationalize this, a qualitative consideration of the initial conditions before each potential step is required. Prior to the step from -200 mV, there should only be $Fe(CN)_6^{-4}$ present in the cell and it should be homogeneously distributed in both the axial and radial directions. When the potential is stepped to 500 mV, only $Fe(CN)_6^{-4}$ in the electrolyte volume above the electrode is initially converted to $Fe(CN)_6^{-3}$ and the oxidized product will largely be retained in this volume. The radial component will begin to contribute more significantly to the measured charge passed as this layer becomes increasingly depleted of $Fe(CN)_6^{-4}$. As discussed in the previous section, any $Fe(CN)_6^{-3}$ generated at the electrode perimeter will diffuse away from the electrode surface but still largely contributes to the measured charge. After stepping the potential back to -200 mV, a significant portion of this material will not be recollected at the electrode within the measurement time scale of the transient and a smaller amount of charge will be measured. Given semi-infinite radial diffusion conditions, as well as 30 seconds potential hold at -200 mV prior to

the next double-step sequence, it is assumed that any complications from the slow accumulation of ferricyanide in the electrolyte near working electrode will be eliminated. In fact, the infrared measurements (*vide infra*), were performed with over 1000 consecutive iterations of this potential step profile (without flowing new electrolyte into the cell) and the first and last transients are nearly identical to one another within experimental error.

6.3.3. Synchrotron Advantage

The subject of synchrotron *versus* conventional thermal (Globar) sources has been addressed elsewhere,[46] but it is prudent to provide a brief overview. Flux is a common measure of source energy output and is defined as the photon density per source unit area per unit time. For a typical commercial Globar the flux is actually greater than that of a synchrotron infrared radiation source, under normal synchrotron operating conditions. However, focusing thermal source radiation leads to significant losses because the emission pattern of a Globar is in all directions, whereas highly directed synchrotron infrared photons can be treated as a near point source and does not suffer such high magnitude losses leading to 2 to 3 orders of magnitude higher brilliance (flux density). Thus, it is primarily when infrared radiation needs to be focused onto small spatial regions that synchrotron radiation is truly advantageous. This is illustrated in Figure 6.7 where an experiment measuring reflected infrared radiation is collected through the *in-situ* SEC cell filled with electrolyte at different aperture sizes. These reflection spectra are the ratio of two successive single interferograms measured at 1 cm^{-1} resolution. As shown in panel (a), the Globar and synchrotron sources provide comparable noise levels for a 40 x 40 μm square aperture for frequencies above 2400 cm^{-1}. Below this frequency, the synchrotron source has

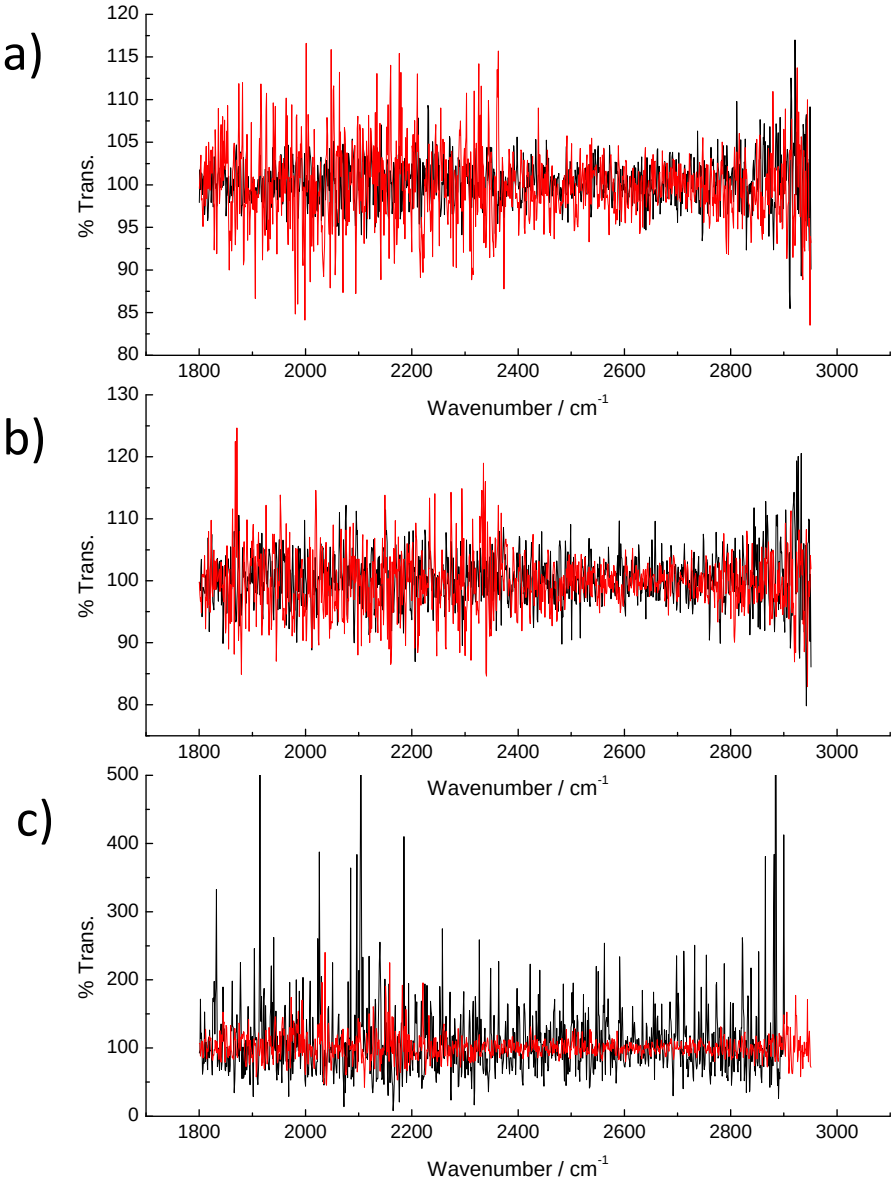

Figure 6.7. Comparison of differing noise levels for various aperture sizes (a) 40 x 40 µm, (b) 20 x 20 µm, (c) 5 x 5 µm measured using synchrotron infrared radiation (red lines) or conventional Globar (black lines) reflected from the working electrode surface of the *in-situ* spectroelectrochemical (SEC) cell. These curves were calculated by taking the ratio between two successive, single interferograms (1 cm^{-1} resolution) through the SEC cell containing an aqueous 0.5 M $NaClO_4$ electrolyte solution.

higher noise levels than the Globar due to absorption from various optics associated with the beamline (diamond window). At the 20 x 20 μm sized aperture, panel (b), shows that the synchrotron and Globar noise levels are very comparable in the wavenumber region from 1800 cm^{-1} to 2400 cm^{-1} but is somewhat more favourable for the synchrotron source outside the region of diamond interference. Most impressively, panel (c) shows that for a 5 x 5 μm aperture, synchrotron infrared radiation noise is significantly smaller across the entire region of interest. Clearly, synchrotron infrared radiation noise levels become increasingly better relative to those of the Globar as the aperture size is decreased. Restated, the synchrotron advantage occurs due to a decrease in the noise levels compared to those of a Globar.

Unfortunately, for this particular study, it should be noted that the attenuation of the synchrotron source due to the diamond window absorption overlaps with the C≡N stretches of both forms of the ferro/ferricyanide redox couple. Nevertheless, even after these losses, there is still about a two-fold decrease in the level of noise when synchrotron radiation is used to study the electrochemistry of ferro/ferricyanide. A more thoughtful choice of redox couple would see an even larger advantage in favour of this synchrotron source.

6.3.4. Synchrotron Infrared Radiation – Electrochemical External Reflection Spectroscopy Results

In Figure 6.8, a subtractively normalized energy curve, $\Delta S/S = (S_{VAR} - S_{REF})/S_{REF}$, for the oxidation of 1.13 mM ferrocyanide, $Fe(CN)_6^{-4}$, in 0.5 M $NaClO_4$ is depicted. The single beam reference spectrum was obtained by holding the potential at -200 mV where only the reduced form, $Fe(CN)_6^{-4}$ will exist in the cavity. The sample spectrum was obtained at 500 mV, $Fe(CN)_6^{-3}$, after waiting 60 seconds. As described in a previous chapter, a positive

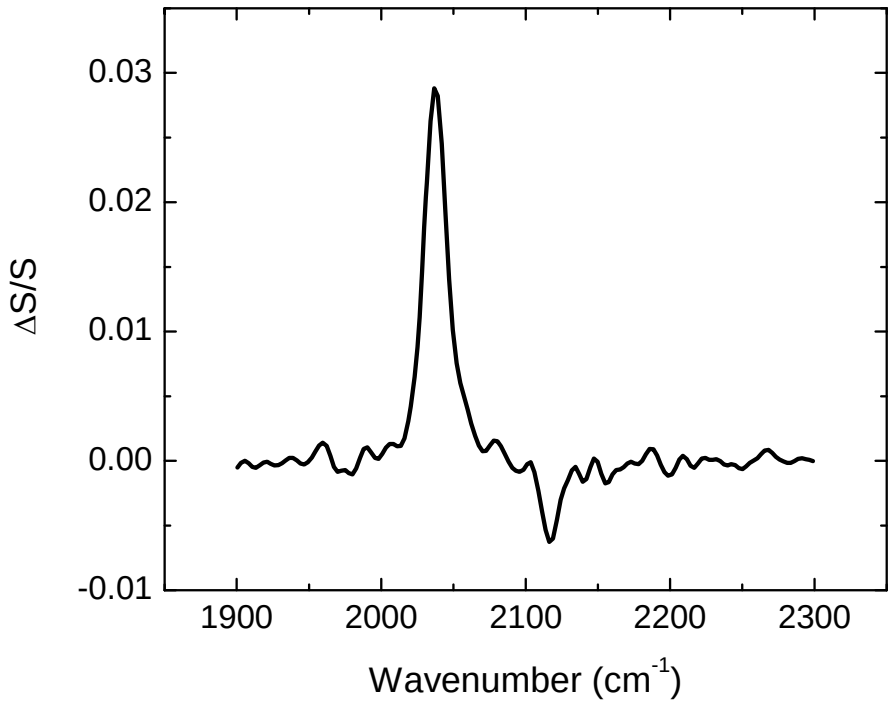

Figure 6.8. Subtractively normalized infrared spectrum of the ferrocyanide oxidation measured at long times. The sample spectrum was acquired by holding the potential, E_{VAR}, at 500 mV for 30 seconds after measuring a spectrum at the reference potential, E_{REF} -200 mV. The strong upwards going band at 2040 cm^{-1} corresponds to a loss of ferroycanide material in the thin-cavity above the electrode whereas the weaker downward band at 2115 cm^{-1} is attributed to the electroformation of ferricyanide.

going peak, 2038 cm^{-1}, is assigned to a loss of that vibrational stretch. In this case, ferrocyanide has been oxidized upon stepping the potential to +500 mV. In contrast, the smaller downward band at 2115 cm^{-1} is assigned to the formation of oxidation product, ferricyanide, in the thin layer. Further inspection of Figure 6.8 reveals no additional peaks or shoulders present even after several hours of repetitive potential steps. There is no evidence of the formation of an adsorbed polymeric hexacyanoferrate (HCF) complex which has been reported by others.[10,29] Although, it is important to note that the instrumental setup is not designed to provide surface sensitivity, due to the small angle of infrared incidence, it is unlikely that adsorbed HCF is formed below detectable levels because of the relatively mild potential perturbations used.[10] This can be further evidenced by the consistency in measured cyclic voltammograms before and after the long duration time-resolved spectroelectrochemical studies.

Rapid scanning interferometry time-resolved synchrotron infrared radiation external reflection spectroelectrochemistry was performed using freshly exchanged ferrocyanide solution and with the same potential perturbation sequence depicted in Figure 6.6. The measurements were recorded at 8 cm^{-1} resolution allowing for the collection of a double-sided interferogram every 120 milliseconds. This time resolution is more than sufficient to follow the mass-transfer controlled redox process studied here. Given that the working electrode used in this SEC cell (0.5 mm diameter) was much larger than a UME, the aperture setting was decreased to 8 x 8 μm to mimic the magnitude of the infrared signal that would be measured from an ultramicroelectrode. To offset the decrease in photon throughput caused by decreasing the illuminated area, a large number of co-added time-resolved spectra had to be collected in order to achieve high enough signal-to-noise ratios to provide a meaningful discussion. This was accomplished by repeating the double potential step sequence 1024 times. The signal-to-noise

value after analysis of the ferrocyanide peak was ~60 which was comparable to the signal-to-noise level after the co-addition of 256 interferograms collected with a much larger 20 x 20 μm aperture size.

The time-resolved infrared absorbance data was calculated from the collected data and is presented in Figure 6.9. The ordinate, shows the change in absorption relative to the infrared signal after the potential was held at –200 mV for 30 seconds. One will notice that there is a rapid change in the infrared signal for both forms of the redox species upon stepping to the more positive potential. However, in less than one second both signals reach a plateau and remain invariant in time until the reverse potential step to – 200 mV is applied at which point they return back to their initial values. This last point is particular important as it reveals that the infrared radiation only interrogates molecules that remain close to the electrode within the time scale of the experiment. When comparing this result to the experimental charge transients, there is no evidence of a longer-time tail which, as described earlier, has been attributed to the contribution of radial diffusion to the overall electrochemical signal. In fact, the shape of the ferricyanide optical transient in Figure 6.9 is qualitatively identical to the charge transients simulated for pure axial diffusion. To further illustrate this point, a quantitative comparison between axial electrochemical diffusion simulations and the spectroelectrochemical measurements was made. In order to do so, the molar absorptivity, ε, of both ferrocyanide and ferricyanide was first determined as described in the Experimental section of this chapter. The determined values of ε for ferrocyanide and ferricyanide were 3.9×10^3 M^{-1} cm^{-1} and 8.8×10^2 M^{-1} cm^{-1} respectively. The absorbance data in Figure 6.9 was converted to the change in species concentration through the application of Beer's law, using the measured molar absorptivities and the path length of the SEC cell. A charge transient for ferrocyanide oxidation was simulated

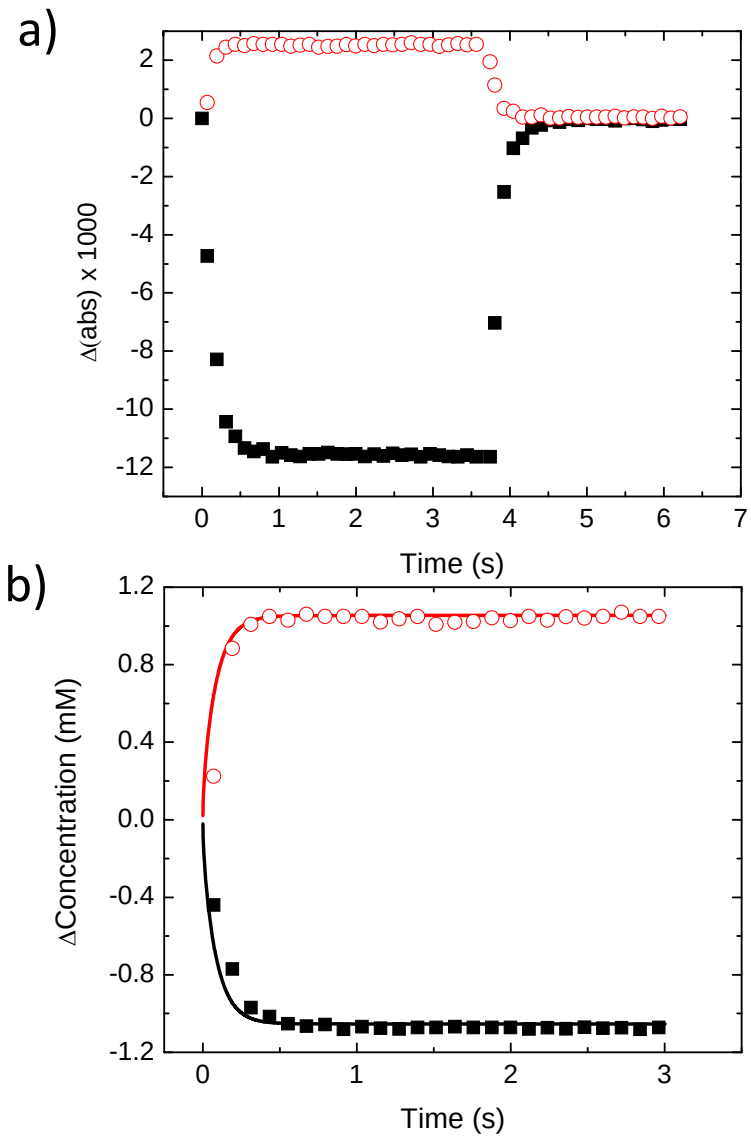

Figure 6.9. (a) Time-resolved changes in infrared absorbances for ferrocyanide (■) and ferricyanide (○) during the double-step (potential step-sequence is taken from Figure 6.6(b)) *in-situ* spectroelectrochemical (SEC) measurements. Each data point represents the co-addition of 1024 co-added scans with 8 cm^{-1} wavenumber resolution. (b) Plot of the *in-situ* SEC concentration changes measured during the forward potential step (first 3 seconds) calculated using Beer's Law (points). Superimposed (lines) are the simulated results of the charge transient during the potential step.

using the integrated form of Equation 6.3 and the following parameters: h = 12 μm, C^* = 1.13 mM, r_e = 0.5 mm and D = 6.4 x 10^{-6} cm^2 s^{-1}.[34] The simulated charge values were converted into concentrations of ferrocyanide and ferricyanide using Faradays constant and division of the volume of the cavity ($h\pi r_e^2$). The results are plotted in Figure 6.9 and show excellent agreement between the two methods (charge simulation and spectroelectrochemical experiment) confirming that the spectroelectrochemical technique is insensitive to species arriving at the electrode through radial diffusion.

This last point has important implications for future studies using infrared microspectroscopy and ultramicroelectrodes and is the topic of Chapter 7. Briefly, there will be a much more pronounced discrepancy between electrochemical and spectroscopic data with decreasing electrode dimensions. Secondly, even though much faster time scales become accessible with UME-based synchrotron *in-situ* spectroelectrochemistry, the electrogenerated spectroscopic signal will always be limited by the amount of species formed from axial diffusion within the period of the potential perturbation.

6.4. Summary and Conclusions

This chapter has provided much of the ground work needed for the use of synchrotron infrared radiation to study electrochemical kinetic processes. Using electrodes near in size to ultramicroelectrodes, it has been shown that synchrotron infrared radiation can be successfully coupled with an external reflectance electrochemical cell to make *in-situ* spectroelectrochemical measurements. Excellent signal-to-noise ratios have been obtained from time-resolved infrared and electrochemical measurements with an illumination area less than 10 x 10 μm. From this work, an important result concerning the differing responses seen for the infrared and

electrochemical measurements were described. Briefly, the purely electrochemical response in the thin-cavity cell include contributions from both axial and radial diffusion; whereas, it was demonstrated that the infrared spectroscopic signal arises only from species originating in the thin-cavity between the electrode surface and the infrared window. Simulations of linear diffusion in a finite volume element are in outstanding agreement with the time dependence of the experimentally measured infrared absorbance. Furthermore, with small aperture settings synchrotron infrared radiation provides significantly higher signal-to-noise ratios compared to a conventional thermal sources.

From an instrumental point of view, these measurements were possible through the successful integration of electrochemical and infrared spectromicroscopy equipment to allow time-resolved studies using synchrotron generated infrared radiation. The instrument setup comprises several commercial components, including a potentiostat, infrared spectrometer and microscope, all interfaced through custom written software in the LabVIEW environment to control the measurement sequence. A simple proof of principle electrochemical system was chosen to demonstrate the capabilities of the instrumental setup and methodology. Once in place, the temporal electrochemical response was measured and analyzed with great success using rapid-scan Fourier Transform Infrared spectroscopy.

The next chapter (Chapter 7) demonstrates a further progression in the development of time-resolved studies by increasing the temporal resolution of both electrochemical and infrared measurements. As mentioned, the electrodes used in this chapter were not truly ultramicroelectrodes but do provide the ground work for the next chapter where a 10 fold decrease in electrode size will be examined using similar thin-cavity *in-situ* SEC cells. In addition to decreasing the electrode size to increase the electrochemical response, the infrared

time-resolution can be greatly improved through the use of step-scan Fourier Transform interferometry.

6.5. References

1. Osawa, M. In-Situ Surface-enhanced Infrared Spectroscopy of the Electrode/Solution Interface. *Diffraction and Spectroscopic Methods in Electrochemistry* **2006**, 269–314.

2. Foley, J. K.; Pons, S. In Situ Infrared Spectroelectrochemistry. *Analytical Chemistry®* **1985**, *57*, 945A–956A.

3. Nichols, R. J. No Title. *Adsorption of Molecules at Metal Electrodes* **1992**.

4. Zamlynny, V.; Lipkowski, J. Quantitative SNIFTIRS and PM IRRAS of Organic Molecules at Electrode Surfaces. *Diffraction and Spectroscopic Methods in Electrochemistry* **2006**, *9*, 315–376.

5. Bewick, A.; Kunimatsu, K.; Pons, B. S.; Russell, J. W. Electrochemically Modulated Infrared Spectroscopy (EMIRS): Experimental Details. *Journal of Electroanalytical Chemistry and Interfacial Electrochemistry* **1984**, *160*, 47–61.

6. Ataka, K.; Hara, Y.; Osawa, M. New Approach to Electrode Kinetics and Dynamics by Potential Modulated Fourier Transform Infrared Spectroscopy. *Journal of Electroanalytical Chemistry* **1999**, *473*, 34–42.

7. Brevnov, D. A.; Hutter, E.; Fendler, J. H. Digital Signal Processing for Step-Scan Phase and Electrochemical Potential Double-Modulation Fourier Transform Infrared Spectrometry. *Applied Spectroscopy* **2004**, *58*, 184–192.

8. Budevska, B. O.; Griffiths, P. R. Step-scan FT-IR External Reflection Spectrometry of the Electrode/electrolyte Interface by Potential Modulation. *Analytical Chemistry* **1993**, *65*, 2963–2971.

9. Pharr, C. M.; Griffiths, P. R. Step-Scan FT-IR Spectroelectrochemical Analysis of Surface and Solution Species in the Ferricyanide/Ferrocyanide Redox Couple. *Analytical Chemistry* **1997**, *69*, 4665–4672.

10. Pharr, C. M.; Griffiths, P. R. Infrared Spectroelectrochemical Analysis of Adsorbed Hexacyanoferrate Species Formed During Potential Cycling in the Ferrocyanide/Ferricyanide Redox Couple. *Analytical Chemistry* **1997**, *69*, 4673–4679.

11. Zhou, Z.-Y.; Lin, S.-C.; Chen, S.-P.; Sun, S.-G. In Situ Step-scan Time-resolved Microscope FTIR Spectroscopy Working with a Thin-layer Cell. *Electrochemistry Communications* **2005**, *7*, 490–495.

12. Zhou, Z.-Y.; Sun, S.-G. In Situ Step-scan Time-resolved Microscope FTIR Spectroscopy Applied in Irreversible Electrochemical Reactions. *Electrochimica Acta* **2005**, *50*, 5163–5171.

13. Zhou, Z.-Y.; Tian, N.; Chen, Y.-J.; Chen, S.-P.; Sun, S.-G. In Situ Rapid-scan Time-resolved Microscope FTIR Spectroelectrochemistry: Study of the Dynamic Processes of Methanol Oxidation on a Nanostructured Pt Electrode. *Journal of Electroanalytical Chemistry* **2004**, *573*, 111–119.

14. Gong, H.; Sun, S.-G.; Chen, Y.-J.; Chen, S.-P. In Situ Microscope FTIRS Studies of CO Adsorption on an Individually Addressable Array of Nanostructured Pt Microelectrodes - An Approach of Combinatorial Analysis of Anomalous IR Properties. *Journal of Physical Chemistry B* **2004**, *108*, 11575–11584.

15. Gong, H.; Sun, S.-G.; Li, J.-T.; Chen, Y.-J.; Chen, S.-P. Surface Combinatorial Studies of IR Properties of Nanostructured Ru Film Electrodes Using CO as Probe Molecule. *Electrochimica Acta* **2003**, *48*, 2933–2942.

16. Chen, Y.-J.; Sun, S.-G.; Chen, S.-P.; Li, J.-T.; Gong, H. Anomalous IR Properties of Nanostructured Films Created by Square Wave Potential on an Array of Pt Microelectrodes: An in Situ Microscope FTIRS Study of CO Adsorption. *Langmuir* **2004**, *20*, 9920–9925.

17. Russell, A. E.; Lin, A. S.; O'Grady, W. E. In Situ Far-Infrared Evidence for a Potential Dependence of Silver-Water Interactions. *Journal of the Chemical Society, Faraday Transactions* **1993**, *89*, 195–198.

18. Russell, A. E.; Rubasingham, L.; Hagans, P. L.; Ballinger, T. H. Cell and Optics Design for in Situ Far-infrared Spectroscopy of Electrode Surfaces. *Electrochimica Acta* **1996**, *41*, 637–640.

19. Russell, A. E.; Williams, G. P.; Lin, A. S.; O'Grady, W. E. Far-Infrared Synchrotron Radiation for In Situ Studies of the Electrochemical Interface. *Journal of Electroanalytical Chemistry* **1993**, *356*, 303–306.

20. Hahn, F.; Mathis, Y.-L.; Bonnefont, A.; Maillard, F.; Melendres, C. A. In Situ Synchrotron Far-infrared Spectromicroscopy of a Copper Electrode at Grazing Incidence Angle. *Journal of Synchrotron Radiation* **2007**, *14*, 446–448.

21. Hahn, F.; Mathis, Y.-L.; Bonnefont, A.; Maillard, F.; Melendres, C. A. In Situ Synchrotron Far Infrared Micro-spectroelectrochemistry with a Grazing Angle Objective. *Infrared Physics and Technology* **2008**, *51*, 446–449.

22. Hahn, F.; Melendres, C. A. Synchrotron Infrared Reflectance Micro-spectroscopy Study of Film Formation and Breakdown on Copper. *Journal of Synchrotron Radiation* **2010**, *17*, 81–85.

23. Melendres, C. A.; Bowmaker, G. A.; Leger, J. M.; Beden, B. In-situ Synchrotron Far Infrared Spectroscopy of Surface Films on a Copper Electrode in Aqueous Solutions. *Journal of Electroanalytical Chemistry* **1998**, *449*, 215–218.

24. Melendres, C. A.; Bowmaker, G. A.; Leger, J. M.; Beden, B. No Title. *Proc. - Electrochem. Soc.* **1996**, *96*, 280–291.

25. Melendres, C. A.; Hahn, F.; Bowmaker, G. A. Oxyanion Adsorption and Competition at a Gold Electrode. *Electrochimica Acta* **2000**, *46*, 9–13.

26. Melendres, C. A.; Hahn, F. `In-situ' Observation of Halide Ion Adsorption on a Gold Electrode Using Synchrotron Far Infrared Spectroscopy. *Journal of Electroanalytical Chemistry* **1999**, *463*, 258–261.

27. Bowmaker, G. A.; Leger, J.-M.; Rille, A. L.; Melendres, C. A.; Tadjeddine, A. Investigation of the Vibrational Properties of OCN- on a Silver Electrode by in Situ Synchrotron Far Infrared Spectroscopy and Visible-infrared Sum Frequency Generation Spectroscopy. *Journal of the Chemical Society - Faraday Transactions* **1998**, *94*, 1309–1313.

28. Melendres, C. A.; Beden, B.; Bowmaker, G. A. Far Infrared Spectroscopy of a Platinum Electrode "In-situ" Using a Synchrotron Source. *Journal of Electroanalytical Chemistry* **1995**, *383*, 191–193.

29. Korzeniewski, C.; Severson, M. W.; Schmidt, P. P.; Pons, S.; Fleischmann, M. Theoretical Analysis of the Vibrational Spectra of Ferricyanide and Ferrocyanide Adsorbed on Metal Electrodes. *Journal of Physical Chemistry* **1987**, *91*, 5568–5573.

30. Pons, S. Infrared Spectroelectrochemistry of the Fe(CN)4- 6/Fe(CN)3- 6. *Journal of Electroanalytical Chemistry* **1984**, *160*, 369–376.

31. Borg, S. J.; Best, S. P. Spectroelectrochemical Cell for the Study of Interactions Between Redox-activated Species and Moderate Pressures of Gaseous Substrates. *Journal of Electroanalytical Chemistry* **2002**, *535*, 57–64.

32. Salsman, J. C.; Kubiak, C. P. Infrared Spectroelectrochemical Investigations of Ultrafast Electron Transfer in Mixed-valence Complexes. *Spectroelectrochemistry* **2008**, 123–144.

33. Evgenij Barsoukov, J. R. M. *Impedance Spectroscopy: Theory, Experiment, and Applications*; John Wiley & Sons, Ltd, 2005.

34. Bard, A. J.; Faulkner, L. R. No Title. *Electrochemical Methods: Fundamentals and Applications* **1980**.

35. Skoog, D. A. Principles of Instrumental Analysis. In; CBS College Publishing: New York, 1985; p. 341.

36. Venyaminov, S. Y.; Prendergast, F. G. Water (H2O and D2O) Molar Absorptivity in the 1000–4000 cm−1Range and Quantitative Infrared Spectroscopy of Aqueous Solutions. *Analytical Biochemistry* **1997**, *248*, 234–245.

37. Hubbard, A. T.; Anson, F. C. Linear Potential Sweep Voltammetry in Thin Layers of Solution. *Analytical Chemistry* **1966**, *38*, 58–61.

38. Keller, H. E.; Reinmuth, W. H. Potential Scan Voltammetry with Finite Diffusion. Unified Theory. *Analytical Chemistry* **1972**, *44*, 434–442.

39. Aoki, K.; Tokuda, K.; Matsuda, H. Theory of Linear Sweep Voltammetry with Finite Diffusion Space. *Journal of Electroanalytical Chemistry and Interfacial Electrochemistry* **1983**, *146*, 417–424.

40. Micka, K.; Kratochvilová, K.; Klíma, J. Electrolysis at a Disc Electrode in a Thin Electrolyte Layer. *Electrochimica Acta* **1997**, *42*, 1005–1010.

41. Roušar, I.; Anastasijević, N. A. Depletion Effect in the Thin Layer Cell for in Situ Spectroelectrochemical Study of Faradaic Reaction with Special Reference to Oxygen Reduction. *Electrochimica Acta* **1988**, *33*, 1157–1160.

42. Anastasijević, N. A.; Roušar, I. Diffusion Relaxation Time of a Thin Layer Cell with a Disk Electrode Arrangement. *Electrochimica Acta* **1989**, *34*, 887–888.

43. Oglesby, D. M. Thin Layer Electrochemical Studies Using Controlled Potential or Controlled Current. *Analytical Chemistry* **1965**, *37*, 1312–1316.

44. Szabo, A.; Cope, D. K.; Tallman, D. E.; Kovach, P. M.; Wightman, R. M. Chronoamperometric Current at Hemicylinder and Band Microelectrodes: Theory and Experiment. *Journal of Electroanalytical Chemistry* **1987**, *217*, 417–423.

45. Mirkin, M. V Theory. *Scanning Electrochemical Microscopy* **2001**.

46. Miller, L. M.; Smith, R. J. Synchrotrons Versus Globars, Point-detectors Versus Focal Plane Arrays: Selecting the Best Source and Detector for Specific Infrared Microspectroscopy and Imaging Applications. *Vibrational Spectroscopy* **2005**, *38*, 237–240.

CHAPTER 7

SYNCHROTRON INFRARED RADIATION FOR ELECTROCHEMICAL EXTERNAL REFLECTION TIME-RESOLVED STEP-SCAN FOURIER TRANSFORM INFRARED SPECTROSCOPY

7.1. Introduction

This final experimental results chapter describes the continued effort to improve the time-resolution of *in-situ* spectroelectrochemical external reflectance infrared spectroscopy. Briefly, this has been achieved by utilizing a synchrotron infrared radiation source coupled to a true ultramicroelectrode in a thin-cavity external reflectance cell. To reiterate the point made in previous chapters, the utilization of mid and far infrared radiation from synchrotron sources is now well-established and described by several recent reviews.[1–3] The relative advantages of synchrotron infrared radiation compared to thermal sources (*e.g.* Globars) have been previously addressed in detail (Chapter 6), particularly with respect to synchrotron infrared radiation enhanced spatial resolution in microspectroscopy.[4]

Although infrared spectroelectrochemistry (SEC) is now a mature field with a host of well-developed external[5] and internal[6] reflection techniques, most studies to date have typically employed large electrodes to facilitate high photon throughput which prevents the study of fast kinetic electrochemical events from being properly performed. This is a consequence of the fact that the establishment of the interfacial potential is determined by the cell's time constant which is the product of the electrolyte resistance, R, and the electrode capacitance, C. As the time constant increases with increasing working electrode area, only very slow processes (on the order of seconds) can be meaningfully studied as a result. Acquisition of spectroscopic data with

temporal resolution smaller than five times the cell constant (5xRC) results in the convolution of a time dependent thermodynamic parameter (electrode potential) and the kinetically controlled response.[7–9] Two approaches exist to reach faster time resolution in infrared spectroelectrochemical studies. Firstly, the use of internal reflection geometry and surface enhanced infrared absorption spectroscopy (SEIRAS) eliminates the highly resistive electrolyte layers found in external reflection methods such as PM-IRRAS. There are several reports where SEIRAS has permitted the study of kinetic processes on the ~1-50 millisecond time scale.[10–12] It is possible for picosecond time-resolved SEIRAS on electrode surfaces through laser-induced temperature jump experiments,[13,14] although this method is not readily amenable to precise control of the electrode's potential. Alternatively, the time constant can be reduced below a microsecond if an ultramicroelectrode (UME) is used. Working with an UME requires the use of reflectance-mode microspectroscopy which can be disadvantageous as the inherently more complex optics of a microscope can lead to higher relative throughput losses compared to internal reflectance SEIRAS.

Sun and co-workers have succeeded in coupling FTIR microscopy, a conventional thermal source, and large ultramicroelectrodes (radius 200 μm) while reporting studies of processes occurring on electrode surfaces on the time scale of tens to hundreds of microseconds.[7,15,16] The particular electrochemical systems Sun *et al*. chose to study, however, had surface enhancement *via* anomalous infrared enhanced spectroscopy (AIRES).[17] It is likely that further improvements in their temporal resolution were prohibited by insufficient signal to noise levels when equivalent experiments using smaller platinum UMEs were attempted. Signal to noise values will be increasingly limited by the ability of the instrument to focus large photon

intensity onto very small areas providing the motivation to move to non-conventional sources of infrared radiation such as synchrotron infrared radiation.

Herein the use of synchrotron infrared radiation as a source for fast, step-scan spectroelectrochemical measurements is described. The high brilliance of synchrotron infrared radiation should, in principle, offer lower noise levels compared to thermal sources when using small electrodes (< *ca.* 70 μm). However, this advantage may be offset by other factors unique to synchrotron infrared radiation particularly source noise inherent to the ring current. To investigate the utility of synchrotron infrared radiation for step-scan spectroelectrochemistry, 25 μm gold UMEs have been prepared and used to analyze a simple electrochemical system. Once again, the ferri/ferrocyanide redox couple from Chapter 6 will be employed for its clear change in spectral response as a function of potential. Time-resolved synchrotron infrared radiation measurements are combined with a detailed analysis of the mass-transport controlled electrochemical conversion within a restricted volume geometry. These results are also used to discuss methods to mitigate the effects of source-intensity variation intrinsic to synchrotrons operating in beam decay mode. It is demonstrated that the present configuration has a minimum time resolution (5xRC) of less than one microsecond and the step-scan measurement has a limit of detection of less than 4×10^{-14} moles of ferrocyanide. This detection limit is discussed in terms of the further improvements and developments needed to achieve the goal of microsecond-resolved infrared detection of sub-monolayer quantities on electrocatalytic surfaces.

7.2. Experimental

7.2.1. Reagents and Solutions

Potassium hexacyanoferrate(III) ($K_3Fe(CN)_6$, ≥ 99.0% trace metals basis), potassium hexacyanoferrate(II) trihydrate ($K_4Fe(CN)_6 \cdot 3H_2O$, ≥ 99.0% trace metals basis), and sodium fluoride (99.998%) were purchased from Sigma Aldrich and were used as received. All aqueous and electrolyte solutions were prepared from Milli-Q water (> 18.2 MΩ cm^{-1}).

7.2.2. Experimental *In-situ* Spectroelectrochemical Cell

The three electrode flow-through *in-situ* spectroelectrochemical (SEC) cell was constructed similarly to the one described in Chapter 6 with the following modifications. The cell was machined from a 25 mm diameter, 5 mm thick PVC plastic disc for its mechanical and electrical insulating properties and supported for the experiments by an aluminum microscope plate. The 50 μm diameter working electrode (Au, 99.998% metals basis, Alfa Aesar) and reference electrode (Ag, 250 μm diameter, 99.9985% metals basis, Alfa Aesar) were first embedded in fiberglass resin (3M Bondo Fiberglass Resin) before being sealed in the PVC disc. The top (reflecting) surface was first machined parallel to the bottom of the disc and then polished to a mirror finish using successively finer grade diamond suspensions (Leco Corporation, St. Joseph MI,US) down to 0.5 μm.

From Figure 7.1, one can see the assembled *in-situ* SEC cell, with a thin cavity created by compressing a nominally 5 μm thick PTFE gasket between a CaF_2 IR window (1 mm thick and 25 mm diameter) and the main body of the cell by tightening a thin aluminum clamping ring to the microscope plate adapter. Through this arrangement a thin cavity of 15 μm was determined

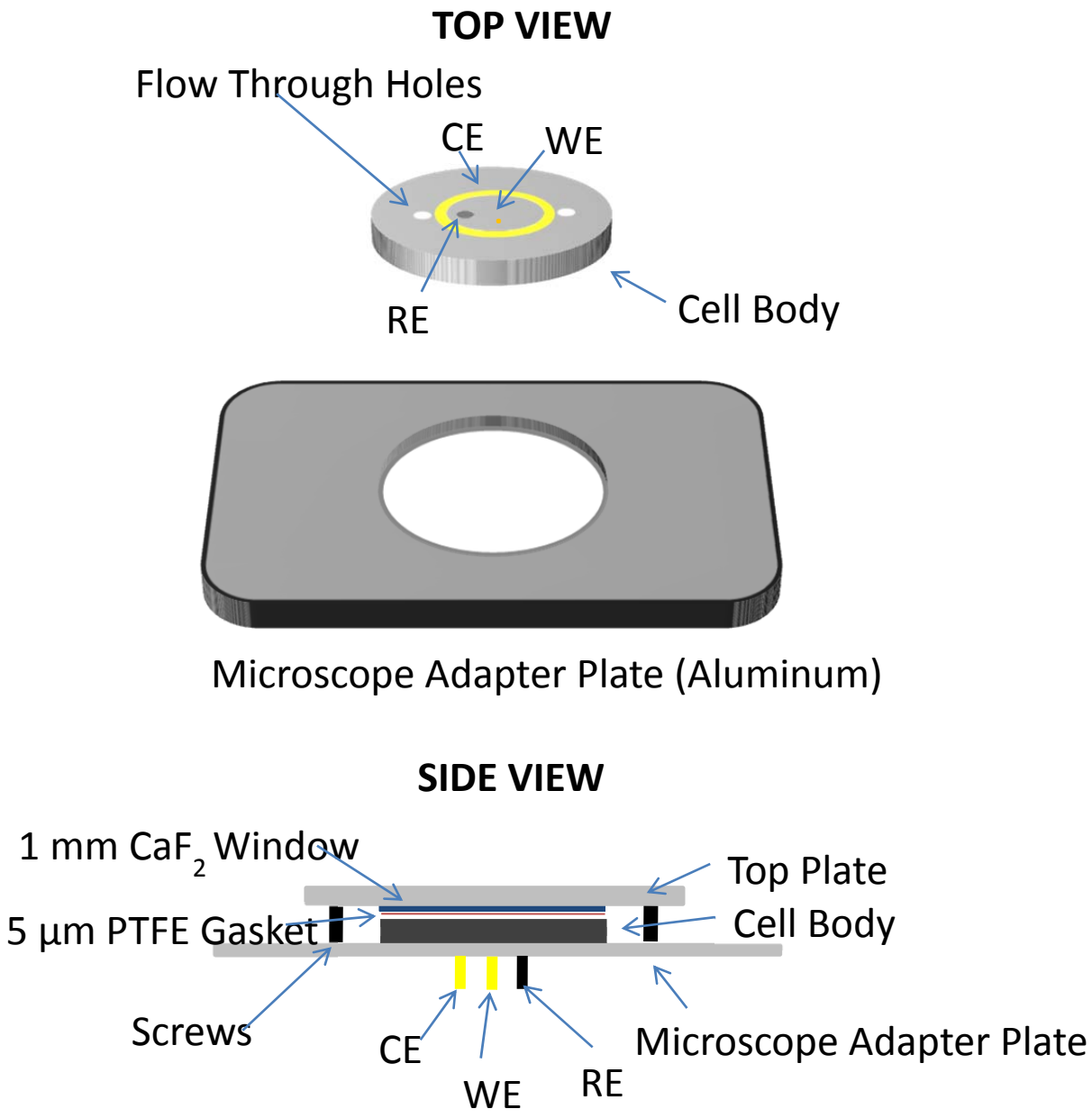

Figure 7.1. Diagram of the *in-situ* spectroelectrochemical (SEC) cell. The thin-cavity electrochemical cell was prepared by compressing a nominally 5 µm thick PTFE gasket between the main cell body and an infrared window (CaF_2, 1 mm thick, 25 mm diameter). The working electrode (WE) and counter electrode (CE) were made from 25 µm radius gold wire and the quasi-reference electrode (RE) from silver wire.

from interference fringes obtained in a dry cell and the equation $b = n/(2\Delta\nu)$, where b is the path length, n is the number of fringes, and $\Delta\upsilon$ is the wavenumber spacing of the fringes. This method was discussed in more detail in the Experimental section of Chapter 6.

7.2.3. Electrochemical Measurements

The electrochemical characterization of the *in-situ* SEC cell was performed on the bench using an AUTOLAB PGSTAT302N (Metrohm Autolab B.V., Netherlands). To determine the time constant of the electrochemical cell, electrochemical impedance spectroscopy was implemented with a 0.5 M NaF electrolyte solution.[18] It was determined that the time constant was 0.1 μs, implying the time needed to establish the desired potential at the interface was 0.5 μs. Further characterization of the electrochemical system was carried out by performing cyclic voltammetry (CV) and chronoamperometry (CA) with 0.5 M NaF electrolyte solutions containing varying concentrations of ferro/ferri-cyanide. All CVs were measured at a scan rate of 10 mV s^{-1} unless otherwise indicated.

For the *in-situ* SEC measurements at the synchrotron, a HEKA PG 590 Potentiostat (HEKA, Mahone Bay, NS, Canada) was used and controlled by software written in the LabVIEW (National Instruments Corporation, Austin, TX, USA) programming environment.

7.2.4. Fourier Transform Infrared Measurements

Fourier Transform Infrared (FTIR) spectroscopy measurements were collected at the Mid-IR Beamline facilities located at the Canadian Light Source (Beamline 01B1-01, Canadian Light Source, Inc., Saskatoon, SK, Canada). The beamline end station consists of a Bruker Optics Vertex 70v FTIR Spectrometer (Step-Scan capable) coupled to a Hyperion 3000 IR

Microscope (Bruker Optics, Billerica, MA, USA). Light was focused and collected in reflectance mode using a 15x Schwarzschild objective (NA 0.4). The collected light was measured using a narrowband fast DC coupled mercury cadmium telluride (MCT) (liquid nitrogen cooled) Kolmar (Kolmar Technologies, Inc., Newburyport, MA, USA) detector with Bruker preamp. An optical band pass filter was constructed and placed in-front of the microscope consisting of a Long Pass Edge Filter (4.50-25 μm) and a LiF window (both windows from ISP Optics Corporation, Irvington, NY, USA) to provide a small optical window to decrease measurement times and to prevent spectral aliasing.

7.2.5. Step-Scan Measurements

In regular FTIR spectroscopic measurements using modern Michelson based FTIR spectrometers, a mirror is continuously moved and the interferogram sampled as a function of mirror position, δ. This limits the time-resolution of FTIR measurements to the speed of the moveable mirror, which is on the order of the millisecond time scale. This constraint is lifted when instead of sampling the interferogram during a continuous mirror drive, the movable mirror stops are predetermined positions and at each position time-resolved data are collected. Once the mirror has stepped to all the positions and the time resolved data acquired, an interferogram can be reconstructed from each temporal period with a resolution between microseconds and nanoseconds. The actual minimum time resolution in a step-scan configuration is limited by the bandwidth of the detector, preamplifier and digitization rather than the speed of the moveable mirror drive.

The time-resolved single-sided step-scan interferograms were collected at a spectral resolution of 16 cm^{-1} in the wavenumber region 2400-1250 cm^{-1} (corresponding to the

transmission range of the optical bandpass filter). With these parameters and a phase resolution of 64 cm^{-1} a total of 170 interferogram points (mirror positions) were measured with a temporal resolution of 100 μs for a total of 1.5 s (15000 points) of time-resolved data per interferogram scan. Each scan took roughly 10 minutes to acquire and was repeated a total of 256 times to increase the signal to noise of the measurement over the course of two days. More information on the timing and acquisition of the data will be discussed in the following section.

After all the time-resolved infrared measurements were collected, the data was converted to single beam energy curves using the Fourier Transform algorithms in OPUS (Bruker) 7.2 software (Mertz phase correction, Blackman-Harris 3-term apodization and a zerofilling factor of 2).

7.2.6. Interfacing Hardware and Software

The most challenging aspect of this experiment was setting up and interfacing all the various elements of the hardware and software. Specifically, the main challenge was interfacing the FTIR spectrometer and the potentiostat to ensure consistent and synchronized measurements.

The *in-situ* time-resolved step-scan experiment was directed by several LabVIEW Virtual Instruments (VI) and two National Instruments multifunctional Data Acquisition (DAQ) cards PCI 6251 X Series and USB 6009 devices as depicted in Figure 7.2. One VI was solely responsible for the timing of the experiment by applying the appropriate trigger signal to start the infrared data acquisition in OPUS and the potentiostat to apply the potential step to the *in-situ* SEC cell. This master trigger signal was gated by the Vertex 70v FTIR spectrometer (to ensure the mirror had stepped and settled at the appropriate mirror position to begin the infrared

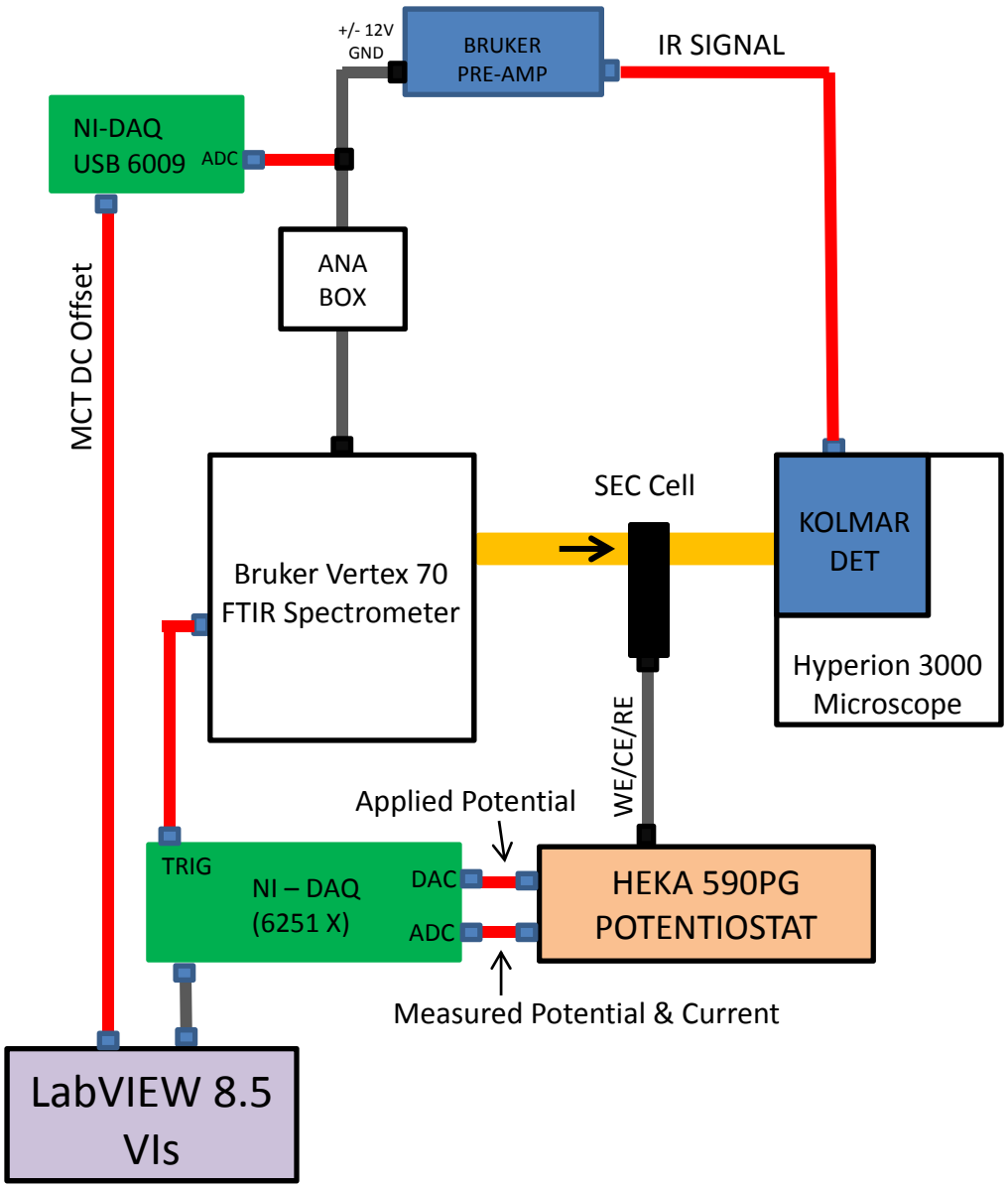

Figure 7.2. Interfacing diagram for the *in-situ* spectroelectrochemical step-scan time-resolved Fourier Transform infrared synchrotron radiation measurements.

measurement) and also started the acquisition of the resulting electrochemical data, the magnitude of the synchrotron beam current and average DC value of the Kolmar MCT IR detector. The two DAQ devices had different sampling rates depending on the specific data they were measuring. For example, the short time current transient measurements were measured using the PCI 6251 X Series card and for the long average DC MCT values the USB 6009 device. A routine was setup between all the VIs and OPUS to be able to repeat measurements with minimal interaction from the user.

The Kolmar MCT IR detector was made to be DC coupled by adjusting the appropriate jumper settings on the Bruker Pre-Amp and Bruker ADC device (ANA-101). To monitor the DC level of the MCT detector, the raw infrared signal was measured by the USB 6009 before being digitized by the ANA-101 device (*i.e.* between the pre-amp and ADC device).

7.3. Results and Discussion

7.3.1. Electrochemistry in Confined Thin Cavity Geometry

The thin layer geometry of the spectroelectrochemical cell used in these experiments creates a restricted diffusion space. In this environment, there exist semi-infinite diffusional conditions extending radially from the electrode circumference but there is a finite diffusion volume perpendicular to the electrode surface (directly above the electrode). Cyclic voltammetry (CV) measurements were made to emphasize the effect this thin-geometry has on the electrochemical properties of the *in-situ* SEC cell. Figure 7.3 provides the cyclic voltammogram measurements with a 25 μm radius gold UME in 10 mM ferricyanide (0.5 M NaF supporting electrolyte) with both a 14 μm cavity (as determined by infrared measurements

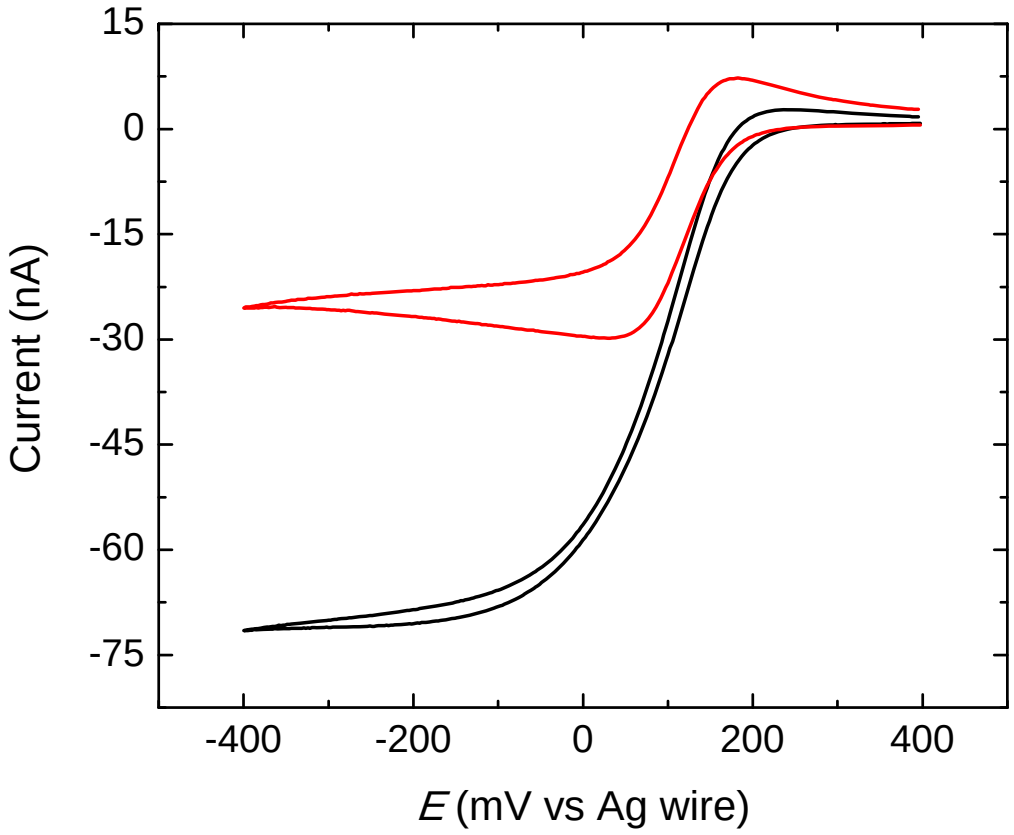

Figure 7.3. Cyclic voltammetry for 10 mM $Fe(CN)_6^{-3}$ in 0.5 M NaF supporting electrolyte using an embedded 25 μm radius Au ultramicroelectrode in a 5 mm thick cavity (black line) and a 14 μm thick cavity (red line). The scan rate in both cases was 10 mV s^{-1}.

described in Chapter 6) and a 5000 μm cavity. One can see that in the thicker cavity there is enhanced mass-transfer, which arises from the fact that the diffusion geometry is best described as quasi-hemispherical, when electrolysis is occurring at the electrode. As a result, nearly ideal steady-state current behaviour is reported and is consistent with expectations for electrochemistry using UMEs.[19] This electrochemical behaviour drastically changes in the experiments measured using the 14 μm cavity. From Figure 7.3, it should be noticed that much smaller limiting currents are observed and the overall shape of the CV exhibits current peaks rather than the sigmoidal shape measured in the thick cavity configuration. This highlights the fact that during the experiments performed in the restricted volume, the growing diffusion layer fully encompasses the cavity thickness depleting the flux of redox species to the electrode. As such, the electrochemistry measured in the thin cavity geometry of the *in-situ* SEC cell experiences mass-transfer limitations to a much greater extent than those experiments performed in the thicker cell volume.

To further analyze this effect of cavity thickness on the electrochemical behaviour, it is convenient to define the spatial distribution of $Fe[CN]_6^{-3}$ concentrations in the thin cavity volume by using cylindrical coordinates, $C(r,z)$, where the *r* and *z* axes run parallel and perpendicular to the electrode surface respectively placing the origin at the center of the electrode's surface. This treatment is similar to the approach taken in the previous chapter. The initial condition is easily defined when only the oxidized half of the ferri/ferrocyanide couple ($Fe(CN)_6^{-3}$) is present throughout the cell volume. This is accomplished, experimentally, by applying a potential substantially positive of the ferri/ferrocyanide formal potential for an adequate period of time. Upon, stepping to a potential sufficiently negative of the formal potential,

$$C(r, z=0, t)=0 \qquad (r \le r_e,\ t>0),$$

and the generation of $Fe(CN)_6^{4-}$ will be mass-transport controlled. The diffusion equation describing this situation for an embedded disk electrode of radius, r_e, under a potential bias well negative of the formal potential of ferri/ferrocyanide is

$$\frac{\partial C(r,z,t)}{\partial t} = D\left[\frac{\partial^2 C(r,z,t)}{\partial r^2} + \frac{1}{r}\frac{\partial C(r,z,t)}{\partial r} + \frac{\partial^2 C(r,z,t)}{\partial z^2}\right] \tag{7.1}$$

under these additional initial and boundary conditions;

$$C(r,z,0) = C^*$$

$$\lim_{r\to\infty} C(r,z,t) = C^*$$

$$\lim_{z\to h} \frac{\partial C(r,z,t)}{\partial z} = 0$$

where D and C^* are the diffusion coefficient and the bulk concentration of the redox species being consumed (ferricyanide, $Fe(CN)_6^{-3}$, in this case) and where h represents the cavity thickness. In Chapter 6, the electrode used was 0.5 mm in diameter and Equation 7.1 was treated under two limiting cases. At short times, the current was dominated by finite volume, linear diffusion in the thin cavity between the electrode surface and the infrared window. This resulted in the concentration of the diffusing analyte to become nearly exhausted in the cavity rather quickly. As the electrolysis proceeded, radial diffusion continued to supply a state-state flux of the electroactive analyte and dominated the current transients at much longer times. In the previous chapter it was concluded that the time at which mass transfer switched from primarily linear diffusion to primarily radial diffusion, decreased with decreasing electrode radius. By moving to an order of magnitude smaller electrode, a more satisfactory model of this diffusion problem is required and is the focus of the rest of this section.

This problem of diffusion to an embedded disk electrode in restricted geometries is often modeled by using finite element (FE) simulations and finds many applications in negative feedback scanning electrochemical microscopy (SECM) studies.[20–22] To aid in the analysis of the diffusion problem described above (Equation 7.1), commercial finite-element software package (FlexPDE) was employed to model and simulate the results. The code for these simulations is modified from that provided by Mirkin *et al*.[22] Simulations were performed for both thin and thick cavity geometries, and the simulated results were compared to experimental data. From Figure 7.4 one can see the semi-logarithmic plots of both the simulated and measured current transients for the 25 μm radius UME and 10 mM $Fe(CN)_6^{-3}$. Comparisons between the simulation and experiment for the larger cavity allows for evaluation of the microelectrode response. This also provided a means to assess the appropriateness of the simulation routine by comparing the results described by the studies of Shoup and Szabo who used the following equations for the current arising from semi-infinite diffusion to a disk UME[23] (equivalent to the thick cavity cell geometry),

$$i(\tau) = 4nFDC^{*}r_e f(\tau) \tag{7.2}$$

where

$$f(\tau) = 0.7854 + 0.8862\tau^{-1/2} + 0.2146e^{-0.782\tau^{-1/2}} \tag{7.3}$$

and

$$\tau = \frac{4Dt}{r_e^2} \tag{7.4}$$

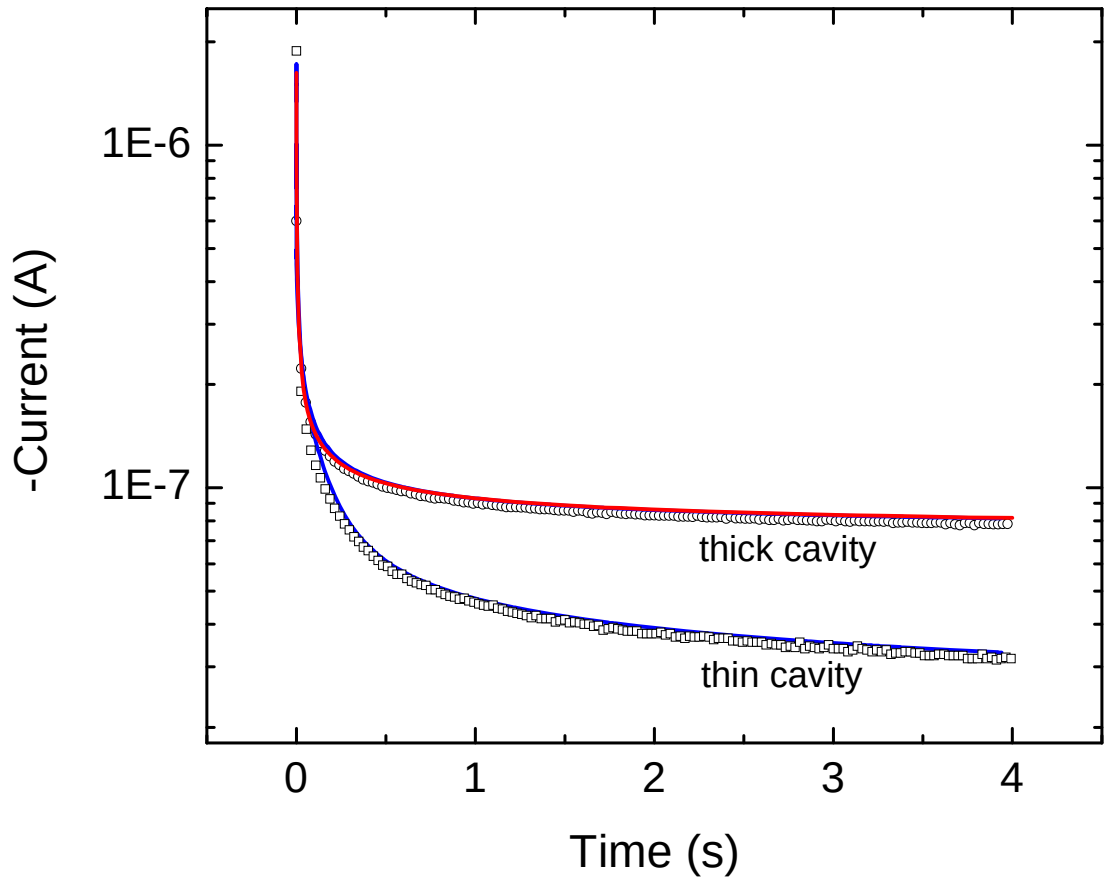

Figure 7.4. Current transients for an embedded 25 µm radius Au ultramicroelectrode in 10 mM $Fe(CN)_6^{3-}$ with 0.5 M NaF supporting electrolyte. The larger magnitude curves are for a thick (5 mm) cavity and the smaller currents are for a 14 µm thick cavity using the same *in-situ* SEC cell. Open data points are experimental data, blue lines are simulations using finite difference methods, and the solid red line is calculated from Equation 7.2.

As is shown in Figure 7.4, the simulated current response and the calculated current transient are almost superimposable and compared to the experimental results, neither deviate by more than ~3-4%, which is in very close agreement to the acknowledged ~1% error known to be applicable in the results of Shoup and Szabo (Equations 7.2-7.4).[23] Similar results have been reported by Mauzeroll *et al.* when modeling the response of SECM approach curves.[24] A possible explanation for the slight differences in response measured experimentally with those modeled using r_e = 25 μm is most likely due to the polishing procedure used in the preparation of the SEC cell which slightly distorts the electrode geometry. The finite difference simulations and experimentally measured $i(t)$ curves for the 14 μm (thin) cavity are also presented in Figure 7.4. Here, it is easily seen that there is good agreement between the simulation and experiment results and the difference in the total charge passed (integral of the transients) for the two plots is less than 2.5%. In accordance with the cyclic voltammetry reported in Figure 7.3, the steady-state current response observed for the thick cavity experiment is not observed in the thin cavity and the limiting current is attenuated by roughly a factor of one-third.

It is possible to assess the amount of electrogenerated material produced as a result of the potential step by utilizing the simulation results. Also, general comparisons between the simulated electrochemical signal and the simulated infrared spectroscopy can be made. It is important to remember that these two analytical signals will be significantly different as the former will be dominated by semi-infinite diffusion to the perimeter of the electrode whereas the measurements obtained through infrared microspectroscopy are indifferent to this source of $Fe(CN)_6^{-3}$ electrolysis. Figure 7.5 highlights this edge effect by providing a contour map of the simulated $Fe(CN)_6^{-4}$ concentration in the electrode vicinity one second after the potential step. In the snapshot provided in Figure 7.5, one can observe a pronounced concentration differential

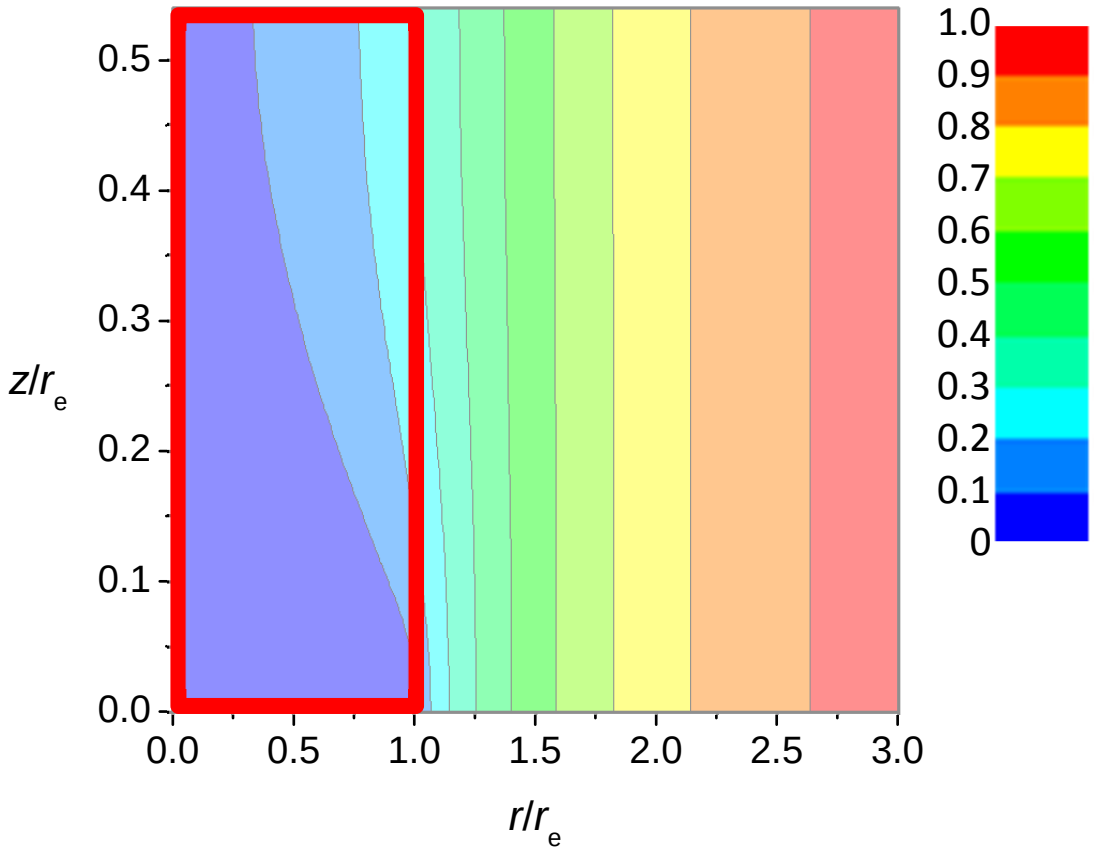

Figure 7.5. Contour maps of the simulated $Fe(CN)_6^{-3}$ normalized concentration profiles within the thin (14 μm) *in-situ* spectroelectrochemical cell one second after the potential step. The red box defines the cross-section of the cavity volume that is sampled by the incident infrared radiation from the microscope and objective used in these experiments.

extending radially along the electrode mantle ($z = 0$, $r/r_e > 1$) which gives rise to a large flux of material to the electrode circumference. The volume sampled by the infrared incident radiation is delimited by the solid red line in Figure 7.5. It can be seen that this cavity volume does not contain large concentration gradients but instead shows a much more uniform distribution of $Fe(CN)_6^{-4}$ concentrations. It is evident that the majority of the charge measured at long times at the electrode during the potential step arises from edge effects. It should also be noted that the current distribution on the electrode surface is heterogeneous and is heavily weighted around the electrode circumference. Again, it is important to realize that species electrogenerated at the edges will not be sampled by the infrared radiation. This is because they remain excluded from the volume element bounded by the CaF_2 infrared window and the UME surface.

In order to better illustrate the differences in the measured infrared and electrochemical signals, the simulated diffusion results for the thin cell geometry were used to determine the number of moles of ferrocyanide, $Fe(CN)_6^{-4}$, produced during the potential step. This is a simple procedure for the purely electrochemical signal and is achieved by numerically integrating the current transient and applying Faraday's Law ($Q = nF$). However, to simulate the signal response expected from the infrared measurements, the concentration contour maps at different times (from simulation) were integrated in cylindrical coordinates within the region bounded by the electrode surface and the infrared window with respect to both spatial variables (*i.e.* z and r). The resulting areas were then normalized by the area at $t = 0$ to determine the fraction of ferricyanide converted and finally scaled by the number of moles initially present within the volume element based on the initial bulk concentration. The results from Chapter 6 with much larger electrode surfaces showed excellent agreement between the experimentally measured results and the calculated response for finite linear diffusion (*i.e.* radial diffusion could

be considered negligible). From the independent work of Micka *et al.*[25] and Olgesby *et al.*[26] the corresponding mass-transfer limited, chronoamperometric response for finite linear diffusion can be expressed analytically as follows:

$$i(t) = \frac{2nFADC^*}{h} \sum_{m=0}^{\infty} exp\left[-\left(m+\frac{1}{2}\right)^2 \left(\frac{\pi}{h}\right)^2 Dt\right] \tag{7.5}$$

where *A* and *h* are the area of the embedded electrode and the thickness of the cavity respectively. From Figure 7.6, the three simulated responses (calculated number of ferrocyanide moles produced) are plotted as a function of time for comparative purposes. As expected, the signal from the current transient greatly exceeds the two other curves and, as indicated in the inset of Figure 7.6, increases with respect to time. In contrast, the finite linear-diffusion treatment depicts the eventual conversion of all of the $Fe(CN)_6^{-3}$ initially present within the thin cavity volume and has essentially no contribution from species diffusing from outside this space. This result plateaus after the conversion of 2.7 x 10^{-13} moles, approximately 0.5 seconds after the potential step perturbation. The finite differences solution of this diffusion problem can also simulate the change in the concentration of ferricyanide species in the thin-volume cavity which would be in the beam path of the infrared radiation. Figure 7.6 shows that the simulated infrared response is similar to the finite-volume transient albeit with a systematically smaller (~13 %) extent of conversion. The rationalization for this result is somewhat intuitive by considering the case of finite linear diffusion where the depletion zone rapidly extends across the entire cell cavity and exhaustively consumes the ferricyanide. However, if the radius of the electrode is comparable to the thickness of the electrolyte cavity, as is the case presented here, the depletion zone of $Fe(CN)_6^{-3}$ rapidly extends radially from the electrode center and the cavity volume above

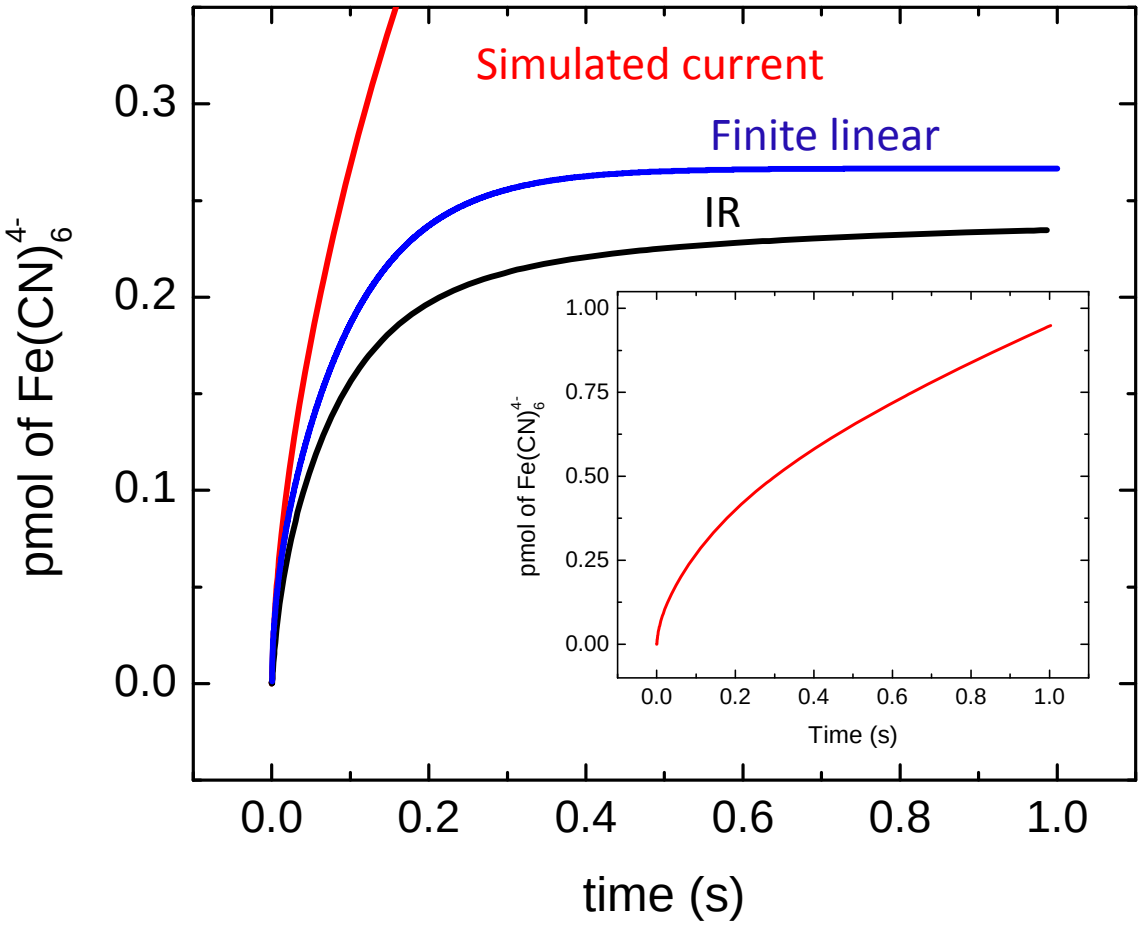

Figure 7.6. Comparison of the predicted amount of $Fe(CN)_6^{-4}$ produced as a result of the potential step in the thin cavity *in-situ* spectroelectrochemical cell. The red line is the result of integrating the current transient (inset and main body), the blue line is the calculated response assuming finite linear diffusion, and the black line is the simulated infrared response.

the electrode cannot be completely electrolyzed within the duration of the experiment. In the remainder of this chapter, the experimental result obtained *via* step-scan time-resolved Fourier Transform Infrared *in-situ* spectroelectrochemistry will be compared to the simulated results in an effort to demonstrate the capabilities of step-scan synchrotron infrared radiation for electrochemical studies.

7.3.2. Fourier Transform Infrared Step-Scan Spectroelectrochemistry with Synchrotron Radiation in Decay Mode

As mentioned previously it is important to have an electroactive molecule that has measurable infrared vibrational bands that respond to electrochemical perturbation in order to perform *in-situ* spectroelectrochemical studies. The ferri/ferrocyanide redox couple is one such molecule owing to the clear spectral shift in the cyanide stretches of the reduced and oxidized forms which are both baseline resolved from water absorption bands.[27–30] In Chapter 6, subtractively normalized infrared spectra, $\Delta S/S = (S_{VAR} - S_{REF})/S_{REF}$, for the ferri/ferrocyanide redox system were presented for continuous rapid-scan interferometry. The spectra obtained using step-scan interferometry exhibit a strong peak at 2038 cm^{-1} which is assigned to ferrocyanide (Figure 7.7a), similar to the results presented in Chapter 6. A much weaker band at 2115 cm^{-1} is attributable to ferricyanide and becomes more pronounced with higher spectrometer resolution (Figure 7.7b). Figure 7.7a also demonstrates the advantage of increased brilliance by overlaying the synchrotron infrared radiation spectrum with an equivalent measurement made using a conventional thermal source. Any analytical signal in the latter spectrum is masked by significant noise levels. While it is clear from Figure 7.7 that step-scan interferometry using synchrotron infrared radiation is suitable to follow the ferro/ferricyanide

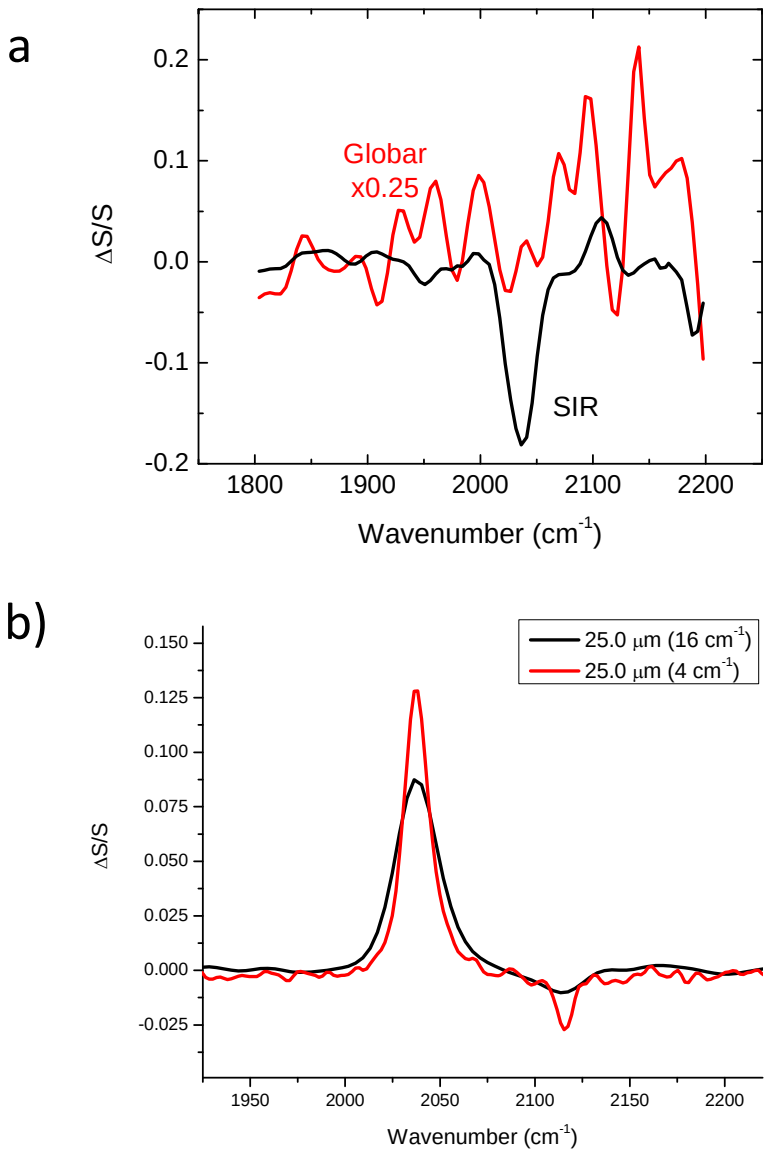

Figure 7.7. a) Step-scan spectra for the ferro/ferricyanide system in the spectroelectrochemical cell at t = 1 second using an embedded 25 μm radius Au ultramicroelectrode in a 14 μm thick cavity. The strong upward band at 2040 cm^{-1} represents the infrared signature for the corresponding cyano ligands for ferrocyanide, whereas the downward band at 2115 cm^{-1} (more visible at 4 cm^{-1} resolution in b)) for ferricyanide. A comparison is made between the co-addition of 35 synchrotron infrared radiation interferograms (black line) and an equivalent number of interferograms using a conventional thermal source (red line).

conversion it is important to also consider data acquisition and noise limitations whose general relevance to step-scan interferometry are described in Chapter 3 and elsewhere.[31–33]

As discussed at the beginning of this chapter, the use of a true ultramicroelectrode enables one, in theory, to approach microsecond temporal resolution (of both electrochemical and infrared measurements) through implementation with step-scan interferometry. Step-Scan Fourier Transform infrared spectroscopy for fast processes is a well-established experimental technique; however, there have been very few reports in the literature of step-scan infrared spectroscopy using synchrotron infrared radiation.

In-depth discussions of data acquisition and noise limitations in step-scan interferometry have been previously discussed in Chapter 3, however it is prudent to discuss two aspects that are particularly relevant to this case study. The successful utilization of step-scan spectroscopy requires a system that exhibits long-term stability and repeatable responses to a triggered perturbation. In the measurements described herein, a double potential step ($E_{+400\ \mathrm{mV}} \rightarrow E_{-400\ \mathrm{mV}}$ and $E_{-400\ \mathrm{mV}} \rightarrow E_{+400\ \mathrm{mV}}$) was applied to the ultramicroelectrode at each of the 170 individual mirror positions constituting a complete single interferogram. In the process of acquiring 256 individual interferograms, the potential was stepped approximately 90 000 times across the ferri/ferrocyanide formal potential. To ensure the stability of the system would not adversely affect the step-scan measurements, the current transients for each potential step were continuously recorded through the experiment. Numerical integration of the resulting $i(t)$ curves, to measure the total charge passed, revealed a decrease of only ~15% over the course of the two-day experiment indicating remarkable electrochemical stability.

The second aspect related to the data acquisition and noise limitations in step-scan interferometry is associated with the infrared radiation source. Unlike a conventional thermal

source (Globar), the infrared radiation from a synchrotron operating in normal mode (as was the case at the Canadian Light Source at the time of the experiments) provides a source intensity that decays exponentially with a time constant of roughly 40 hours. At the time of these measurements, the storage ring was refilled every eight hours to a maximum beam current of 200 mA and decayed by about 25% over this period. Figure 7.8 illustrates how this affects data processing through a schematic representation of the time course of a step-scan experiment. The position of the moveable mirror is plotted as a function of time. Each rectangular point corresponds to the triggered acquisition of t = 1.5 seconds worth of data. The black dotted box in Figure 7.8 encloses a complete set of mirror positions representing a single block of 100 μs time resolved inteferograms. A single block of data, *i.e.* one interferogram, requires about 10 minutes of measurement time and is repeated N = 256 times resulting in a total experiment time of nearly 48 hours. Two different data processing approaches were employed to explore the potential impact of source intensity variation throughout the course of the experiment. In method *A*, each block was treated individually by first Fourier transforming the interferogram for every time slice to produce a family of energy curves, and then subtractively normalized using the energy curves for $t < 0$ (*i.e.* prior to the potential step) as a reference. Each of the 256 blocks was processed in this fashion, on an individual basis, and finally the average of all blocks was calculated as expressed mathematically below;

$$\left\langle \frac{\Delta S\left(t,\tilde{\upsilon}\right)}{S} \right\rangle_A = \left\langle \frac{S_n\left(t,\tilde{\upsilon}\right)}{S_n\left(t=0,\tilde{\upsilon}\right)} - 1 \right\rangle \tag{7.5}$$

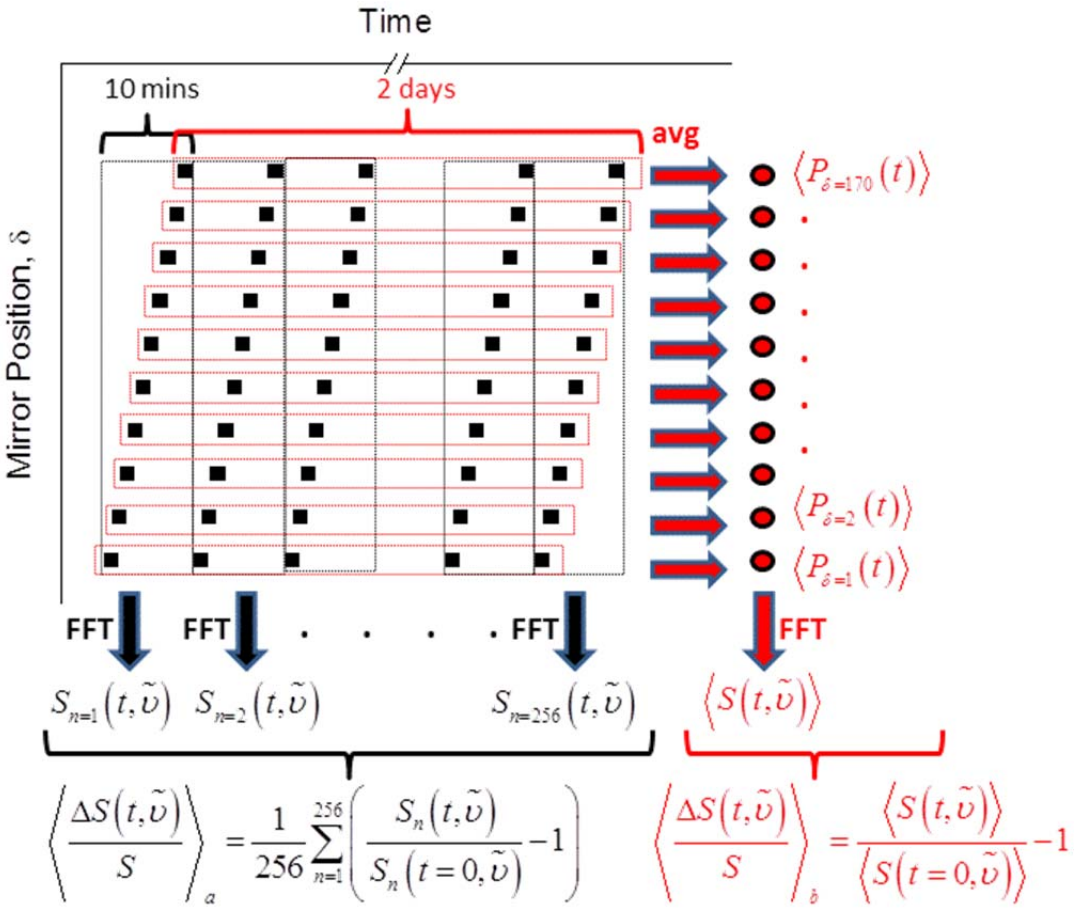

Figure 7.8. Schematic representing the time progression of the step-scan experiment. Two possible methods (*A* and *B*, as described in the text) to generate subtractively normalized spectra are shown. The black points represent the acquisition of 1.5 seconds of 100 μs binned data at each mirror position, δ. Black dotted boxes enclose the mirror positions that constitute a complete interferogram whereas the red dotted boxes comprise all measurements made at a given mirror position.

In method *B*, the 256 interferogram blocks for every time slice at each mirror position were first averaged to produce $\left\langle P_{\delta}(t) \right\rangle$ (*i.e.*, red-dotted boxes in Figure 7.8). A single Fourier transform was applied to the averaged signals to generate one average energy curve for each time slice, $S(t, \tilde{\nu})$, and finally, subtractively normalized as follows,

$$\left\langle \frac{\Delta S\left(t, \tilde{\upsilon}\right)}{S} \right\rangle_{B} = \frac{\left\langle S\left(t, \tilde{\upsilon}\right) \right\rangle}{\left\langle S\left(t = 0, \tilde{\upsilon}\right) \right\rangle} - 1 \tag{7.6}$$

Simply described, the two methods can be considered to be *A*) an average of normalized spectra and *B*) a normalization of averaged spectra. Of note, method *A* is more demanding computationally due to the greater number of FFTs needed to be performed. A distinct advantage, however, to method *A* is that it provides an internal normalization of source variation over a much shorter time period (~10 minutes) compared to method *B*, (~48 days and several strong ring refills). To illustrate this difference, the same ferricyanide spectroelectrochemical data was analyzed using both data processing methodologies and utilizing calculated signal-to-noise ratios as a comparative metric between the two techniques. The noise level, s_N, of each method was first determined by considering the standard deviation of the noise in a 50 millisecond window of the subtractively normalized signal at 2040 cm^{-1} just prior to the application of the potential step (*i.e.* t = -0.25 seconds ± 25 milliseconds). Figure 7.9 depicts plots of the inverse of s_N as a function of the square root of the number of co-added and averaged spectra, N. After co-adding all 256 data blocks, the noise level from method *B* is found to be nearly double that of method *A*. This result clearly emphasizes the advantage, and need, of a data processing method that inherently accounts for source intensity variation. Interestingly, the order in which the spectra were co-added affects the shape of the ensemble averaging results for method *A*. If the 256 subtractively normalized spectra are sequentially co-added in the order of

which they were measured (*i.e.* chronologically), portions of the plot are linear (with varying slope) but in other regions additional co-additions do not improve the overall noise level. Instead, if the 256 spectra produced using method *A* are randomly co-added, a nearly perfect linear dependence of s_N^{-1} on $n^{1/2}$ results. This highlights the degree of noise variation that can occur during the course of a prolonged synchrotron infrared experiment which is more than likely synchrotron source dependent. A mechanism to isolate the parameter, or parameters, that lead to vacillating noise levels is not completely obvious nor is a means to readily identify and discriminate anomalously noisy interferograms (from the nearly 4 million collected for this experiment) that degrade the signal-to-noise. However, Figure 7.9 does indicate that the overall quality of the step-scan synchrotron infrared data is somewhat degraded by a relatively few number of compromised interferograms. Further improvements in terms of the data acquisition and processing in this regard should improve the benefits of ensemble averaging.

The unfiltered infrared transient showing the formation of eletrogenerated ferrocyanide is presented in Figure 7.10a. The subtractively normalized peak height at the position of the ferrocyanide band maximum ($\tilde{\nu}_{MAX} = 2040\text{cm}^{-1}$) was first converted to an absorbance, $Abs = \log\left(\left\langle {}^{\Delta S\left(t,\tilde{\upsilon}=2040\right)}\!/_{S} \right\rangle_A + 1\right)$, before determining the number of moles of ferrocyanide produced *via* Beer's law and the cavity volume, $V_c = h\pi r_e^2$. In addition, the molar extinction coefficient for ferrocyanide as a function of step-scan spectrometer resolution was required and a discussion on the determination of this value was provided in the Experimental section of Chapter 6. A 50 Hz low pass Fourier Filter was applied to the data presented in Figure 7.10a and is plotted in Figure 7.10b to compare these experimental results to those determined from the finite difference simulations previously described. One can see from Figure 7.10b that the simulation of diffusion within the thin cavity is in very good qualitative agreement with the measured result.

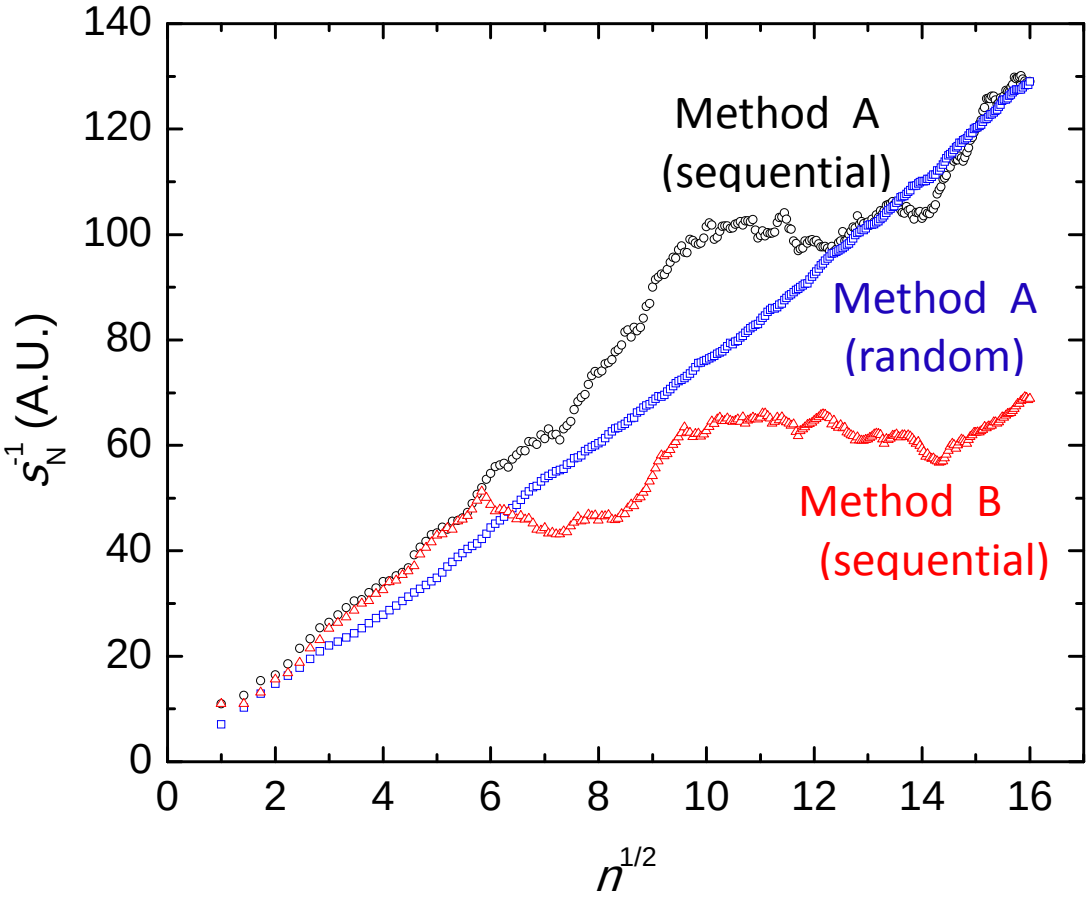

Figure 7.9. Inverse of the standard deviation of the noise plotted as a function of the square root of the number of co-added spectra. The black open circles are calculated from the sequential co-additions method (Method *A*) using Equation 7.5 and the red open triangles (Method *B*) using Equation 7.6. The blue open squares are the result of randomly co-adding the 256 normalized spectra using Equation 7.5.

This confirms that the majority of ferricyanide flux sustaining the electrochemically measured current transient occurs at the electrode perimeter and is not spectroscopically detected. From Figure 7.10b, it can also be seen that that treatment of the thin cavity volume in terms of finite, linear diffusion overestimates the actual signal by approximately 15%. This is in contrast to the previous chapter (Chapter 6) where linear, finite diffusion was found to be in excellent agreement with the experimental result. This difference is attributed to the size of the electrodes used in the different experiments with the electrode used in Chapter 6 being an order of magnitude larger. The influence of the electrode size is easily understood through consideration of the diffusion space (*vide supra*).

Figure 7.10 also provides insight to the maximum achievable sensitivity using synchrotron infrared spectromicroscopy and ultramicroelectrodes at the Canadian Light Source. As shown in Figure 7.10(a), the limit of detection (LOD) calculated as three times the standard deviation about the noise level) is 36 fmol and the analytical signal giving rise to the LOD is not reached until 10 milliseconds after the potential step. The thickness of the depletion layer, z_d, after this time (10 milliseconds) can be estimated using $z_d = \sqrt{4Dt}$, to be approximately 5 μm. Clearly, with no surface enhancement in the current experimental configuration, detection limits on the order of tens of femtomoles can be obtained. Further optimization of these conditions, particularly by using different redox couples that have larger intrinsic absortivities and peak absorbances at frequencies well removed from beamline/synchrotron interferences (*e.g.* a diamond window at the 01B1 Mid-IR Beamline at the CLS attenuates the throughput at 2000-2200 cm^{-1} by approximately 80%) could lower the LOD by a further order of magnitude.

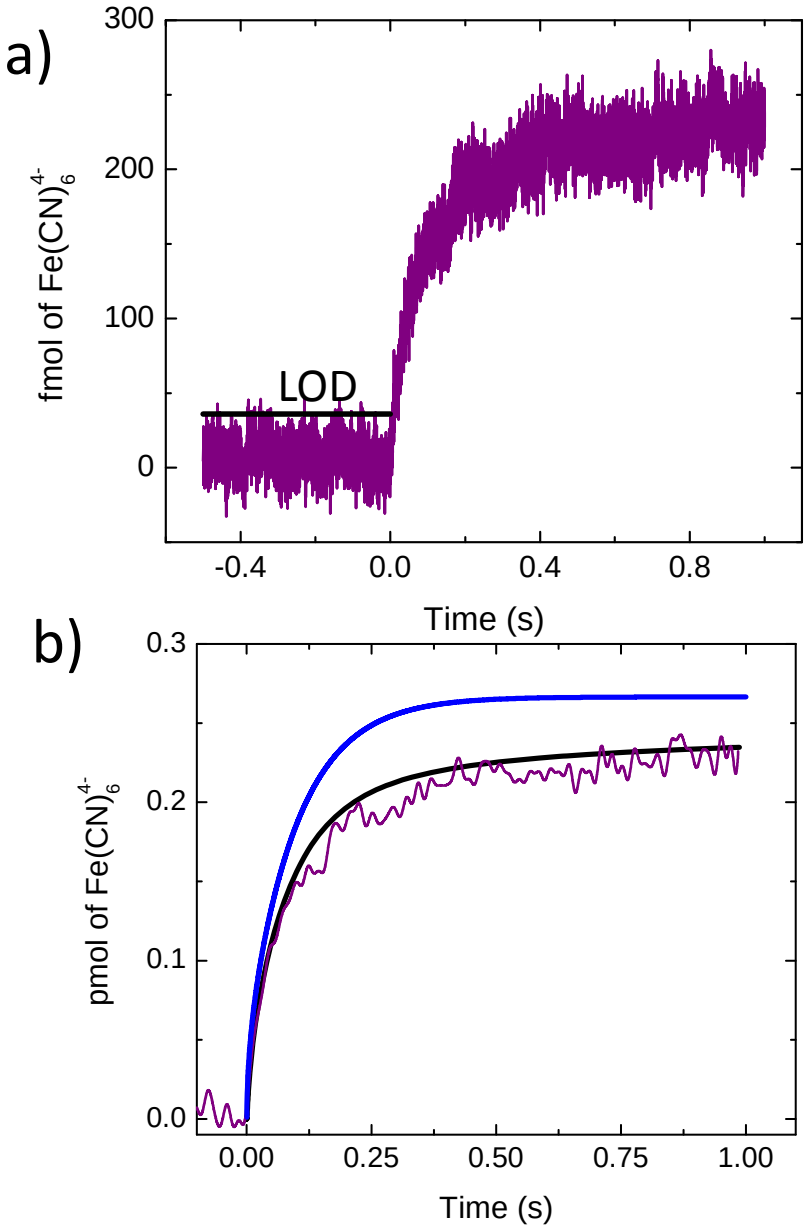

Figure 7.10. a) Transient response measured spectroscopically for the 2040 cm^{-1} band during a potential step. B) The filtered transient measurement (purple line) compared to the calculated results for finite, linear diffusion (blue line) and the simulated results using finite differences (black line). The limit of detection (LOD) is shown as the horizontal black line in the part a) of the figure.

7.4. Summary and Conclusions

The work presented in this chapter has greatly improved the previous spectroelectrochemical studies, presented in Chapter 6, using synchrotron infrared radiation through the technically challenging implementation of step-scan Fourier Transform interferometry and true ultramicroelectrodes. From an electrochemical perspective, a theoretical time constant of less than 1 μs for the *in-situ* spectroelectrochemical cell has been achieved and the mass-transport limited electrochemical signal has been successfully modelled using a finite-differences approaches. As such, the diffusion behaviour within a finite cavity volume has been fully described and the majority of electrochemical current arises from diffusion to the perimeter of the embedded electrode rather than from material flux to the middle of the electrode surface. The contribution to the overall current from edge effects becomes increasingly more dominant with increasing time after the potential step. Expanding from the results in Chapter 6, the purely electrochemical response in the thin-cavity cell include contributions from both linear and radial diffusion, it has been shown for both large (0.5 mm diameter) and small (25 μm diameter) electrodes that the infrared spectroscopic signal arises solely from redox species originating in the thin-cavity created between the electrode surface and the infrared window. As demonstrated by this present case, a maximum analytical signal of 235 fmol was obtainable. The time-resolved detection of electrogenerated ferrocyanide from ferricyanide has been accomplished by coupling Fourier Transform step-scan experiments with synchrotron infrared radiation. *In-situ* spectroelectrochemical measurements, with time resolution approaching the time constant of the electrochemical cell (~ 1 μs), can be readily made with the configuration described herein and were only prohibited by the relatively slow, diffusion controlled electrochemical process studied.

This work has also provided a description of data processing methods that illustrate the possible deleterious effect caused by synchrotron-derived source variation. Careful consideration of data processing strategies is needed to account for beam current decay when operating in normal decay mode. By correctly doing so, noise signals behave in a random fashion and ensemble averaging provides the expected √n dependence. The estimated limit of detection for ferrocyanide detection approaches the femtomole level. However, it is evident that further advancement in microsecond-resolved spectroelectrochemical measurements of electrochemical processes will require surface sensitivity and microscope objectives/UME preparations that provide surface enhancements. These next steps are beyond the scope of this work but will be discussed as possible further directions in the final chapter (Chapter 8).

7.5. References

1. Dumas, P.; Miller, L. The Use of Synchrotron Infrared Microspectroscopy in Biological and Biomedical Investigations. *Vibrational Spectroscopy* **2003**, *32*, 3–21.

2. Dumas, P.; Sockalingum, G. D.; Sule-Suso, J. Adding Synchrotron Radiation to Infrared Microspectroscopy: What's New in Biomedical Applications? *Trends in Biotechnology* **2007**, *25*, 40–44.

3. Miller, L. M.; Dumas, P. Chemical Imaging of Biological Tissue with Synchrotron Infrared Light. *Biochimica et Biophysica Acta, Biomembranes* **2006**, *1758*, 846–857.

4. Miller, L. M.; Smith, R. J. Synchrotrons Versus Globars, Point-detectors Versus Focal Plane Arrays: Selecting the Best Source and Detector for Specific Infrared Microspectroscopy and Imaging Applications. *Vibrational Spectroscopy* **2005**, *38*, 237–240.

5. Zamlynny, V.; Lipkowski, J. Quantitative SNIFTIRS and PM IRRAS of Organic Molecules at Electrode Surfaces. *Diffraction and Spectroscopic Methods in Electrochemistry* **2006**, *9*, 315–376.

6. Osawa, M. In-Situ Surface-enhanced Infrared Spectroscopy of the Electrode/Solution Interface. In *In Diffraction and Spectroscopic Methods in Electrochemistry*; Alkire, R. C., Kolb, D., Lipkowski, J., Ross, P. N., Ed.; 2006; pp. 269–314.

7. Zhou, Z.-Y.; Lin, S.-C.; Chen, S.-P.; Sun, S.-G. In Situ Step-scan Time-resolved Microscope FTIR Spectroscopy Working with a Thin-layer Cell. *Electrochemistry Communications* **2005**, *7*, 490–495.

8. Nowak, C.; Luening, C.; Schach, D.; Baurecht, D.; Knoll, W.; Naumann, R. L. C. Electron Transfer Kinetics of Cytochrome C in the Submillisecond Time Regime Using Time-Resolved Surface-Enhanced Infrared Absorption Spectroscopy. *Journal of Physical Chemistry C* **2009**, *113*, 2256–2262.

9. Ataka, K.; Hara, Y.; Osawa, M. New Approach to Electrode Kinetics and Dynamics by Potential Modulated Fourier Transform Infrared Spectroscopy. *Journal of Electroanalytical Chemistry* **1999**, *473*, 34–42.

10. Wisitruangsakul, N.; Zebger, I.; Ly, K. H.; Murgida, D. H.; Ekgasit, S.; Hildebrandt, P. Redox-Linked Protein Dynamics of Cytochrome C Probed by Time-Resolved Surface Enhanced Infrared Absorption Spectroscopy. *Physical Chemistry Chemical Physics* **2008**, *10*, 5276–5286.

11. Pronkin, S.; Wandlowski, T. Time-resolved in Situ ATR-SEIRAS Study of Adsorption and 2D Phase Formation of Uracil on Gold Electrodes. *Journal of Electroanalytical Chemistry* **2003**, *550-551*, 131–147.

12. Osawa, M.; Yoshii, K.; Ataka, K.; Yotsuyanagi, T. Real-time Monitoring of Electrochemical Dynamics by Submillisecond Time-Resolved Surface-Enhanced Infrared Attenuated-Total-Reflection Spectroscopy. *Langmuir* **1994**, *10*, 640–642.

13. Yamakata, A.; Osawa, M. Dynamics of Double-Layer Restructuring on a Platinum Electrode Covered by CO: Laser-Induced Potential Transient Measurement. *Journal of Physical Chemistry C* **2008**, *112*, 11427–11432.

14. Yamakata, A.; Uchida, T.; Kubota, J.; Osawa, M. Laser-Induced Potential Jump at the Electrochemical Interface Probed by Picosecond Time-Resolved Surface-Enhanced Infrared Absorption Spectroscopy. *Journal of Physical Chemistry B* **2006**, *110*, 6423–6427.

15. Zhou, Z.-Y.; Sun, S.-G. In Situ Step-scan Time-resolved Microscope FTIR Spectroscopy Applied in Irreversible Electrochemical Reactions. *Electrochimica Acta* **2005**, *50*, 5163–5171.

16. Zhou, Z.-Y.; Tian, N.; Chen, Y.-J.; Chen, S.-P.; Sun, S.-G. In Situ Rapid-scan Time-resolved Microscope FTIR Spectroelectrochemistry: Study of the Dynamic Processes of

Methanol Oxidation on a Nanostructured Pt Electrode. *Journal of Electroanalytical Chemistry* **2004**, *573*, 111–119.

17. Lu, G. Q.; Sun, S. G.; Cai, L. R.; Chen, S. P.; Tian, Z. W.; Shiu, K. K. In Situ FTIR Spectroscopic Studies of Adsorption of CO, SCN-, and Poly(o-phenylenediamine) on Electrodes of Nanometer Thin Films of Pt, Pd, and Rh:Abnormal Infrared Effects (AIREs). *Langmuir* **1999**, *16*, 778–786.

18. Evgenij Barsoukov, J. R. M. *Impedance Spectroscopy: Theory, Experiment, and Applications*; John Wiley & Sons, Ltd, 2005.

19. Heinze, J. Electrochemistry with Ultramicro-electrodes. *Angewandte Chemie* **1993**, *105*, 1327–1349.

20. Bard, A. J.; Denuault, G.; Friesner, R. A.; Dornblaser, B. C.; Tuckerman, L. S. Scanning Electrochemical Microscopy: Theory and Application of the Transient (chronoamperometric) SECM Response. *Analytical Chemistry* **1991**, *63*, 1282–1288.

21. Kwak, J.; Bard, A. J. Scanning Electrochemical Microscopy. Theory of the Feedback Mode. *Analytical Chemistry* **1989**, *61*, 1221–1227.

22. Mirkin, M. V Theory. In *Scanning Electrochemical Microscopy*; Bard, A. J.; Mirkin, M. V, Eds.; Marcel Dekker: New York, 2001; pp. 145–200.

23. Shoup, D.; Szabo, A. Chronoamperometric Current at Finite Disk Electrodes. *Journal of Electroanalytical Chemistry and Interfacial Electrochemistry* **1982**, *140*, 237–245.

24. Mauzeroll, J.; Hueske, E. A.; Bard, A. J. Scanning Electrochemical Microscopy. 48. Hg/Pt Hemispherical Ultramicroelectrodes: Fabrication and Characterization. *Analytical Chemistry* **2003**, *75*, 3880–3889.

25. Micka, K.; Kratochvilová, K.; Klíma, J. Electrolysis at a Disc Electrode in a Thin Electrolyte Layer. *Electrochimica Acta* **1997**, *42*, 1005–1010.

26. Oglesby, D. M. Thin Layer Electrochemical Studies Using Controlled Potential or Controlled Current. *Analytical Chemistry* **1965**, *37*, 1312–1316.

27. Korzeniewski, C.; Severson, M. W.; Schmidt, P. P.; Pons, S.; Fleischmann, M. Theoretical Analysis of the Vibrational Spectra of Ferricyanide and Ferrocyanide Adsorbed on Metal Electrodes. *Journal of Physical Chemistry* **1987**, *91*, 5568–5573.

28. Pharr, C. M.; Griffiths, P. R. Infrared Spectroelectrochemical Analysis of Adsorbed Hexacyanoferrate Species Formed During Potential Cycling in the Ferrocyanide/Ferricyanide Redox Couple. *Analytical Chemistry* **1997**, *69*, 4673–4679.

29. Pons, S. Infrared Spectroelectrochemistry of the Fe(CN)4- 6/Fe(CN)3- 6. *Journal of Electroanalytical Chemistry* **1984**, *160*, 369–376.

30. Pharr, C. M.; Griffiths, P. R. Step-Scan FT-IR Spectroelectrochemical Analysis of Surface and Solution Species in the Ferricyanide/Ferrocyanide Redox Couple. *Analytical Chemistry* **1997**, *69*, 4665–4672.

31. Andrews, S. S.; Boxer, S. G. Analysis of Noise for Rapid-Scan and Step-Scan Methods of FT-IR Difference Spectroscopy. *Applied Spectroscopy* **2001**, *55*, 1161–1165.

32. Rodig, C.; Siebert, F. Instrumental Aspects of Time-Resolved Spectra Generated Using Step-Scan Interferometers. In *Handbook of Vibrational Spectroscopy*; John Wiley & Sons, Ltd, 2006.

33. YaoWu, X.; Mark, B. Step-Scan Time-Resolved FT-IR Spectroscopy of Biopolymers. In *Vibrational Spectroscopy of Biological and Polymeric Materials*; CRC Press, 2005; pp. 353–418.

CHAPTER 8

CONCLUSIONS AND FUTURE WORK

8.1. Conclusions

The advancement of several research techniques for *in-situ* infrared spectroelectrochemistry (SEC) is highlighted in this thesis. It has long been recognized by electrochemists that electrochemical measurements alone do not always provide definite identification of electroactive molecules at or near the electrified interface. For example, a particular diffusion current might be correlated to a known species, but the molecular identity can still only be inferred from these measurements. This was evident in the work discussed in Chapter 4 where Surface Enhanced Infrared Absorption Spectroscopy (SEIRAS) was used to study the adsorption of dimethylaminopyridine (DMAP) on gold substrates. Previous work solely based on electrochemical data and thermodynamic models provided adsorption geometries of DMAP that were shown to depend on the pH of the aqueous solutions and the surface charge density of the substrate. This thesis has described the development of a SEIRAS technique that allowed for further evidence to be gathered verifying the pre-described thermodynamic models. More interestingly, however, was the newly recognized concept that in acidic electrolytes and at negative potentials, there is a small amount of adsorption of the conjugate acid ($DMAPH^+$). This result, likely due from an electrostatic attraction, was not forthcoming from previous electrochemical studies and was only realized because of the additional information provided through *in-situ* infrared spectroelectrochemistry.

Further instrumental advances were made to improve the data-collection capabilities to of *in-situ* SEC measurements, specifically, time-resolved kinetic information. The added step of

complexity in the collection and processing of data provided a foundation to study complicated, kinetic responses of electrochemical systems. Chapter 5 highlighted this work through the study of the time-resolved kinetics of a proton-coupled electron transfer (PCET) redox reaction on modified self-assembled monolayers (SAMs) using Rapid-Scan FTIR spectroscopy. A method to prepare chemically modifiable SAMs was developed and allowed for the attachment of an electrochemically-active moiety, 1,4-benzoquinone, suitable for the study of PCET thermodynamics and kinetics. A new *in-situ* SEIRAS spectroelectrochemical cell was designed to be robust and reliable and was proven to be very effective for time-resolved measurements. Formal potentials and the heterogeneous rate constants were measured using traditional electrochemical techniques and *in-situ* spectroelectrochemical techniques over a wide range of pHs. The results from different methodologies were in good agreement and demonstrated a shift in the formal potential to more positive potentials with increasing electrolyte acidity with a ~60 mV pH^{-1} dependence. This was the predicted result for a two-proton two electron system. However, what was not predicted by literature models was the observation that the logarithm of the apparent standard rate constant decreasing linearly with pH. It is speculated that more subtle changes in the rate constant dependence were most likely obscured by the kinetic heterogeneity of the system, which was purposely designed to exhibit relatively slow electron transfer kinetics such that they could be measured using this SEIRAS technique.

The ability to measure faster electrochemical systems requires the use of small working electrodes in order to increase the electrochemical responsiveness of the system. Complimentary to this, faster infrared spectroscopic collection techniques need to be employed to match the increase in electrochemical dynamics. This represents a paradox in experimental terms as small electrodes are required electrochemically whereas large electrodes are preferred

spectroscopically to achieve high photon throughput. If the size of the working electrode is decreased to afford fast electrochemistry, there is a considerable decrease in the infrared photon flux incident on the smaller electrode surface. With fewer infrared photons probing the electrode and fewer electrochemically active molecules in the infrared beam path, the diminishing loss of sensitivity in the spectroscopic measurements limits the feasibility of moving towards faster electrochemical systems measured with fast infrared spectroscopic techniques. Developments to mitigate these two incongruent concepts were the primary focus of the last two experimental chapters (Chapter 6 and 7) and highlight the largest contributions this body of work has made in advancing *in-situ* infrared SEC techniques.

To overcome these problems, methodologies were developed to utilize the high brilliance and spatial resolution of synchrotron infrared sources. This necessitated switching from internal reflection geometries (SEIRAS) to external reflection geometries and required the use of focused (*via* an infrared microscope) synchrotron infrared radiation. To the best of the author's knowledge, this work represented the first instances in which dynamic (non-equilibrium) electrochemical interfaces were studied using synchrotron sources for infrared *in-situ* SEC. In Chapter 6, these ideas were first explored through the development of a thin-cavity *in-situ* SEC cell, required for external reflectance, housing a near ultramicroelectrode (UME) sized working electrode (250 μm radius). Electrochemically, this cell was shown to be capable of achieving millisecond time-resolution (5xRC = 1.25 milliseconds) and through experimental measurements of the ferro/ferri-cyanide redox system demonstrated diffusion current limited responses. Spectroscopically, the *in-situ* measurements were made using rapid-scan (continuous mode) Fourier Transform Infrared Spectroscopy allowing for temporal measurements in the ~ 100 millisecond time regime. Efforts to understand the diffusion current characteristics of the thin-

cavity electrochemical cell lead to various theoretical simulations and fitting to the experimentally obtained data. An empirical model was developed that fit the electrochemical data at short times to contributions mainly from the electroactive material directly above the electrode in the thin-cavity and at long times from the radial diffusion towards the edge of the electrode. Importantly, the infrared spectral response can only describe the molecular changes in the material directly above the electrode and not the material contributing to the radial electrochemical signal.

Chapter 7 continued the work from Chapter 6 by introducing the use of a true ultramicroelectrode and increased time-resolved spectroscopic data collection through step-scan Fourier Transform Infrared Spectroscopy and synchrotron infrared radiation. Using a ten times smaller working electrode (25 μm radius), sub-millisecond (5xRC ~ 1 microsecond) time responses were obtained with a spectral time-resolution on the order of tens of microseconds. The ferro/ferri-cyanide redox couple was employed to examine the diffusion current behaviour within the thin-cavity *in-situ* SEC cell. Unlike the analysis performed for the larger electrode (Chapter 6), this problem was analyzed through numerical simulations.

As a result of this treatment, the diffusion behaviour within a finite thin-cavity volume has been fully described and it was shown that the majority of the electrochemical current arises from diffusion to the perimeter of the embedded electrode rather than from material flux to the electrode surface. As such, the contribution to the overall current from edge effects becomes the more dominant source with increasing time after the potential step. From these results, and those described in Chapter 6, the purely electrochemical response in a thin-cavity cell includes contributions from both linear and radial diffusion. Also, both electrodes only report the infrared

spectroscopic signal arising solely from redox species originating in the thin-cavity created between the electrode surface and the infrared window.

A further result demonstrated a spectroscopic limit of detection (LOD) to be ~36 fmol for the ferro/ferricyanide redox couple. It is important to keep in mind that this LOD could be improved by analysis of electroactive species with spectroscopic signals away from the large diamond window absorbance present in the beamline optics at the Canadian Light Source. Through the discussion presented in Chapter 7, a description of different data processing methods illustrate the possible deleterious effect caused by synchrotron-derived source variations. Careful consideration of data processing strategies are required to account for beam current decay when operating in normal decay mode and also to correct for other sources of noise present in synchrotron infrared sources. By correctly doing so, noise signals behave in a random fashion and ensemble averaging provides the expected $\sqrt{n}$ dependence.

In summary, *in-situ* infrared spectroelectrochemistry is a powerful tool to elicit molecular information at or near an electrified interface providing insight into structure, orientation and kinetic details of electrochemical processes. This thesis has highlighted a progression from developing methodologies and instrumentation to providing improved understanding of electrochemical related phenomena of surfaces. This advancement has required the adaptation of previously developed methods, *e.g.* surface enhanced infrared absorption spectroscopy (SEIRAS), to completely new areas of utilizing bright highly focused synchrotron infrared radiation with ultramicroelectrodes to measure *in-situ* spectroelectrochemical information on the microsecond time scale. This thesis concludes with a section detailing possible directions and future enhancements to address some of the current limitations in detection and time-resolution as well as some possible applications that would benefit from this work.

8.2. Future Work

Given the successes demonstrated in combining electrochemistry with synchrotron infrared radiation in the latter part of this thesis, further instrumental developments to improve the sensitivity of these measurements is a logical place to continue the work in this field. In particular two projects worth pursuing in this area use different methodologies to construct substrates for surface enhanced infrared absorption spectroscopy (SEIRAS) that are compatible with microscope objectives commonly used in infrared microscopy. In doing so, the surface sensitivity of these experiments should be increased, decreasing the limit of detection. For example, the continued development of microstructured silicon wafers fabricated in such a way to couple infrared radiation for attenuated total-internal reflection (ATR) is a possible means to achieve surface sensitivity. Current methods use monolithic silicon, germanium or zinc selenide prisms, typically hemispherical for single bounce or wedged shaped for multi-bounce geometries. A disadvantage to these particular optical elements is the large path lengths the light must travel in the ATR element, often with absorption losses. For example, the most commonly used infrared ATR element, silicon, has strong infrared absorptions due to silicon lattice vibrations that absorb infrared radiation between 300 cm^{-1} and 1500 cm^{-1}. By decreasing the thickness of the ATR element to the thickness of commonly available silicon wafers (~500 μm), high optical throughput throughout the entire mid-infrared range can be achieved with the flexibility to host a variety of *in-situ* or *ex-situ* applications. The microstructured silicon ATR elements considered here consist of a periodic array of v-shaped grooves chemically wet-etched onto the backside of a Si (100) wafer (Figure 8.1a).[2]

The primary function of etching an array of periodic grooves in the Si ATR element is to overcome the problem of coupling infrared radiation through a Schwarzchild objective lens for

total-internal reflection. The shallow angle of incidence (~ 24^{o} half angle, for an objective with NA = 0.4) is below the critical angle required for total-internal reflection within the Si wafer. The array of "v-shaped" grooves preferentially etched in the Si wafer changes the angle of incidence from the infrared microscope to the wafer as the grooves form a 54.7^{o} angle from the surface normal of the wafer. In this arrangement, the incident light from the infrared microscope is now capable of entering the Si wafer above the critical angle and can be totally-internally reflected.

In addition to this, there is an angle dependence of the incident radiation polarization. From Chapter 3, only p-polarized radiation is responsible for any SEIRAS related signals and increases in intensity to a maximum angle of incidence at 80^{o} to the reflection surface normal.[3] By etching these grooves in the Si wafer, not only does it allow the incident beam to be totally internally reflected, but it moves the angle of incidence closer to the maximum angle and results in an increase in intensity.

The preparation of these ATR elements utilizes common silicon processing technologies developed in the semi-conductor industry. Initial attempts to prepare these substrates are presented in Figure 8.1b following the procedure outlined by Schumacher *et al.*[2] From this figure, one can see that the desired v-shaped pattern has been successfully wet-etched into the backside of the silicon wafer. Further refinements to this pattern are needed by optimization of the groove spacing and depth for maximum total internal reflection. Once adjusted, one could theoretically metalize the non-machined side of the ATR element with gold, similar to the work presented in Chapters 4 and 5, to allow for *in-situ* spectroelectrochemical SEIRAS measurements. These substrates could be utilized for SEIRAS measurements using a conventional infrared source and a bench-top spectrometer, or coupled with a synchrotron

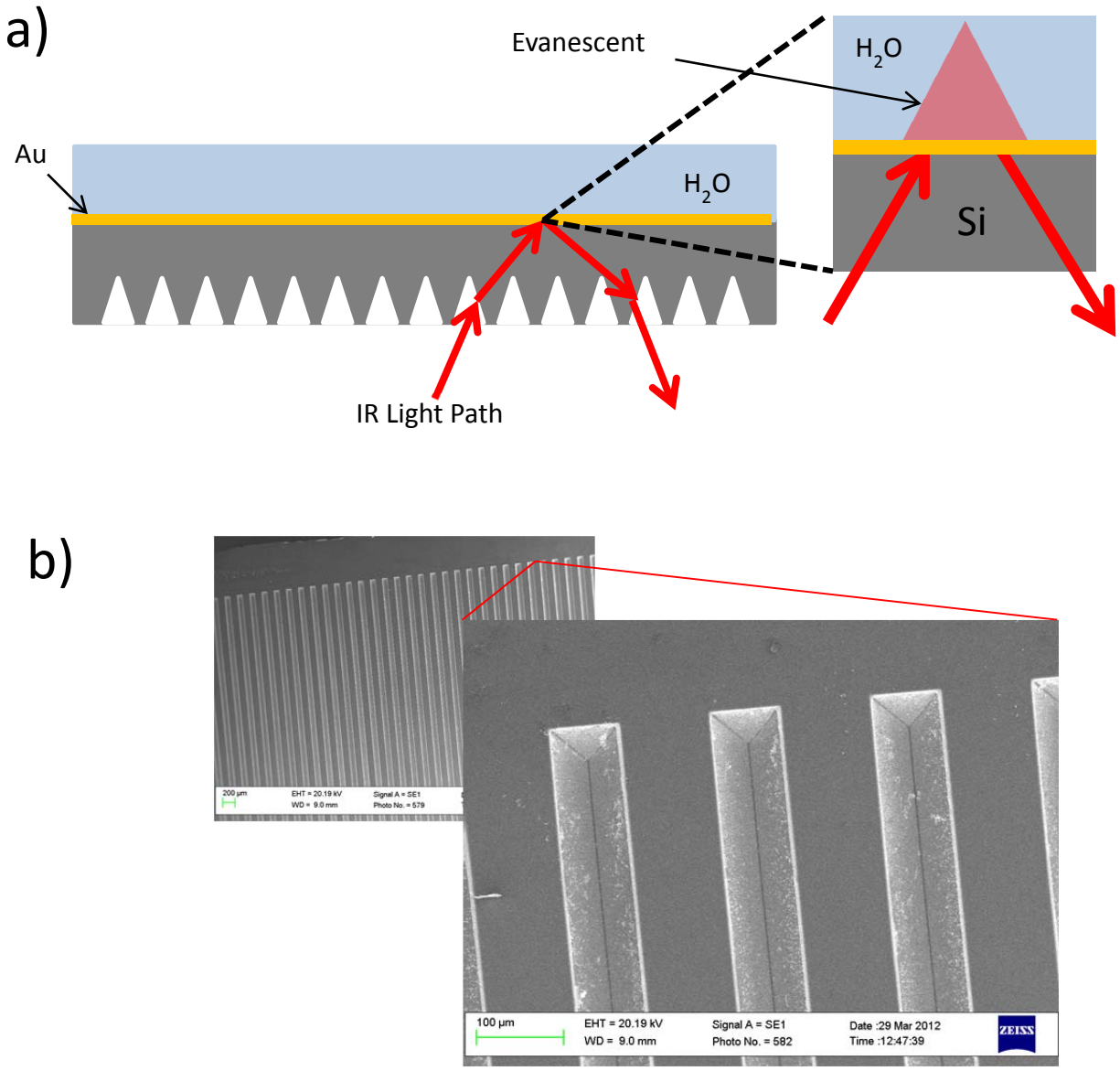

Figure 8.1. a) Schematic of the microstructured silicon attenuated total-internal reflection (ATR) element with optical path and evanescent wave propagation for surface enhanced infrared absorption spectroscopy (SEIRAS). b) Scanning electron microscope images of the initial attempts to construct microstructured Si ATR elements.

infrared radiation source and an optical/infrared microscope.

A particular problem with the above described Si microstructured ATR elements is that although highly transparent in the infrared, they are opaque in the visible light region of the electromagnetic spectrum. This makes it incredibly difficult for microscopy related applications which provides the motivation for the next project. An optically transparent, both in the visible and infrared portions of the electromagnetic spectrum, CaF_2 (and ZnSe partially transparent in the visible) window can be patterned with gold nanostructures to produce highly sensitive plasmonic substrates. Halas *et al.*[4] have demonstrated, through the use of electron beam lithography, that long (between 575 – 1800 nm) and narrow (50 nm) gold antenna cross structures can be fashioned to produce theoretical surface enhancement factors of more than 12000. The large enhancement of the electric field at the surface of the plasmonic structures allows for near zeptomolar sensitivities in the infrared. This is accomplished by specifically engineering the structures, by changing their size and shape, to tune the electric fields created around them through illumination of appropriate infrared light. This enhancement effect, similar to that proposed to be responsible for surface enhanced Raman spectroscopy (SERS), is due to the collective excitation and oscillations of the metal electrons present in the structure.[5] These surface plasmons can be tailored in such a way that their resonant frequency can be matched with a given molecular vibration coupling the intensities and providing an enhancement of the molecular vibration. By this means, small and weak infrared absorption signals can effectively be enhanced to measurable levels allowing for near single molecule sensitivities.

An issue with the above approach taken by Halas and co-workers is the high costs associated with electron beam lithography. To produce just one mask, costs can amount to tens

of thousands of dollars. However, a low-cost alternative for tunable resonant structure for SEIRAS can be realized.[6] This is a current direction of interest within the author's current research group and is demonstrating some encouraging preliminary results. Briefly, strong electric-field enhancements can be realized by tuning fabricated arrays of triangular gold microstructures, antennas, on infrared transparent windows. This is accomplished through low-cost colloidal lithography with micrometer-sized polystyrene spheres. These substrates are prepared by drop casting polystyrene sphere suspensions onto CaF_2 windows. Once the solvent has evaporated, a thin layer of gold is deposited on the substrate coating both the polystyrene spheres and the holes formed between the spheres (Figure 8.2a). Removal of the spheres results in a honeycomb pattern of gold triangular antennas capable of enhancing infrared vibrations specific to the size of the antennas (Figure 8.2b). By varying the size of the micrometer-sized polystyrene spheres, one can tune the antenna resonance across the infrared spectrum and tailor the substrate to the particular chemical systems of interest. Transitioning this fabrication technique to use conductive glass materials (*i.e.* indium titanium oxide, ITO), one could imagine the eventual incorporation of these substrates for *in-situ* spectroelectrochemical measurements utilizing highly brilliant focused synchrotron radiation.

With the infrared enhancements to the sensitivity described above, more challenging electrochemical systems can be examined. For example, the long experimental times required to achieve adequate signal-to-noise levels for the step-scan time-resolved *in-situ* spectroelectrochemical measurements meant it was not feasible to measure the kinetics of irreversible electrochemical reactions. In order to perform these measurements, after each potential step the analyte would need to be flushed from the thin-cavity cell and replenished with

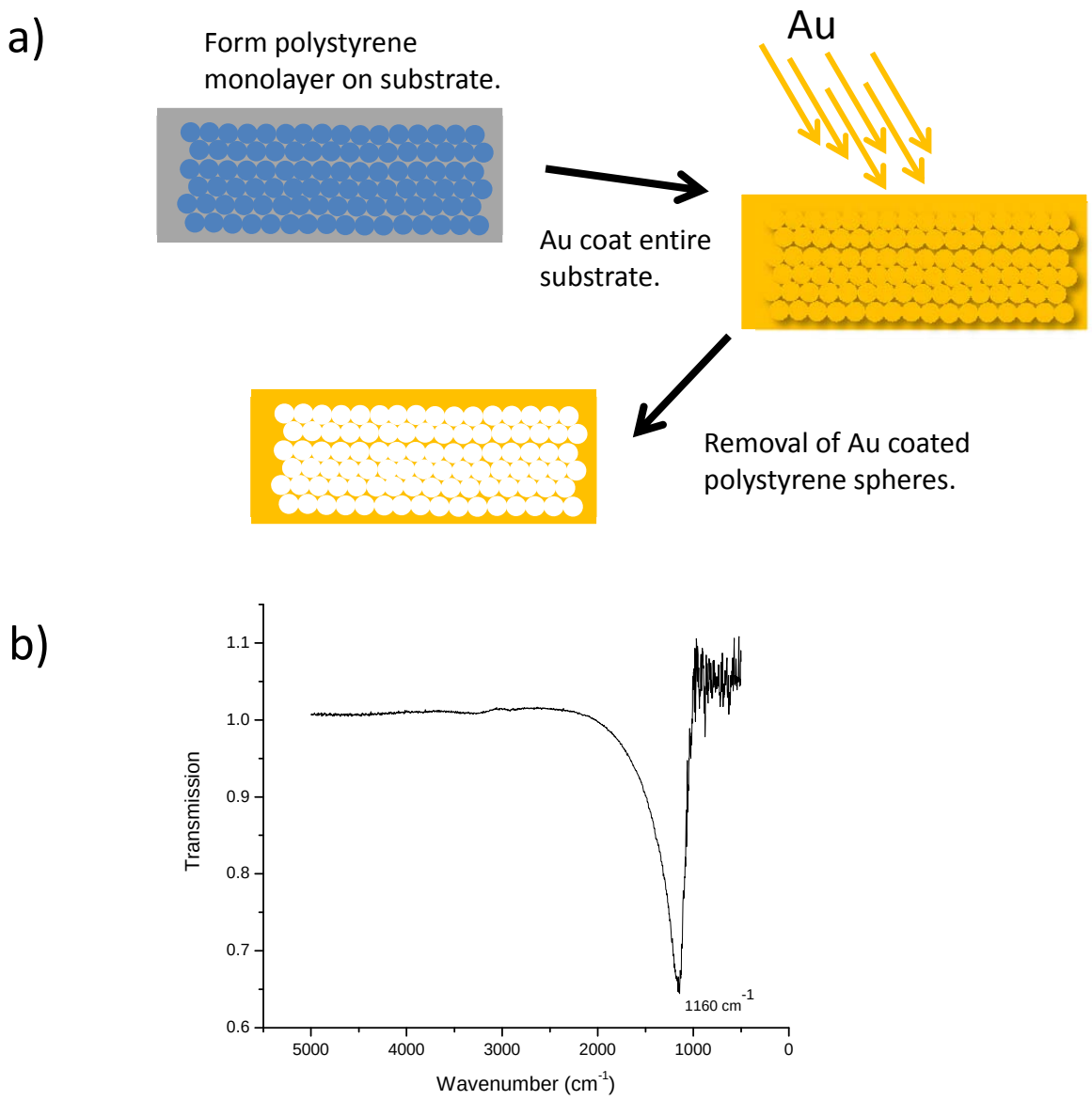

Figure 8.2. a) Step-by-step procedure in the construction of the triangular antennas surface enhanced infrared absorption spectroscopy. B) Example infrared spectrum demonstrating the enhancement of the infrared signal by the strong electric-field enhancements provided by the fabricated array of antennas on the infrared window substrate at the resonance frequency (1160 cm^{-1}). Substrates and measurements were prepared and taken with permission from by Tyler Morhart.

fresh material. This added step, although easily achieved using peristaltic pumps and control systems, adds seconds to each potential step measurement. In the context of the step-scan measurements described in Chapter 7, with 170 mirror positions measured for one interferogram adding seconds to each mirror measurement translates to minutes for an interferogram. Co-adding multiple interferograms will add hours (potentially days) to a given step-scan measurement.

With the larger surface enhancements that could be achieved with one of the methods described above, these measurements become more achievable as several orders of magnitude improvements to the signal-to-noise are predicted.[3] This has the potential to decrease the total number of co-added scans required to complete a time-resolved kinetic *in-situ* spectroelectrochemical measurement using step-scan interferometry. Coupled with the fully described diffusion current properties of thin-cavity electrochemical cells (described in Chapters 6 and 7), valuable information can obtained for important irreversible electrochemical reactions. Some example systems include the endo-cyclization of dopamine[7] and the analysis of the byproducts produced during the oxidation of methanol in fuel cells.[8–10]

These are just a few potential ideas to move the field of *in-situ* infrared spectroelectrochemical techniques forward and a brief example of what more complicated and advanced electrochemical problems that could be analyzed. Much of the work presented in this thesis has focused on the challenging instrumental foundations required to move forward to understand more complicated electrochemical processes. Along this development, meaningful results in the understanding of electrochemical related phenomena of surface adsorption, proton-coupled electron transfer processes and diffusion in thin-cavity environments were realized.

8.3. References

1. Mirkin, M. V Theory. *Scanning Electrochemical Microscopy* **2001**.

2. Schumacher, H.; Künzelmann, U.; Vasilev, B.; Eichhorn, K.-J.; Bartha, J. W. Applications of Microstructured Silicon Wafers as Internal Reflection Elements in Attenuated Total Reflection Fourier Transform Infrared Spectroscopy. *Applied spectroscopy* **2010**, *64*, 1022–7.

3. Osawa, M. In-Situ Surface-enhanced Infrared Spectroscopy of the Electrode/Solution Interface. In *In Diffraction and Spectroscopic Methods in Electrochemistry*; Alkire, R. C., Kolb, D., Lipkowski, J., Ross, P. N., Ed.; 2006; pp. 269–314.

4. Brown, L. V; Zhao, K.; King, N.; Sobhani, H.; Nordlander, P.; Halas, N. J. Surface-Enhanced Infrared Absorption Using Individual Cross Antennas Tailored to Chemical Moieties. *Journal of the American Chemical Society* **2013**, *135*, 3688–3695.

5. Chen, K.; Adato, R.; Altug, H. Dual-band Perfect Absorber for Multispectral Plasmon-enhanced Infrared Spectroscopy. *ACS nano* **2012**, *6*, 7998–8006.

6. Hoffmann, J. M.; Yin, X.; Richter, J.; Hartung, A.; Maß, T. W. W.; Taubner, T. Low-Cost Infrared Resonant Structures for Surface-Enhanced Infrared Absorption Spectroscopy in the Fingerprint Region from 3 to 13 Mm. *The Journal of Physical Chemistry C* **2013**, *117*, 11311–11316.

7. González-Diéguez, N.; Colina, A.; López-Palacios, J.; Heras, A. Spectroelectrochemistry at Screen-Printed Electrodes: Determination of Dopamine. *Analytical Chemistry* **2012**, *84*, 9146–9153.

8. Chen, Y. X.; Miki, A.; Ye, S.; Sakai, H.; Osawa, M. Formate, an Active Intermediate for Direct Oxidation of Methanol on Pt Electrode. *Journal of the American Chemical Society* **2003**, *125*, 3680–3681.

9. Marković, N. M.; Ross Jr., P. N. Surface Science Studies of Model Fuel Cell Electrocatalysts. *Surface Science Reports* **2002**, *45*, 117–229.

10. Korzeniewski, C.; Childers, C. L. Formaldehyde Yields from Methanol Electrochemical Oxidation on Platinum. *The Journal of Physical Chemistry B* **1998**, *102*, 489–492.